CONTENTS

Page

2.3-ii

INTENTIONALLY LEFT BLANK

TABLES

Page

INTENTIONALLY LEFT BLANK

FIGURES

Page

INTENTIONALLY LEFT BLANK

2.3   MODEL ABSTRACTION

Section 2.3 and its subsections describe the technical basis for the total system performance assessment (TSPA) abstraction models associated with the Upper Natural Barrier, the Engineered Barrier System (EBS), and the Lower Natural Barrier. These abstraction models reproduce, or bound, the essential elements of the more detailed process models. These models are used to assess the effects of included processes and events on natural and engineered features.

To clarify terminology, an abstraction model may also be referred to as an "abstraction," "model abstraction," or "abstracted model." Subject matter areas addressed through one or more abstraction models are referred to herein as "model abstraction topics," which is consistent with the terminology in NUREG-1804. The structure of Section 2.3 and its subsections has been modified somewhat from the structure of the model abstraction topics provided in NUREG-1804, Section 2.2.1.3, in order to allow a more direct correlation between the Section 2.3 subsections; the TSPA model (Section 2.4); and the individual features, events, and processes (FEPs) identified in Section 2.2. The table below shows the subject (i.e., information category) of each Section 2.3 subsection as well as the regulatory requirements and NUREG-1804 acceptance criteria that are related to each subsection.

SAR Section	Information Category	Proposed 10 CFR Part 63 Reference	NUREG-1804 Reference
2.3.1	Climate and Infiltration	63.21(c)(1)(iii)[a] 63.21(c)(9)[a] 63.21(c)(15)[a] 63.114(a)(1) 63.114(a)(2) 63.114(a)(3) 63.114(a)(4) 63.114(a)(5) 63.114(a)(7) 63.114(b) 63.342(c)	Section 2.2.1.3.5.3: Acceptance Criterion 1 Acceptance Criterion 2 Acceptance Criterion 3 Acceptance Criterion 4 Acceptance Criterion 5
2.3.2	Unsaturated Zone Flow	63.21(c)(1)(ii)[a] 63.21(c)(9)[a] 63.21(c)(15)[a] 63.114(a)(1) 63.114(a)(2) 63.114(a)(3) 63.114(a)(4) 63.114(a)(5) 63.114(a)(7) 63.114(b) 63.342(c)	Section 2.2.1.3.6.3: Acceptance Criterion 1 Acceptance Criterion 2 Acceptance Criterion 3 Acceptance Criterion 4 Acceptance Criterion 5

SAR Section	Information Category	Proposed 10 CFR Part 63 Reference	NUREG-1804 Reference
2.3.3	Water Seeping into Drifts	63.21(c)(1)(ii)[a] 63.21(c)(9)[a] 63.21(c)(15)[a] 63.114(a)(1) 63.114(a)(2) 63.114(a)(3) 63.114(a)(4) 63.114(a)(5) 63.114(a)(7) 63.114(b) 63.342(c)	Section 2.2.1.3.3.3: Acceptance Criterion 1(1) Acceptance Criterion 1(2) Acceptance Criterion 1(3) Acceptance Criterion 1(4) Acceptance Criterion 1(5) Acceptance Criterion 1(7) Acceptance Criterion 1(8) Acceptance Criterion 1(9) Acceptance Criterion 1(12) Acceptance Criterion 2(1) Acceptance Criterion 2(2) Acceptance Criterion 2(3) Acceptance Criterion 3(1) Acceptance Criterion 3(2) Acceptance Criterion 3(3) Acceptance Criterion 3(4) Acceptance Criterion 3(6) Acceptance Criterion 4 Acceptance Criterion 5 Section 2.2.1.3.6.3: Acceptance Criterion 1(6)
2.3.4	Mechanical Degradation of the Engineered Barrier System	63.21(c)(1)(ii)[a] 63.21(c)(9)[a] 63.21(c)(15)[a] 63.114(a)(1) 63.114(a)(2) 63.114(a)(3) 63.114(a)(4) 63.114(a)(5) 63.114(a)(6) 63.114(a)(7) 63.114(b) 63.342(c)	Section 2.2.1.3.2.3: Acceptance Criterion 1(1) Acceptance Criterion 1(2) Acceptance Criterion 1(3) Acceptance Criterion 1(4) Acceptance Criterion 1(5) Acceptance Criterion 1(7) Acceptance Criterion 2 Acceptance Criterion 3 Acceptance Criterion 4 Acceptance Criterion 5 Section 2.2.1.3.3.3: Acceptance Criterion 1(3) Acceptance Criterion 1(4) Acceptance Criterion 3(3) Acceptance Criterion 3(4) Acceptance Criterion 4(4) Acceptance Criterion 5(3)

SAR Section	Information Category	Proposed 10 CFR Part 63 Reference	NUREG-1804 Reference
2.3.5	In-Drift Physical and Chemical Environment	63.21(c)(1)(ii)[a] 63.21(c)(9)[a] 63.21(c)(10)[a] 63.21(c)(15)[a] 63.114(a)(1) 63.114(a)(2) 63.114(a)(3) 63.114(a)(4) 63.114(a)(5) 63.114(a)(6) 63.114(a)(7) 63.114(b) 63.342(a) 63.342(c)	Section 2.2.1.3.3.3: Acceptance Criterion 1(1) Acceptance Criterion 1(2) Acceptance Criterion 1(3) Acceptance Criterion 1(4) Acceptance Criterion 1(5) Acceptance Criterion 1(6) Acceptance Criterion 1(7) Acceptance Criterion 1(8) Acceptance Criterion 1(9) Acceptance Criterion 1(10) Acceptance Criterion 1(12) Acceptance Criterion 2(1) Acceptance Criterion 2(2) Acceptance Criterion 2(3) Acceptance Criterion 2(4) Acceptance Criterion 3(1) Acceptance Criterion 3(2) Acceptance Criterion 3(3) Acceptance Criterion 3(4) Acceptance Criterion 3(6) Acceptance Criterion 4 Acceptance Criterion 5
2.3.6	Waste Package and Drip Shield Corrosion	63.21(c)(9)[a] 63.21(c)(15)[a] 63.114(a)(1) 63.114(a)(2) 63.114(a)(3) 63.114(a)(4) 63.114(a)(5) 63.114(a)(6) 63.114(a)(7) 63.114(b) 63.342(c)	Section 2.2.1.2.2.3: Acceptance Criterion 3 Acceptance Criterion 4 Acceptance Criterion 5 Section 2.2.1.3.1.3: Acceptance Criterion 1(1) Acceptance Criterion 1(2) Acceptance Criterion 1(3) Acceptance Criterion 1(4) Acceptance Criterion 1(5) Acceptance Criterion 1(7) Acceptance Criterion 2 Acceptance Criterion 3 Acceptance Criterion 4 Acceptance Criterion 5 Section 2.2.1.3.2.3: Acceptance Criterion 1(1) Acceptance Criterion 1(2) Acceptance Criterion 1(3) Acceptance Criterion 1(4) Acceptance Criterion 1(5) Acceptance Criterion 2 Section 2.2.1.3.3.3: Acceptance Criterion 1(3) Acceptance Criterion 1(6) Acceptance Criterion 1(10) Acceptance Criterion 2(5)

SAR Section	Information Category	Proposed 10 CFR Part 63 Reference	NUREG-1804 Reference
2.3.7	Waste Form Degradation and Mobilization and Engineered Barrier System Flow and Transport	63.21(c)(1)(ii)[a] 63.21(c)(9)[a] 63.21(c)(15)[a] 63.114(a)(1) 63.114(a)(2) 63.114(a)(3) 63.114(a)(4) 63.114(a)(5) 63.114(a)(6) 63.114(a)(7) 63.114(b) 63.342(c)	Section 2.2.1.3.1.3: Acceptance Criterion 1(1) Acceptance Criterion 1(2) Acceptance Criterion 1(3) Acceptance Criterion 1(4) Acceptance Criterion 1(5) Acceptance Criterion 1(7) Acceptance Criterion 2 Acceptance Criterion 3(1) Acceptance Criterion 3(2) Acceptance Criterion 3(3) Acceptance Criterion 3(5) Acceptance Criterion 4 Acceptance Criterion 5 Section 2.2.1.3.2.3: Acceptance Criterion 1(2) Section 2.2.1.3.3.3: Acceptance Criterion 1(1) Acceptance Criterion 1(2) Acceptance Criterion 1(3) Acceptance Criterion 1(4) Acceptance Criterion 1(5) Acceptance Criterion 1(6) Acceptance Criterion 1(7) Acceptance Criterion 1(8) Acceptance Criterion 1(9) Acceptance Criterion 1(10) Acceptance Criterion 1(12) Acceptance Criterion 2(1) Acceptance Criterion 2(2) Acceptance Criterion 2(4) Acceptance Criterion 3(1) Acceptance Criterion 3(2) Acceptance Criterion 3(3) Acceptance Criterion 3(4) Acceptance Criterion 3(6) Acceptance Criterion 4 Acceptance Criterion 5 Section 2.2.1.3.4.3: Acceptance Criterion 1(1) Acceptance Criterion 1(2) Acceptance Criterion 1(3) Acceptance Criterion 1(4) Acceptance Criterion 1(5) Acceptance Criterion 1(6) Acceptance Criterion 1(8) Acceptance Criterion 2 Acceptance Criterion 3(1) Acceptance Criterion 3(2) Acceptance Criterion 3(3) Acceptance Criterion 3(4) Acceptance Criterion 3(5) Acceptance Criterion 3(8) Acceptance Criterion 3(9) Acceptance Criterion 4 Acceptance Criterion 5(1) Acceptance Criterion 5(2) Acceptance Criterion 5(3)

SAR Section	Information Category	Proposed 10 CFR Part 63 Reference	NUREG-1804 Reference
2.3.8	Radionuclide Transport in Unsaturated Zone	63.21(c)(1)(ii)[a] 63.21(c)(9)[a] 63.21(c)(15)[a] 63.114(a)(1) 63.114(a)(2) 63.114(a)(3) 63.114(a)(4) 63.114(a)(5) 63.114(a)(7) 63.114(b) 63.342(c)	Section 2.2.1.3.7.3: Acceptance Criterion 1 Acceptance Criterion 2 Acceptance Criterion 3(1) Acceptance Criterion 3(2) Acceptance Criterion 3(4) Acceptance Criterion 3(5) Acceptance Criterion 4 Acceptance Criterion 5
2.3.9	Saturated Zone Flow and Transport	63.21(c)(1)(ii)[a] 63.21(c)(9)[a] 63.21(c)(15)[a] 63.114(a)(1) 63.114(a)(2) 63.114(a)(3) 63.114(a)(4) 63.114(a)(5) 63.114(a)(7) 63.114(b) 63.115(a)[a] 63.115(b)[a] 63.115(c)[a] 63.342(c)	Section 2.2.1.3.8.3: Acceptance Criterion 1 Acceptance Criterion 2 Acceptance Criterion 3 Acceptance Criterion 4 Acceptance Criterion 5 Section 2.2.1.3.9.3: Acceptance Criterion 1 Acceptance Criterion 2 Acceptance Criterion 3(1) Acceptance Criterion 3(2) Acceptance Criterion 3(4) Acceptance Criterion 3(5) Acceptance Criterion 3(6) Acceptance Criterion 4 Acceptance Criterion 5 Section 2.2.1.3.12.3: Acceptance Criterion 1 Acceptance Criterion 2 Acceptance Criterion 3 Acceptance Criterion 4 Acceptance Criterion 5

SAR Section	Information Category	Proposed 10 CFR Part 63 Reference	NUREG-1804 Reference
2.3.10	Biosphere Transport and Exposure	63.21(c)(1)(iv)[a] 63.21(c)(9)[a] 63.21(c)(15)[a] 63.102(i)[a] 63.114(a)(1) 63.114(a)(2) 63.114(a)(3) 63.114(a)(4) 63.114(a)(5) 63.114(a)(7) 63.114(b) 63.305(a)[a] 63.305(b)[a] 63.305(c) 63.305(d)[a] 63.311 63.312(a)[a] 63.312(b)[a] 63.312(c)[a] 63.312(d)[a] 63.312(e)[a] 63.342(c)	Section 2.2.1.3.13.3: Acceptance Criterion 1 Acceptance Criterion 2 Acceptance Criterion 3 Acceptance Criterion 4 Acceptance Criterion 5 Section 2.2.1.3.14.3: Acceptance Criterion 1 Acceptance Criterion 2 Acceptance Criterion 3 Acceptance Criterion 4 Acceptance Criterion 5

SAR Section	Information Category	Proposed 10 CFR Part 63 Reference	NUREG-1804 Reference
2.3.11	Igneous Activity	63.21(c)(1)(ii)[a] 63.21(c)(9)[a] 63.21(c)(15)[a] 63.114(a)(1) 63.114(a)(2) 63.114(a)(3) 63.114(a)(4) 63.114(a)(5) 63.114(a)(6) 63.114(a)(7) 63.114(b) 63.342	Section 2.2.1.2.2.3: Acceptance Criterion 1 Acceptance Criterion 2 Acceptance Criterion 3 Acceptance Criterion 4 Acceptance Criterion 5 Section 2.2.1.3.2.3: Acceptance Criterion 1(1) Acceptance Criterion 1(2) Acceptance Criterion 1(3) Acceptance Criterion 1(4) Acceptance Criterion 1(5) Acceptance Criterion 1(7) Acceptance Criterion 2 Acceptance Criterion 3 Acceptance Criterion 4 Acceptance Criterion 5 Section 2.2.1.3.3.3: Acceptance Criterion 1(1) Acceptance Criterion 1(2) Acceptance Criterion 1(3) Acceptance Criterion 1(4) Acceptance Criterion 1(5) Acceptance Criterion 1(6) Acceptance Criterion 1(7) Acceptance Criterion 1(8) Acceptance Criterion 1(12) Acceptance Criterion 2(1) Acceptance Criterion 2(2) Acceptance Criterion 2(4) Acceptance Criterion 3(1) Acceptance Criterion 3(2) Acceptance Criterion 3(3) Acceptance Criterion 3(4) Acceptance Criterion 3(6) Acceptance Criterion 4(1) Acceptance Criterion 4(2) Acceptance Criterion 4(3) Acceptance Criterion 4(4) Acceptance Criterion 5 Section 2.2.1.3.10.3: Acceptance Criterion 1 Acceptance Criterion 2 Acceptance Criterion 3 Acceptance Criterion 4 Acceptance Criterion 5 Section 2.2.1.3.11.3: Acceptance Criterion 1 Acceptance Criterion 2 Acceptance Criterion 3 Acceptance Criterion 4 Acceptance Criterion 5

SAR Section	Information Category	Proposed 10 CFR Part 63 Reference	NUREG-1804 Reference
2.3.11 (Continued)	Igneous Activity (Continued)		Section 2.2.1.3.13.3: Acceptance Criterion 1 Acceptance Criterion 2 Acceptance Criterion 3 Acceptance Criterion 4 Acceptance Criterion 5

NOTE: aNot changed by the proposed rule.

In most instances, each model abstraction topic referred to in NUREG-1804 is addressed in a single subsection. However, in four instances, elements of a particular model abstraction topic were separated into different subsections.

First, elements of the model abstraction for quantity and chemistry of water contacting the EBS and waste forms (NUREG-1804, Section 2.2.1.3.3.3) are divided primarily into three subsections: Section 2.3.3 (Water Seeping into Drifts), Section 2.3.5 (In-Drift Physical and Chemical Environment), and Section 2.3.7 (Waste Form Degradation and Mobilization and Engineered Barrier System Flow and Transport). These subsections reflect the different processes that act within different features and affect this model abstraction topic. Additional subsections addressing aspects of NUREG-1804, Section 2.2.1.3.3.3, are Section 2.2 (Scenario Analysis and Event Probability), Section 2.3.4 (Mechanical Degradation of the Engineered Barrier System), Section 2.3.6 (Waste Package and Drip Shield Corrosion), Section 2.3.11 (Igneous Activity), and Section 2.4 (Demonstration of Compliance with the Postclosure Public Health and Environmental Standards).

Second, elements of the model abstraction for nonmechanical degradation of the EBS (NUREG-1804, Section 2.2.1.3.1.3) are divided into two subsections: Section 2.3.6 (Waste Package and Drip Shield Corrosion) and Section 2.3.7 (Waste Form Degradation and Mobilization and Engineered Barrier System Flow and Transport). Section 2.3.6 describes the different features and processes that act upon the waste package and drip shield features, and Section 2.3.7 describes features and processes acting on the waste form and waste package internal features.

Third, elements of the model abstraction for mechanical degradation of the EBS (NUREG-1804, Section 2.2.1.3.2.3) are divided into two subsections: Section 2.3.4 (Mechanical Degradation of the EBS) and Section 2.3.6 (Waste Package and Drip Shield Corrosion). Section 2.3.6 presents the treatment of corrosion processes affecting the waste package and drip shield including stress corrosion cracking, and Section 2.3.4 describes mechanical degradation of the EBS features induced by natural or seismically induced rockfall within the emplacement drifts.

Fourth, elements of the model abstraction for redistribution of radionuclides in soil (NUREG-1804, Section 2.2.1.3.13.3) are also divided into two subsections: Section 2.3.10 (Biosphere Transport and Exposure) and Section 2.3.11 (Igneous Activity). The abstraction model described in Section 2.3.11 includes processes not included in the biosphere model for the nominal scenario, such as fluvial redistribution and redistribution by vertical diffusion in nonirrigated soils. This

model provides the source term for the volcanic eruption biosphere modeling described in Section 2.3.10.

The subsections of Section 2.3 describe how the included FEPs are combined in conceptual and numerical models, and present the technical basis for each of the model abstractions. Section 2.2 describes the FEP screening process and provides the screening decision for each FEP. Some excluded FEPs are described in the Section 2.3 subsections in order to provide a comprehensive understanding of the topic. All of the included FEPs analyzed for the 10,000-year period after repository closure are also included in the analyses of the period beyond 10,000 years and within the period of geologic stability, as defined by proposed 10 CFR Part 63. In the latter period, specific seismic, igneous, climate, and general corrosion events and processes were implemented as prescribed by proposed 10 CFR Part 63. Conceptual models capture the significant FEPs relating to the abstraction topic. Analyses and process models are developed that mathematically represent those FEPs, or combinations thereof, identified for inclusion in the TSPA. Within each model abstraction topic, the grouping of individual models used to represent the FEPs varies depending on the degree of coupling or integration among and between the models. However, for each model abstraction topic, the information specified by the NUREG-1804 acceptance criteria is incorporated by (1) presenting the description of the conceptual model and its relationship to the relevant FEPs; (2) describing the data and data uncertainty related to the understanding of these FEPs and the parameters that are included in the models and analyses; (3) describing the process models and numerical models, including the treatment of uncertainty in the models and the propagation of these uncertainties to the TSPA; and (4) describing the abstraction of the process models in the TSPA.

Integration of the Process and Abstraction Models in the TSPA—The TSPA model presented in Section 2.4 is developed on the basis of the scenario analysis described in Section 2.2 and the abstraction of modeled FEPs and event probabilities presented in the Section 2.3 subsections. Figure 2.3-1 displays the overall framework for the TSPA, beginning with the broad foundation of the pyramid, which represents field and laboratory data about the Yucca Mountain site that have been collected over nearly 30 years, as well as a description of the repository design, waste form, waste package and other EBS properties, and studies and analyses of the potential future behavior of the repository. This foundation provides the basis for identifying the FEPs that must be analyzed to appropriately represent the repository system. The suite of conceptual and process models at the next level in the pyramid consists of mathematical expressions of the FEPs and of their associated uncertainties, as described in Sections 2.3.1 to 2.3.11. The TSPA model incorporates key uncertainties in both the data and models used to simulate the future performance of the repository and considers the effect that alternative models or representations could have on the results. The uncertainty inherent in the data and the distributions of parameters used in the model are described, as is the propagation of uncertainty through the abstractions incorporated in the TSPA model. Process models and the TSPA explicitly consider both epistemic uncertainty (i.e., uncertainty due to a lack of knowledge) and aleatory uncertainty (i.e., uncertainty due to random processes). Through abstraction, the TSPA model components are developed and used to analyze the projected evolution of the various components of the repository system through time. The top level of the pyramid consists of the integrated TSPA numerical model used to simulate the behavior of the repository system.

Abstraction for the TSPA model (Section 2.4) starts with building conceptual models that account for included FEPs and possible outcomes regarding repository performance. These conceptual

models consist of sets of hypotheses, including assumptions, simplifications, and idealizations that describe the aspects of a system or subsystem as they relate to performance. Model conceptualization identifies and selects FEPs that collectively comprise the scenario classes considered in the conceptual models. Because the TSPA deals with future outcomes and includes uncertainty in process descriptions, data, and parameters, there may be several alternative conceptual models that provide reasonable descriptions of a particular system or subsystem. Therefore, an essential element of the TSPA is to capture uncertainty in probabilistic analyses that represent likely outcomes based on the available data, parameter values, and modeling approaches involved.

Mathematical representations of conceptual models are then developed as detailed quantitative expressions of processes that can be used together to simulate various aspects of repository performance. These representations are referred to as process models. The mathematical representations might include algebraic expressions, ordinary differential equations, partial differential equations, or integral equations characterizing accepted conservation laws, such as the conservation of mass, energy, or momentum, as well as appropriate constitutive equations that describe material behavior in the domain of the conceptual model. Abstractions are developed for either a single modeled process or combination of processes to reduce complexity while maintaining the validity of the process models for incorporation into the TSPA model. Abstracted representations of the more detailed process models are provided to the TSPA as response surfaces, lookup tables, parameter distributions, or other functions or correlations.

The TSPA model integrates the abstraction models, which describe the included FEPs as informed by site-specific information, analogues that assist in building confidence in the long-term processes evaluated in the TSPA, and relevant laboratory data concerning the natural and engineered materials. The TSPA approach provides for an analysis of the system that appropriately incorporates parameter distributions that are used to quantify uncertainty. By incorporating this uncertainty in multiple stochastic realizations, the TSPA model produces a range of long-term projections of repository performance. The multiple simulations of repository performance thus provide a means for a risk-informed analysis of system behavior that incorporates uncertainty in models and parameters based on scientific observations. The TSPA model then uses these data and models to assess the capability of the repository system to comply with the applicable regulatory standards.

Figure 2.3-2 provides a schematic representation of the TSPA model for multiple scenario classes. The nominal scenario class includes all of the FEPs identified through the FEP screening process described in Section 2.2, except for certain specific FEPs related to early failures, igneous activity, seismic activity, or a human intrusion. The early failure scenario class includes two modeling cases that incorporate FEPs that describe the potential for early waste package and drip shield failure in the absence of disruptive events. The igneous scenario class includes two modeling cases that address FEPs pertaining to disruptive igneous activity (igneous intrusion and volcanic eruption) that could affect the repository. The seismic scenario class considers two modeling cases that describe disruptive seismic activity (ground motion and fault displacement). Section 2.2.1 provides a discussion of the development of these scenario classes.

The model abstraction topics discussed in the Section 2.3 subsections are treated in terms of TSPA model architecture as TSPA model components and submodels, as presented in Table 2.3-1. Integration of the results for the individual abstraction topics in the TSPA model components and

submodels is described in Sections 2.4.1 and 2.4.2.3.2.1. As shown in Figure 2.3-2, the nominal scenario class component models that feed directly into the TSPA include unsaturated zone flow, the EBS environment, waste package and drip shield degradation, waste form degradation, EBS transport, unsaturated zone transport, saturated zone flow and transport, and the biosphere. These abstractions are described in Sections 2.3.1 to 2.3.3 and 2.3.5 to 2.3.10. The other scenario classes also include these same processes and abstraction topics and, in addition, include events (early failure, igneous, and seismic) that may affect the performance of the engineered features. The potential for early waste package and drip shield failures is described in Section 2.3.6. For the igneous scenario class, magma intrusion into the repository and volcanic eruption modeling cases are analyzed in Section 2.3.11. For the seismic scenario class, seismic events with ground motions affecting the repository or fault ruptures intersecting the repository are analyzed, as are the potential coupled effects associated with drift collapse (Section 2.3.4).

Section 2.4.2.3.2.1.12 contains overviews of the models that are integrated within the TSPA model for the early failure, seismic, and igneous scenario classes. This section describes implementation of the process or abstraction model results in the TSPA and summarizes the flow of information between and among the models.

Integration with the Administrative and Safety Control Program—In the development of model abstractions for the TSPA, the analytical basis of the design has assumed that particular operating conditions will exist at the time the repository is closed. To ensure that those conditions exist at the time of closure, several operational parameters have been identified that will be subject to operational controls.

Table 1.9-9 identifies parameters that require either inspection, verification, or control during preclosure operations in order to ensure the TSPA analytical bases, including the development of contributing process models and their abstractions, are satisfied at the time of closure. The model abstractions have been developed using one representative configuration for emplaced waste that can accommodate a degree of variation in the details of the waste stream and emplacement. Variations in the waste stream and emplacement will undoubtedly occur, as may variations in the natural setting. The Performance Confirmation Program described in Chapter 4 will address the geologic conditions actually encountered in the repository and compare them to conditions analyzed. The repository is designed to accommodate a range of operational considerations and waste characteristics (e.g., thermal load, age of waste at time of disposal, sequence and separation of waste packages) related to receipt and emplacement. This information is presented in Section 2.3.5 and in Section 2.3.4 (for geomechanical response). As the repository is constructed, the details of waste characteristics and emplacement will be considered in order to establish the specific values of the control parameters for each drift loading configuration. The development of these specific values will be performed through additional analysis prior to emplacement. The control of these parameter values will occur by use of the management systems, such as procedural safety controls or configuration management controls implemented during preclosure operations.

Integration with the Performance Confirmation Program—The TSPA abstraction models described in the Section 2.3 subsections are also integrated with the Performance Confirmation Program described in Chapter 4. Performance confirmation means the program of tests, experiments, and analyses that is conducted to evaluate the adequacy of the information used to demonstrate compliance with the performance objectives in proposed 10 CFR Part 63. The

Performance Confirmation Program began during site characterization and will continue through construction, emplacement, and operation until permanent closure. The Performance Confirmation Program will monitor or test selected parameters, including some that serve as inputs to the abstraction models, to identify any significant changes in the conditions described in the license application that may affect compliance with the postclosure individual protection and groundwater protection standards. The risk-informed, performance-based Performance Confirmation Program will emphasize the monitoring and testing of parameters that have a significant impact on repository performance. The development of these parameters is based on the processes providing an important contribution to barrier capability as identified in Section 2.1.2. The data generated by performance confirmation activities will be used to evaluate abstraction models and increase confidence in the TSPA results. The performance confirmation activities relevant to the abstraction models are discussed in Chapter 4.

Table 2.3-1. Model Abstraction Topics and TSPA Model Components Crosswalk

Model Abstraction Areas (Section 2.3)	TSPA Model Components (Section 2.4)	TSPA Submodels (Section 2.4)
Climate and Infiltration (Section 2.3.1)	Unsaturated Zone Flow	Climate
		Infiltration
Unsaturated Zone Flow (Section 2.3.2)		Unsaturated Zone Flow Fields
Water Seeping into Drifts (Section 2.3.3)		Drift Seepage
In-Drift Physical and Chemical Environment (Section 2.3.5)		Drift Wall Condensation
	EBS Environment	EBS Thermal-Hydrologic Environment
		EBS Chemical Environment
Waste Package and Drip Shield Corrosion (Section 2.3.6)	Waste Package and Drip Shield Degradation	Waste Package and Drip Shield Degradation
Waste Form Degradation and Mobilization and EBS Flow and Transport (Section 2.3.7)	Waste Form Degradation and Mobilization	Radionuclide Inventory
		In-Package Chemistry
		Cladding Degradation
		Waste Form Degradation
		Dissolved Concentration Limits
		EBS Colloids
	EBS Flow and Transport	EBS Flow
		EBS Transport
		EBS-Unsaturated Zone Interface
Radionuclide Transport in Unsaturated Zone (Section 2.3.8)	Unsaturated Zone Transport	Unsaturated Zone Transport
Saturated Zone Flow and Transport (Section 2.3.9)	Saturated Zone Flow and Transport	Saturated Zone Flow and Transport
Biosphere Transport and Exposure (Section 2.3.10)	Biosphere	Biosphere

Table 2.3-1. Model Abstraction Topics and TSPA Model Components Crosswalk (Continued)

Model Abstraction Areas (Section 2.3)	TSPA Model Components (Section 2.4)	TSPA Submodels (Section 2.4)
Waste Package and Drip Shield Corrosion (Section 2.3.6)	Events	Drip Shield Early Failure
		Waste Package Early Failure
Igneous Activity (Section 2.3.11)		Igneous Intrusion
		Igneous Event Time and Probability
		Igneous Intrusion EBS Damage
		EBS Thermal-Hydrologic Submodel Modifications for Igneous Intrusion
		EBS Chemical Environment Submodel Modifications for Igneous Intrusion
		Volcanic Eruption
		Volcanic Interaction with the Repository
		Atmospheric Transport
		Tephra Redistribution
Biosphere Transport and Exposure (Section 2.3.10)		Volcanic Ash Exposure
Mechanical Degradation of the EBS (Section 2.3.4)		Ground Motion Damage
		Fault Displacement Damage
Water Seeping into Drifts (Section 2.3.3)		Drift Seepage Submodel for Seismic Disruption
Mechanical Degradation of the EBS (Section 2.3.4)		EBS Thermal-Hydrologic Environment Submodel Modifications for Seismic Disruption
		Waste Package and Drip Shield Degradation Submodel Modifications for Seismic Disruption
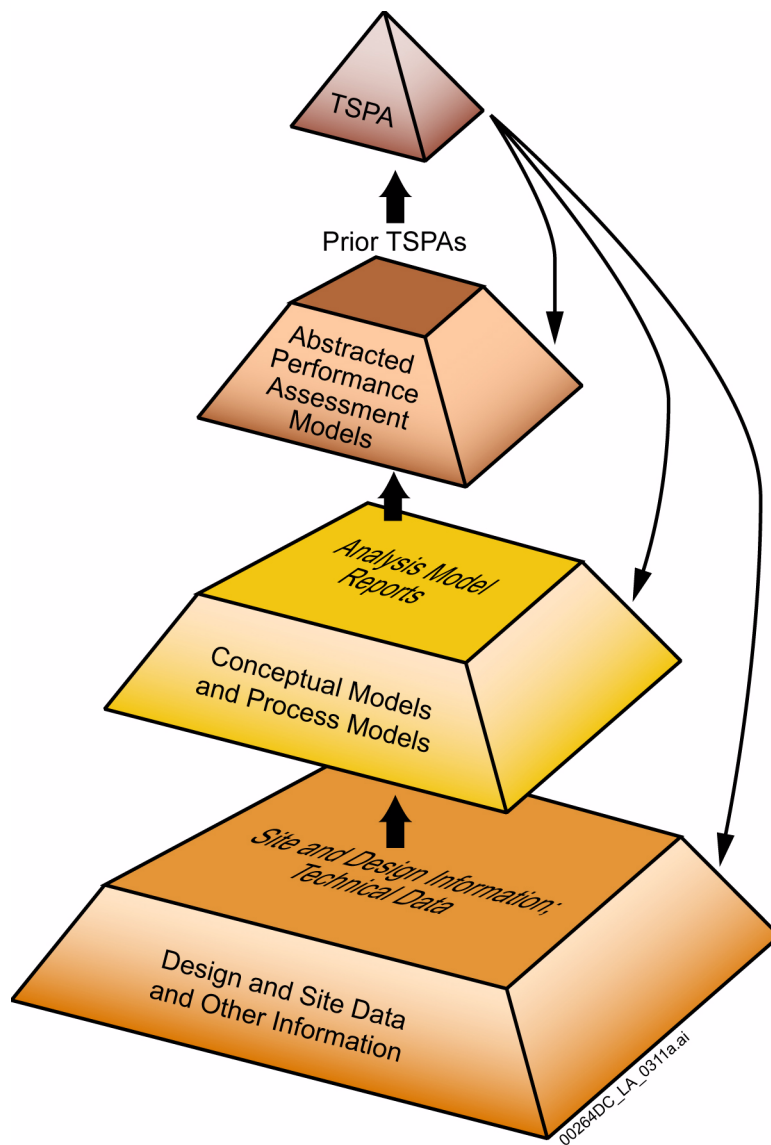
Figure 2.3-1. Pyramid Illustrating the Iterative Process Utilized Over the Past 15 Years to Synthesize Design Information, Site Data, and Process Models to Build the Technical Basis for TSPA
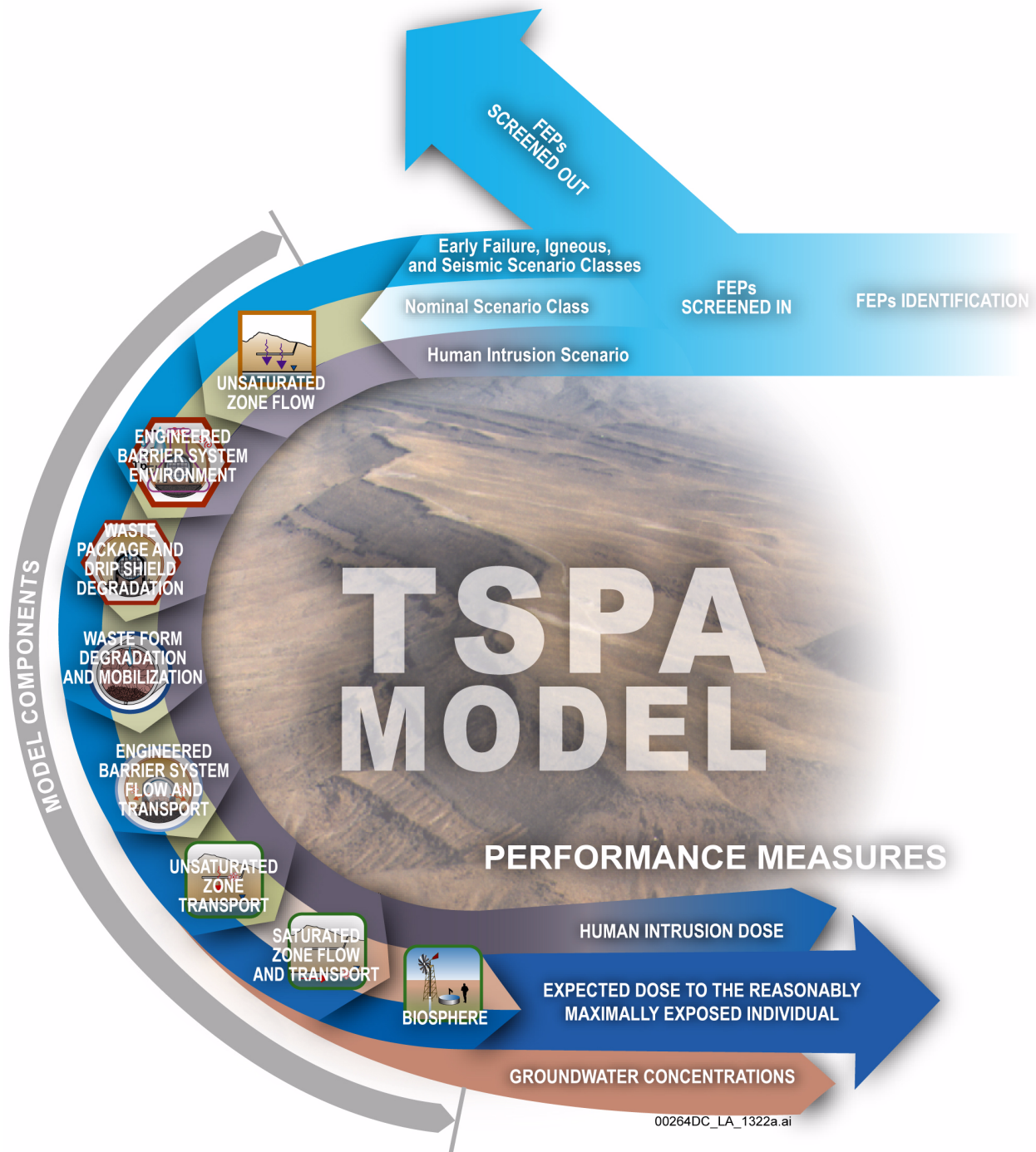
Figure 2.3-2.   Schematic Representation of the Development of the TSPA, Including the Nominal, Igneous, and Seismic Scenario Classes

CONTENTS

Page

INTENTIONALLY LEFT BLANK

TABLES

TABLES (Continued)

FIGURES

Page

FIGURES (Continued)

FIGURES (Continued)

Page

INTENTIONALLY LEFT BLANK

2.3.1   Climate and Infiltration
[NUREG-1804, Section 2.2.1.3.5.3: AC 1, AC 2, AC 3, AC 4, AC 5]

The information presented in this section addresses the requirements of proposed 10 CFR 63.114(a)(1) through (a)(5), (a)(7), and (b) for conducting the climate and infiltration portion of a performance assessment. The requirement of proposed 10 CFR 63.114(a)(6) is not referenced below because the degradation, deterioration, and alteration processes that are the subject of that section are addressed in Sections 2.2, 2.3.4 to 2.3.7, and 2.3.11. This section also provides information that addresses specific acceptance criteria in Section 2.2.1.3.5.3 of NUREG-1804.

The purpose of Section 2.3.1 is to describe and justify the climate and infiltration analyses and models used to define (1) the range of timing of climate change; (2) the analogue sites used to represent future climate states for the next 10,000 years; (3) the four infiltration maps for each of the present-day, monsoon, and glacial-transition climates (a total of 12 maps), showing areally distributed infiltration, and representing the 10th, 30th, 50th, and 90th percentile of infiltration; and (4) the initial weightings of these four maps.

With regard to climate and infiltration, this section presents the following:

- Data from the Yucca Mountain site and surrounding region, uncertainties and variabilities in parameter values, and alternative conceptual models used in the analyses

- Specific features, events, and processes (FEPs) included in the analyses, with appropriate technical bases for inclusion

- Technical bases for models used in the performance assessment.

The categories of information provided in this section, as well as the corresponding proposed 10 CFR Part 63 regulatory requirements and NUREG-1804 acceptance criteria, are presented below. With regard to Acceptance Criteria 1(8) and 2(7) in Section 2.2.1.3.5.3 of NUREG-1804, no formal peer reviews were used to support development of the current models and analyses discussed in Section 2.3.1. Similarly, while an expert elicitation on unsaturated zone flow was conducted, the resulting information was not directly used in the development of the current models and analyses. In addition, Section 2.3.1 does not discuss the approach used for data qualification. However, scientific analyses, model development, and data qualification activities were conducted in accordance with project procedures that comply with Quality Assurance Program requirements. The project procedures governing data qualification are consistent with NUREG-1298 (Altman et al. 1988) in keeping with Acceptance Criterion 1(8).

SAR Section	Information Category	Proposed 10 CFR Part 63 Reference	NUREG-1804 Reference
2.3.1	Climate and Infiltration	63.114(a)(1) 63.114(a)(2) 63.114(a)(3) 63.114(a)(4) 63.114(a)(5) 63.114(a)(7) 63.114(b) 63.342(c)	Section 2.2.1.3.5.3: Acceptance Criterion 1 Acceptance Criterion 2 Acceptance Criterion 3 Acceptance Criterion 4 Acceptance Criterion 5
2.3.1.1	Summary and Overview	Not applicable	Not applicable
2.3.1.2	Climate	See details in sections below	See details in sections below
2.3.1.2.1	Conceptual Description of Climate	63.114(a)(1) 63.114(a)(4) 63.114(a)(5) 63.342(c)	Section 2.2.1.3.5.3: Acceptance Criterion 1(1) Acceptance Criterion 1(2) Acceptance Criterion 1(7)
2.3.1.2.2	Paleoclimatological Data and Data Uncertainty	63.114(a)(1) 63.114(a)(2)	Section 2.2.1.3.5.3: Acceptance Criterion 1(2) Acceptance Criterion 1(3) Acceptance Criterion 1(4) Acceptance Criterion 1(7) Acceptance Criterion 2(1) Acceptance Criterion 2(2) Acceptance Criterion 2(3) Acceptance Criterion 2(4) Acceptance Criterion 3(1) Acceptance Criterion 3(2)
2.3.1.2.3	Climate Analysis and Uncertainty	63.114(a)(2) 63.114(a)(3) 63.114(a)(7)	Section 2.2.1.3.5.3: Acceptance Criterion 1(3) Acceptance Criterion 1(5) Acceptance Criterion 1(6) Acceptance Criterion 1(7) Acceptance Criterion 2(2) Acceptance Criterion 2(3) Acceptance Criterion 2(4) Acceptance Criterion 2(5) Acceptance Criterion 2(6) Acceptance Criterion 3(1) Acceptance Criterion 3(3) Acceptance Criterion 3(4) Acceptance Criterion 4
2.3.1.3	Infiltration	See details in sections below	See details in sections below
2.3.1.3.1	Conceptual Description of Infiltration Processes	63.114(a)(1) 63.114(a)(4) 63.114(a)(5)	Section 2.2.1.3.5.3: Acceptance Criterion 1(1) Acceptance Criterion 1(2)

SAR Section	Information Category	Proposed 10 CFR Part 63 Reference	NUREG-1804 Reference
2.3.1.3.2	Infiltration Data and Data Uncertainty	63.114(a)(1) 63.114(a)(2) 63.114(b)	Section 2.2.1.3.5.3: Acceptance Criterion 1(2) Acceptance Criterion 1(3) Acceptance Criterion 1(4) Acceptance Criterion 1(7) Acceptance Criterion 2(1) Acceptance Criterion 2(2) Acceptance Criterion 2(3) Acceptance Criterion 2(4) Acceptance Criterion 3(1) Acceptance Criterion 3(2)
2.3.1.3.3	Infiltration Modeling and Uncertainty	63.114(a)(2) 63.114(a)(3) 63.114(a)(7) 63.114(b) 63.342(c)	Section 2.2.1.3.5.3: Acceptance Criterion 1(3) Acceptance Criterion 1(5) Acceptance Criterion 1(6) Acceptance Criterion 1(7) Acceptance Criterion 2(2) Acceptance Criterion 2(3) Acceptance Criterion 2(4) Acceptance Criterion 2(5) Acceptance Criterion 2(6) Acceptance Criterion 3(1) Acceptance Criterion 3(3) Acceptance Criterion 3(4) Acceptance Criterion 4
2.3.1.3.4	Confidence Building and Abstraction of the Infiltration Model	63.114(a)(7) 63.114(b) 63.342(c)	Section 2.2.1.3.5.3: Acceptance Criterion 1(2) Acceptance Criterion 1(3) Acceptance Criterion 4(1) Acceptance Criterion 5
2.3.1.4	Conclusions	Not applicable	Not applicable

2.3.1.1   Summary and Overview

Section 2.1.2.1 describes the capability of the Upper Natural Barrier, which is the natural environment located between the repository horizon and the ground surface, to prevent or substantially reduce the amount and the rate of water seeping into emplacement drifts. This barrier prevents or substantially reduces the rate of movement of water from the repository to the accessible environment. The capability of the Upper Natural Barrier is affected by the processes of climate change, precipitation, and infiltration that are described in this section. In the climate analysis, annual precipitation and air temperatures for future climate states were forecast on the basis of paleoclimate data and earth-orbital parameters. Analogue sites were identified with weather conditions similar to future climate states expected to occur at Yucca Mountain, and data from these sites were used to estimate upper and lower ranges of precipitation and temperatures for the future climates. Using this information, an infiltration model was developed on the basis of geologic and hydrologic studies of soil and bedrock properties, as well as data from precipitation and temperature monitoring. This model was used to develop spatial and temporal infiltration predictions for

present-day conditions, and for the climate states expected during the first 10,000 years after disposal. These infiltration predictions serve as inputs to the site-scale unsaturated zone flow model that is described in Section 2.3.2.

To address the time period after 10,000 years and during the period of geologic stability, the U.S. Nuclear Regulatory Commission (NRC) has proposed revisions to 10 CFR Part 63 that specify a deep percolation flux to vary between 13 and 64 mm/yr. Net infiltration estimates are not calculated for the period after 10,000 years, because the proposed NRC rule specifies deep percolation and not infiltration. The implementation of the proposed NRC rule is described in Section 2.3.2.3.5.1, where deep percolation in the unsaturated zone is described. As a result, the discussion of climate and net infiltration is limited to the first 10,000 years following repository closure.

The features and processes relating to climate and infiltration that have been determined to be important to the capability of the Upper Natural Barrier (Section 2.1.2.1 and Table 2.1-2) include the following:

- **Climate Change**—The Upper Natural Barrier substantially reduces the amount of precipitation entering the repository. Long-term climate change processes can significantly affect the amount of precipitation that falls in any year, as well as temperature, humidity, and vegetation. As a result, the climate state affects the amount of water available and the key processes that control infiltration into the surficial soils and percolation through the unsaturated zone. The effects of climate change have been included in the analysis described in Sections 2.3.1.2.1.2, 2.3.1.2.3.1, 2.3.1.3.3.1.2, and 2.3.1.4.

- **Climate Modification Increases Recharge**—The net effect of climate change in the 10,000 years after closure is to increase the amount of water that precipitates and can infiltrate and eventually percolate through the unsaturated zone. This increased net infiltration (potential recharge) is calculated by the infiltration model presented in Section 2.3.1.3.3.1.

- **Precipitation**—Precipitation processes are important in the evaluation of the net infiltration into the bedrock below the surficial soils. Given the arid climate at Yucca Mountain, precipitation events are intermittent and result in long periods of time when there is a net evapotranspiration from the surficial soils interspersed with short-duration precipitation events that can result in some infiltration. Precipitation rates during past, current, and future climate states are described in Sections 2.3.1.2.3.1, 2.3.1.2.3.2, and 2.3.1.3.2.1.1.

- **Topography and Morphology**—The topography and morphology of the ground surface above the repository are such that a portion of the precipitation that falls at Yucca Mountain is unavailable for infiltration due to surface runoff. The effects of temporal variability in precipitation and the effects of topography on surface runoff have been included in the assessment of net infiltration and the uncertainty in net infiltration set forth in Sections 2.3.1.3.1.3, 2.3.1.3.2.1.1, and 2.3.1.3.4.1.

- **Rock Properties of Host Rock and Other Units**—The hydrologic characteristics of the surficial soils (and bedrock underlying surficial soils) above the repository affect the amount of net infiltration. Soil retention and evapotranspiration processes limit net infiltration. The hydrologic characteristics of the surface soils and bedrock underlying surficial soils at Yucca Mountain are described in Sections 2.3.1.3.2.1.3 and 2.3.1.3.2.1.4.

- **Surface Runoff and Evapotranspiration**—Surface water runoff and evapotranspiration are components in the water balance, together with precipitation, infiltration, and change in soil water storage. Surface runoff produces erosion and can feed washes, arroyos, and impoundments, where flooding may lead to increased recharge. Evapotranspiration removes water from soil and rock by evaporation and transpiration via plant root water uptake. Surface runoff and evapotranspiration processes are described in Sections 2.3.1.3.1.1, 2.3.1.3.1.2, 2.3.1.3.2.1.5, 2.3.1.3.3.1.1, and 2.3.1.3.4.1.

- **Infiltration and Recharge**—Net infiltration is the net result of the above processes. These processes result in a significant reduction in the amount of water available to percolate into the unsaturated zone beneath the surficial soils. Net infiltration is calculated in the infiltration model presented in Sections 2.3.1.3.1, 2.3.1.3.1.1, 2.3.1.3.3, and 2.3.1.3.3.1.2. The process of groundwater recharge is described in Section 2.3.2.

- **Fractures**—Open fractures in the bedrock will tend to increase the bedrock effective hydraulic conductivity and result in an increased rate of net infiltration into the subsurface. However, a lower effective conductivity of the bedrock will tend to increase water storage in the surficial soil and increase the effectiveness of runoff and evapotranspiration, thereby reducing the rate of net infiltration into the subsurface. The effects of fractures on bedrock permeability are described in Section 2.3.1.3.2.1.4.

- **Fracture Flow in the Unsaturated Zone**—Fracture flow in the bedrock beneath the surficial soil affects the rate of water movement below the soil–bedrock contact, especially in areas of thin soils. The rate of water flow in fractures at the soil–bedrock interface is influenced by fracture properties such as fracture frequency and permeability. The effects of fractures on bedrock permeability are described in Section 2.3.1.3.2.1.4.

Role of Climate Analysis and Infiltration Model in the Total System Performance Assessment—Figure 2.3.1-1 provides an overview of some of the key information and data sources used to develop the analysis and models described in this section; it also illustrates linkages to the models that use the infiltration estimates to develop inputs to the total system performance assessment (TSPA). Figure 2.3.1-2 shows the overall information transfer within the model components and submodels of the TSPA for the nominal scenario class, which represents the undisturbed performance of the repository system. The upper right portion of the figure represents the flow of information from the climate analysis and infiltration model through the site-scale unsaturated zone flow model, which provides the unsaturated zone flow fields for use in both unsaturated zone transport and the multiscale thermal-hydrologic model.

The climate analysis provides a forecast of the mean annual temperature and precipitation for future climate states at Yucca Mountain that were developed through evaluation of paleoclimate data, earth-orbital parameters, and analogue sites (meteorological stations selected to provide

precipitation and temperature data). Upper and lower bounds for the important climatic conditions for each future climate state were developed to account for uncertainty in the analysis. The infiltration model provides spatially distributed net infiltration of meteoric water, which is used as input to the site-scale unsaturated zone flow process model (Section 2.3.2). The net infiltration rates are varied for three climate states: present-day, monsoon, and glacial-transition. For each of the three climate states, 40 realizations of net infiltration were simulated that produced 40 maps of areally distributed net infiltration across the infiltration model domain. These maps include the effect of uncertainty in the climate, surface, and near-surface parameters that affect infiltration. Of the 40 maps generated per climate, 4 maps representing the 10th, 30th, 50th, and 90th percentiles of the average net infiltration are selected to be passed to the unsaturated zone flow model. With three climate states and four maps per state, a total of 12 net infiltration maps are used to represent the range of infiltration conditions over the next 10,000 years (SNL 2007, Table 6.1-2). The initial values of the relative weights for these four maps are 0.2, 0.2, 0.3, and 0.3, for the 10th, 30th, 50th, and 90th percentile maps, respectively. The values of these weights are adjusted as part of the unsaturated zone model calibration and validation activities to obtain appropriately weighted boundary conditions for analysis of deep percolation in the unsaturated zone, as described in Section 2.3.2.4.1.2.4.2. This approach incorporates potentially significant uncertainties in infiltration into the estimate of water flux reaching the repository.

Features, Events, and Processes Evaluated in the Climate Analysis and Infiltration Model—The complete list of FEPs, both included and excluded, is presented in Table 2.2-1. Table 2.3.1-1 lists the FEPs addressed in Section 2.3.1, and summarizes the technical basis and approach for their inclusion in the climate analysis and infiltration model. Features that are included are surface characteristics, such as topography, and rock properties and stratigraphic information that are necessary for estimating net infiltration. Processes that are included are climate change, precipitation, surface runoff and evapotranspiration, and infiltration and recharge as well as other processes necessary to develop the climate analysis and infiltration model. The basis for exclusion of climate- and infiltration-related FEPs from the TSPA is provided in Table 2.2-5.

Results of Climate Analysis and Infiltration Modeling—The climate analysis forecasts three climate states over the next 10,000 years (Section 2.3.1.2.3.1.1). The next 600 years is forecast to continue with present-day climate conditions. For the subsequent 1,400 years, a warmer and much wetter monsoon climate is forecast, which has approximately 60% greater average annual precipitation, and average annual infiltration ranges from 1.2 to 2.4 times greater than present-day values for the infiltration modeling domain. The remainder of the 10,000 year period is forecast to experience a glacial transition climate that is wetter and cooler than the present-day and monsoon climates. Average precipitation during this glacial-transition climate state is slightly higher than during the monsoon climate, while the average annual infiltration ranges from 1.8 to 3.3 times greater than present-day values for the infiltration modeling domain. The mean net infiltration over the infiltration model domain during the present-day, monsoon, and glacial-transition climates is predicted to be 14.3, 25.5, and 30.0 mm/year, respectively. The mean precipitation over the infiltration model domain during the present-day, monsoon, and glacial-transition climates is predicted to be 173.6, 275.2, and 283.4 mm/year, respectively. Evapotranspiration is predicted to account for 87.7%, 84.9%, and 86.2% of precipitation during the present-day, monsoon, and glacial-transition climates, respectively. Runoff is predicted to account for 2.1%, 5.4%, and 0.4% of precipitation during the present-day, monsoon, and glacial-transition climates, respectively. Net infiltration is predicted to account for 8.0%, 8.7%, and 10.4% of precipitation during the

present-day, monsoon, and glacial-transition climates, respectively. The predicted net infiltration generally is lowest for the present-day climate, and increases in the monsoon and glacial-transition climates. However, net infiltration predictions for the monsoon climate span a greater range than predictions for the glacial-transition climate. This is the result of a greater amount of uncertainty in the expected precipitation in the monsoon climate than for the glacial-transition climate (SNL 2008a, Section 6.5.7.8[a]).

The infiltration model provides spatially distributed, time-averaged (steady-state) net infiltration rates for each of the three climate states described above. The net infiltration rates are provided as 12 maps representing the 10th, 30th, 50th, and 90th percentile realizations of the total of 40 maps produced for each climate (Section 2.3.1.3.3.1.2). Using the infiltration maps as boundary conditions, the site-scale unsaturated zone flow model generates 12 three-dimensional flow fields to represent the present-day, monsoon, and glacial-transition climates, which serve as input to the TSPA (SNL 2007, Table 6.1-2; Section 2.3.2.1). These 12 unsaturated zone flow fields are based on net infiltration boundary conditions for analysis of deep percolation in the unsaturated zone (Section 2.3.2). Tables 2.3.1-2, 2.3.1-3, and 2.3.1-4 show the minimum, mean, median, maximum, standard deviation, and the 10th, 30th, 50th, and 90th percentile net infiltration and precipitation results for present-day, monsoon, and glacial-transition climate states. Section 2.4.2.3.2.1.1 describes the implementation and integration of outputs from the site-scale unsaturated zone flow model in the TSPA.

2.3.1.2   Climate
[NUREG-1804, Section 2.2.1.3.5.3: AC 1(1), (2), (4) to (7), AC 2(1) to (6), AC 3(1) to (4), AC 4(1) to (3)]

Climate describes the characteristic weather conditions for a location. Dominant climate states for the next 10,000 years at Yucca Mountain have been defined as present-day, monsoon, and glacial-transition. Applied to Yucca Mountain, climate is used to distinguish between periods of significantly different precipitation, distribution of precipitation, and temperature. Weather is characterized by the detailed measurements of atmospheric conditions at a location (rainfall, temperature, wind speed, relative humidity, barometric pressure, etc.). Weather conditions vary over time scales that are much smaller than changes in climate states. The characteristics of the local weather and the present and future climate at Yucca Mountain are both required to predict net infiltration at Yucca Mountain.

The climate analysis (BSC 2004a) is used to interpret past climate indicators in order to (1) determine a method to select future climate states; (2) identify the future climate states; (3) determine the timing of the future climate states; and (4) identify analogue locations with climates that best represent the future climates to be expected at Yucca Mountain. The weather records at these analogue climate sites are used to simulate weather conditions at Yucca Mountain during the future climate states.

2.3.1.2.1   Conceptual Description of Climate
[NUREG-1804, Section 2.2.1.3.5.3: AC 1(1), (2), (7)]

The present climate at Yucca Mountain and the analysis by which future climate is forecast are presented below. The FEPs included in the climate analysis are provided in Table 2.3.1-1. The

climate at Yucca Mountain will change from the present-day climate state to future climate states that are generally wetter and, except for the monsoon climate, generally cooler than present-day. For the monsoon climate, mean annual precipitation and air temperature are predicted to increase. The representation of the post-10,000-year climate is a constant percolation flux specified in proposed 10 CFR 63.342(c)(2).

2.3.1.2.1.1   Regional Climatic Characteristics

The section provides some general information on the climatic and meteorological conditions in the Yucca Mountain area. For details on the current climate and meteorology in the vicinity of Yucca Mountain, see Section 1.1.3.

The Basin-and-Range topography of Nevada has a strong influence on local meteorological conditions, and longer-term regional climatic and meteorological data have been supplemented with more than 20 years of site-specific data to characterize the meteorological conditions in the Yucca Mountain area. Both regional and site-specific data show the influence of elevation on precipitation and temperature: generally, the higher the elevation, the higher the precipitation and the lower the temperature (CRWMS M&O 1997a, pp. 4-10 and A-19; SNL 2006, Sections 6.1.5 and 6.2.5).

Precipitation—The aridity of southern Nevada is partly due to the blocking of Pacific moisture in westerly airflow by the Sierra Nevada mountains, which is an example of the rain-shadow effect. Some maritime polar air masses have strong enough westerly airflow and moisture sources to bring storms and precipitation into southern Nevada, typically during the winter months. These storms can be accompanied by strong winds and periods of relatively steady rainfall. Snowfall is a rare occurrence at the lower elevations in southern Nevada, but it can occur a few times during the winter at the elevations of the upper portion of Yucca Mountain (CRWMS M&O 1997a, p. 4-1). During the summer months, moisture from both the eastern Pacific and the Gulf of Mexico can be transported into the southwestern United States during a monsoon season of southerly moist airflow. Occasionally, this moisture can travel sufficiently north and west to reach southern Nevada, causing convective air mass thunderstorms with periods of intense rainfall, wind, and lightning in the region (Hansen et al. 1977, p. 12).

In a study of atmospheric circulation patterns relevant to streamflow in the southwestern United States, strong correlations were noted between regional streamflow and Type I El Niño Southern Oscillation and La Niña occurrences (CRWMS M&O 1997a, p. 4-2). Type I El Niño Southern Oscillation occurrences are typically followed by a wet December through July precipitation season. Seven such events occurred during the period of 1948 to 1988. Conversely, the La Niña occurrences are typically followed by a dry February through July period. The study identified 1983—an intense Type I El Niño Southern Oscillation occurrence—as the only year having streamflows above median levels during all 12 months. The impact of El Niño conditions on Yucca Mountain weather is described in the *Yucca Mountain Site Description* (BSC 2004b, Section 6.3.3). At Yucca Mountain, winter precipitation was sufficient in water years 1995 and 1998 to produce runoff in several subbasins on the Yucca Mountain site that was used during validation of the net infiltration model (SNL 2008a, Section 7.1.3).

Precipitation and temperature data are available from meteorological stations in the vicinity of Yucca Mountain and the Nevada Test Site (Figure 2.3.1-3) for simulating net infiltration during the present day climate, and from meteorological stations in the Western United States for simulating net infiltration during future climates (Figure 2.3.1-4) (SNL 2006, Figures 4.1-1 and 4.1-2, and Section 4.1). Station 4JA is located in Jackass Flats about 15 km east–southeast from Yucca Mountain, at an elevation of 1,043 m above mean sea level. Records from station 4JA collected from 1959 to 2004 indicate that mean annual precipitation at that location was 145 mm. At Amargosa Farms, 30 km south of Yucca Mountain, at an elevation of 747 m, mean average annual precipitation for 1965 to 2004 was 106 mm. At Area 12 on the Nevada Test Site (Site A12), located 43 km north-northeast of Yucca Mountain at an elevation of 2,283 m, mean annual precipitation for 1960 to 2004 was 319 mm (SNL 2006, Section 6.2.5.1). Two other stations in the vicinity of Yucca Mountain include 40MN, located about 24 km northeast at an elevation of 1,469 m, mean annual precipitation for 1961 to 2004 of 209 mm/yr and Cane Spring, located about 32 km east at an elevation of 1,219 m, mean annual precipitation for 1965 to 2004 of 195 mm/yr (SNL 2006, Section 6.2.5.1).

Site-specific data for Yucca Mountain are available from a meteorological network operated since December 1985 (BSC 2004b, Table 6-2). The network site locations (Figure 2.3.1-3) and measurements were chosen to characterize local airflow and atmospheric dispersion, support engineering design of surface facilities, and comply with the State of Nevada air-quality permit conditions related to site characterization field activities. Site 2 (Yucca Mountain station) is on the ridgetop of Yucca Mountain, near its northern end, at an elevation of 1,478 m above mean sea level. Mean average annual precipitation at Site 2 for the 12-year period from 1993 through 2004 was 191 mm (SNL 2006, Table 6.1-4). For the 12-year period from 1993 through 2004, the highest average annual precipitation of 213 mm was observed at Site 6 (elevation of 1315 m), and the lowest average annual precipitation of 110 mm was observed at Site 9 (elevation 838 m) (SNL 2006, Table 6.1-4). The average annual precipitation of the four stations on Yucca Mountain (Sites 1, 2, 3, and 6) is 199 mm. Although there are several other weather stations near Yucca Mountain (such as Sites 8 and 9), Sites 1, 2, 3, and 6 are primarily used here because they are the closest stations to the repository footprint.

Temperature—Air temperatures in the Yucca Mountain region show less variation with elevation than precipitation (CRWMS M&O 1997a, p. 4-12; SNL 2006, Section 6.1.5.3). For the period of 1993 through 2004, average daily minimum and maximum temperatures vary systematically during the year at Sites 1, 2, 3, 6, and 9. The lowest average daily minimum temperatures of about 0°C occur at Site 6 in the winter, and the highest average daily maximum temperatures of 38°C occur in the summer at Site 9 (SNL 2006, Figures 6.1-26 and 6.1-27). Within the region of Yucca Mountain, two other stations (MEDA 12 and MEDA 26) have been used to provide temperature records. These two stations are used to substitute temperature records at stations Area 12 and 4JA, which do not have temperature records.

Evapotranspiration—Evapotranspiration is the combined process of evaporation and plant transpiration. To quantify this process, precipitation is compared with the water equivalent of energy available for evaporation and sensible heat flux. In arid regions such as Yucca Mountain, precipitation is less than the available energy for evapotranspiration. As mentioned above, the average precipitation at Yucca Mountain is approximately 199 mm/yr for the period of 1993 through 2004. Average annual potential evapotranspiration has been calculated to be

approximately 1,700 mm/yr for two sites near Yucca Mountain (Area 3 and Area 5 within the Nevada Test Site (DOE 2001, p. 10)), and approximately 1,500 mm/yr using a potential evapotranspiration atlas for Nevada (Shevenell 1996, Figure 21). Using these values, potential evapotranspiration is approximately 8 times greater than the average annual precipitation rate at Yucca Mountain.

2.3.1.2.1.2   Climate and Climate Change

An analysis was performed to estimate climatic variables for the next 10,000 years by forecasting the timing and nature of climate change at Yucca Mountain. The future-climate forecast is based on an analysis of paleoclimate data for timing, magnitude, and duration of climate change. Analogue meteorological stations were selected from sites throughout the western United States to represent future climate conditions. The analogue stations provide the upper and lower bounds for precipitation and temperature conditions for each future climate state forecast to occur at Yucca Mountain during the next 10,000 years. Current meteorological data from the analogue climate sites (SNL 2006, Section 6.3) were then used as input to the infiltration model (BSC 2004a, Section 6.6.2; SNL 2008a, Appendix F).

Forecasting future climatic conditions was employed, rather than numerical modeling, because numerical modeling requires that future climate boundary conditions be known (BSC 2004a, Section 7.1). Future boundary conditions are not known, and use of present-day values or estimates of future values would produce output of limited value. However, the forecasting approach is reasonable in that it is based on both a consistent interpretation of a large body of paleoclimatic data and sound conclusions about the relation between climate change and specific earth-orbital cycles: the orbit shape (eccentricity) and the tilt wobble (precession) (BSC 2004a, Section 6.4; Sharpe 2003, Section 6.4.2).

The technical basis for forecasting future climate is based on well-established scientific observations and theory (BSC 2004a, Section 5; Sharpe 2003, Section 5):

- Climate is cyclical, so past climates provide insight into future climates.

- A relationship exists between the timing of long-term past climate change (i.e., glacial and interglacial cycles) and the timing of changes in certain earth-orbital parameters. This relationship establishes a millennial-scale climate-change clock, which provides a means to predict the timing of future climate changes.

- A relationship also exists between the characteristics of past climates and the sequence of those climates in the long, approximately 400,000 year, earth-orbital cycle. The characteristics of past glacial and interglacial climates within the long earth-orbital cycle differ from each other and do so in a systematic way. This climate sequence relationship provides a sound basis for the selection of a particular past climate as an analogue for future climate.

- Long-term earth-based climate forcing functions, primarily tectonics, operate on a million-year timescale and have remained relatively constant during the last long earth-climate cycle (400,000 years) and will not change during the next 10,000 years.

Consequently, the potential impact of long-term earth-based forcing functions on climate need not be considered for the next 10,000 years.

Table 2.3.1-5 summarizes the paleoclimate data used for forecasting future climate change. These data consist of calcite data from Devils Hole that span the period of 59,800 to 567,700 years before present (Landwehr et al. 1997, Table 1); earth-orbital information that spans 800,000 years (two 400,000-year-long climate cycles), including the younger long climate cycle and the older long climate cycle; and fossil and microfossil data from Owens Lake that span over 800,000 years (Bischoff et al. 1997). Section 2.2.1.3.5 of NUREG-1804 (AC 1(7)) states that projections of future climate change should be based on evaluation of paleoclimate information over the past 500,000 years. Although the data sets described above cover more than 500,000 years, because the earth-orbital cycle is a 400,000 year period, only those portions of the developed data sets, such as the composite stratigraphic distribution of common lacustrine ostracode species (small crustaceans routinely used in fossil dating) from the Owens Lake record, and the Devils Hole calcite $\delta^{18}O$ data, covering the last 400,000 years, are required for climate analyses (BSC 2004a, Section 6.5.1). For example, although calcite $\delta^{18}O$ and radiometric dating data from Devils Hole are available for 507,900 of the past 567,700 years (Landwehr et al. 1997), only the data representing the period of 425,000 to 59,800 years before present were used in the analysis of the cyclical nature of climate change for the last 400,000 year cycle (BSC 2004a, Figure 6-3).

2.3.1.2.1.2.1 Relations between Present and Past Climate

The present-day earth climate system is a three-component system (Figure 2.3.1-5) consisting of two active components—the tropical (Hadley) cell and polar cell air masses—and a more passive mixing zone between them (the westerlies or Ferrel cell) (BSC 2004a, Section 6.2). At the northern edge of the tropical air masses, the subtropical highs consist of high-pressure, descending air that creates a hot, dry, low-precipitation, and high-evaporation climate. The subtropical highs define the global hot desert belts and dominate the climate of the Yucca Mountain region today. Regions south of the subtropical highs fall under the influence of the much wetter subtropical easterlies. At the southern edge of the polar air masses, the polar lows consist of low-pressure, rising air that creates a cool, wet, high-precipitation and low-evaporation climate. The average seasonal position of the polar lows corresponds with the southern extent of the boreal forests (forest areas and tundras of the northern temperate zone and Arctic region); the southward movement of these polar lows also influenced some past glacial climates in the Yucca Mountain region. The northernmost part of the polar air mass is characterized, especially in winter, by dense, cold, descending, high-pressure air, low-precipitation, and low-evaporation climates. Airstreams flow southward from these high-pressure cells producing the Arctic (polar) easterlies. The Arctic highs also influenced some past glacial climates in the Yucca Mountain region (BSC 2004a, Section 6.2).

The mixing zone between the tropical and polar air masses, the westerlies, is a complex weather system consisting of high- and low-pressure air masses or cells that often produce storms along their boundaries. These high- and low-pressure cells may be short-lived (hours or days), or they may persist for a week or more. The precipitation and temperature characteristics within the westerlies are typically seasonal and are related to the proximity of the tropical or the polar air masses. The southern edge of the polar lows, along the boundary with the westerlies, is commonly called the polar front and is the area where the polar jet stream resides. The polar jet stream acts as a steering

current for westerly storms. Similarly, the northern edge of the subtropical highs is referred to as the subtropical front and is the location of the subtropical jet stream (BSC 2004a, Section 6.2).

In southern areas of the United States, tropical air masses and warm westerlies dominate the climate, whereas, in northern areas, the climate is dominated by polar air masses. The general climate associated with these air masses is often modified by regional features, such as topography, large lakes, and the oceans. The Sierra Nevada and the Transverse Range have exerted significant control over the past and present-day Yucca Mountain climate. These mountain ranges cut the Yucca Mountain region off from its major moisture source, the Pacific Ocean, and especially the subtropical Pacific Ocean. By creating and sustaining a major rain shadow in the Yucca Mountain region, the mountain ranges also have amplified the evaporative action of the subtropical highs during present-day and past interglacial climates. This subtropical high-dominated climate regime has dominated the regional climate for about the past 9,000 to 10,000 years, with some episodes being hotter and drier, others being cooler and wetter, and others being warmer and wetter than the present-day (BSC 2004a, Section 6.2).

The present-day interglacial climate, and that of the past 8,000 years or so, is not typical of climate during the last several hundred thousand years. Past climates have included glacial periods and a variety of intermediate climates between glacial and interglacial, which may be thought of in terms of dominance of the polar and tropical air masses. The expansion of continental ice into the United States during glacial periods means that the polar air masses expanded and became persistent in more southern areas throughout the year. Because the basic physical laws of atmospheric circulation are conserved when the polar air masses expand and become more persistent, the polar lows must also move southward, both in the sense of the seasonal extreme and their average position. As the polar lows expand southward, the wet, cool, boreal realm moves southward, resulting in wetter and cooler conditions in places that today are warmer and drier (BSC 2004a, Section 6.2).

In the Yucca Mountain region, a glacial climate would mean subtropical highs would be less persistent, so mean annual temperature, summer temperature, and the high summer evaporation would be lower, resulting in the potential for more infiltration. In addition, more frequent and persistent incursions of polar-low activity would result in more rain and snow during glacial periods than today. Infiltration would be increased further during these periods because winter precipitation, as melting snow, would be less likely to evaporate or be used by the vegetation (i.e., evapotranspiration would be much lower). During some glacial periods, when large continental ice sheets existed, Arctic highs were likely resident in the Yucca Mountain region for much or perhaps all of the year, resulting in very cold and dry conditions with limited evaporation. Relative to present-day climate, infiltration would be higher during these cold, dry climates because evapotranspiration would be lower (BSC 2004a, Section 6.2).

The Yucca Mountain region also has experienced different types of interglacial periods, some of which were warmer and wetter than the present-day interglacial period. During these periods, the subtropical highs expanded or intensified or both, resulting in a northward shift of the southwestern monsoon. Summer precipitation likely increased, resulting in higher mean annual precipitation, but much of it was lost to evapotranspiration due to higher air temperatures and active transpiration by vegetation. Conversely, there were also times during glacial-transition climates that were wetter and cooler (but not extremely cold) than during some glacial periods, potentially enhancing infiltration (BSC 2004a, Section 6.2).

On timescales of hundreds of thousands of years, climate change is large, and change in climate parameters affecting infiltration is also large. Historically, the largest amounts of infiltration at Yucca Mountain probably occurred when very large continental ice sheets existed, resulting in cold, low evaporative conditions in the region. Evidence shows that glacial periods were of limited duration, lasting from a few thousand years to as much as 35,000 years for a major glacial period that occurred from about 140,000 to 175,000 years ago. The interglacial (present-day) climates persisted for only about 20% of the documented interglacial and glacial history. Thus, much of the Yucca Mountain climate history is dominated by glacial-transition climates. In addition, it appears that each glacial and interglacial period had a characteristic climate with unique infiltration characteristics (BSC 2004a, Section 6.2).

Understanding the controls exerted on present climates in the Yucca Mountain region by atmospheric circulation patterns, as well as the importance of local and regional topography, provides a framework for analyzing the various paleoclimate data sources. The duration of past climates affecting the Yucca Mountain region reflects the manner in which these atmospheric controls have been influenced by earth-orbital parameters, which are discussed in Section 2.3.1.2.1.2.3. The combined effects are responsible for the cyclical nature of past climates, which is an element of the technical basis for forecasting future climates.

2.3.1.2.1.2.2   The Devils Hole Oxygen Isotope Record as Evidence of Cyclical Climate Change

Isotopic information in the geologic record indicates that past climate change exhibits a cyclical pattern, making it possible to deduce that future climate change should exhibit a similar pattern (BSC 2004a, Section 6.3). The $\delta^{18}O$ isotope record from a calcite core at Devils Hole, Nevada, about 50 km south of Yucca Mountain (Figure 2.3.1-6), indicates that past climate cycles are a series of glacial–interglacial couplets (Figure 2.3.1-7). Devils Hole is a water-filled, cave-like, active extensional fracture in the Paleozoic limestone that composes the regional Paleozoic aquifer. During the last 567,700 years, calcite has precipitated on the walls of the fracture, leaving an isotopic record of the regional groundwater flowing through the fracture (Winograd, Coplen et al. 1992, p. 255; Landwehr et al. 1997, Table 1). The $\delta^{18}O$ data from the calcite deposits show an irregular cyclicity between high and low values of $\delta^{18}O$ over the period of calcite deposition (Landwehr et al. 1997, Table 1). Uranium-series ages were also determined for the calcite core to provide chronologic control for interpretation of the $\delta^{18}O$ data (Ludwig et al. 1992, pp. 284 to 287).

Analysis of the cycles in the $\delta^{18}O$ data from Devils Hole covers the past 425,000 years (Figure 2.3.1-7). The 425,000 year data set encompasses the younger long 400,000 year climate cycle (400,000 years ago to present) and the end of the older long 400,000 year climate cycle. This data set reflects a cyclic change from interglacial to glacial climates, each of which can be identified by a number for a marine isotope stage, or an oxygen isotope stage (OIS), where odd numbers are interglacials and even numbers are glacials (BSC 2004a, Section 6.3). The OISs, derived from the marine carbonate $\delta^{18}O$ records, are widely accepted climate benchmarks and reflect changes in $\delta^{18}O$ values of ocean water as continental ice sheets expanded and contracted. The correlation between the OISs and the Devils Hole chronology differ in the timing of the glacial terminations. This lack of exact correlation is likely due to the resolution in the Devils Hole uranium-series age-dating methodology and the time-transgressive nature of climate change. The Devils Hole chronology provides the most appropriate timeline for the Yucca Mountain region because the Devils Hole

record is a continuously dated (59,800 to 567,700 years before present) terrestrial record of climate variation in the Yucca Mountain region. The Devils Hole $\delta^{18}O$ record, as interpreted in terms of changes in isotopic values of infiltration in the recharge area, shows that climate is cyclic on a 100,000 year timescale, even though the cycles differ in exact duration (Winograd, Coplen et al. 1992, p. 258; Winograd, Landwehr et al. 1997, Figure 2).

2.3.1.2.1.2.3   Earth-Orbital Parameters and the Timing of Past and Future Climate Change

As described previously in Section 2.3.1.2.1.2.1, relationships exist between long-term past climate change and certain earth-orbital parameters. These relationships between earth-orbital parameters and the timing of past climate change provide the technical basis for forecasting future climate change (BSC 2004a, Section 6.4). There are three orbital parameters, each having its own periodicity: (1) eccentricity, the shape of the earth's orbit changing in a systematic way from an ellipse to a circle and back to an ellipse with time, about every 100,000 years; (2) obliquity, the angle of the earth's axis of rotation changing a few degrees with time, about every 41,000 years; and (3) precession, the wobble of the earth's axis like that of a spinning top changing with time, about every 23,000 years. Precession, which dominates insolation (heat from the sun as measured at the top of the atmosphere) at low latitudes, is the primary parameter used to identify the timing of climate change. Because of precession, the point in the orbit nearest the sun shifts from one hemisphere to the other about every 11,500 years. Eccentricity amplifies or dampens the precession value, as indicated in Figure 2.3.1-8. Obliquity, which influences the nature of seasonality at high latitudes, did not show any consistent relationship with the Devils Hole record, so it is not considered further in this analysis (BSC 2004a, Section 6.4).

To identify an orbital clock that can be used to forecast the timing of future climate change, the orbital cycles were compared with the Devils Hole climate change chronology because Devils Hole is the only continuous and independently dated climate record (using uranium-series age-dating methods) documented in the scientific literature (BSC 2004a, Section 6.4). A general qualitative relationship between Devils Hole data and precession is evident where certain maximal values of precession mark the ends of the Devils Hole interglacials and other warm periods (Figure 2.3.1-9). The qualitative relationship was used to develop a correlation between the Devils Hole $\delta^{18}O$ profile, precession, and eccentricity from direct inspection of the respective curves. The correlation provides an orbital clock that offers a rationale for timing future climate change in the Yucca Mountain region. Although the correlation of the timing of past climate change and changes in the earth-orbital parameters provides information about the timing of climate change, it does not imply magnitude or nature of climate change (BSC 2004a, Section 6.4).

By comparing the Devils Hole $\delta^{18}O$ and uranium-series age data (Ludwig et al. 1992) with orbital parameter data, the precession values that define the beginning or the end of a glacial period were determined (BSC 2004a, Section 6.4). The relationship, starting with the end of the interglacial period around 400,000 years ago, identifies the primary inflection points in the available Devils Hole record. Inspection of precession plots (Figure 2.3.1-10) and of the timing of precession versus Devils Hole $\delta^{18}O$ data (Figure 2.3.1-9) shows that a maximal positive precession (letter I in Figure 2.3.1-10) marks the approximate termination of the interglacials defined by the Devils Hole record. Terminations of interglacials are the times when the Devils Hole $\delta^{18}O$ curve moves from high interglacial values toward lower values (i.e., the terminal inflection point in an interglacial

sequence coming forward in time), identified by the number below the letter I in Figure 2.3.1-10. Minimal precession values mark the ends of glacial periods, when the Devils Hole $\delta^{18}O$ record reverses its trend from low values and moves progressively toward high values (i.e., the primary inflection point in the curve beyond which the values become progressively higher), identified by the number near the letter T in Figure 2.3.1-11.

Final glacial inflection points (i.e., the Devils Hole inflection point after which the $\delta^{18}O$ values become progressively higher) are defined by the first minimal precession value (letter T in Figure 2.3.1-11) following an eccentricity minimum value (letter m in Figure 2.3.1-10). If a precession minimum coincides with an eccentricity minimum, which happens with the first glacial period in the 400,000 year cycle, the next precession minimum marks the final glacial inflection point. The next (younger) interglacial inflection point (i.e., the inflection point in the Devils Hole record after which the $\delta^{18}O$ values become progressively lower) occurs at the first precession maximal value about 30,000 years after the preceding precessional minimum (Figure 2.3.1-10). The primary inflection points probably reflect that a change toward an interglacial climate has occurred, rather than an abrupt change in climatic conditions. Though the Devils Hole $\delta^{18}O$ profile is a relatively smooth curve, indicating a continuous transition toward and into interglacial climates, the Devils Hole data points integrate about 1,800 years that may contain numerous small-magnitude climate reversals (BSC 2004a, Section 6.6.1). Nevertheless, the correspondence between the precession-based and Devils Hole–based sets of values (Figure 2.3.1-11) is nearly identical in most cases (BSC 2004a, Section 6.4).

The precession methodology was used to forecast the timing of climate change over the next 100,000 years (Figure 2.3.1-12). The timing of possible climate change toward and away from the next glacial period is the same as for the cycle beginning about 400,000 years ago because of a repeat of the earth's long eccentricity cycle (Figures 2.3.1-10 and 2.3.1-11). The duration of the period between the initiation (I) of climate change toward the glacial climate at 399,000 years ago and the climate change away (T) from the glacial climate is 44,000 years. In Figure 2.3.1-12, the time between a change toward the glacial climate (I) at 1,000 years ago to the change away (T) at 44,000 years in the future is 45,000 years. As shown in Figure 2.3.1-11, the timing for the change toward and away is much longer for the remaining three glacial periods in the 400,000-year cycle, with durations of 58,000, 80,500, and 83,000 years, respectively.

A precession-based orbital clock, calibrated with the Devils Hole chronology, provides a basis to time climate change from the interglacials toward glacials and from glacials toward interglacials. This clock times the beginning and end of the major climate events during the last 400,000 year cycle and provides a clock for such events in the future (BSC 2004a, Section 6.4). Climate change does not occur steadily from interglacials to glacials and back again; instead, it is a complex array of glacial-transition climates between interglacial and glacial extremes (BSC 2004a, Section 6.4). A good example of this is the interstatial period that occurred from 59,000 to 24,000 years ago between two other glacial periods. While it is recognized that this period is one of warmer temperatures, it is generally not thought of as a true interglacial period and occurs at the same time as the North American Wisconsin Glaciation (80,000 to 10,000 years ago) and the Tahoe, Tenaya, and Tioga ice ages of the Sierra Nevada mountains. In future climate predictions, the period of 71,000 to 12,000 years ago might be best treated as a single glacial period, which corresponds to the period from 478,000 to 423,000 years ago. The close match in timing, length, and $\delta^{18}O$ values between these two periods supports the 400,000 year climate cycle. The glacial-transition climates

may be intermediate or, at times, may be warmer (whether wetter or drier) than the interglacials and colder (whether wetter or drier) than the glacials. Because the timing of glacial-transition climates is potentially important to performance of the repository, the precession methodology was investigated as a means to forecast climate change for shorter intervals of time.

The 10,000 year period from 399,000 to 389,000 years ago in the Devils Hole δ^{18}O record (Figure 2.3.1-13) was examined as an analogue of future climate conditions at Yucca Mountain (BSC 2004a, Section 6.4). Even at that timescale, it is apparent that variations in the Devils Hole δ^{18}O data approximately correspond to changes in precession values. Specifically, the change in precession from a maximal value 399,000 years ago to a minimal value 389,000 years ago corresponds with the end of an interglacial period and a change from a maximal to a lower δ^{18}O value (Figures 2.3.1-10 and 2.3.1-13). Other periods also show a rough synchroneity between rises and falls in δ^{18}O values and precessional values. In general, the data indicate approximate correlations between the timing of minor inflection points in the Devils Hole record and subcycles in orbital precession values. Consequently, the timing of future subcycles of precession should also approximate the times of climate variations over relatively short (e.g., 10,000 year) periods (BSC 2004a, Section 6.4).

The precession curve in Figure 2.3.1-12 is similar to the precession curve in Figure 2.3.1-13. Based on the analysis of the future precession curve, glacial-transition climates will characterize the southern Nevada climate for approximately the next 30,000 years. Then, about 30,000 years from now, climate will change into the full glacial climate for a period of about 20,000 years (BSC 2004a, Section 6.4).

2.3.1.2.1.2.4   Reconstruction of Past Climate Details Using Data about Fossil Ostracodes in Owens Lake and Sizes of Prehistoric Lakes in the Great Basin

The technical basis for forecasting future climates depends on paleoclimate data that reflects the characteristics and sequences of past glacial and interglacial climates so similarities in the past two 400,000 year earth orbital cycles can be identified. The last 800,000 years includes two full eccentricity cycles, each approximately 400,000 years long. The present climate is poised to begin another 400,000 year earth-orbital cycle. Based on past precession and eccentricity parameters, it appears that the next 400,000 year cycle will be most similar to the last 400,000 year cycle (BSC 2004a, Section 6.5). Comparison of climate series from different 400,000 year cycles requires that climates from the last 400,000 year cycle be known in enough detail to serve as a basic reference for comparison of climates in the older 400,000 year cycle.

Although the Devils Hole stable isotope record (Section 2.3.1.2.1.2.2) provides the best-dated record for climate change chronology, it does not provide a means of determining the magnitude of climate events. Accordingly, the microfossil record from cores drilled at Owens Lake was used to reconstruct a climate history for the last 400,000 year earth-orbital cycle. Because the hydrology of Owens Lake is closely linked to climate (Bischoff et al. 1997), the microfossil record (specifically, the ostracode occurrence) from cores drilled at Owens Lake was used to determine the sequence and nature of past climates over the last 400,000 year climate cycle. Additionally, because areal extent and depth of lakes and lake sediment have been correlated to climate change, the record of changes

in the lake sizes in the Great Basin provided additional data for the analysis (BSC 2004a, Section 6.5).

Owens Lake is a present-day playa (dry lake) on the eastern side of the Sierra Nevada Mountain Range in Inyo County, California, about 140 km west of Yucca Mountain (Figure 2.3.1-6). In 1992, the U.S. Geological Survey took three cores from the south–central part of Owens Lake playa. The composite core (OL-92) represents 80% of the section and provided the lake sediment record used in the Yucca Mountain climate analysis. The cored record of Owens Lake spans the past 800,000 years. Studies by Forester et al. (1999, p. 13) utilized diatom data covering 500,000 years and ostracode data covering 400,000 years (Table 2.3.1-5). Details on Owens Lake hydrology, diatom data, and the ostracode record are given in Section 2.3.1.2.2.1.2.

Figure 2.3.1-14 depicts the ostracode abundance data as a function of the depth of the core sample. In addition, the oxygen isotope stages (also called Marine isotope stages) are shown on the right side of the figure. The data on the figure display the last 400,000 year orbital cycle. As noted on the figure, oxygen isotope stages with even numbers indicate glacial climate periods and odd numbers indicate interglacial climate periods. The first two ostracode species on the left side (*Cytherissa lacustris* and *Candona caudata*) are ostracodes that require low salinity water in order to grow and reproduce. The presence of these two species is indicative of a spill and fill lake that would be present during a wet and cooler climate. The middle species on the plot (*Limnocythere ceriotuberosa*) is common in lakes receiving seasonal surface flow followed by a base-flow phase. The presence of this species implies greater surface flow than is typical today but less than that during the periods when *C. lacustris* and *C. caudata* are common. The species most associated with warm climates is *Limnocythere sappaensis*. This species requires high alkalinity/high calcium waters typical of base flow in the Owens River. The presence of *L. sappaensis* is indicative of a warm and dry interglacial climate. The final species is *Limnocythere bradburyi* which is similar to *L. sappaensis* in that it requires warm water (it cannot survive in cold water) but is more salinity sensitive than *L. sappaensis*.

The ostracode microfossil record from Owens Lake cores provides the basis to make a number of general observations about paleoclimate. Some of these observations for the last 400,000 year earth-orbital cycle include the following:

- The third glacial period in the sequence (OIS 6) was the coldest of the glacial climates and had the highest level of effective moisture, but not necessarily the highest mean annual precipitation.

- The first glacial period in the sequence (OIS 10) was the warmest and perhaps the wettest of the glacial climates, but probably had a moderate level of effective moisture relative to higher effective moisture in the colder glacial periods in the sequence.

- There were numerous interglacial and related warm climate periods, such as OIS stages 5A and 5C, when the climate was warm and dry with low effective moisture.

- The warm, dry climate periods were occasionally punctuated by warm and wet, tropical-dominated climates that had low effective moisture.

- There were extensive periods when climate characteristics were intermediate in nature between full-glacial high effective moisture and interglacial, warm-climate, low effective moisture periods.

- The rate of change between the various climates was rapid, occurring on a decade to century timescale.

The Owens Lake ostracode hydrologic and climatic record indicates that the regional climate history for the past 400,000 years was comprised of a series of alternating glacial and interglacial periods, which varied in temperature extremes and durations. Each of the glacial climates, denoted by OISs 10, 8, 6, and 4/2, was different from the others, initially became colder as the sequence progressed, and reached the coldest and most persistent glacial climate with OIS 6. A complex set of climates followed OIS 6, ranging from the wet and warm interglacial OIS 5E to the cold and relatively short-lived glacial climates OIS 4 and 2 (BSC 2004a, Section 6.5.2).

In terms of an orbital clock, the climate currently resides at the beginning of a new 400,000 year cycle. Accordingly, the transition climate at the beginning of the last 400,000 year cycle (OIS 11 to OIS 10) is an analogue for future climate at Yucca Mountain for the next 10,000 years. This conclusion is supported by comparing the last 400,000 year cycle (referred to as the younger long climate cycle), to the cycle occurring between 800,000 years and 400,000 years ago (referred to as the older long climate cycle).

Evaluation of the general order of climate change magnitude from the size of old lakes provides insights to compare the climate characteristics of glacial periods within and between 400,000 year cycles. Aspects of the events seen in the younger part of the Owens Lake record (younger long climate cycle) can be identified in the older long climate cycle climate records. During the younger long climate cycle, the coldest and highest effective moisture climate was interpreted, based on the ostracode and other records, as the third glacial (OIS 6). Reheis (1999, Figures 2 and 3) presents evidence for OIS 16, the third glacial period in the older long climate cycle, being the biggest and deepest lake in several basins throughout the Great Basin. A detailed analysis by Reheis (1999, p. 201) of prehistoric lakes in the Great Basin shows that the pattern of the sequence of lake sizes and depths during the older long climate cycle was repeated during the younger long climate cycle. Moreover, the details of lake sizes and depths can be used to infer details about the climate associated with each lake. Support for the interpretation comes from, for example, the OIS 6 lake in Death Valley that was at least 175 m deep in contrast to a depth of only about 70 m deep during OIS 2 (BSC 2004a, Section 6.5.2). These data further demonstrate the repetition of climate over a 400,000 year period and provide additional basis for estimating future climates.

The information presented above indicates that there is repetition between the types of climate in the older long climate cycle and the younger long climate cycle. Taken together, the data concerning microfossil ostracodes in Owens Lake and the cyclical variation in lake characteristics in the Great Basin imply that the transition from OIS 11 to OIS 10—which occurred 400,000 years ago—is expected to repeat and, therefore, provides the basis for forecasting the climate at Yucca Mountain for the next 10,000 years. Sections 2.3.1.2.3.1 and 2.3.1.2.3.2 provide a discussion of the rationale for the forecast of climate change for the next 10,000 years, as well as a summary of the uncertainties in the forecasting approach.

2.3.1.2.2   Paleoclimatological Data and Data Uncertainty
[NUREG-1804, Section 2.2.1.3.5.3: AC 1(2), (3), (4), (7), AC 2(1) to (4), AC 3(1), (2)]

The paleoclimatological data and associated data uncertainty that were used to support the climate analysis are presented in this section.

2.3.1.2.2.1   Paleoclimatological Data

The climate analysis for the Yucca Mountain area used a number of paleoclimate data sets, including ostracode and diatom data from drill cores from Owens Lake and radiometric dating and $\delta^{18}O$ data from Devils Hole (Table 2.3.1-5). The microfossil record from cores drilled at Owens Lake (Figure 2.3.1-6), along with the Devils Hole data, are the primary sources of paleoclimate data used to reconstruct the climate history in the Yucca Mountain area for the last long earth-orbital cycle that has occurred over the last 400,000 years (BSC 2004a, Section 6.5.1). Because climate phenomena operate on regional scales, past climates at Owens Lake are likely to resemble the past climates at Yucca Mountain.

2.3.1.2.2.1.1   Devils Hole Oxygen Isotope Record

Devils Hole is an active extensional fracture in the limestone that composes the regional Paleozoic aquifer (Section 2.3.1.2.1.2.2). The $\delta^{18}O$ isotopic composition of calcite deposited from groundwater flowing through the Devils Hole fracture records the isotopic composition of infiltration in the recharge area of the regional aquifer. The isotopic values of infiltration are related to three factors: (1) the isotopic composition and temperature of the source water; (2) the path that the water vapor takes from the source to the recharge area and the amount of precipitation that occurs along the path; and (3) the temperature at which the precipitation in the recharge area forms. When water evaporates from a source water, the degree of fractionation (separation of isotopes) under equilibrium conditions depends on the temperature of the source: the colder the source, the greater the fractionation. The resulting vapor has a $\delta^{18}O$ value that is equal to the source minus the fractionation factor and, thus, is a lower value than the source water. Some of the ocean-derived vapor moves over the continent, forming precipitation as snow or rain, and, over time, that precipitation returns to the ocean, completing the hydrologic cycle. However, during glacial periods, a significant amount of the precipitation is stored as snow and ice and, thus, does not return to the ocean. Consequently, the isotope value of the ocean becomes higher during glacial periods. The cycle in $\delta^{18}O$ values in marine carbonates between high and low values records the storage or loss of continental ice and, hence, glacial or interglacial climates (BSC 2004a, Section 6.3).

The path and conditions along the path taken by vapor as it moves from the source area toward the recharge area have an important effect on the $\delta^{18}O$ values of precipitation in the recharge area. As vapor is chilled, whether from rising through the atmosphere due to thermal expansion over topography or due to mixing with cooler air, some vapor turns to rain or snow. The fractionation that occurs when vapor turns into precipitation reverses the fractionation that occurs during evaporation. Therefore, precipitation has higher $\delta^{18}O$ values than its vapor source, and following each precipitation event, the $\delta^{18}O$ in the remaining vapor is depleted. If the path to the recharge area involves extensive precipitation, the precipitation in the recharge area will have low $\delta^{18}O$ values. If the vapor path does not involve extensive precipitation, the precipitation in the recharge area will

have higher $\delta^{18}O$ values. Typically, interglacial precipitation has higher $\delta^{18}O$ values than glacial precipitation because the glacial path involves more precipitation. Thus, in the calcite record from Devils Hole, high $\delta^{18}O$ values represent interglacial climates, and low $\delta^{18}O$ values represent glacial or glacial-transition climates (BSC 2004a, Section 6.3). Figure 2.3.1-7 shows the timing and cyclical nature of climate change interpreted from the calcite core $\delta^{18}O$ record from Devils Hole, as well as the oxygen isotope stages.

2.3.1.2.2.1.2   Owens Lake Ostracode and Diatom Record

Owens Lake Hydrology, Chemistry, and Paleontology—The Owens Lake playa contains a thick sequence of lacustrine deposits, which includes diatom, ostracode, and pollen evidence for paleohydrology and climate. The U.S. Geological Survey obtained three cores of the playa sediments to a total depth of 323 m from the south–central part of the playa in 1992. Although the cored record of Owens Lake spans the past 850,000 years (BSC 2004b, Section 6.4.1.2), climate studies for Yucca Mountain focused on the portion of the sediment data spanning the last 400,000 years representing the last long earth-orbital cycle (BSC 2004a, Section 6.5.2).

The Owens River system (Figure 2.3.1-6), with its sequence of downstream basins (Owens, China, Searles, Panamint, and Death Valley), forms a comparatively simple network where the upstream lakes must spill before the lakes lower in the chain receive sufficient water to freshen (Forester et al. 1999, p. 11). During the middle to late 19th century, natural flow from the Owens River maintained a lake that was alkaline and about 15 m deep. Between 1872 and 1905, flow was reduced to about 25% of its natural level due to irrigation in the Owens Valley. Even so, the inflow was sufficient to maintain a perennial, if saline, lake about 6 m deep. The construction of the Los Angeles Aqueduct in 1913 diverted the lake's principal source of water, and the lake soon desiccated in a climate with an evaporation rate of about 1.65 m/yr. Locally, alkaline springs discharge along the margin of the lake basin. For Owens Lake to spill today, it must be about 65 m deep with an area of 690 km^2 (Forester et al. 1999, p. 13).

The major dissolved-ion composition of high-elevation waters from the Sierra Nevada, Inyo, and White Mountains throughout the Owens Lake drainage is dominated by solutes rich in calcium and bicarbonate, and contains moderate to low concentrations of sulfate. The total dissolved-ion concentration of the high-elevation waters is low, usually less than 100 mg/L. The solute composition of valley-floor waters, largely derived from springs, is very different from those at high elevation. The low-elevation waters are dominated by sodium bicarbonate and chloride. Sulfate is variable, and calcium and magnesium are at low concentrations. Given the initial alkalinity-to-calcium ratio of the dilute high-elevation waters, their solute composition will evolve toward carbonate-depleted and calcium-enriched waters or a solute composition low in both ions. The waters at low elevation with higher total dissolved solids have exactly the opposite relationship between bicarbonate and calcium: bicarbonate is enriched, and calcium is depleted. Thus, the solute composition of the low-elevation waters must be derived from a process other than evaporation of the high-elevation waters (Forester et al. 1999, p. 13).

Because spring discharge at low elevation contains solutes dominated by sodium bicarbonate and chloride (at moderate to high total dissolved solids and often at elevated temperatures), these waters are derived from the interaction of basin groundwaters with reactive, fine-grained, volcanic rocks. Although the primary sources of water for the Owens River apparently come from high elevation,

the solute composition of the river at low elevation is characterized by spring and other groundwater discharge rather than evaporation of the dilute high-elevation waters. These hydrochemical relationships are important because the fossil diatoms and ostracodes in the Owens Lake core reflect the water-chemistry spectrum found in the Owens River's past drainage. Calcium bicarbonate–rich waters contain freshwater planktic diatoms indicative of large, deep freshwater lakes and/or ostracodes generally found in dilute, cold lakes commonly found in the boreal forest. Sodium bicarbonate–rich waters contain diatoms and ostracodes that are indicative of a period of shallow water and high specific conductivity (Forester et al. 1999, pp. 13 to 14).

The microfossil record can be translated into a chronological progression of climate-induced hydrochemical environments. Microfossils of fresh, calcium bicarbonate–rich water indicate cool, wet climates when the Owens River was dominated by discharge from high-elevation watersheds, whereas fossils of shallow, sodium bicarbonate–rich water indicate dry climates with reduced mountain flow and greater relative importance of low-elevation spring discharge into Owens Lake (Forester et al. 1999, pp. 13 and 14).

Owens Lake Diatom Record—Diatom and planktic species are common in the cored sediments dating from about 500,000 to 400,000 years ago, indicating that during this time Owens Lake was shallow and consisted of open water associated with a through-flowing marsh. Marsh environments indicate climates of intermediate moisture and a shallow basin filled by sediment. Major episodes of freshwater diatoms occur several times during this period, and are separated by intervals rich in saline diatoms or by intervals with sediments barren of diatoms, which suggest shallow, alkaline water conditions. Thus, the diatoms are representative of the long-term climate–hydrologic behavior of the Owens River system (Forester et al. 1999, p. 15).

Overall, the stratigraphic continuity of freshwater diatoms from Owens Lake indicates a record of a longer-lasting and more persistent fresh and overflowing lake system, rather than a shallow, saline system. The concentration of freshwater diatoms, in direct contrast to the ostracodes, is generally an order of magnitude greater than concentrations of saline diatoms, partly reflecting poor diatom preservation in saline systems. Therefore, rare and short-lived episodes of high concentrations of saline planktic diatoms—implying large and possibly deep saline lakes—may be underrepresented in the Owens Lake record and contrast with the paleolimnology of internally draining Great Basin lakes, such as Walker Lake. Over the past 500,000 years, Owens Lake has been fresh (implying climates wetter than today) about 80% of the time and saline (implying climates like today) about 20% of the time. Although there is some variation, the lengths of intervals of wet climate (freshwater conditions) average about 32,000 years, whereas the lengths of intervals of dry climate (saline conditions) average about 13,000 years (Forester et al. 1999, p. 15).

Owens Lake Ostracode Record—Ostracode species are common in the cored sediments that accumulated over the past 400,000 years. The climate interpretations derived from the ostracodes found in the Owens Lake cores are based on 672 samples covering the past 400,000 years, 75% of which contained sufficient ostracodes for environmental interpretations (Forester et al. 1999, Figure 7). The stratigraphic profile of the ostracodes found in the Owens Lake record (Forester et al. 1999, Figure 7) shows how the lake's hydrochemistry has changed during the last 400,000 years. Ostracodes can be classified according to their hydrochemical tolerances. Some ostracodes live in springs that discharge onto the lake floor, indicating periods like those of today when flow from high elevation was minimal and flow plus solute input from low elevation was maximal.

Other ostracodes represent limnological and climatic periods least like those of today, with a large, deep, seasonally stable, cold, dilute freshwater lake dominated by source waters from high elevations (Forester et al. 1999, p. 15).

Like the diatoms, the ostracode profiles indicate that through much of the last 400,000 years, climate was wetter than today (Forester et al. 1999, p. 18). The ostracode data indicate that present-day climate–hydrologic environments with very alkaline waters occurred about 20% of the time, whereas wetter climates than today with dilute, fresh waters occurred about 80% of the time. In addition, the data indicate that extreme cold or wet (or both) conditions occurred about 5% of the time, but almost exclusively so from about 170,000 to 130,000 years ago and sporadically so from about 60,000 to 18,000 years ago. Furthermore, the ostracode data also indicate that the two glacial periods occurring between about 400,000 to 170,000 years ago were warmer, and possibly wetter, than the subsequent two glacial periods. Thus, the ostracode climate hydrologic record of Owens Lake indicates that the four 100,000 year climate subcycles are not climatically identical to one another (Forester et al. 1999, p. 18).

The ostracode record also indicates that climate can rapidly change in this region. Change from periods like those of today to wetter periods typically occurred in hundreds, not thousands, of years. Such rapid changes from warm and dry to cold and wet climates indicate a southerly shift in the average position and strengthening of the westerly–polar front associated with the polar jet stream (Forester et al. 1999, p. 18).

2.3.1.2.2.1.3   Correlation of Owens Lake Paleolimnology and Devils Hole Oxygen Isotope Records

Because the Owens Lake microfossil chronology is based on a constant sediment-accumulation-rate age model (40 cm/1,000 yrs), the modeled age of a particular sample may not be the same as the actual age if sediment accumulation rates were not constant (Forester et al. 1999, p. 18). However, the overall chronology explains the major paleolimnologic fluctuations of the Owens Lake record in a manner that is generally consistent with well-dated changes in the Devils Hole record. When the age estimates from the Owens Lake data for the glacial and interglacial periods are compared to the Devils Hole chronology, the agreement in the timing of events varies, which is not surprising given the natural variability reflected in the estimates. However, both records have the same sequence of glacial and interglacial events. Consequently, the Owens Lake record can be tuned (or timed) to the Devils Hole record.

The Owens Lake diatom record indicates prominent intervals of large freshwater lakes that correspond to the glacial periods OIS 12, OIS 10, OIS 6, OIS 4, and generally OIS 3+2 until the Holocene. (The discrepancy between the diatom record and OIS 8 is likely due to the assumption of constant sediment accumulation rates used in the Owens Lake sediment-accumulation-rate age model.) The Owens Lake ostracode record shows a pattern similar to that of the diatoms, but the ostracode record, with its better preservation, offers a better indication of the interglacial periods and transitions to glacial periods than of the glacial intervals themselves. The ostracode record beginning 400,000 years ago shows the predominantly saline conditions of OIS 9, OIS 7, OIS 5, OIS 3, and OIS 1. The ostracode data also identify prominent wet periods during OIS 6, and sporadically during OIS 3, and OIS 2. Significantly, the ostracode data indicate that the first two glacial periods in the past 400,000 year cycle (OIS 10 and OIS 8) were not as cold as the last two

glacial periods in that cycle (OIS 6, OIS 4/2). This would mean that the upcoming two glacial periods (similar to OIS 10 and OIS 8) would not be as cold and wet as OIS 6 and OIS 4/2. Cold air temperatures reduce evaporation and raise effective moisture, even when mean annual precipitation is low (Forester et al. 1999, pp. 18 to 19, Figure 9).

The paleoclimate data, combined with correlation to earth-orbital parameters described in Section 2.3.1.2.1.2.3, provide the foundation for forecasting future climate conditions at Yucca Mountain (BSC 2004a, Sections 5, 6.1, and 6.4).

2.3.1.2.2.1.4   Uncertainty in Paleoclimate Data

There are two primary uncertainties in the data sets used to forecast future climate at Yucca Mountain: (1) the standard deviation associated with the Devils Hole ages; and (2) the uncertainty of the timing of climate change implied by the Devils Hole record. The standard deviations about the mean of the Devils Hole ages are, by their nature, an estimate of uncertainty. The uncertainty of the timing of climate change reflected in the Devils Hole record has two components. The first component involves the uncertainties associated with changes in mean annual precipitation and mean annual temperature and their impact on the isotope values. There could be lead or lag time between change in regional climate parameters and the record of recharge at Devils Hole. The second component involves the nature of the Devils Hole samples themselves, each of which integrates a particular thickness of carbonate in a continuous sample series and represents about 1,800 years for the dataset that was used for this analysis (Winograd, Coplen et al. 1992). Consequently, a rapid change in the recharge recorded at Devils Hole could have occurred anytime within those 1,800 years (BSC 2004a, Section 6.6.1).

Although the climate analysis relied on a section of Devils Hole calcite representing approximately 60,000 to 568,000 years, there are additional data that fill in most of this gap. Winograd et al. (2006) describe additional boreholes that overlap the original dataset such that the Devils Hole record now extends from 4,500 to 567,700 years, with reduced uncertainty compared to the dataset reported by Winograd, Coplen et al. (1992). Winograd et al. (2006) reports that the sampling step for the new cores represents about 400 years versus the 1,800 years reported by Winograd, Coplen et al. (1992). In addition, the thorium-uranium age dating reported in Winograd et al. (2006, Tables 1 and 2) indicates that the absolute age dating has a resolution of approximately +/− 429 and 525 years for the first and second cores, respectively. In addition, the data presented in Winograd et al. (2006, Figure 2) indicate the age dates of the new cores lined up with perfectly with the original dataset.

2.3.1.2.3   Climate Analysis and Uncertainty
[NUREG-1804, Section 2.2.1.3.5.3: AC 1(3), (5) to (7), AC 2(2) to (6), AC 3(1), (3), (4), AC 4]

The analysis of combining the historic climate data from the Devils Hole calcite core record and the Owens Lake core in concert with the earth orbital parameters is presented in this section. The process to determine the states and sequence of past and future climates is given in Section 2.3.1.2.3.1.1, and the selection of analogue future climates follows in Section 2.3.1.2.3.1.2.

2.3.1.2.3.1   Climate Analysis

Selecting specific past climates to forecast future Yucca Mountain climates requires that a relation exists between the characteristics of past glacial and interglacial climates and the sequence of those climates within the long, 400,000 year earth-orbital cycle. Although temperature and precipitation characteristics of past glacial–interglacial climate couplets differed from each other in a systematic way within a particular 400,000 year cycle, the sequence of climate couplets in adjacent 400,000 year cycles was similar. Therefore, although a strict repetition of climate characteristics is not expected, general characteristics of future precipitation and temperature for a particular interglacial–glacial couplet should be similar to the corresponding couplet in the past 400,000 year cycle (BSC 2004a, Section 6.5).

2.3.1.2.3.1.1   Nature and Sequence of Past and Future Climates

Comparison of climate series from the last two 400,000 year cycles required that climates from the most recent 400,000 year cycle be known in enough detail to serve as the basic reference for comparison with older climate cycles. Although the Devils Hole stable isotope record provides the best-dated record for sequence study, it does not provide a means of determining the nature and magnitude of climate events. Therefore, the microfossil record from cores drilled at Owens Lake was used to reconstruct a climate history for the last long earth-orbital cycle (BSC 2004a, Section 6.5.1).

Owens Lake Paleoclimate Record—Present-day evaporation in the Owens Basin, estimated to be from 1.5 m/yr (BSC 2004a, p. 6-26) to 1.65 m/yr (Forester et al. 1999, p. 13) relative to 140 mm/yr average local precipitation, would result in a saline Owens Lake if flow were not diverted. During glacial and glacial-transition climates in the past, however, the lake filled with fresh water and had outflow. A relationship exists between total dissolved solids, the alkalinity (bicarbonate)-to-calcium ratio in the lake water, flow in the Owens River, and level of evaporation in the Owens Basin, all of which are directly related to climate. Because of their sensitivity to total dissolved solids, alkalinity-to-calcium ratio, and temperature, the presence or absence of various ostracode and diatom species provide a basis for constructing past and future climate profiles of the Owens Lake area. Although diatom and ostracode data from Owens Lake were evaluated, the paleoclimate analysis employed mainly ostracode data because they are similar to those for diatoms and better preserved under saline conditions. Diatom data were used when necessary to support the ostracode findings (BSC 2004a, Section 6.5.1).

Some ostracode species require high-salinity, high alkalinity-to-calcium ratio water, both of which are associated with base flow in the Owens River and are characteristic of warm climate episodes occurring during interglacial periods. Other ostracode species require low-salinity, low alkalinity-to-calcium ratio water, and their abundant presence in a zone of the stratigraphic record indicates a glacial period when an overflowing, relatively low-salinity lake existed. These extremes represent interglacial and glacial conditions. Glacial-transition climates might be somewhat wetter or cooler than the present-day, or a combination of both, but not as wet or cold as the full-glacial climates. The glacial-transition climate states can be represented by ostracode species alternating between interglacial and glacial conditions. The presence of still other ostracode species represents monsoon climate conditions, indicating wetter and perhaps warmer climates than present-day (BSC 2004a, Section 6.5.1).

A composite stratigraphic distribution of common lacustrine ostracode species from the Owens Lake record for about the last 400,000 years was developed (BSC 2004a, Section 6.5.1, Figure 6-12), and is presented in Figure 2.3.1-14. The chronologies were based on a mass-sediment accumulation model calibrated by radiocarbon ages at the top of the core and the Bishop Ash (a volcanic ash that serves as a marker horizon) at the base of the core, but with no direct dating in between. Comparison of the climate intervals determined by the Devils Hole $\delta^{18}O$ record indicated that the sediment mass-accumulation age model does not provide a precise chronology at Owens Lake. Consequently, the timing of the Owens Lake stratigraphic record was determined by identifying the interglacial and glacial stratigraphic environmental signatures from the record and then correlating them with the Devils Hole record. Alternating ostracode assemblages that reflected the climate conditions associated with each glacial (cold, fresh, overflowing lakes) and interglacial (closed, saline lakes) environment were identified. Ostracode assemblages that reflect glacial-transition and monsoon climatic conditions also were identified, and the relation between the ostracode species assemblages and Owens Lake hydrology was documented (Forester et al. 1999, pp. 10 to 21).

Repetition of Past Climates—In order to select a climatic period from the last 400,000 years as an analogue for the next 10,000 years at Yucca Mountain, it was necessary to demonstrate that the younger long climate cycle (400,000 years ago to present) was similar to the older long climate cycle (800,000 to 400,000 years ago) in terms of the sequence and magnitude of climate variation. In terms of the earth-orbital clock, at present the climate system is at the beginning of a new 400,000 year cycle. Therefore, the transition climate at the beginning of the younger long climate cycle, OIS 11 to OIS 10 (Figures 2.3.1-7 and 2.3.1-14), would be the appropriate analogue for future climate at Yucca Mountain. The Owens Lake ostracode hydrologic climatic record indicates that the regional climate history for the younger long climate cycle was a complex array of climates. Each of the glacial climates (OIS 10, OIS 8, OIS 6, OIS 4, and OIS 2) was different from the others, with OIS 6 being the coldest glacial climate. OIS 6 was followed by climates, ranging from the wet and warm interglacial OIS 5E to the cold and relatively short-lived glacial climates OIS 4 and OIS 2. Although data for the older long climate cycle are more sparse than for the younger long climate cycle, sufficient, lake-level, lake-size, marine-isotope, and ice-volume data are available to confirm the similarity between the older long climate cycle and the younger long climate cycle. For example, the apparent largest lakes during both the older long climate cycle and the younger long climate cycle occurred during the third glacial in each cycle. Consequently, the third glacial in each cycle had the highest effective moisture, due to cold temperatures, high precipitation, or both (BSC 2004a, Section 6.5.2).

In addition, the largest ice sheets are those from OIS 16, 12, 6, and 2. OIS 16 and 12 in the older long climate cycle are analogous to OIS 6 and 2 in the younger long climate cycle. As continental ice sheets expand in area and become higher in elevation, they force the polar air masses to the south. Therefore, large ice sheets should result in cold and wet climates or both in the vicinity of Yucca Mountain. Large ice sheets also result in climates in the Yucca Mountain area with cooler summers than today, which enhances effective moisture. Conversely, OIS 20, 18, and 14, in the older long climate cycle, and OIS 10, 8, and 4 in the younger long climate cycle apparently had smaller or lower ice sheets, potentially allowing for warmer climates with lower effective moisture in the Yucca Mountain region, as smaller lakes associated with those periods imply (BSC 2004a, Section 6.5.2).

This information implies that there is repetition between the types of climate in the older long climate cycle and the younger long climate cycle. Accordingly, the nature of the next glacial period at the beginning of the upcoming 400,000 year cycle should be more like the glacial period at the beginning of the past 400,000 year cycles. Thus, while the younger long climate cycle paleoclimate record was used to project future climate change in the next 10,000 years, analysis of the older long climate cycle paleoclimate record (800,000 to 400,000 years ago) confirmed the basis of the 400,000 year climate cycle. Thus, the transition from OIS 11 to OIS 10 (Figure 2.3.1-7) provides a past analogue for forecasting future climate change, and is used as the basis to establish a potential climate scenario for the next 10,000 years (BSC 2004a, Section 6.5.2).

Climate Change for the Next 10,000 Years—To forecast climate for the next 10,000 years, a point representing the equivalent to the present-day is identified in the younger long climate cycle series, a past–present point. The orbital clock that is based on the precession, obliquity, and eccentricity earth-orbital parameters provides the means to approximately identify the past–present point in the Devils Hole record. Figure 2.3.1-10 shows the linkage of the present-day position in the orbital clock (I equal to 1,000 years ago) and the equivalent point during OIS 11 (I equal to 399,000 years ago). The orbital-clock relation is readily transferred to Devils Hole through their respective chronologies (Figure 2.3.1-11). The first data point in the Devils Hole record indicates that climate change away from the OIS 11 interglacial climate occurred at 397,300 years ago, or 1,700 years after the precession maximum. A precession maximum in the southern hemisphere during the present interglacial climate occurred 1,000 years ago (Figure 2.3.1-10). The OIS 11/10 timing indicates the beginning of climate change away from the present interglacial may be about 700 years in the future (BSC 2004a, Section 6.6.1).

Placement of a past–present point in the Owens Lake sedimentary record required that the sedimentary chronology be placed in the context of the Devils Hole chronology (BSC 2004a, Section 6.6.1). The Owens Lake chronology is based on a sediment mass-accumulation curve (BSC 2004a, Figure 6-12). Analysis of the Owens Lake sedimentary record by comparison with the Devils Hole chronology indicates the sediment accumulation ages at Owens Lake are variously too old or too young. To further refine the Owens Lake ages and estimate where the past–present point belongs, the ostracode and diatom data in the Owens Lake record are used to identify environmental change during and from the OIS 11 interglacial and then from the sequence of environmental change. Interpretation of the ostracode sequence indicates a transition from a full and overflowing lake during a glacial or glacial-transition climate, to an intermediate climate between glacial and interglacial, to an interglacial climate. Between 400,000 and 440,000 years ago, microfossils are observed that are indicative of a period of intense summer monsoon activity (BSC 2004a, Section 6.6.1).

When the past–present point in the OIS 11 sequence at Owens Lake is extrapolated to the present, using an average sediment accumulation rate of 40.1 cm per thousand years (Bischoff et al. 1997, p. 95), the length of present-day climate remaining before the monsoon climate begins is about 600 years, and the duration of the monsoon climate is about 1,400 years (BSC 2004a, Section 6.6.1). The monsoon interval, in turn, should be followed by more than 8,000 years of glacial-transition climate. This timing of climate change is used in the TSPA.

Alternative sediment-accumulation rates have been proposed. Litwin et al. (1999) indicated that the Owens Lake sediment-accumulation rates vary with the climate stage. Estimates range from

26.4 cm per thousand years for OIS 6 up to 167.3 cm per thousand years for OIS 5E (Litwin et al. 1999, Table 1). The analysis indicates that sediment accumulation is less during glacial periods. Litwin et al. (1999) present sediment-accumulation rate estimates of 60 and 66 cm per thousand years for the interglacial intervals OIS 1 and OIS 5, respectively. Using an average of 63 cm per thousand years, the timing of climate change at Yucca Mountain for the next 10,000 years is as follows (BSC 2004a, Section 6.6.1): a present-day climate for about 400 years after present, followed by a monsoon climate for about 900 years, followed by a glacial-transition climate for the remaining 8,700 years. While the theory that sediment accumulation is influenced by the climate stage is reasonable, interpretation of the data is complicated.

The Bischoff et al. (1997, Table 2) sediment-accumulation rate of 40.1 cm per thousand years is an average based on a 6 to 304 m section of the Owens Lake borehole OL-92. The report (Bischoff et al. 1997) also presents a sediment-accumulation rate for the upper (younger) 6 to 24 m section of the borehole that indicated a sediment-accumulation rate of 78.8 cm per thousand years. It should be noted that the 6 to 24 m borehole interval is dominated by the last glacial interval. Correcting for differences in porosity and density, the 6 to 24 m interval and the 6 to 304 m interval had nearly identical mass-accumulation rates (52.4 and 51.4 g/cm^2 per thousand years). This indicates that the greater sediment-accumulation rate of the 6 to 24 m interval was due to less compaction.

Other work with the borehole OL-92 core (Litwin et al. 1999, p. 1162) found that, although a Holocene age section of silt had a sediment-accumulation rate of 64.2 cm per thousand years, the mass-accumulation rate was 42.6 g/cm^2 per thousand years, less than the average mass-accumulation rate derived by Bischoff et al. (1997). The data indicate that sediment-accumulation rates of 60 and 66 cm per thousand years need to be adjusted for the impact of compaction. Because the 6 to 304 m borehole interval accounts for much of the compaction forces (by nature of its length), the 40.1 cm per thousand-year average sediment-accumulation rate is likely the most representative value (BSC 2004a, Section 6.6.1). The calculated climate durations determined from the average mass-accumulation rate of 40.1 cm per 1,000 years yields the length of present-day climate remaining before the monsoon climate begins of about 600 years and the duration of the monsoon climate of about 1,400 years as used in the TSPA models (SNL 2008b, Section 6.3.1.2). The selection of these lengths of climate states based on mass-accumulation rates is also consistent with the timing away from the OIS 11/10 interglacial climate (700 years), based on Devils Hole data. Additional uncertainty in the timing of climate change states is discussed in Section 2.3.1.2.3.2.

2.3.1.2.3.1.2   Selection of Analogue Meteorological Stations

To implement the climate forecast at Yucca Mountain for the next 10,000 years, as described above, each forecast climate regime is represented by present-day, analogue meteorological stations (BSC 2004a, Section 6.6.2) whose data are used to represent the daily variation in precipitation (SNL 2008a, Section 6.5.1.2 and Appendix F) and temperature (SNL 2008a, Appendix F) in the net infiltration model. Each climate regime was characterized with upper-bound and lower-bound analogue climate stations representing ranges in mean annual precipitation and mean annual temperature. This was done because (1) bounds are needed to quantify uncertainty in input values for the infiltration and TSPA models; and (2) there are uncertainties in the paleoclimate record in regard to extrapolating climate proxy data into climate values. Therefore, establishing possible bounds is more appropriate than establishing mean values, especially for the periods of time under

consideration. Because the net infiltration model (SNL 2008a) utilizes annual, seasonal, and daily climate values, the upper-bound and lower-bound values for each climate state were established with meteorological stations selected as representative of the particular climate regime. Stations with complete and long records were given priority in the selection process (BSC 2004a, Section 6.6.2).

Present-Day Climate—The present-day climate regime is characterized by a time when Owens Lake was supported by groundwater discharge, and the Owens River was predominantly at base flow without artificial diversion. Summers are warm to hot, and very evaporative, with evaporation greatly exceeding precipitation at lower elevations. Snowpack at high elevation is typically low to moderate because the polar front does not remain fixed at a southerly position during the winter, and does not cause significant Pacific moisture to be carried over the Sierra Nevada Mountains. Consequently, with low snowpack, surface-water flow in the Owens River is usually low and seasonal. Owens Lake remains saline and at a low lake level for long periods of time. Precipitation, whether as rain or snow, is typically recycled to the atmosphere by evaporation or used by the local vegetation (BSC 2004a, Section 6.6.2).

The wettest years, which represent the upper-bound moisture regimes during the present-day climate, are typically years when Pacific airflow is commonly focused toward the Sierra Nevada Mountains, increasing snowpack and, hence, the seasonal duration of surface-water flow in the Owens River and its potential to dilute or flush Owens Lake and, thus, dilute the salt content. Such climates also focus Pacific moisture toward southern Nevada, such as during El Niño events. Dry years, which represent the lower-bound moisture regimes during present-day climate, are those years with minimal winter precipitation, which are typically years when the polar front remains largely north of the region and summer precipitation is dominated by subtropical high activity but not to the degree necessary to generate a monsoon-type climate (BSC 2004a, Section 6.6.2).

Present-day meteorological data come from available stations in the region, including Yucca Mountain project and nonproject data. The process of creating the synthetic present-day climate is presented in *Simulation of Net Infiltration for Present-Day and Potential Future Climates* (SNL 2008a, Section 6.5.1 and Appendix F). The climate records from 13 stations in the vicinity of Yucca Mountain (Figure 2.3.1-3) were compiled in *Data Analysis for Infiltration Modeling: Extracted Weather Station Data Used to Represent Present-Day and Potential Future Climate Conditions in the Vicinity of Yucca Mountain* (SNL 2006, Section 4.1). The mean annual precipitation across the site area varies from 106 mm/yr in the Amargosa Farms area to 319 mm/yr at Area 12 (SNL 2006, Section 6.2). These 13 locations represent a variety of climates across the Yucca Mountain region, from hot and dry in the Amargosa Farms area to a cooler and wetter climate near Area 12 on the Nevada Test Site. The mean daily temperature (for 1993 through 2004) recorded at six of the 13 locations described above ranges from below freezing (less than $-5°C$ in the winter) to greater than $36°C$ in the summer.

Monsoon Climate—The monsoon climate is characterized in the Owens Lake record by a mixture of microfossils consisting of *Limnocythere bradburyi* and *L. sappaensis* (BSC 2004a, Section 6.6.2). Because *L. bradburyi* has a lower salinity tolerance than *L. sappaensis* (Forester 1983; Forester 1985), and does not appear to be tolerant of cold winters (Smith and Forester 1994), its existence in Owens Lake implies a relatively lower total dissolved solids (less than about 10,000 mg/L) and a source water derived from something other than snow melt. Surface

flow derived from snow melt probably is not a factor for *L. bradburyi*, but the cold winter climates that generate the snowpack are a problem for this species. The hydrology of Owens Lake is strongly linked to winter precipitation. As such, dilute deeper lakes are due to seasonal flow derived from snowpack. An expansion and intensification of the summer rain system (i.e., monsoon) sufficient to generate diluting surface flow in Owens River explains the occurrence of this species. The diatoms that occur during the *L. bradburyi* interval include saline planktic species, implying the lake was deeper and less alkaline during this period. The diatom paleoenvironment is consistent with that implied by *L. bradburyi*.

Accordingly, analogue meteorological stations for the *L. bradburyi* monsoon climate should be located to the south of Owens Lake today in the southernmost United States. An analogue in the southernmost United States would fulfill the taxonomic temperature requirements and identify sites where precipitation falls primarily in the summer season. The level of precipitation would need to be higher than present-day Owens Lake mean annual precipitation in order to maintain a lower salinity lake that is supported largely by summer precipitation within the present-day warm evaporation regime. Summer rain and associated cloud cover would tend to lower evaporation relative to today.

Selection of monsoon climate analogue sites must come from regions that experience a strong summer monsoon and where *L. bradburyi* live. There are two meteorological stations in the southern United States with long, complete records: the station at Hobbs, New Mexico (405 mm mean annual precipitation), and the station at Nogales, Arizona (421 mm mean annual precipitation) (SNL 2006, Section 6.3). Two stations were selected to minimize the influence of local meteorological phenomena on the input to the infiltration model (SNL 2008a, Section 6.5.1 and Appendix F). Because *L. sappaensis* exists throughout the climate interval and at some horizons and is the only ostracode, the conditions at Yucca Mountain today are representative of the dry lower bound for the monsoon climate. The meteorological stations selected to establish the lower bound for the monsoon climate are those from the Yucca Mountain meteorological monitoring sites (Figure 2.3.1-3) (BSC 2004a, Section 6.6.2).

Glacial-Transition Climate—The change from the monsoon climate to the glacial-transition climate will occur rapidly within 100 to 200 years, based on the sediment-accumulation rate from the Owens Lake record. The magnitude of the climate change will be as large as it is rapid, shifting from a strong monsoon climate state dominated by summer precipitation to a glacial-transition climate state dominated by winter precipitation, with sufficient effective moisture to sustain a fresh and overflowing Owens Lake. For the lake to be full and overflowing, the polar front must be resident in the region during much of the winter, both lowering mean annual temperature and, therefore, evaporation and increasing snowpack and, hence, surface flow to the lake. A greater snowpack associated with a resident polar air mass would also lower mean annual temperature and increase mean annual precipitation at Yucca Mountain. While the cooler climate will have a high effective moisture, it is unlikely to become as cold as the last two full glacial periods (BSC 2004a, Section 6.6.2).

Selecting upper-bound and lower-bound meteorological stations for the glacial-transition climate required identifying sites with cool, wet winter seasons and warm to cool, dry summers (i.e., areas north of the summer rain regime). Furthermore, the analogue sites needed to lie on the east side of large mountain ranges and, hence, in the rain shadow of those ranges. Based on the ostracode

assemblage in the Owens Lake record, the upper-bound analogue should lie within the contiguous United States. The mean annual temperature for the glacial-transition climate should be no colder than, and preferably warmer than, 8°C. Finally, the analogue stations should be in the semiarid west because, although the glacial-transition climate is wetter and cooler than the current interglacial climate, effective moisture is still negative, as is true for the glacial and glacial-transition climates at Owens Lake and Yucca Mountain (BSC 2004a, Section 6.6.2).

Because a full and overflowing Owens Lake is related to seasonal and possibly annual residence of the polar front, the upper-bound meteorological station should be selected in an area where, in today's climate, the polar front resides through most or all of the winter season and where its average position resides most of the year. Given the above qualifying conditions, the upper-bound glacial-transition meteorological site was selected in the northwestern United States east of the Cascade Mountains. Located east of a high mountain range, the area falls within a rain shadow, as does Yucca Mountain. The regional mean annual precipitation is dominated by winter precipitation, and is under the influence of the polar front during the winter and during other times of the year. Furthermore, unlike localities farther north in Canada, the region does not experience extended dominance by very cold, Arctic high pressure, which is typical of the cold, full-glacial periods. Based on meteorological-station data from eastern Washington, three stations were selected for the upper-bound glacial-transition climate: Spokane, Rosalia, and St. John (Figure 2.3.1-4). The three stations are close to each other but do not have identical records, thereby reflecting local differences in mean annual precipitation and mean annual temperature. As with other climate states, selection of multiple meteorological stations was intended to minimize local effects on the climate parameters used as input to the infiltration model (BSC 2004a, Section 6.6.2).

The meteorological stations representing the lower-bound glacial-transition climate scenario should be in a place where mean annual temperature is higher than for the upper bound and, thus, will be south of the upper-bound localities. The mean annual temperature should, however, be lower than that for the Owens Lake Basin today so that effective moisture is higher, which is consistent with a full and overflowing lake. The stations should have a lower mean annual precipitation than the upper-bound sites because the record from the Owens Lake Basin shows episodes of either saline diatoms or ostracodes, implying less surface flow in the Owens River. However, the absence of abundant saline taxa that implies effective moisture is higher than in the present-day climate, reflecting cooler than present-day mean annual temperature rather than high mean annual precipitation. Thus, the lower-bound glacial-transition meteorological sites may have mean annual precipitation values similar to or even lower than present-day Owens Lake Basin. As with the upper-bound meteorological sites, the region should be winter-precipitation dominated, should be north of the summer rain regime, and should have some or all of the ostracode or diatom species found in the fossil record at Owens Lake (BSC 2004a, Section 6.6.2).

Inspection of meteorological sites that fit these conditions revealed that there were few choices available. However, one site with meteorological data that fit these criteria—and that also has a long and complete record—was found at Delta, Utah (Figure 2.3.1-4), which was selected as one of the lower-bound sites. Because its meteorological data meet most of the criteria, the site at Beowawe, Nevada (Figure 2.3.1-4), also was selected as a lower-bound station to avoid using a single site for input into the infiltration model (BSC 2004a, Section 6.6.2).

A comparison of the meteorological characteristics (precipitation and temperature) of the meteorological analogue sites is shown in Table 2.3.1-6. Comparison of the upper-bound monsoon and upper-bound glacial-transition mean annual precipitation values (421 and 405 mm and 455, 419, and 431 mm, respectively) with the present-day mean annual precipitation value of about 199 mm/yr (the average from present-day sites Site 1, 2, 3, and 6) indicates that future climate states are forecast to be moderately wetter than the present-day climate (SNL 2006, Sections 6.1, 6.2, and 6.3). In addition, the lower-bound glacial-transition mean annual precipitation values (207 and 241 mm) are about the same or slightly larger than the lowest average annual precipitation at Yucca Mountain today (183 mm at Site 1). Comparison of the present-day average daily minimum and maximum temperature range values (approximately 4.8°C to 27.6°C) with the glacial-transition lower-bound values (−0.3°C to 18.8°C) shown in Table 2.3.1-6 indicates that the principal difference between present-day climate and the future glacial-transition climate is the lower temperatures that will occur during the glacial-transition climate. An important conclusion from these comparisons is that the glacial-transition climate is cooler than the present-day climate, so evaporation is lower than under present conditions. A lower level of evaporation means that precipitation will be more readily stored (and, hence, available for infiltration) than in today's climate (BSC 2004a, Section 7.1).

2.3.1.2.3.2   Consideration of Uncertainty in the Climate Analysis

Uncertainties in paleoclimate interpretations and the approach used to forecast future climates are summarized in the following sections.

2.3.1.2.3.2.1   Uncertainty in Paleoclimate Interpretations

Uncertainties in the climate analysis include the location of the past–present point in the Owens Lake record and the uncertainty of climate change itself. There is a sound technical rationale for the selection, as previously discussed, although the exact placement of the past–present point in the Owens Lake record is subjective. The other source of uncertainty comes from the chaotic nature of the climate system itself. The climatic conditions reflected in the Owens Lake cores show decade- or century-scale variability that may or may not have significance to the timing of climate change on the multicentury or millennia timescales. Although these uncertainties cannot be directly quantified, the upper and lower bounds placed on uncertainty estimates for temperature and precipitation for present and future climate states are expected to adequately account for these sources of uncertainty. Section 2.3.1.2.2.1.4 discusses uncertainties in age dating calcite in Devils Hole, and Section 2.3.1.3.3.2 discusses uncertainties in the infiltration estimates.

2.3.1.2.3.2.2   Uncertainty in the Climate Forecasting Approach

The future climate predictions have some level of uncertainty. The inherently chaotic nature of climate makes it difficult to forecast future climate based on past climates (BSC 2004a, Section 7.1). Uncertainty also arises in the selection of a particular past climate sequence to forecast the future. Despite the uncertainties, the climate analysis results are based on a consistent interpretation of a body of available data. The uncertainties in the climate analysis are addressed, for the purpose of the TSPA, through use of a range of lower-bound to upper-bound precipitation and temperature data for each future climate state.

The uncertainties associated with selection of analogue meteorological stations can generally be grouped into two categories: epistemic and aleatoric uncertainties. Epistemic uncertainty arises from the lack of knowledge about the processes and parameters because the data are limited, or because alternative conceptual interpretations of the available data exist. This type of uncertainty was addressed by the knowledge gained from testing and data collection. Aleatoric uncertainty arises from the existence of spatial and temporal variability of climatic processes and parameters, which can typically be accounted for using geostatistical approaches. This type of uncertainty cannot be reduced through further testing or data collection. The uncertainty in selection of the analogue sites to represent Yucca Mountain during potential future climates is captured using upper and lower bounds for each climate state to account for the sources of uncertainty (Section 2.3.1.3.2.1.1).

2.3.1.3   Infiltration
[NUREG-1804, Section 2.2.1.3.5.3: AC 1(1) to (7), AC 2(1) to (6), AC 3(1) to (4), AC 4(1) to (3), AC 5(1) to (3)]

The net infiltration model, MASSIF (Mass Accounting System for Soil Infiltration and Flow) (SNL 2008a), is a mass balance calculation of the surface and near surface water budget. Water enters the infiltration model domain as precipitation, which is simulated from a stochastic model of daily precipitation based on historical weather records from Yucca Mountain and analogue sites identified in Section 2.3.1.2.3.1.2. MASSIF simulates processes occurring at the soil layer, including: (1) flow through and storage of water in the soil layer; (2) return of water vapor to the atmosphere by evaporation and plant transpiration (evapotranspiration); (3) flow along the surface (runoff/run-on); and (4) infiltration into the bedrock below the soil. MASSIF also simulates infiltration and runoff/run-on processes that occur on exposed bedrock at locations without soil. The infiltration model domain is defined by 11 watersheds, and covers an area of approximately 125 square kilometers.

2.3.1.3.1   Conceptual Description of Infiltration Processes
[NUREG-1804, Section 2.2.1.3.5.3: AC 1(1), (2)]

Near surface hydrologic processes are generally described in the context of the hydrologic cycle, which describes the pathways and reservoirs through which water moves near and on the surface of the earth (SNL 2008a, Section 6.2.1[a]). The near-surface hydrologic reservoirs consist of the atmosphere, biomass, soil, surface water (such as streams, lakes, and puddles), and snow. Water moves between these reservoirs through a set of natural processes, including precipitation, run-on, runoff, snowmelt, infiltration, evaporation, transpiration, soil water movement and retention, and net infiltration (see Figure 2.3.1-15) (SNL 2008a, Section 6.2.1[a], Figure 6.2.1-1[a]). Net precipitation is defined as the supply of water to the soil surface in the form of rain and snowmelt, minus evaporation of liquid water stored on the surface and sublimation of snowpack.

The term "infiltration" refers to the volumetric flux of water passing across the surface-atmosphere interface into the active zone. Infiltration through the soil atmosphere boundary is the sum of the net precipitation and run-on minus runoff. The active zone is defined as the region below the surface-atmosphere interface where evaporation and transpiration are significant processes. The active zone often coincides with the root zone or may extend below it. The amount of water in the active zone varies substantially over time. The water content changes below the active zone are

attenuated and tend toward constant values. The term "net infiltration" refers to the volumetric flux of water discharging from the active zone and passing through the soil-bedrock interface, or below the root zone (whichever is shallower for a given grid cell), or into a deep soil zone. In general, when thin soils predominate, as at Yucca Mountain, the active zone is confined to the soil layer on top of the rock, and net infiltration is defined as the amount of water that moves from the surface layer of soil into the underlying rock. In arid and semiarid regions, such as the desert basins of the southwestern United States, the processes controlling net infiltration are highly variable in both time and space, and the dominant mechanisms may vary throughout the basin. In this section, "net infiltration" is occasionally referred to simply as "infiltration." This is done for simplicity, and should not cause confusion since infiltration (as defined as water passing across the surface-atmosphere boundary) is not discussed further. The focus of the remainder of this section is climate and (net) infiltration.

Net infiltration is also referred to as potential recharge; that is water available for replenishment of groundwater. Net recharge is the water that actually reaches the water table. Net recharge to underlying groundwater in desert basins is the sum of several distinct dominant processes occurring in different regions of the basin.

The FEPs included in the infiltration model are provided in Table 2.3.1-1. Key processes of the near-surface water balance that affect net infiltration are described in the following sections.

2.3.1.3.1.1   Precipitation, Runoff, and Infiltration

In general, for net infiltration to occur at a location, water must be delivered to the ground surface as net precipitation and/or run-on (surface flow) (SNL 2008a, Section 6.2.1[a]). Run-on is water that has moved on the surface from adjacent areas. Precipitation may be in the form of liquid water (rain) or a solid (snow), which later melts to supply liquid water to the soil surface. Precipitation can be described by the type (e.g., rain or snow), the amount (typically in depth units, e.g., mm), and the duration of the precipitation event. Precipitation intensity is defined as the average precipitation rate (amount divided by duration). Snow has the added characteristic of water depth equivalent, averaging 10% water by volume. Some precipitation is temporarily stored on the surface and returned to the atmosphere before it infiltrates or runs off through evaporation of water intercepted by vegetation and/or accumulated in surface depressions and sublimation of snowpack. Evaporation of surface water and sublimation of snowpack will depend principally upon climatic conditions. In the case of exposed bedrock, precipitation either enters the bedrock, runs off, or evaporates from surface depressions.

Water movement in near-surface soil can be described by a flux law of the form: *Flux = gradient * conductivity.* The applicable gradient for this flux law is that of the soil water potential. The net soil water potential gradient, and the resulting water movement, can be in any direction (e.g., upward, downward, or laterally); the net soil water potential can also be zero corresponding to equilibrium conditions and no water movement.

Water delivered to the soil surface from rain, snowmelt, or run-on from adjacent areas will infiltrate the soil at a rate that depends on soil properties, transient soil water content, and water potential conditions. The rate of infiltration relative to the rate at which water is supplied to the surface will determine the amount that accumulates and/or runs off.

The amount of water in a soil layer or profile within the active zone will change with time in response to water that enters or leaves the system from downward or upward water movement and/or evapotranspiration. The amount of soil water retained is a function of many soil properties that determine the relationship between the soil water potential and the water content.

Whenever the water delivery rate (precipitation + run-on) exceeds the soil's infiltration capacity, water accumulates on the soil surface. This standing water is often referred to as surface water excess. Some water can be stored on vegetation surfaces as well. Because the soil surface is not flat and smooth, the surface water excess collects in depressions, forming puddles (ponding). If ponding exceeds the surface water storage capacity of the depressions, surface runoff commences.

Runoff comprises a wide variety of flow patterns. Overland flow is often the primary type of surface runoff, and is characterized by thin, sheet-like flow on the ground surface. As runoff accelerates and gains in erosive power, it eventually forms channels. Further erosion can deepen these channels, and individual channels may eventually converge, forming dendritic networks characteristic of stream flow.

2.3.1.3.1.2   Evapotranspiration

Water within the active zone can be removed by direct evaporation or through extraction and transpiration by plants (SNL 2008a, Section 6.2.1[a]). Direct evaporation is the dominant mechanism of water transfer from the soil to the atmosphere when the soil surface is bare or vegetation is sparse, while transpiration may dominate when soil surfaces are covered with vegetation. However, since the processes of evaporation and transpiration are often difficult to distinguish, they are commonly grouped into a single process called evapotranspiration. Evapotranspiration is dependent on a variety of biotic and abiotic factors, including vegetation characteristics (e.g., root density), climatic conditions (e.g., solar radiation), and soil properties (e.g., hydraulic conductivity).

Direct evaporation from the soil occurs when three conditions persist: (1) the presence of a sustained supply of thermal energy to change water from liquid to gas phase (latent heat); (2) the presence of a water vapor pressure gradient at the soil-atmosphere surface; and (3) the presence of a continuous supply of water from or through the soil.

Transpiration—that is, the loss of water from plants to the atmosphere—is a direct result of the process of plant physiology. Terrestrial plant growth requires CO_2 for photosynthesis, which diffuses through open stomata on plant leaf surfaces to intercellular spaces inside the leaf. Concurrently, water vapor diffuses out of the leaf, from wet cell membranes through stomatal pores to the much dryer atmosphere (transpiration). Some of the water extracted from the soil by plant roots is used in photosynthesis and other essential metabolic processes. However, 95% to 99% of the water that passes through a plant is lost to the atmosphere through transpiration (Nobel 1983, p. 506). Similar to evaporation, transpiration requires energy to convert water within the vegetation to water vapor, and also requires a water vapor gradient between the vegetation and the atmosphere.

Although plant roots have occasionally been observed to penetrate bedrock fractures at Yucca Mountain, this transpiration mechanism is not included in MASSIF (SNL 2008a, Table 5.1). There are no locally relevant studies or data that quantify the relative amount of water that roots might

remove from bedrock compared to soil. The lack of such a water removal mechanism in MASSIF is a conservative assumption in that net infiltration is likely over-estimated by not including this mechanism for removal of water from the unsaturated zone (SNL 2008a, Table 5.1, Section 8.3[a]).

2.3.1.3.1.3   Geomorphology and Surficial Features

The topographic features of Yucca Mountain result from the interaction of tectonic and geomorphic processes. The topography is controlled primarily by the high-angle, westward-dipping faults and the eastward tilt of the resistant volcanic strata. The surface has been shaped by erosional processes on the eastward-sloping ridge of the mountain and along faults and fault scarps that have created a series of washes that are downcut to varying degrees into different bedrock layers. Slopes are locally steep on the west-facing escarpments eroded along the faults, and in some of the valleys that cut into the more gentle, eastward-facing dip slopes. Narrow valleys and ravines are cut in bedrock; wider valleys are filled by alluvial deposits with terraces cut by intermittent streams. Locally, small sandy fans extend down the lower slopes and spread out on the valley floors. East of the crest of Yucca Mountain, drainage is into Fortymile Wash; west of the crest, streams flow southwestward down fault-controlled canyons and discharge into Crater Flat (Rousseau et al. 1999, p. 10).

The mountain comprises two distinct geomorphic types: one south and one north of Drill Hole Wash. The washes in the southern area trend eastward, are relatively short (less than 2 km), and have erosional channels with gently sloping sides. The washes north of Drill Hole Wash, such as Yucca Wash, northwest trending, are 3 to 4 km long, and have steeper side slopes because they are controlled by fault features (Rousseau et al. 1999, p. 10).

Alluvial deposits, consisting of fluvial sediments and debris flows, are present in the valley floors and washes. These deposits have varying degrees of soil development and thickness and have a gravelly texture with rock fragments constituting between 20% and 80% of the total volume. The alluvial deposits range from 100 m thick in Midway Valley to less than 30 m thick in the mouths of the smaller washes. In the middle of the washes, most alluvial fill is less than 15 m thick. Many of these soils contain cemented calcium carbonate layers. More stable surfaces, generally on the flat upland ridges, have developed soils 0.5 to 2.0 m thick with greater clay contents (Rousseau et al. 1999, p. 10). There are also areas where soil is absent or patchy, resulting in exposed bedrock.

Although topography has an important impact on the spatial distribution of precipitation and potential evapotranspiration, when runoff occurs, topography also channels surface flow and causes the concentration of large volumes of water in channels during short periods of time. In addition to topography, other important site-specific conditions and factors include the water storage capacity of the soil; the permeability of the soil and underlying bedrock; and vegetation type, density, and root zone development (SNL 2008a, Sections 6.4.5.3, 6.5.2.1[a], and 6.5.3.1[a]). Maximum soil water storage capacity is determined by soil thickness and porosity. However, a more typical measure of the amount of water that can be held in the soil without vertical drainage is the field capacity of the soil (SNL 2008a, Section 5.1[a]). Soil thickness tends to be dependent on local topography, with the upland areas generally having thinner soils and the lower washes and alluvial fans having thicker soils. Soil porosity and permeability, along with other hydrologic properties, such as residual water content and field capacity, can be correlated to soil type (and texture) (BSC 2006a, Section 6.3). Bedrock permeability or hydraulic conductivity can also be correlated to lithology (BSC 2006b, Section 6.2.2; SNL 2008a, Sections 6.5.2.2[a] and 6.5.2.5[a]).

The topography at Yucca Mountain has the following infiltration zones: ridge tops, side slopes, terraces, and channels. The ridge tops generally are flat to gently sloping, and are higher in elevation than the other topographic features. They have surficial deposits that are thin (less than 1 m thick) to nonexistent but are relatively stable morphologically. Existing soils are fairly well developed, commonly containing thin calcium carbonate layers. The underlying bedrock on the ridge tops is moderately to densely welded and moderately to highly fractured. The higher elevations of the ridge tops and upper slopes (above 1,400 m) have a greater potential for sustaining a thin snow cover for up to several weeks during the winter (BSC 2004b, Section 7.1.3.3).

Side slopes are distinguished from the terraces and channels by depth of soils and slope. The soil cover on the side slopes is thin to nonexistent and, in most locations, bedrock is densely welded and highly fractured. The side slopes are approximately north- or south-facing in the southern part of the site and, therefore, have different seasonal solar radiation loads. In the northern washes, where the side slopes face more southwestward and northeastward, the steepness of the slopes accentuates seasonal radiation differences. The differences in evapotranspiration between north and south facing slopes is modeled in MASSIF (SNL 2008a, Section 6.4.5.3).

Terraces and channels are located at lower elevations of primary washes and have thin soil cover in the upper washes and thick soils farther down. Very little bedrock is exposed in the washes. The soil in washes has varying degrees of calcium carbonate cementation that commonly is quite extensive. The surface of terraces and washes is relatively flat and dissected by old soil channels and active channels. Channels differ from terraces in that the periodic runoff that occurs in the channels in response to extreme precipitation conditions can rework the channel materials (BSC 2004b, Section 7.1.3.3).

2.3.1.3.1.4   Factors Controlling Net Infiltration

The two main factors that control the amount of water than can enter the bedrock as net infiltration are (1) the amount and frequency of precipitation (and run-on) supplying water to the soil surface, and (2) the extent to which the soil can store the water and allow the processes of evapotranspiration to return water to the atmosphere. In this analysis, future weather (precipitation) patterns are controlled by a combination of climate characteristics and stochastic processes. The extent to which water can be stored in the soil is controlled by a combination of soil hydraulic properties, soil depth, and bedrock conductivity (especially in thin soil regions). Evapotranspiration rates are controlled by a combination of soil and vegetation properties, and vegetation properties are highly dependent on climate.

2.3.1.3.2   Infiltration Data and Data Uncertainty
[NUREG-1804, Section 2.2.1.3.5.3: AC 1(2) to (4), (7), AC 2(1) to (4), AC 3(1), (2)]

To construct the inputs needed for MASSIF, various field and laboratory activities were conducted to collect, analyze, and synthesize pertinent hydrologic data. Additional datasets were used to test and validate various aspects of the conceptual model, and to validate the numerical model.

Because of the complexity of MASSIF, it was necessary to synthesize a wide variety of hydrologic data and information. These data and parameters consisted of many data sets, including (1) digitized

topographic, Landsat, geologic, and soil maps; (2) soil and bedrock hydrologic properties; and (3) meteorological data (SNL 2008a, Section 4.1[a], Table 4-1[a]).

2.3.1.3.2.1   Infiltration Model Input Data

Each of the parameters that serve as an input to the infiltration model were technically evaluated and selected based on their appropriateness for use in calculating net infiltration. Input parameters are summarized in the following sections, which are grouped as follows:

- **Weather Data**—Includes precipitation, temperature, and wind speed measured at Yucca Mountain and future climate analogue weather stations. In addition, parameters used to simulate snowmelt and sublimation are also developed for use in the model. Runoff data are used only for model validation activities.

- **Distribution of Soils and Bedrock and Laboratory Measurements of Soil and Bedrock Hydrologic Properties**—Includes the geologic input to MASSIF (soils and bedrock types and spatial distributions, and soil depth classes over the modeling domain), the geographic inputs (cell coordinates, elevations, slope, azimuth, watershed delineations), and other site characteristics.

- **Vegetation Parameters**—Includes maximum rooting depth, plant height, basal transpiration coefficients, normalized difference vegetation index (NDVI) corrected for the Yucca Mountain environment, and the slope and intercept of the least squares regression between the basal transpiration coefficient and NDVI.

2.3.1.3.2.1.1   Weather Data

Calculation of net infiltration requires an input file containing precipitation, minimum and maximum air temperatures, and mean wind speed on a daily basis. The MASSIF model varies precipitation and temperature with elevation. It also requires a linear fit to hours of precipitation as a function of total precipitation for the day in order to calculate the rainfall duration relationship. Additional inputs to MASSIF include snowmelt and snow sublimation coefficients.

Section 2.3.1.2 describes the three climate states forecast to occur during the next 10,000 years at Yucca Mountain, which are identified as present-day, monsoon, and glacial-transition (BSC 2004a, Section 6.6, Table 6-1). Existing weather records for Yucca Mountain and analogue sites representing future climate states, however, cover less than 100 years. In order to capture the full range of infiltration uncertainty, the performance assessment must assure that low probability extreme precipitation years have been considered. Therefore, rather than use the meteorological records directly as input, MASSIF characterized each record in terms of periodic functions that summarized the records of precipitation, temperature, and wind speed at each meteorological station (SNL 2008a, Section 6.5.1). This approach of developing synthetic datasets of precipitation, air temperature, and wind speed enabled the simulation of average infiltration over periods of time that span hundreds and thousands of years.

Precipitation—The precipitation record at each location was stochastically generated and characterized by four probabilistic parameters: (1) two parameters that describe occurrence of

precipitation based on a first-order Markov process, (a) the probability that day d is dry given that day $d-1$ is dry, and (b) the probability that day d is dry, given that day $d-1$ is wet; and (2) two parameters from a lognormal distribution describing the amount of precipitation that occurs if day d is wet, the mean of the lognormal distribution, and the mean of the natural logarithm of the amount of precipitation:

$p_{00}(d)$ = the probability that day d is dry, given that day $d-1$ is dry

$p_{10}(d)$ = the probability that day d is dry, given that day $d-1$ is wet

$\lambda(d)$ = mean of the lognormal precipitation distribution, given that day d is wet

$m(d)$ = mean of the natural logarithm of the amount of precipitation, given that day d is wet.

Each of these four parameters varies throughout the year. This temporal behavior is described by a two-term Fourier series with three parameters. For example:

$$p_{00}(d) = a_{00} + b_{00} \sin(\theta_{00} + 2\pi d / 365) \qquad \text{(Eq. 2.3.1-1)}$$

Therefore, there are 12 parameters that represent the precipitation record for a meteorological station: a_{00}, b_{00}, θ_{00}, a_{10}, b_{10}, θ_{10}, a_{λ}, b_{λ}, θ_{λ}, a_m, b_m, and θ_m. For each of the 10 stations, the four probabilistic parameters are determined from the available records (SNL 2008a, Appendix F). The climate behavior at each site is strongly correlated with elevation, and each of the four probabilistic parameters for each site was adjusted for elevation using a linear lapse rate correction (SNL 2008a, Appendix F). After the parameters were lapse corrected, the Fourier parameters for each location and for each of the four probabilistic parameters were calculated (SNL 2008a, Tables F-4[a], F-5[a] and F-6[a]).

Temperature—Unlike the periodic functions developed for modeling precipitation, the periodic functions that simulate the temperature record for a meteorological station are not stochastic. Rather, they represent the average minimum and maximum temperatures for each day of the year. Because wet days tend to have smaller differences between the minimum and maximum, wet days and dry days have separate representations, resulting in a total of four periodic temperature functions: dry minimum, dry maximum, wet minimum, and wet maximum.

For example:

$$Tdry_{max} = \alpha dry_{max} \sin\left(\frac{x - \beta dry_{max}}{365/(2\pi)}\right) + \gamma dry_{max} \qquad \text{(Eq. 2.3.1-2)}$$

where

     χ =   the day of year from 1 to 365 (January 1 through December 31; February 29 on leap years is ignored).

     α =   half the annual difference in temperature (minimum or maximum) between summer and winter values, according to the model. It is the amplitude of the sine function and is in units of temperature.

     β =   the calendar day of the year when the model temperature is rising and passes through its central value.

     γ =   the mean value for the temperature, according to the model.

Because each of these periodic temperature functions is also represented by a two-term Fourier series, there are 12 parameters that represent the temperature record for a meteorological station. *Simulation of Net Infiltration for Present-Day and Potential Future Climates* describes the method used to calculate this set of temperature parameters from a meteorological record, and reports the results for each relevant meteorological station (SNL 2008a, Appendix F).

Wind Speed—Wind speeds are calculated by averaging the monthly wind data collected at the four Yucca Mountain meteorological stations: Site 1, Site 2, Site 3, and Site 6. Therefore, there were 12 wind speed parameters, one for each month. These values are then converted to equivalent wind speed at 2 m above ground level. Each monthly average is applied at the middle of the month and the wind speeds for other days are interpolated between two monthly averages. Wind speed data for the monsoon and glacial transition climates are approximated by the present day climate wind speed, because the analogue sites are not appropriate for approximating wind speed due to geomorphic differences between sites. The wind speed averages have normal distributions, based on the mean and standard error (SNL 2008a, Section 6.5.1.3[a]).

Present-Day Climate—Data from 10 local and regional meteorological stations in the Yucca Mountain region provide precipitation, temperature, and/or wind speed parameters for the present-day climate. These include 5 Yucca Mountain stations, 4 Nevada Test Site stations, and 1 National Climatic Data Center station located at Amargosa Valley (SNL 2008a, Section 6.5.1.3[a]).

Temperature and precipitation lapse rates are used to adjust each meteorological station's parameters to an elevation equivalent to the top of Yucca Mountain. The *Handbook of Hydrology* provides a dry adiabatic temperature lapse rate (Maidment 1993, p. 2.27). The parameters for the 10 stations are used to develop a lapse rate for each zero-order precipitation parameter (a_{00}, a_{10}, a_{λ}, a_m) of the present-day climate (SNL 2008a, Appendix F).

Using the probabilistic parameters described above, the mean annual precipitation for each of the 10 stations was estimated, and adjusted to the elevation at the top of the mountain. The adjusted values for mean annual precipitation for each station range from 170 to 250 mm. The potential range of mean annual precipitation was corroborated by other data sets (SNL 2008a, Appendix F).

Comparisons of the ranges of precipitation data and the ranges of modeled precipitation are described in Section 2.3.1.3.4.

For the present-day climate, a uniform uncertainty distribution was assigned to each zero-order precipitation parameter. The extremes of the distribution are the minimum and the maximum values among those obtained by analysis of the 10 stations, extended by one standard error (SNL 2008a, Section 6.5.1.3[a], Appendix F). The phase parameters were assigned uniform distributions (SNL 2008a; Table 2.3.1-7).

For each of the eight first-order precipitation parameters (b_{00}, θ_{00}, b_{10}, θ_{10}, b_λ, θ_λ, b_m, and $\theta_{m)}$, the assigned uncertainty distribution was usually a normal distribution, established by the mean and standard deviation for the 10 stations. The values for the phase parameters were consistent with peak precipitation in the winter (SNL 2008a, Section 6.5.1.3[a]). The phase parameters were assigned uniform distributions (SNL 2008a; Table 2.3.1-7).

All of the temperature parameters were assigned uncertainty distributions that were uniform, with a range determined by the minimum and maximum values for four sites (Yucca Mountain Sites 1, 2, 3, and 6). (SNL 2008a, Section 6.5.1.3[a]). The nominal values, uncertainties, and distribution types for all precipitation, temperature, and wind speed parameters for the present-day climate are shown in Table 2.3.1-7.

Monsoon Climate—Section 2.3.1.2.3.1.2 describes the manner in which the stations at Hobbs, New Mexico, and Nogales, Arizona, were selected to represent the wet upper bound for the monsoon climate. Section 2.3.1.2.3.1.2 states that the conditions at Yucca Mountain today are representative of the dry lower bound for the monsoon climate. As for seasonal variation, the climate during this period would vary from episodes of intense summer rain to present-day-like climates with relatively more winter and less summer precipitation (BSC 2004a, pp. 6-47 to 6-50).

The National Climatic Data Center precipitation normals provide corroboration for the Fourier coefficients for these stations. Using the probabilistic parameters described above yields mean annual precipitation of 406 mm for Hobbs and 421 mm for Nogales. The phases for the first-order Fourier terms correspond to peak precipitation in the summer (SNL 2008a, Section 6.5.1.4).

The zero-order precipitation parameters indicate that precipitation in Hobbs is characterized by generally less frequent storms and greater precipitation per storm than is observed in Nogales. Combining the "wetter" value of each probabilistic parameter yielded a mean annual precipitation of 516 mm. This level of precipitation exceeds the National Climatic Data Center normals, and could have been enough to generate the appropriate lake in the Owens Basin during the previous cycle (SNL 2008a, Section 6.5.1.4).

For the zero-order precipitation terms, the assigned uncertainty distribution was a uniform distribution. To assure that the extremes captured the full range of uncertainty, they were the minimum and maximum of all values from the analyses of present-day and upper-bound monsoon sites (SNL 2008a, Section 6.5.1.4).

The monsoon climate is a climate where winter precipitation exists but does not dominate mean annual precipitation. The climate during this period would vary from episodes of intense summer

rain to present-day-like climates with relatively more winter and less summer precipitation (BSC 2004a, p. 6-50). Moreover, the uncertainty in phase for the lower-bound representative climate and the two upper-bound representative climates is low relative to other sources of uncertainty and screened out of the uncertainty analysis (SNL 2008a, Table I-7). Therefore, as the winter and summer periods lead to opposite phases, this bimodal behavior is captured by using the phase of the summer precipitation and using uncertainty on the amplitude to switch from summer precipitation to winter precipitation (SNL 2008a, Section 6.5.1.4).

A monsoon climate has strong seasonal variation, which makes the first-order terms more important than for other climates. The amplitudes for the first-order terms differ greatly between the two upper-bound stations. Nogales has the greater seasonal variation in the probability that a day is wet. Hobbs has the greater variation in the average precipitation on wet days. Some first-order magnitudes for the two stations differ by more than a factor of two, with standard deviations larger than the standard deviations in the corresponding zero-order terms (SNL 2008a, Section 6.5.1.4).

As a result of uncertainty associated with the analogue sites, a range from 1 σ below the lower value to 1 σ above the upper value was used to capture about 90% of the hypothetical distribution between the two stations. Therefore, the assigned uncertainty distribution for the magnitude of a first-order term for the upper-bound monsoon climate is a uniform distribution from 1 σ below the lower value to 1 σ above the upper value (SNL 2008a, Section 6.5.1.4). The assigned uncertainty distribution for the phase of each first-order precipitation term is a uniform distribution. The extreme values are the values for the two upper-bound stations (SNL 2008a, Section 6.5.1.4).

Because the first-order terms for the lower-bound stations are completely out of phase with the upper-bound terms, they may be represented by negative values of the amplitude coefficients. Therefore, the amplitude of a first-order term may range from the largest value for the present-day climate, plus 1 σ, but taken as negative, to the larger of the values from the upper-bound stations, plus 1 σ, taken as positive (SNL 2008a, Section 6.5.1.4).

All of the temperature parameters were assigned uniform uncertainty distributions, with a range determined by the minimum and maximum values for four sites (Yucca Mountain Sites 1, 2, 3, and 6). It was assumed that the wind speed approximated for the present-day climate was an adequate approximation for the wind speed expected during the monsoon climate (SNL 2008a, Section 6.5.1.4). The nominal values, uncertainties, and distribution types for all precipitation, temperature, and wind speed parameters for the monsoon climate are shown in Table 2.3.1-8.

Glacial-Transition Climate—Weather stations in eastern Washington State were chosen to represent the upper bound glacial-transition climate, and weather stations in Beowawe, Nevada, and Delta, Utah, were chosen to represent the lower bound glacial-transition climate (Section 2.3.1.2.3.1.2). The National Climatic Data Center precipitation mean provides corroboration for the Fourier coefficients for these stations. For the upper-bound stations, the phase parameters correspond to peak storm frequency in December through February, but peak storm magnitude in May through June. The lower-bound station parameters reflect peak frequency in the winter, but peak magnitude in June through August. The difference in wettest months arises because the upper-bound stations have larger seasonal variation in frequency, while the lower-bound stations have a larger seasonal variation in magnitude (SNL 2008a, Section 6.5.1.5).

Most of the assigned uncertainty distributions for precipitation and temperature parameters have uniform distributions because there is no basis for weighting one analogue site over another, or for weighting these parameters in any shape other than uniform. The extremes of the distributions are the minimum and the maximum values among those obtained by analysis of the five glacial-transition meteorological stations, extended by one standard error. The nominal value is the midpoint between these extremes. The exceptions are the phase coefficients for precipitation; a normal distribution is assigned to the phase coefficients for the Markov probabilities using the weighted average and standard deviation (SNL 2008a, Section 6.5.1.5, Appendix F).

It was assumed that the wind speed approximated for the present-day climate was an adequate approximation for the wind speed expected during the glacial-transition climate, because there is no basis for predicting wind speed during the monsoon and glacial-transition climate states. The analogue sites for future climate states are used for developing precipitation and temperature data inputs, not wind speed inputs. The nominal values, uncertainties, and distribution types for all precipitation, temperature, and wind speed parameters for the glacial-transition climate are shown in Table 2.3.1-9.

Generation of Weather-File Input—One of the inputs to MASSIF is a weather file with data for each day. Each day's data set consists of the amount of precipitation, the minimum and maximum temperatures, and the average wind speed at 2 m above the ground. For a given set of weather parameters, a stochastic algorithm produces a 1000 year sample of daily precipitation. For wet days, the amount of precipitation was determined from a random number and the cumulative lognormal probability distribution (SNL 2008a, Section 6.5.1.6[a]).

The MASSIF model domain covers approximately 125 km^2 and generates a map of daily infiltration through each of 139,092 grid cells, averaged over a sample of years. Therefore, it was not practical to calculate daily infiltration through each area for 1,000 years. This challenge was addressed by taking a sample of the simulated years, including several years with high precipitation. Long-term mean annual net infiltration was calculated as the weighted mean net infiltration for 10 representative precipitation years, each with its associated probability of occurrence. The 10 representative years have recurrence intervals of 1.0, 1.2, 1.6, 2.2, 3.6, 10, 33, 100, 333, and 1000 years. Each sample year was weighted by its relative probability in calculating the map of average annual infiltration. This approach assured that the effects of extreme events were recognized but given appropriate weight in the analysis (SNL 2008a, Section 6.5.7.5).

Long-term mean net infiltration is calculated as the weighted mean net infiltration for 10 representative precipitation years, each with its associated probability of occurrence. In general, low probability years experience higher net infiltration but contribute only a small percentage to the long-term mean. Since the sum of the probabilities of occurrence equals 1, and the years were selected from a set of 1,000, the recurrence interval for a given representative year represents the average number of years that would pass before annual precipitation exceeded that predicted for the representative year. The recurrence interval is calculated as:

$$T_k = \frac{1}{1 - p_k} \qquad \text{(Eq. 2.3.1-3)}$$

where T_k is the recurrence interval (in years) of year k and p_k is the probability that annual precipitation in any one year will be less than the annual precipitation during year k (Maidment 1993, p. 18.3). Thus the quantity $(1-p_k)$ represents the exceedance probability, which is the probability that annual precipitation during any one year will equal or exceed annual precipitation during year k. It is also possible to calculate the percent contribution to the long term mean net infiltration of each representative year. This is done by multiplying annual net infiltration for each year of each realization by the probability of occurrence for that year and then dividing by the long-term (weighted) mean net infiltration for each realization. Tables 2.3.1-10 to 2.3.1-12 list the exceedance probability, the mean annual net infiltration, the recurrence interval, and the fraction of contribution to long-term mean net infiltration for each of the 10 representative years ($k = 1$ to 10) for each of the three climates, respectively.

Other Climate Parameters—The lognormal fit to the wet-day precipitation amount did not fit the probability of extreme events very well. Although the assigned probability for extremely heavy precipitation was very small, it was higher than the data. Therefore, an input that limited the total precipitation for one day was implemented in MASSIF (SNL 2008a, Section 6.5.1.7[a]). The value chosen was the largest observed rainfall in the USA during a 24 hr period, which was 983 mm in Yankeetown, FL in 1950 (Maidment 1993, p. 3.36, Table 3.10.2). However, it is important to note that the infiltration calculated for a water year containing such an extreme event is weighted, as previously described, effectively reducing its impact on average annual net infiltration. It is also notable that very extreme rainfall events are likely to result in significant overland flow and runoff, and will not greatly affect net infiltration.

A temperature-index snowmelt equation from the *Handbook of Hydrology* (Maidment 1993, p. 7.24) was implemented in MASSIF for calculating daily snowmelt for days with snow accumulation. Maidment (1993, p. 7.24) provides temperature-index expressions for calculating daily snowmelt for various regions of North America. The closest such site to Yucca Mountain is Sierra Nevada, California. This site has latitude similar to that of Yucca Mountain, and was therefore the most appropriate site to use in this table. A uniform distribution was assumed to represent snowmelt conditions at Yucca Mountain during the glacial-transition climate. This distribution was used for all climates because there was not significant snow during the present-day and monsoon climates (SNL 2008a, Section 6.5.1.7[a]).

Estimates of sublimation of snowpack vary widely. A range of 0% to 20% (with a uniform distribution) was assumed to represent reasonable annual snow sublimation amounts at Yucca Mountain during the glacial-transition climate. This value was used for all climates because there was not significant snow during the present-day and monsoon climates. The sublimation coefficient was multiplied by daily precipitation for days when the mean daily air temperature was less than 0°C, and that amount was removed from the precipitation total in the form of snow sublimation (SNL 2008a, Section 6.5.1.7[a]).

Precipitation duration is a highly variable parameter in desert environments. For each climate, a linear function was developed that related the precipitation duration to the amount of rain that fell on a given day. Four sets of analyses were done to characterize precipitation duration parameters for each climate (SNL 2008a, Section 6.5.1.7[a]). For the MASSIF calculation, which uses a daily time step, an assumption was made that daily precipitation occurred as a single event rather than multiple shorter events separated by dry periods during the day. Given this assumption, and for a given

precipitation day, the number of hourly intervals was, on average, equal to one hour greater than the actual precipitation duration for that day. Although there is a large standard error associated with this linear function, results of the uncertainty analysis (Section 2.3.1.3.3.2.2) indicate that net infiltration was insensitive to the slope of this function (SNL 2008a, Section 6.5.5).

The hydrologic processes of run-on and runoff are validated in the MASSIF model by comparison of measured streamflow data with MASSIF predictions of runoff (streamflow) at the discharge cells at the base of streamflow watersheds. There were six streamflow gauges located within the Yucca Mountain infiltration model domain used in this validation analysis (SNL 2008a, Section 7.1.3). These six gauges were part of the U.S. Geological Survey streamflow monitoring network (SNL 2008a, Section 7.1.3, Table 7.1.3-1). Streamflow data were recorded at some of these six gauges during storms in water years 1993, 1994, 1995, and 1998. Data with zero streamflow and incomplete records were not used, so streamflow data from water years 1995 and 1998 were used in the net infiltration analysis (SNL 2008a, Section 7.1.3). Section 2.3.1.3.4.1 describes the comparison of runoff data to simulations using MASSIF.

2.3.1.3.2.1.2   Geologic and Geographic Inputs

Geologic inputs to MASSIF included parameters for Yucca Mountain soils and bedrock, and spatial distributions for soil types, soil depth classes, and bedrock types over the modeling domain. Geographic inputs included data used to define cell coordinates, elevations, slope, azimuth, watershed delineations, surface flow routing, and other site characteristics. The geologic and geographic parameters were organized into a "geospatial" database (SNL 2008a, Appendix B). Geospatial parameters were handled in two different ways. The values of some parameters were specified such that they varied independently from cell to cell (e.g. elevation and potential vegetation response). Other parameters, such as bedrock hydraulic conductivity or soil properties, were identified as a group of grid cells representing regions where particular properties were assigned ranges of values.

The accuracy of net infiltration estimates at any one location is limited by spatial variability and uncertainties in soil, bedrock, and vegetation properties at that location. For example, soil depth can vary from zero to tens of meters within a single 30×30 grid cell, and bedrock saturated hydraulic conductivity can change by two orders of magnitude depending on whether fractures are filled or not at a given location. In order to run the model, it was necessary to define these properties for every 30×30 m grid cell in the infiltration modeling domain. The approach taken was to upscale and group the available measurements and estimates for properties. This approach assumes that small scale variations in soil and rock properties are not as significant as variations that occur between different soil and rock types. This assumption is valid because small scale spatial variations in net infiltration are not important for downstream users of model output.

An example of this limitation is the answer to the question of whether net infiltration at Yucca Mountain is focused beneath stream channels, or if it predominantly occurs in shallow soils. Since there is very little direct information about such a spatial distribution, there is considerable and significant uncertainty in the spatial distribution of net infiltration results. Furthermore, because soil and bedrock properties are represented as uniform over a spatial area assumed to define a given soil or rock type, the actual spatial variability of net infiltration is likely underestimated by the model.

The spatial inputs of elevation, azimuth, and slope were used for calculations of runoff and temperature and precipitation adjustments for elevation, and were important for developing other parameters relating to evapotranspiration (SNL 2008a, Section 6.5.2.1[a]).

The Shuttle Radar Topography Mission data were selected as the best source for topography data for infiltration modeling (SNL 2008a, Appendix B). The Shuttle Radar Topography Mission data were obtained from the U.S. Geological Survey Earth Resources Observation and Science Data Center.

The MASSIF infiltration model domain included the area that drains Yucca Mountain above the repository waste emplacement area where 11 separate drainages (or watersheds) were delineated; 3 larger basins drain the east face of the ridge, and 8 smaller basins drain the west face. The watersheds were delimited using elevation and slope to define surface water flow direction to a single outlet (Figure 2.3.1-16) (SNL 2008a, Section 6.5.2.1[a]).

Elevation data from Shuttle Radar Topography Mission required processing for use in the geospatial database, as the Shuttle Radar Topography Mission cell size and map coordinate projections did not correspond to those needed for the infiltration model. Once cell size and map coordinate projections were revised, the elevation data served as the base data layer from which multiple derivative data layers were created. These additional layers provided information, such as slope and aspect, which were required by the MASSIF infiltration model (SNL 2008a, Section 6.5.2.1[a]). Uncertainties in the Shuttle Radar Topography Mission data were analyzed by Rodriguez et al. (2005). The absolute error for Shuttle Radar Topography Mission data in North America is 12.6 m, for a 90% confidence interval. The absolute elevation error for Shuttle Radar Topography Mission data in North America is 7 m, for a 90% confidence interval. A map of elevation within the model domain from the Shuttle Radar Topography Mission dataset is shown in Figure 2.3.1-17.

2.3.1.3.2.1.3   Soil Properties

Soil maps and soil depth estimates, including uncertainty and spatial variability, were developed in *Data Analysis for Infiltration Modeling: Technical Evaluation of Previous Soil Depth Estimation Methods and Development of Alternate Parameter Values* (BSC 2006c) and were further summarized for the MASSIF model in *Simulation of Net Infiltration for Present-Day and Potential Future Climates* (SNL 2008a, Section 6.5.2.4[a]). Assumptions were made, based on scientific judgment, that soil depth and properties could be considered to be constant for the next 10,000 years (SNL 2008a, Section 5). Soil hydraulic properties and associated uncertainties are developed in *Data Analysis for Infiltration Modeling: Development of Soil Units and Associated Hydraulic Parameter Values* (BSC 2006a).

Soil classifications and mapping based on analyses performed by the U.S. Geological Survey in 1996 were evaluated for technical adequacy for use in infiltration modeling. The initial U.S. Geological Survey soil classifications were developed from a map of surficial deposits that characterized soil types based primarily on extent of soil development, geomorphic character, and topographic position (BSC 2006a, Section 6.2.1). The original 40 map units were combined into 10 soil units. The group of 10 soil units, referred to as the "base case" units, are based on depositional character and relative age (BSC 2006a, Section 6.2.3). An alternative soil classification system consists of four soil groups, which are combinations of the base case soil units. The alternative grouping was developed because several of the base case soil units had similar properties

but a very limited number of samples upon which to base the hydrologic properties for each unit. By combining soil units into fewer groups, based on depositional character, the sample size for each group was increased, thus providing a better basis for performing statistical analysis on the data sets without loss of relevant information or the characterization of uncertainty. MASSIF used properties derived for the alternative soil grouping (Figure 2.3.1-18) (SNL 2008a, Section 6.5.2.2[a]).

Representative hydraulic parameter values of each of the soil units were developed by matching the texture of samples from Yucca Mountain soil units to similar soil textures in an analogous site (Hanford, WA) database (BSC 2006a, Section 6.1). This pedotransfer function approach (BSC 2006a, Section 6.3) is nonparametric and is beneficial when the form of the relationship between the inputs and outputs is not known in advance, such as is the case with soil hydraulic properties. Saturated hydraulic conductivity (K_{sat_soil}), field capacity (θ_{FC}), permanent wilting point (θ_{WP}), saturated moisture content (θ_s), and water-holding capacity (θ_{HC}) were determined for each of the soil groups (Tables 2.3.1-13 and 2.3.1-14). The pedotransfer approach introduces uncertainty due to the fact that the Hanford soil property database represents soils in a location and depositional environment that is different from Yucca Mountain. The use of the Hanford soil property database is likely to be conservative because the field capacity of the Hanford soils is less than the field capacity reported for Nye County soils, which are likely to be more representative of site-specific soils than Hanford soils (BSC 2006a, Section 6.4.6, Figures 6-20 and 6-21).

In order to evaluate soil depths, the infiltration model area was divided into five soil depth classes (Figure 2.3.1-19). The five depth classes have median depths of 95.1 m, 12.19 m, 2.07 m, 0.25 m, and 0 m (exposed bedrock), for soil depth classes 1, 2, 3, 4, and 5, respectively. Each soil depth class region was associated with a distribution of soil depths and recommendations on the treatment of soil depth for infiltration modeling.

The distribution of one of the soil depth classes (soil depth class 4) was especially important because of the significant sensitivity of net infiltration to shallow soil depth (Section 2.3.1.3.3.1.2) and the large relative proportion of the modeling domain covered by this soil depth class (70% of the unsaturated zone model domain) (SNL 2008a, Table 6.5.2.4-1[a]). For these reasons, multiple analyses were performed on two soil depth data sets. The first data set consists of the 35 observations of soil depth that are documented in *Data Analysis for Infiltration Modeling: Technical Evaluation of Previous Soil Depth Estimation Methods and Development of Alternate Parameter Values* (BSC 2006c). However, it was unclear how well the 35 observations represented the actual spatial distribution of this soil depth class. There may be a bias toward deeper soils, since none of the 35 observations include soil depth of 0 m, while observations of patches of bare rock have been made in the area covering soil depth class 4 during field trips to the site. Therefore, the use of this dataset alone could lead to overestimating soil depth and underestimating net infiltration (SNL 2008a, Section 6.5.2.4.1[a]).

For this reason, a second source of corroborating information was used to create a second spatial distribution of shallow soil depth. *Simulation of Net Infiltration for Present-Day and Potential Future Climates* (SNL 2008a, Section 6.5.2.4.1[a]) contains soil depth observations in several places at Yucca Mountain. Most of the observations are for shallow soil and should correspond to regions of soil depth class 4. This new distribution was defined using eight ranges of soil depths. To represent the piecewise distribution, a series of two random numbers was generated. The first was used to randomly select from the predefined ranges of soil depth, and the second was used to sample

a soil depth from within the selected bin. This Monte Carlo approach was repeated 1,000 times to create a distribution.

Two fitting methods (probability plotting and least squares) were applied to the soil depth ranges in the second dataset. However, because 25% of the distribution is equal to 0 m, and a lognormal distribution is not defined for values of zero, each of these fitting methods had to be modified. Two approaches were considered for modifying the fitting methods:

- In the first approach, it is assumed that the information available is known only for values greater than zero, and that nonzero values represent only 75% of the distribution. This assumption allows calculation of the arithmetic and geometric means of the fitted lognormal distributions directly, but it does not necessarily result in a good fit.

- In the second approach, it is assumed that the distribution is bimodal. Like the first approach, the fitting is done with nonzero values; however, they are considered to represent the whole distribution. The final estimates of the arithmetic and geometric means are corrected to include 25% of zero values. This approach leads to a better fit, but makes the estimation of the geometric mean more difficult.

The minimum value of soil depth for soil depth class 4 is equal to 0.1 m. This value corresponds to the bounds for the geometric mean on the second data set using the first approach, and the geometric mean on the second data set using the second approach. The maximum soil depth for depth class 4 is equal to 0.5 m. This value corresponds to the upper bound of the arithmetic mean using a probability-plot fitting method on first dataset. Because there is no reason to favor any of these values (or any intermediate value), a uniform distribution for soil depths between 0.1 m and 0.5 m was selected to represent uncertainty in the upscaled quantity used to represent an effective uniform value of soil depth class 4. This range does not represent the spatial variability of soil depth class 4 (which would have a range of 0 to 3 m). This approach ensures that soil depth is not overestimated (and, therefore, net infiltration is not underestimated because the selected range is large for an upscaled uniform value, and has a bias towards shallower soil depths) (SNL 2008a, Section 6.5.2.4.1[a]).

Soil depths were also measured by the Center for Nuclear Waste Regulatory Analyses staff and contractors during two site visits to Yucca Mountain in 1998. A total of 56 values of representative soil depth were recorded (Fedors 2007). The Center's sampling locations are further west than all but a few of the 35 Yucca Mountain Project sample locations (first dataset described above). This difference in sampling locations should be expected to result in the Center's samples having slightly shallower soil depths than the Yucca Mountain Project samples, because the Center's samples are closer to the mountain crest, and are likely to be located at higher elevation than the Yucca Mountain Project samples. Comparison of these two datasets indicates that the Center's dataset is not statistically equivalent to the Yucca Mountain Project dataset, and the Center's samples are slightly shallower than the Yucca Mountain Project samples. If there is a bias toward deeper soils in the Yucca Mountain Project dataset than in the Center's dataset, then such a bias is likely to be counteracted by the impact of using a uniform rather than a lognormal distribution for upscaled uniform soil depth (SNL 2008a, Section 7.2.4[a]). Although the Center's dataset is slightly shallower than the Yucca Mountain Project dataset, 51 of the 56 Center's samples are between

0.08 and 0.61 m (Fedors 2007), which compares well to the range of the effective upscaled uniform value for soil depth class 4 (0.1 to 0.5 m).

The Center for Nuclear Waste Regulatory Analyses dataset provides additional confidence in the range of soil depth values used for the shallow depth class 4 with MASSIF, since this independent dataset closely overlaps the Yucca Mountain Project dataset, especially given the heterogeneity of soil depth measurements at Yucca Mountain (SNL 2008a, Section 7.2.4[a]).

2.3.1.3.2.1.4   Bedrock Properties

An infiltration hydrogeologic unit system was developed consisting of bedrock types (infiltration hydrogeologic units) that have differing hydrogeologic properties with special emphasis on hydraulic conductivity (Table 2.3.1-15) (BSC 2006b, Section 6.2). The infiltration hydrogeologic units were defined on the basis of lithostratigraphic contacts in boreholes (BSC 2004c). The correlation of lithostratigraphic units and infiltration hydrogeologic units enabled the extrapolation of the infiltration hydrogeologic units to exposures at the ground surface, where most of the correlated lithostratigraphic units have been documented on the following geologic maps:

- *Preliminary Geologic Map of Yucca Mountain, Nye County, Nevada, with Geologic Sections* (Scott and Bonk 1984)

- *Bedrock Geologic Map of the Central Block Area, Yucca Mountain, Nye County, Nevada* (Day et al. 1998)

- *Digital Geologic Map of the Nevada Test Site and Vicinity, Nye, Lincoln and Clark Counties, Nevada, and Inyo County, California, Revision 4; Digital Aeromagnetic Map of the Nevada Test Site and Vicinity, Nye, Lincoln, and Clark Counties, Nevada, and Inyo County, California; and Digital Isostatic Gravity Map of the Nevada Test Site and Vicinity, Nye, Lincoln, and Clark Counties, Nevada, and Inyo County, California* (Slate et al. 2000).

For map units that did not have any correlative infiltration hydrogeologic units, proxy infiltration hydrogeologic units were proposed based on similarities in lithostratigraphic characteristics. These correlations of infiltration hydrogeologic units to lithostratigraphic units to map units provided the basis for the bedrock hydraulic conductivity map shown in Figure 2.3.1-20 (SNL 2008a, Section 6.5.2.5[a]).

The model area included the entire Busted Butte 7.5 min quadrangle and the southern half of the Topopah Spring NW 7.5 min quadrangle. Because bedrock hydrologic properties were assigned on the basis of lithology, bedrock geologic units were assigned to each grid cell. This was accomplished with a digital manipulation of existing geologic mapping data covering the area (BSC 2006b, Section 6.2.2).

Uncertainty in bulk bedrock conductivity includes the possibility that some portion of the filled bedrock fractures contains open conduits, and, therefore, the potential for net infiltration is not underestimated (SNL 2008a, Section 8.3[a]).

Saturated hydraulic conductivity (K_{sat}) data were developed for each of 38 rock types or infiltration hydrogeologic units that form the bedrock at Yucca Mountain. Bulk hydraulic conductivity (K_{sat}) was calculated for a composite porous medium consisting of matrix and fractures filled with permeable caliche. For each bedrock geologic unit, the approach used to calculate the mean and the variance of the bulk bedrock saturated hydraulic conductivity was as follows:

- The bedrock was modeled as consisting of matrix rock and fractures. Bedrock K_{sat} values were calculated for filled fractures and open fractures, and a nominal value was selected for K_{sat} between these values. For two rock types (405 and 406), bedrock K_{sat} was sampled within a range representing filled to open fractures (with 200 um aperture) (SNL 2008a, Table 6.5.2.6-1, Section 6.5.5).

- Each of these materials was characterized by its median and standard deviation of log K_{sat} (BSC 2006b, Sections 6.4.3 and 6.4.4).

- The fraction of the soil-bedrock interface occupied by fractures—termed the fracture volume fraction, was characterized by a beta distribution (BSC 2006b, Section 6.3). Because fracture volume fraction must fall in the range of zero to one, a beta distribution is suitable to describe the spatial variability of the fracture–volume–fraction values. This approach is consistent with the unsaturated zone transport abstraction model (SNL 2008c, Section 6.5.7, Addendum 1), which uses a beta distribution to describe the uncertainty of porosity. Fracture volume fraction is essentially a measure of fracture porosity.

- The bedrock hydraulic conductivity was calculated by combining these data and by propagating the uncertainty (BSC 2006b, Section 6.4.5 and Appendix B).

Conceptually, flow in the matrix and filled-fracture material is through parallel flow paths. K_{bulk} for the composite porous medium of matrix and fractures filled with permeable caliche is, therefore, calculated as the arithmetic mean of the two K_{sat} values weighted by volume fraction.

$$K_{bulk} = f_{vf} K_{ff} + (1 - f_{vf}) K_m \qquad \text{(Eq. 2.3.1-4)}$$

where f_{vf} is the fracture volume fraction; K_{ff} is the K_{sat} of the fracture-filling material, and K_m is the K_{sat} of the matrix; K_{bulk} is the K_{sat} of the composite bedrock (BSC 2006b, Tables 6-6 and 6-8).

A Monte Carlo approach was used to estimate the shape of the resulting distribution: 30,000 values were sampled from the distribution of each input variable from which K_{bulk} is estimated (BSC 2006b, Section 6.4.5.1). The resulting Monte Carlo distribution of K_{bulk} values, representing the spatial variability, is close to a lognormal distribution in shape for most of the 38 infiltration units. For most of the model area, bedrock saturated hydraulic conductivity based on the consideration of filled fractures is 2.4×10^{-7} m/s or less.

Field observations indicate that caliche infilling of fractures and other voids is pervasive in many areas, but in others, particularly where soil cover is thin (because soil is the source of the caliche),

it is spotty, does not completely fill fractures, or is absent. Comparison of the infiltration rate measured in the Alcove 1 infiltration test with the mean bulk bedrock K_{sat} for infiltration hydrogeologic unit 404 (BSC 2006b, Section 6.4.5.3) also suggests that the fractures at that location are not completely filled. In view of these observations, the bulk bedrock saturated hydraulic conductivity calculated for filled fractures must be regarded as a lower bound of bulk bedrock saturated hydraulic conductivity. The upper bound of bulk bedrock saturated hydraulic conductivity must be set by some estimate of the percent of fractures containing an additional hydraulic aperture (SNL 2008a, Section 6.5.2.6).

Although few data are available to directly quantify either the proportion of fractures that are unfilled or the hydraulic aperture to characterize them, reasonable values may be inferred from the sources identified in *Data Analysis for Infiltration Modeling: Bedrock Saturated Hydraulic Conductivity Calculation* (BSC 2006b, Section 6.4.5.4.2), including the Alcove 1 and Fran Ridge infiltration tests, and analysis of fracture air-permeability data and fracture frequency data. Based on these field data values, the upper bound of bulk bedrock K_{sat} has been calculated using a 200 µm hydraulic aperture with all fractures. For the purpose of stochastic simulation, the distribution of bulk bedrock K_{sat} between these bounds is taken as loguniform. The use of a loguniform uncertainty distribution between the upper and lower bounds allows for the contribution of unfilled fractures while still recognizing that most fractures are filled. A loguniform distribution is appropriate to represent the uncertainty because bedrock K_{sat}, including the effect of partially filled fractures, may cover a large range (orders of magnitude) and little information is known about the shape of the distribution (BSC 2006b, Section 5.2.7). The upper and lower bounds for bulk bedrock K_{sat} for the 38 rock types used in MASSIF are shown in Figure 2.3.1-21. The bulk bedrock K_{sat} inferred from the Alcove 1 test is also shown in this figure, which is about a factor of three lower than the mean value given in Table 2.3.1-15. This difference suggests that the methodology used to estimate bedrock K_{sat} is probably biased towards higher K_{sat} rather than lower K_{sat} values. The nominal (mean) values of bedrock K_{sat} given in Table 2.3.1-15 were used with MASSIF for 36 of the 38 rock types. Rock types 405 and 406 were sampled in the uncertainty analysis because they occupy more than 15% of the model area (SNL 2008a, Section 6.5.2.5[a]).

2.3.1.3.2.1.5   Vegetation Parameters

Parameters used to describe the characteristics of the vegetation that are expected to be present at Yucca Mountain during the present day and two future climate states include maximum rooting depth (Z_r), plant height (h_{plant}), basal transpiration coefficients (K_{cb}), NDVI, and the slope and intercept of a linear least-squares regression between K_{cb} and NDVI (SNL 2008a, Section 6.5.3).

Maximum Rooting Depth and Plant Height—To develop distributions for plant height and rooting depth for monsoon and glacial-transition climates, it was necessary to consider what taxa might reasonably be expected to occur at Yucca Mountain. The species composition of future vegetation communities at Yucca Mountain is a complex issue. It is recognized that multiple possibilities for vegetation assemblages exist, and outcomes are dependent on several factors, including climate, disturbance, and species specific ability to adapt or migrate. The potential for certain plant taxa to occur was evaluated by considering several factors, including predicted future-climate rainfall and temperature patterns, natural vegetation associated with the climate at analogue meteorological station locations, historical vegetation change in response to climate change, species tolerance ranges and requirements, and current species composition of plant

communities at Yucca Mountain. Factors influencing vegetation at Yucca Mountain, such as soil types and topography, differ from those of natural vegetation stands associated with analogue meteorological station locations. Therefore, species were not selected as potential components of future vegetation simply on the basis that they were likely to occur in natural vegetation stands associated with the analogue meteorological stations. *Simulation of Net Infiltration for Present-Day and Potential Future Climates* describes the method used to the determine ranges for the maximum rooting depth and plant height for each of the three climates. Taxa that currently exist at Yucca Mountain, and that are also found within the climatic regions of the analogue meteorological stations, are likely to persist and in some cases perhaps expand their distributions. These include shrubs, yuccas, cacti, and grasses. While establishment of new species at Yucca Mountain during the monsoon climate cannot be ruled out, it is assumed instead that the abundance of grasses would increase, and shrub species would increase in abundance. During the glacial-transition climate, changes in species composition, community types, and distribution ranges are expected. Pinyon-juniper woodlands and other Great Basin species are predicted to dominate during this climate state (SNL 2008a, Section 6.5.3.1.3). The ranges of rooting depths are 0.6 to 2.6 m for the present-day and monsoon climates, and 0.7 to 4.3 m for the glacial-transition climate. The rooting depth for a given grid cell is set equal to soil depth if soil depth is less than the rooting depth. The ranges for plant heights are 0.2 to 0.6 m for the present-day and monsoon climates, and 0.64 to 1.8 m for the glacial-transition climate.

Maximum rooting depth is assumed to be uniform over the whole domain. Actual rooting depth is limited by the soil depth because it is also assumed that nearly all of the water that is transpired comes from the soil layer in which active roots are present. It is recognized that roots do sometimes extend into bedrock along fractures; however, no locally or regionally relevant studies or data were identified that could be used to quantify the relative amount of water these roots might remove compared with roots in the soil. Accordingly, evapotranspiration from the bedrock immediately below the soil is not explicitly accounted for in the MASSIF model. This is conservative because plant roots have occasionally been observed to penetrate bedrock fractures.

Basal Transpiration Coefficients and Normalized Difference Vegetation Index—Plant water use is an important component of the water balance for vegetated natural systems and is the primary mechanism controlling water loss from the soil during periods when plants are active (i.e., during the growing season when soil moisture is available). Because of the inevitable loss of water through stomates during the acquisition of carbon for photosynthesis, 95%–99% of the water that passes through a plant is lost through transpiration (Nobel 1983, p. 506). Thus, transpiration is an accurate estimate of water uptake by plant roots (Nobel 1983, p. 506).

The arid climate at Yucca Mountain is characterized by low and unpredictable rainfall, extreme temperatures, and high evaporative demand. Vegetation cover in the Yucca Mountain area is limited by both timing and amount of precipitation. Characterizing the timing and magnitude of vegetation response to precipitation, and converting that response to values that can be used in the MASSIF model, are important to the representation of infiltration at the Yucca Mountain site (SNL 2008a, Appendix D).

Two methods of characterizing vegetation at Yucca Mountain were used: NDVI data derived from satellite imagery, and basal transpiration coefficients (K_{cb}) derived from ground measurements of vegetation characteristics. These two methods are used together to develop vegetation maps of the

infiltration model domain. The linear relationship between K_{cb} and the NDVI makes it possible to estimate K_{cb} from NDVI data (Bausch and Neale 1987; Duchemin et al. 2006). This linear relationship is used in the MASSIF model to estimate K_{cb} from NDVI data for each grid cell in the infiltration model domain (SNL 2008a, Appendix D).

The NDVI is an indicator of vegetation vigor often used for measurement of environmental response to landscape-scale hydrology. Vegetation indices are calculated using the pixel values for the red and near-infrared wavelengths from satellite images. A total of 33 images from three representative years (a very dry, an average, and a very wet year) were analyzed. The choice of image dates was made with regard to the satellite data available and ancillary data that were measured on and near Yucca Mountain. The images represented "snapshots" of the site during the growing season, emphasizing those times when the vegetation response was greatest (March through June of each year). These images were assembled to represent responses during a water year that runs from October 1 through September 30 of subsequent years. A water year more naturally captured the cycle of winter precipitation and annual plant growth that is generally senescent in this environment during late summer (SNL 2008a, Appendix E).

In order to directly compare images taken on different dates, data was adjusted as follows:

- Adjusted for the gains and biases of each sensor

- Adjusted to account for the effect of having different solar zenith angles and compensated for different values of the exoatmospheric solar irradiances arising from spectral band differences

- Corrected for differing atmospheric conditions

- Corrected for non-systematic variations, such as atmospheric opacity, soil albedo, ground level water content, atmospheric water content, and illumination geometry

- Aligned to a common geospatial coordinate system.

The combined corrections resulted in a set of processing parameters for each image. These parameters were developed for the general site flora in *Simulation of Net Infiltration for Present-Day and Potential Future Climates* (SNL 2008a, Appendix E). Analyses were completed to assure that the general processing parameters were appropriate for each of the three vegetation associations defined for Yucca Mountain in *Simulation of Net Infiltration for Present-Day and Potential Future Climates* (SNL 2008a, Appendix D).

Once the NDVI images had been processed so that they were directly comparable, a seasonal response to precipitation was developed that contained an annual peak for vegetation (occurring in about mid April). General response curves were developed that captured the variability induced by slope and azimuth. Slope and azimuth combinations will result in different amounts of sunlight reaching the ground at different times of the year and, thus, influence the magnitude and/or timing of the vegetation growth response at that location. These influences are independent of soil conditions at a specific point, and were examined by comparing responses for various slope/azimuth combinations. The calculations used averages of pooled sample groups in order to

determine overall trends. Comparison of a predicted vegetation response using the general response curves to image data from lowlands showed that the general response curves somewhat under-estimate vegetation response. However, because the repository footprint is overlain by rocky uplands, the vegetation response curves were developed to be most accurate for these areas. The curves conservatively estimate the proportion of precipitation that will be available from infiltration in the lowlands (SNL 2008a, Appendix E).

To account for spatially varying conditions at the site, such as amount of exposed rock, soil depth, and water holding capacity, a potential vegetation response for each model grid cell was produced. Potential vegetation response was calculated on a per pixel basis (each pixel being 0.2 acres in size) by subtracting the NDVI from the driest period of the driest year (when vegetation is expected to be inactive) from the NDVI measured at the peak of the growing season during the wettest year and dividing this difference by the average difference from these two extremes over the area of interest. This measurement is thus an estimate of the capability for each pixel in the modeled region to support vegetation. The minimum NDVI values, measured during a very dry year, represent non-vegetation signals, including the signal from desert varnish. Potential vegetation response was normalized by dividing each value by the average value for model grid cells for a subset area overlying the repository. The area of interest was chosen as a rectangle of 12,702 grid cells (11.43 km^2). Normalization provided scaling to permit a better understanding of potential vegetation response distribution: a potential vegetation response of 1.0 represents the approximate average vegetation response overlying the repository (SNL 2008a, Appendix E).

An algorithm was developed to simulate vegetation for each model grid cell using results from the analyses. The general response curves provided the shape of the vegetation response through the growing season. They were then scaled for the general conditions for each growing year by a ratio of the precipitation of the year of interest to the wettest year (1998) that was used to fit the response curve. Potential vegetation response was used as a scalar to represent plant growth potential within each model grid cell (SNL 2008a, Appendix E).

The uncertainty associated with the vegetation algorithm was only evaluated for the mathematical processing necessary to isolate the vegetation signal within the satellite data. Additional uncertainty associated with the response curve or the algorithm was analyzed in the uncertainty of the MASSIF model (SNL 2008a, Appendix E).

The use of NDVI data allows for the identification of vegetative patterns over large areas, which would otherwise be difficult to discern based on ground observations alone. However, in order to use NDVI data as an indicator of the amount of water that could potentially be used by a stand of vegetation if water were not limiting, it is necessary to compare NDVI data with vegetation measurements made on the ground. The MASSIF model used a dual transpiration coefficient in conjunction with reference evapotranspiration (ET_0) to estimate actual evapotranspiration (ET) (Section 2.3.1.3.3.1.1). The methods for estimating crop water use were standardized in the Food and Agriculture Organization of the United Nations Irrigation and Drainage Paper 56 (hereafter referred to as FAO-56) (Allen et al. 1998). The FAO-56 methods were extended to natural vegetation using measured values of leaf area index (LAI, a unitless measure of leaf area per ground area) or effective ground cover (percent of ground covered by vegetation) and adjustments for stomatal control (Allen et al. 1998, pp. 187 to 193). To account for the effects of soil evaporation, the FAO-56 methods included a dual transpiration coefficient ($K_c = K_{cb} + K_e$). This dual coefficient

consisted of a basal transpiration component (K_{cb}), representing plant transpiration under nonlimiting water conditions, and an evaporation component (K_e). K_{cb} profiles (or curves) are time based and are calculated at a set of ecological study plots at Yucca Mountain for the growing seasons of three representative wet, dry, and average precipitation years (SNL 2008a, Section 6.5.3.4).

The FAO-56 K_{cb} profile for agricultural crops reflects transpiration under optimal growth and nonlimiting water conditions. The generalized K_{cb} profile includes four growth stages (Allen et al. 1998, pp. 95 to 96): (1) an initial growth stage (planting date to approximately 10% ground cover); (2) a development stage (10% ground cover to effective full cover); (3) a mid-season stage (effective full cover to start of maturity); and (4) a late season stage (maturity to harvest or senescence). Effective full cover is defined as the time when soil shading is nearly complete (Allen et al. 1998, p. 95). Transpiration coefficients are developed for the initial growth stage ($K_{cb\ ini}$), the mid season stage ($K_{cb\ mid}$), and the end of the late season stage ($K_{cb\ end}$) (SNL 2008a, Section 6.5.3.6).

Characteristics of desert vegetation at Yucca Mountain differ from agricultural crops in several ways, including low effective ground cover that rarely exceeds 30% during peak growth periods, little morphological change in perennial vegetation across growth stages (e.g., little change in average maximum vegetation height and maintenance of a percentage of green canopy throughout the year), and a greater degree of stomatal control resulting in lower rates of water loss compared to agricultural crops. Additionally, desert vegetation assemblages consist of a variety of plant species that have different growth stage lengths and contribute differently to total ground cover when compared to agricultural crops that are generally planted in monocultures. Climatic conditions at Yucca Mountain differ from standard FAO-56 conditions, with lower minimum relative humidity (RH_{min}) and higher wind speeds (u_2). To account for these differences, FAO-56 methods for calculating K_{cb} for natural vegetation using effective ground cover, adjustments for stomatal control over water loss, and adjustments for local RH_{min} and u_2 were used (Allen et al. 1998, pp. 187 to 193). Details for the calculations are provided in *Simulation of Net Infiltration for Present-Day and Potential Future Climates* (SNL 2008a, Appendix D). The analysis used a simple classification scheme to delineate the Yucca Mountain vegetation into four associations named for dominant or co-dominant species: *Coleogyne*, *Larrea-Ambrosia*, *Lycium Grayia*, and *Larrea-Lycium-Grayia* (CRWMS M&O 1996, pp. 7 to 8, Table 2-1). The *Larrea-Ambrosia*, *Lycium-Grayia*, and *Larrea-Lycium-Grayia* vegetation associations are the most common in the infiltration model domain. The *Lycium-Grayia* association is representative of the vegetation that overlies the repository on the upper slopes and crest of Yucca Mountain (elevation = 1300 to 1600 m), and is thus important to the infiltration modeling effort. Vegetation cover and plant species composition data from the *Larrea-Ambrosia*, *Lycium-Grayia*, and *Larrea-Lycium-Grayia* vegetation associations were used to develop K_{cb} profiles over time using FAO-56 methods. K_{cb} values estimated for the *Lycium-Grayia* association are used to develop the least squares regression between K_{cb} and NDVI data (SNL 2008a, Section 6.5.3.7). K_{cb} values estimated for the *Larrea-Ambrosia*, *Larrea-Lycium-Grayia*, and *Lycium-Grayia* associations are used to evaluate appropriateness of NDVI data (SNL 2008a, Appendix E, Sections E2 and E7), and to determine whether the magnitude of K_{cb} values is appropriate for desert vegetation (SNL 2008a, Appendix D, Section E7).

Use of separate K_{cb}–NDVI regressions for each vegetation association would have required that each model grid cell be assigned to one of the three associations. This was not applicable due to lack

of detailed spatial data for vegetation associations and the potential for vegetation change through time. As an alternative to using separate K_{cb}–NDVI regressions for each association, and for use in uncertainty analyses, upper and lower bounds for K_{cb} values were calculated for the *Lycium-Grayia* association profiles for water year 1991 and water year 1993. Upper and lower bounds for daily K_{cb} values were determined for each profile by using high and low input values for vegetation cover, plant height, and stomatal resistance. The high and low values were taken from the input data sets. The uncertainty bounds for the *Lycium-Grayia* association K_{cb} profiles encompassed the variation observed among associations. Therefore, the K_{cb} values with uncertainty bounds for water year 1993 and water year 1991 for the *Lycium-Grayia* association were applied to K_{cb}–NDVI regressions for the Yucca Mountain area (SNL 2008a, Section 6.5.3.7).

In order to implement the FAO-56 methodology for estimating evapotranspiration at Yucca Mountain, it was necessary to estimate values for basal transpiration coefficients (K_{cb}) as a function of the NDVI data. Verification analyses of the NDVI algorithm showed strong linear relationships between estimated K_{cb} values and simulated NDVI and between average percent ground cover data collected during peak growth and simulated peak NDVI data for the ecological study plots at Yucca Mountain (SNL 2008a, Appendix E, Sections E7.2 and E7.3). Based on evidence that the K_{cb}–NDVI data relationship is generally linear, a least-squares method was selected to fit a linear relationship to the K_{cb} values and NDVI developed for Yucca Mountain. The slope and intercept parameters that defined the linear fit between K_{cb} and NDVI were used in the MASSIF model to predict K_{cb} from the NDVI for each model grid cell. The predicted K_{cb} is used in the calculation of evapotranspiration for each model grid cell (SNL 2008a, Section 6.5.3.7).

Uncertainties in the intercept and slope were calculated as the variance in each parameter, based on uncertainties associated with individual estimated points. Two sources of uncertainty were considered in the calculation of the variance in K_{cb} values. These sources included a direct contribution due to uncertainties in K_{cb} values, and an indirect contribution from uncertainties in NDVI to the total uncertainty in predicted K_{cb} values. The standard deviations calculated for the slope and intercept were 2.1 and 0.05, respectively. These values were used to establish 90% confidence intervals for the least squares regression (SNL 2008a, Figure 6.5.3.7-3). Table 2.3.1-16 summarizes the recommended values and distributions for the slope and intercept for the regression line for predicting K_{cb} from NDVI in the MASSIF model. Because the magnitude of the intercept (C_{Kcb1}) is relatively small, it is appropriate to consider this parameter as a constant for the purposes of calculating net infiltration. The rationale is that when K_{cb} is small, its value is controlled by the uncertainty in the value of $K_{c\,min}$ rather than C_{Kcb1}. When K_{cb} is large, its value is controlled by the value of C_{Kcb2}, which has a larger influence and uncertainty than C_{Kcb1}. The linear relationship derived between NDVI and K_{cb} measurements was also used for the monsoon and glacial-transition climates. Differences in vegetation during these future climates states were accounted for by changing rooting depth, and plant height ranges.

2.3.1.3.3   Infiltration Modeling and Uncertainty
[NUREG-1804, Section 2.2.1.3.5.3: AC 1(3), (5) to (7), AC 2(2) to (6), AC 3(1), (3), (4), AC 4)]

Development of the MASSIF model and uncertainties associated with both the MASSIF model and the input parameters for the model are addressed below.

2.3.1.3.3.1   MASSIF Model

The MASSIF model estimates net infiltration at the Yucca Mountain site based on a daily water balance calculation of the near-surface soils. The water balance includes net precipitation as input, water storage and movement within the soil (including evapotranspiration), and water moving either from soil into the underlying bedrock or directly into bedrock where it is exposed at the surface.

The model domain is composed of a number of cells with equal surface area that extend from the surface to the contact with the underlying bedrock. The description of each cell includes the cell depth as defined by the soil layer depth; soil type and associated properties; cell elevation, azimuth, and slope; fraction of the surface covered by the vegetation canopy; and vegetation related characteristics. Each cell is composed of one to three soil layers, depending on the soil depth (Figure 2.3.1-22). However, some grid cells have no soil and therefore have no soil layer in the model (SNL 2008a, Table 6.5.7.6-2[a]). Any precipitation that lands on these grid cells becomes net infiltration or runoff. The topmost soil layer is designated as the evaporation zone, and is relatively thin. It is divided into two sections (nodes) representing the bare surface fraction and the fraction of the surface covered with vegetation (canopy fraction). Layer 2 extends from the bottom of layer 1 to the bottom of the root zone or to the soil-bedrock interface in the case that the maximum rooting depth is greater than the soil depth. Together, layers 1 and 2 comprise the evapotranspiration zone. Layer 3 extends from the bottom of the root zone (layer 2) to the soil-bedrock interface. When soil depth is less than maximum rooting depth, layer 3 is not represented (thickness is set to zero) (SNL 2008a, Section 6.3.1).

Daily climatic data are input to the model, including precipitation and maximum and minimum air temperature. Precipitation and mean temperature are adjusted for cell elevation. Snow, snowmelt, and sublimation are included in the model (SNL 2008a, Section 6.3.1).

The model allows rain and snowmelt to run off the top of one cell onto an adjacent cell that is at a lower elevation. Runoff can occur if the net precipitation exceeds the ability of the thin surface soil layer to store and transmit water to underlying soil layers. Runoff will also occur if the entire cell from the bedrock to the surface saturates. In the case of runoff, water is diverted to the surface of the next downstream cell (SNL 2008a, Section 6.3.1).

Subsurface vertical water movement is estimated by means of a daily water balance approach for each cell. Subsurface water movement within the model is one-dimensional; that is, there is no subsurface water movement between adjacent cells. Downward water movement from layer to layer within a cell is based on the field capacity concept. Field capacity of the soil represents the amount of water that is held by the layer after gravity drainage. Water in excess of the field capacity will be available to move downward to a lower layer. Water is removed from the root zone based on a daily calculation of evapotranspiration for each cell. The evapotranspiration calculation is derived from the dual crop version of the FAO-56 method, which produces separate estimates of evaporation and transpiration. Evapotranspiration is calculated proportional to a reference evapotranspiration, which accounts for the atmospheric demand for water based on daily climatic conditions at each cell (SNL 2008a, Section 6.3.1).

Water above field capacity in the bottom-most soil layer can enter the underlying bedrock layer, limited by the effective saturated hydraulic conductivity of the bedrock. Any water that moves into the bedrock layer is net infiltration for that cell and passes out of the bottom of the model (SNL 2008a, Section 6.3.1).

2.3.1.3.3.1.1   Development of MASSIF Infiltration Model

The objective of the MASSIF model is to calculate net infiltration for each cell of a grid representing a watershed bounded by surface water divides. The limitations and input requirements of the model are described in *Simulation of Net Infiltration for Present-Day and Potential Future Climates* (SNL 2008a, Sections 1.2[a] and 6). The mathematical basis for the model is discussed below in terms of the water balance components that comprise MASSIF. The basis of the model is the following mass balance equation that is solved for each computational cell for each day of the simulation (SNL 2008a, Section 6.4):

$$R_{off} = P_{rain} + R_{on} + SM - \Delta\theta - ET - NI \qquad \text{(Eq. 2.3.1-5)}$$

where

R_{off} is runoff

P_{rain} is precipitation (excluding snow)

R_{on} is run-on

SM is snowmelt

$\Delta\theta$ is the change in water storage in the soil

ET is evapotranspiration

NI is net infiltration. Note that the water balance equation is solved for runoff. Net infiltration is not calculated as the residual of the water balance equation. Rather, it is calculated as being equivalent to the bedrock K_{sat} when the water content of the soil layer above bedrock exceeds field capacity.

Additionally, a water (volume) balance equation for the snowpack of each cell is solved for each day of the simulation:

$$\Delta SP = P_{snow} - SUB - SM \qquad \text{(Eq. 2.3.1-6)}$$

where

ΔSP	is the change in the water storage of the snowpack
P_{snow}	is precipitation as snow
SUB	is the sublimation
SM	is snowmelt

Figure 2.3.1-23 illustrates that the soil and snowpack form the two water reservoirs represented in the water balance. Snowmelt (*SM* in Figure 2.3.1-23) is the only pathway for P_{snow} to reach the soil.

Water movement in the model is considered to be vertical below the surface until it encounters the unsaturated zone flow model domain (Section 2.3.2). The only water transport between cells is through runoff from one cell, which is added to a downstream cell as run-on (SNL 2008a, Section 6.4). Following are descriptions of how each of these quantities is represented in the model.

Precipitation (*P*)—Precipitation is assumed to be snow whenever the average daily temperature at a cell location is equal to or less than 0°C. Inputs to the model are maximum and minimum daily air temperatures at the reference elevation. Average daily temperature at the reference elevation is calculated in the model as the mean of the minimum and maximum temperatures. These temperatures are then corrected for elevation from the reference elevation for each grid cell in the geospatial database. The elevation correction decreases temperature linearly with increasing elevation at a rate referred to as the temperature lapse rate (SNL 2008a, Section 6.4.1.2).

Precipitation can occur over a range of durations from brief and intense thunderstorms to prolonged storms that last the entire day. For the purposes of modeling the water transport in the soil, the period of time that water is available at the surface of the soil may be important. The MASSIF model requires as input an effective duration in hours for each day of precipitation (duration) (SNL 2008a, Section 6.4.1.3).

Snowpack will melt on days when the average air temperature at a cell location is above 0°C. The snow melts at a rate proportional to the average daily air temperature (T_{avg}) at a cell. If it rains on a day when there is snowmelt, the rain and snowmelt are combined and applied as input to the topsoil surface over the effective precipitation duration for that day. On days without precipitation, snowmelt is applied over a 12 hour duration. Rain is input to the top soil surface on the day of precipitation regardless of whether there is snow accumulated on the surface from prior snow events (SNL 2008a, Section 6.4.1.4).

Some portion of snow will sublimate; the total annual sublimation can be described as a percentage of the total annual amount of snow (Hood et al. 1999). In MASSIF, daily sublimation (*SUB*, mm) was calculated as a fixed percentage ($C_{sublime}$) of the precipitation (*SF*, mm) on days that it snows (SNL 2008a, Section 6.4.1.4).

Water Transport and Storage ($\Delta\theta$)—Rather than employing a Richards equation approach to solve for subsurface water movement, a simpler "field capacity" approach is adopted. In this approach, the soil at a given location is divided into a series of layers and nodes (Figure 2.3.1-22). In this context, layers refer to vertical soil horizons and nodes refer to distinct volumes of soil considered in the water mass balance. The model accommodates up to three layers and four nodes.

The top or surface layer is divided into two nodes, and the bottom two layers are each represented by a single node. A daily water balance is performed on each node in each cell of the watershed.

In each of the soil nodes, the amount of water is accounted for by the water level. Water level is the equivalent height of water in the layer per unit area. Typically, the amount of water that can be stored in a layer is defined by the field capacity of the layer. Drainage or downward daily water movement from a soil node to the next lower node is assumed to occur when the water level exceeds the field capacity for that node. Layers 2 and 3 (Nodes 3 and 4) can accept water at a maximum rate defined by the saturated hydraulic conductivity and the precipitation duration. The duration (hr) is the amount of time during the day during which precipitation occurs. If there is only snowmelt on a day, a 12 hour duration is assumed. The amount of water that moves downward is a function of the maximum the layer can accept water, the water level, and the field capacity. The water level of the layer is reduced by this amount, and the water level of the underlying layer is increased by this amount, thereby passing water to a lower layer (SNL 2008a, Section 6.4.2).

The shading of the vegetative canopy retards evaporation under the canopy. As a result, the surface layer of soil under the canopy frequently has higher water content than the adjacent exposed soil. To reflect this, the surface layer is divided into two nodes. Node 1 (the "evaporation node") models the bare soil; Node 2 (the "canopy node") models the canopy region. The water levels in these two nodes are calculated separately (SNL 2008a, Section 6.4.2).

During a precipitation event, one of the two surface nodes in a cell may exceed field capacity before the other. For instance, the canopy node (Node 2) may reach field capacity before the adjacent bare soil node (Node 1). The distance between the two nodes (Node 1 and Node 2) reflects the physical dimensions of the individual plant canopies and the inter-plant spacings. This distance is expected to be much smaller than the cell dimension (30 m). Therefore, in the MASSIF model, surplus water from Node 2 is supplied to Node 1 before it is supplied as runoff to the downstream cell. Conversely, surplus water from Node 1 is supplied to Node 2 before it is supplied as runoff to the downstream cell. Water will drain from layers 1 and 2 only after the water levels of both Node 1 and Node 2 exceed field capacity (SNL 2008a, Section 6.4.2).

Net infiltration or drainage from the bottom-most soil layer is calculated and is compared to the maximum amount of water the bedrock can accept. This maximum amount of water accepted by the rock is calculated from Darcy's law for saturated flow where a unit gradient is assumed (gravity flow) and is a function of the saturated hydraulic conductivity of the rock and the duration (SNL 2008a, Section 6.4.2).

The bedrock may not be able to accept all of the excess water from the bottommost soil layer. In this case, the soil layer (Node 4) is permitted to exceed field capacity to accommodate the water that cannot move into the bedrock layer. If there is sufficient excess water to exceed the porosity of the layer, then the excess water above full saturation is distributed to the next layer above (layer 2, Node 3). If layer 2 saturates, water is passed to Nodes 1 and 2 in proportion to the amount that was originally drained from them (SNL 2008a, Section 6.4.2).

On days with precipitation events with durations less than 24 hours, the water redistribution calculation is conducted twice. First, the calculation is conducted for the duration equal to the precipitation event duration. It is during this calculation that water is added to the top of the cell. In

the second calculation, if there is water in excess of field capacity in the bottom layer, it has the opportunity to enter the bedrock during the remainder of the day at a rate limited by the rock hydraulic conductivity. During this calculation, the duration is the difference between a full day and the precipitation event duration (SNL 2008a, Section 6.4.2).

Surface Runoff and Run-on (R_{off} and R_{on})—Runoff from a cell can result from the water redistribution calculation when either (1) the entire soil profile becomes saturated, or (2) the first layer becomes saturated due to the soil conductivity infiltration limit. In either case, the water in excess of saturation will produce runoff from the cell. This runoff is then added to the next downstream cell, which is identified in the input to the model. For this reason, the calculation for a watershed is conducted for cells in order of decreasing elevation. The run-on duration is assumed to be the precipitation duration (SNL 2008a, Section 6.4.3).

Evapotranspiration—Water is removed from the root zone via evapotranspiration, as illustrated in Figure 2.3.1-24. There are five discrete components of evapotranspiration in the model: (1) bare soil evaporation, which occurs only in the fraction exposed and wetted (few) portion of surface layer; (2) transpiration from the f_{ew} portion of the surface layer; (3) transpiration from the canopy (f_c) portion of the surface layer; (4) transpiration from layer 2; and (5) diffusive evaporation from layer 2 (not shown on figure) (SNL 2008a, Section 6.4.4).

The evapotranspiration calculations are made after the daily water redistribution calculation described above. The evapotranspiration calculation follows the dual crop FAO-56 method, where ET is proportional to the reference evapotranspiration (ET_0,), and explicitly accounts for soil evaporation and transpiration separately (SNL 2008a, Section 6.4.4, Eq. 6.4.4-1):

$$ET = (K_e + K_s K_{cb}) * ET_0 \qquad\qquad \text{(Eq. 2.3.1-7)}$$

where

K_e is the soil evaporation coefficient (dimensionless)
K_{cb} is the basal transpiration coefficient (dimensionless)
K_s is a water stress coefficient (dimensionless).

The ET_0 calculation depends only on cell-specific, climatic conditions.

The basal transpiration coefficient depends on the amount and type of vegetation present within a cell, and on the time of year. The value of K_{cb} is near zero when the plants are absent or dormant at the beginning and end of the growing season. K_{cb} reaches its peak near the middle of the growing season. For agricultural crops FAO-56 provides lookup tables for determining K_{cb}. For native vegetation, FAO-56 provides methods for estimating K_{cb} based on specific plant characteristics (e.g., stomatal conductance) and fractional cover data which can be either measured directly or estimated from satellite data. For the purpose of describing the mathematical foundation of the MASSIF model, K_{cb} is treated as an input to the calculation of evapotranspiration. The development of K_{cb} values for the Yucca Mountain net infiltration calculation required developing a site specific methodology, which is discussed as part of the analysis in *Simulation of Net Infiltration for*

Present-Day and Potential Future Climates (SNL 2008a, Section 6.5.3, Appendix D and Appendix E).

Comparison between observed site vegetation and image analysis results showed there was a nonvegetation source that produced a strong depression in the red wavelength mimicking a vegetation response. It was concluded that the natural rock weathering processes over time produced desert varnish that caused this response. Because the site is very arid, the measured vegetation responses tend to be very low, and it was found that the signal from the desert varnish was high in comparison (SNL 2008a, Appendix E). Therefore, an adjusted NDVI quantity was defined as NDVI, that subtracted off the influence of the nonvegetation signal.

The basal transpiration coefficient is constrained to be between a minimum and maximum value. The maximum basal transpiration coefficient ($K_{c\,max}$) represents an upper limit of the evaporation and transpiration that can occur on a given day based on available energy. $K_{c\,max}$ ranges between 1.05 and 1.30 and is a function of the basal transpiration coefficient, average daily wind speed at 2 m, minimum daily relative humidity, and characteristic plant height (m). The minimum basal transpiration coefficient represents dry soil with no vegetation cover ($K_{c\,min}$). $K_{c\,min}$ may be greater than zero to account for evaporation occurring from layer 2 (Node 3) and beneath the vegetation canopy (Node 2), as these evaporative losses are not explicitly included in the calculation of evaporation from the evaporative node (Node 1) (SNL 2008a, Section 6.4.4). $K_{c\,min}$ values range from 0 to 0.2.

The soil evaporation coefficient (K_e) is found from Equation 71 of FAO-56 (Allen et al. 1998). It is a function of the maximum basal transpiration coefficient, the basal transpiration coefficient, the exposed and wetted portion of surface layer, and a soil evaporation reduction coefficient (K_r) described in the next section (SNL 2008a, Section 6.4.4).

Vegetative cover varies seasonally. In the spring, the vegetative cover coefficient (f_c) increases as the plants grow. Later in the year, as the ground dries out and transpiration drops due to water stress, the vegetative cover coefficient declines. The correlation recommended in FAO-56 (Allen et al. 1998, Equation 76) is used to model the time variation of the canopy coefficient (SNL 2008a, Section 6.4.4).

The amount of soil water in the root zone affects the daily evapotranspiration. In the FAO-56 method, the amount of water in a soil layer is described in terms of depletion. Depletions are calculated for the evaporation node of the surface layer, for the canopy node of the surface layer, and for the entire root zone. The approach used for these calculations is based on the approach outlined in the FAO-56 method, but is somewhat different in that depletions are calculated after the redistribution of water in the two surface nodes. The depletion for the evaporation and canopy nodes are calculated from the field capacities and water levels in these nodes. Depletion of the root zone is calculated from the field capacities and water levels in the surface layer and layer 2 using area-weighted values for the evaporative (Node 1) and canopy (Node 2) nodes (SNL 2008a, Section 6.4.4.2).

The total amount of water available for evaporation (*TEW*) is calculated from FAO-56, Equation 73 (Allen et al. 1998). It is a function of the intrinsic field capacity (θ_{FC}), the intrinsic wilting point (θ_{WP})—below which vegetation cannot extract moisture from the soil, and the

surface layer thickness (Z_e). Z_e is dependent on soil texture and length of drying periods common to the model area (SNL 2008a, Section 6.4.4.2):

$$TEW = \theta_{FC} - 0.5* \theta_{WP}) *Z_e \qquad \text{(Eq. 2.3.1-8)}$$

The soil evaporation reduction coefficient (K_r) depends on the amount of water in the evaporation node (Node 1). When the soil surface is wet, the maximum rate of evaporation is controlled by the amount of available energy at the soil surface (Allen et al. 1998, p. 145). Readily evaporable water (*REW*) is the maximum depth of water that can be evaporated from the upper soil layer prior to the onset of hydraulic limitations that reduce the rate of water supply below that of energy demands. When the depth of evaporation exceeds readily evaporable water, there is a reduction of the evaporation rate. K_r is a function of the total amount of water available for evaporation, readily evaporable water, and the depletion (D_e) of the evaporative node (Node 1). K_r is constrained to be between 0 and 1 (SNL 2008a, Section 6.4.4.2):

$$K_r = (TEW - D_e) / (TEW - REW) \qquad \text{(Eq. 2.3.1-9)}$$

Depletion of the root zone is calculated from the field capacities and water levels in the surface layer and layer 2, using area-weighted values for the evaporative and canopy nodes. Two additional parameters are used to describe the water status in the root zone, the total available water (*TAW*), and the readily available water. Total available water is the amount of water available for evapotranspiration in the root zone, and is calculated from FAO-56, Equation 82 (Allen et al. 1998). It is a function of the intrinsic field capacity, the intrinsic wilting point, and the root zone thickness (Z_r):

$$TAW = (\theta_{FC} - \theta_{WP}) *Z_r \qquad \text{(Eq. 2.3.1-10)}$$

Readily available water (*RAW*) is the limit of the water in the root zone below which the transpiration rate is affected. It is calculated as a function of total available water and p, the fraction of total available water that vegetation can remove without suffering stress (Allen et al. 1998, Equation 83). Characteristics of the vegetation as well as the climate and soil type determine the value of p. An adjustment of p as a function of daily evapotranspiration is recommended in FAO-56 (Allen et al. 1998, p. 162) (SNL 2008a, Section 6.4.4.2):

$$RAW = p * TAW \qquad \text{(Eq. 2.3.1-11)}$$

The impact of water stress in the root zone on transpiration is reflected in the transpiration stress coefficient. The transpiration stress coefficient, *Ks*, is calculated from FAO-56, Equation 84

(Allen et al. 1998). It is a function of the total available water, the readily available water, and the root zone depletion (D_r) (SNL 2008a, Section 6.4.4.2):

$$K_s = (TAW - D_r) / (TAW - RAW) \qquad \text{(Eq. 2.3.1-12)}$$

Transpiration from the evaporation node (Node 1) is calculated as a portion of the total calculated transpiration, and is based on the amount of water in the surface layer compared to the amount of water in the entire root zone. This fractional partitioning coefficient (K_{tie}) (Allen, Pereira et al. 2005, Equation 27) is a function of the total available water, the total amount of water available for evaporation, the root zone depletion, the depletion of the evaporative node (Node 1), the thickness of the surface layer, and the root zone thickness (SNL 2008a, Section 6.4.4.2):

$$K_{tie} = [(1 - D_e/TEW)/(1 - D_r/TAW)] * (Z_e/Z_r)_{0.6} \qquad \text{(Eq. 2.3.1-13)}$$

Unlike MASSIF, the FAO-56 procedure does not explicitly keep track of the water content of the surface layer under the vegetation canopy (Node 2). Therefore, the fractional partitioning coefficient for the canopy region (K_{tic}) is calculated in a manner similar to K_{tie}, and is a function of the total available water, the total amount of water available for evaporation, the root zone depletion, the thickness of the surface layer, the root zone thickness, and the depletion of the canopy node (D_c) (SNL 2008a, Section 6.4.4.2):

$$K_{tic} = [(1 - D_c/TEW)/(1 - D_r/TAW)] * (Z_e/Z_r)_{0.6} \qquad \text{(Eq. 2.3.1-14)}$$

The evapotranspiration is calculated as the sum of the evaporative losses from the evaporative node portion of the surface layer and transpiration from the root zone. Daily evaporation (E) is calculated as a function of the soil evaporation coefficient and the reference evapotranspiration. The calculated daily evaporation is applied to the entire surface area of a cell. In reality, the evaporation only takes place in the bare soil portion of the cell (Node 1). Hence, the depth of water evaporated from the fraction of evaporative node is E/f_{ew}. E is constrained so that the total amount of water available for evaporation is not exceeded (SNL 2008a, Section 6.4.4.3).

Daily transpiration (T) from the root zone is calculated as a function of the water stress coefficient, the basal transpiration coefficient, and reference evapotranspiration. The total daily transpiration is partitioned between the surface layer nodes (Nodes 1 and 2) and layer 2 (Node 3). The daily transpiration from the evaporative node (T_e) is calculated using the fractional partitioning coefficient for the canopy region and transpiration. For the canopy node, the daily transpiration (T_c) is also calculated using the fractional partitioning coefficient for the canopy region and transpiration. The daily transpiration from layer 2 (Node 3) is $T2 = T - T_e * f_{ew} - T_c * f_c$ (SNL 2008a, Section 6.4.4.3, Eq. 6.4.4.3-5). Transpiration is limited so that the water level of any of the nodes does not go below the wilting point (SNL 2008a, Section 6.4.4.3).

After the evapotranspiration calculation, the water levels in each node are updated. For the evaporative node (Node 1) and canopy node (Node 2), the changes in the water level due to evapotranspiration is $(-E/f_{ew} - T_e)$ and $(-T_c)$, respectively. The change in the water level of layer 2 is $(-T2)$ (SNL 2008a, Section 6.4.4.3).

Reference Evapotranspiration (ET_0)—The evapotranspiration rate from a reference surface, not short of water, is called the reference crop evapotranspiration or reference evapotranspiration (Allen, Walter et al. 2005, p. 2) (SNL 2008a, Section 6.4.5).

The concept of the reference evapotranspiration was introduced to study the evaporative demand of the atmosphere independent of vegetation type, plant development stage, and management practices. As water is abundantly available at the reference evapotranspiring surface, soil factors do not affect evapotranspiration. Relating evapotranspiration to a specific surface provides a reference to which evapotranspiration from other surfaces can be compared. This approach obviates the need to define a separate evapotranspiration level for each type of vegetation and stage of growth. ET_0 values measured or calculated at different locations (or in different seasons) are comparable as they refer to the evapotranspiration from the same reference surface (SNL 2008a, Section 6.4.5).

For convenience and reproducibility, the reference surface has recently been standardized by the American Society of Civil Engineers as a hypothetical vegetated surface having specific characteristics (Allen, Walter et al. 2005). The reference evapotranspiration (ET_0) is defined as the evapotranspiration rate from a uniform surface of dense, actively growing vegetation having an assumed height of 0.12 m and having a surface resistance of 70 s m^{-1} (for 24 hour calculation time-steps) and an albedo of 0.23, closely resembling the evaporation of an extensive surface of green, cool season grass of uniform height, not short of soil water (Allen et al. 1998, p. 24) (SNL 2008a, Section 6.4.5).

The only factors affecting ET_0 are climatic parameters. Consequently, ET_0 is a climatic parameter and can be computed from weather data. ET_0 expresses the evaporating power of the atmosphere at a specific location and time of the year, and does not consider the local vegetation characteristics, soil factors, or precipitation amounts. Even though there are many methods for calculating ET_0 cited in the literature, the FAO Penman Monteith method is recommended as the standard method for determining ET_0 (Allen et al. 1998, pp. 7 and 65; Irmak et al. 2005, p. 1064; Droogers and Allen 2002, p. 33). The method has been selected because it closely approximates grass ET_0 at the location evaluated, is physically based, and explicitly incorporates both physiological and aerodynamic parameters (Allen et al. 1998, p. 7). Moreover, procedures have been developed for estimating missing climatic parameters when the FAO Penman-Monteith equation is used (SNL 2008a, Section 6.4.5).

The FAO Penman-Monteith method to estimate ET_0 was derived from the original Penman-Monteith equation (Jensen et al. 1990, p. 93) and associated equations for aerodynamic

and surface resistance for 24 hour calculation time-steps (Allen et al. 1998, pp. 24 and 65; SNL 2008a, Section 6.4.4, Eq. 6.4.5-1):

$$ET_0 = \frac{0.408\Delta(R_n - G) + \gamma\frac{900}{T + 273}u_2(e_s - e_a)}{\Delta + \gamma(1 + 0.34u_2)} \qquad \text{(Eq. 2.3.1-15)}$$

where

ET_0 is the reference evapotranspiration [mm d^{-1}]
R_n is the net radiation at the crop surface [MJ m^{-2} d^{-1}]
G is the soil heat flux density [MJ m^{-2} d^{-1}]
T is the mean daily air temperature at 2 m height [°C]
u_2 is the wind speed at 2 m height [m s^{-1}]
e_s is the saturation vapor pressure [kPa]
e_a is the actual vapor pressure [kPa]
$e_s - e_a$ is the saturation vapor pressure deficit [kPa]
Δ is the slope of the vapor pressure curve [kPa °C^{-1}]
γ is the psychrometric constant [kPa °C^{-1}].

The reference evapotranspiration, ET_0, provides a standard to which (1) evapotranspiration during different periods of the year or in other regions can be compared, and (2) evapotranspiration from specific vegetation types and surfaces can be related via some form of a "crop coefficient" (SNL 2008a, Section 6.4.5).

The FAO Penman-Monteith equation is a reasonable, simple representation of the physical and physiological factors governing the evapotranspiration process. By using the FAO Penman-Monteith definition for ET_0, one may calculate crop (or vegetation cover) coefficients (K_c) at research sites by relating the measured crop (or vegetation cover) evapotranspiration (ET) with the calculated ET_0, (i.e., $K_c = ET/ET_0$). In the crop coefficient approach, differences in the vegetation canopy and aerodynamic resistance relative to the hypothetical reference crop are accounted for within the crop coefficient. Thus, the K_c factor serves as an aggregation of the physical and physiological differences between vegetation covers and surface wetness conditions and the reference definition (SNL 2008a, Section 6.4.5).

MASSIF applies the daily computed reference evapotranspiration for each grid cell to account for influences of elevation, slope, and azimuth at each cell. The data for appropriate use of the FAO Penman-Monteith equation consist of the following (SNL 2008a, Section 6.4.5.1):

- Meteorological data

    - Air temperature: daily maximum (T_{max}) and minimum (T_{min}) air temperatures

    - Air humidity: mean daily actual vapor pressure (e_a) derived from psychrometric, dew-point temperature or relative humidity data

- – Wind speed: daily average over 24 hours for wind speed measured at or adjusted to 2 m height (u_2)

- – Radiation: net radiation (R_n) measured or computed from solar and longwave radiation or from the recorded duration of sunshine.

- Location information

  - – Altitude above sea level (m)
  - – Latitude (degrees north or south).

These data are used to adjust air temperature from the reference weather station for the average atmospheric pressure (function of site elevation), and to compute exoatmospheric radiation (R_a).

When a complete dataset of weather parameters is not available, the FAO Penman Monteith equation can be applied using a minimum set of inputs. Daily maximum and minimum air temperature data are the minimum data requirements necessary to apply the FAO Penman-Monteith method (Allen et al. 1998, p. 64; Allen, Walter et al. 2005, p. E-1). The estimation of other weather variables can be based on minimum and maximum air temperature, or on average values (for wind speed). Keying solar radiation and vapor pressure (via dew-point temperature) on daily air temperature extremes helps to preserve the strong correlation among these variables (Allen 1997, p. 56; Allen et al. 1998, p. 60; Allen, Walter et al. 2005, pp. E-4 and E-5).

The use of an alternative ET_0 procedure requiring only limited meteorological parameters (for example, the Priestley-Taylor, Blaney-Criddle or Hargreaves evapotranspiration equations) is not recommended by FAO-56 (Allen et al. 1998, p. 58). The FAO Penman-Monteith method is recommended as the sole standard method for the computation of ET_0 from meteorological data, even for the cases when only a limited dataset is available (Allen et al. 1998, p. 58; Allen, Walter et al. 2005, p. E-1). Procedures used for estimating missing climatic data (solar radiation, vapor pressure and wind speed) for the Yucca Mountain calculation of net infiltration are outlined in *Simulation of Net Infiltration for Present-Day and Potential Future Climates* (SNL 2008a, Appendix C). Differences between the ET_0 estimated by the FAO Penman-Monteith equation, a limited data set, and a full data set are expected to be small especially when averaged over periods of 5 days or longer (Allen et al. 1998, p. 60).

Inclination and exposure of the surface to the sun impact several components of the surface energy balance and, consequently, ET_0 calculated by the FAO Penman-Monteith equation. In addition, substantial variation in surface elevation within a study area requires modification of some parameters. The model adjusted input weather parameters for the FAO Penman Monteith ET_0 equation for elevation, slope, and orientation of a given grid cell (SNL 2008a, Section 6.4.5.3, Appendix C).

Validation of MASSIF is described in Sections 2.3.1.3.4.1 (Confidence Building During Model Development) and 2.3.1.3.4.2 (Post-Model Development Validation).

2.3.1.3.3.1.2　　　　Results of Net Infiltration for Present-Day and Forecast Future Climates

For each of the present-day and two future climate states, two Latin Hypercube Sample replicates were generated. A Latin Hypercube Sample replicate is a complete structured set of Monte Carlo samples covering the entire probability range of all the sampled parameters. Each replicate in this analysis consists of 20 realizations of input parameter values (SNL 2008a, Section 6.5.5). Two replicates were run to test the sensitivity of the distribution of infiltration results, using the full ranges of parameter uncertainty. Those parameters determined to be the most influential on the model results (Section 2.3.1.3.3.2.2) were varied for each climate; parameters that had very little effect on model results were not included with parameters to be varied (SNL 2008a, Section 6.5.5). Parameters were sampled from the determined probability distributions for each parameter. Some of the parameters that were varied included stochastic parameters describing precipitation that affect the generation of the weather input files. For each realization, a separate weather input file was generated, which used the sampled values of these parameters, representing epistemic uncertainty. In addition, each of the weather file realizations used a different set of random numbers, which resulted in differing patterns of precipitation and reflected aleatory uncertainty.

For each realization, the appropriate weather input file and parameter set was selected and the MASSIF net infiltration model was run for each of the 11 watersheds separately.

The results of the net infiltration calculation performed for the infiltration modeling domain around Yucca Mountain are presented in *Simulation of Net Infiltration for Present-Day and Potential Future Climates* (SNL 2008a, Section 6.5.7[a]).

Predicted net infiltration generally is lowest for the present-day climate, and increases in the monsoon and glacial-transition climates. Net infiltration results during the monsoon climate state span a greater range than results for the glacial-transition climate state. This results from a greater uncertainty in the expected precipitation in the monsoon climate state than for the glacial-transition climate state.

Present-Day Results—The mean annual precipitation used for the 40 realizations representing present-day climate is shown as a cumulative distribution function in Figure 2.3.1-25. This figure also includes the cumulative distribution function of precipitation for the monsoon and glacial-transition climates for comparison. For the present-day climate, precipitation calculated for 40 realizations ranges from 134 to 222 mm/yr, with a median of 177 mm/yr (Table 2.3.1-2). The parameters used to represent present-day climate are described in Section 2.3.1.3.3.2.2.

Two replicates (R1 and R2) of 20 realizations each were run for present-day climate net infiltration estimation. Table 2.3.1-2 (SNL 2008a, Section 6.5.7.1.2[a], Table 6.5.7.1-2[a]) compares net infiltration statistics for these realizations. Table 2.3.1-2 (SNL 2008a, Section 6.5.7.1.2[a], Table 6.5.7.1-3[a]) identifies the maps that represent the 10th, 30th, 50th, and 90th percentiles of mean net infiltration over the entire model domain. The maps are shown in Figures 2.3.1-26 through 2.3.1-29 (SNL 2008a, Section 6.5.7.1.2[a], Figures 6.5.7.1-2[a] to 6.5.7.1-5[a]). Figure 2.3.1-30 presents a cumulative distribution function of mean net infiltration averaged over the full domain for the present-day climate results. This figure also includes the cumulative distribution function of infiltration for the monsoon and glacial-transition climates for comparison. For the present-day

climate, the mean of the spatial infiltration calculated for 40 realizations ranges from 2.0 to 35.4 mm/yr, with a median of 13.0 mm/yr.

Monsoon Results—The mean annual precipitation used for the 40 realizations representing monsoon climate is summarized in Figure 2.3.1-25. This figure also includes the cumulative distribution function of precipitation for the present-day and glacial-transition climates for comparison. For the monsoon climate, precipitation calculated for 40 realizations ranges from 132 to 485 mm/yr, with a median of 275 mm/yr (Table 2.3.1-3). It is noteworthy that the maximum value of average annual precipitation is larger than that for the glacial-transition climate, because more extreme precipitation events are predicted for the monsoon than for glacial-transition climate. The parameters used to represent the monsoon climate are described in Section 2.3.1.3.3.2.2.

Two replicates (R1 and R2) of 20 realizations each were run for the monsoon climate net infiltration estimation. Table 2.3.1-3 (SNL 2008a, Section 6.5.7.2.2[a], Table 6.5.7.2-2[a]) compares net infiltration statistics for these realizations. Table 2.3.1-3 (SNL 2008a, Section 6.5.7.2.2[a], Table 6.5.7.2-3[a]) identifies the maps that represent the 10th, 30th, 50th, and 90th percentiles of mean net infiltration over the entire model domain. Figures 2.3.1-31 through 2.3.1-34 (SNL 2008a, Section 6.5.7.2.2[a], Figures 6.5.7.2-2[a] to 6.5.7.2-5[a]) show maps of net infiltration for these four percentiles. Figure 2.3.1-30 (SNL 2008a, Section 6.5.7.2.2[a], Figure 6.5.7.2-6[a]) presents a cumulative distribution function of mean net infiltration averaged over the full domain for the monsoon climate results. This figure also includes the cumulative distribution function of infiltration for the present day and glacial-transition climates for comparison. For the monsoon climate, the mean of the spatial infiltration calculated for 40 realizations ranges from 2.4 to 83.4 mm/yr, with a median of 22.8 mm/yr. It is noteworthy that the maximum average infiltration value of 83.4 mm/yr is higher than the maximum value for the glacial transition climate, and that it is outside of the post-10,000 year percolation flux range of 13 to 64 mm/yr specified by the NRC proposed rule. This is due to the extreme annual precipitation values used to represent the monsoon climate.

Glacial-Transition Results—The mean annual precipitation used for the 40 realizations representing glacial-transition climate is summarized in Figure 2.3.1-25. This figure also includes the cumulative distribution function of precipitation for the present-day and monsoon climates for comparison. For the glacial-transition climate, precipitation calculated for 40 realizations ranges from 170 to 379 mm/yr, with a median of 292 mm/yr (Table 2.3.1-4). The parameters used to represent glacial-transition climate are described in Section 2.3.1.3.3.2.2.

Two replicates (R1 and R2) of 20 realizations each were run for the glacial-transition climate net infiltration estimation. Table 2.3.1-4 (SNL 2008a, Section 6.5.7.3.2[a], Table 6.5.7.3-2[a]) compares net infiltration statistics for these realizations. Table 2.3.1-4 (SNL 2008a, Section 6.5.7.3.2[a], Table 6.5.7.3-3[a]) identifies the maps that represent the 10th, 30th, 50th, and 90th, percentiles of mean net infiltration over the entire model domain. Figures 2.3.1-35 through 2.3.1-38 (SNL 2008a, Section 6.5.7.3.2[a], Figures 6.5.7.3-2[a] to 6.5.7.3-5[a]) show maps of net infiltration for these percentiles. Figure 2.3.1-30 (SNL 2008a, Section 6.5.7.3.2[a], Figure 6.5.7.3-6[a]) presents a cumulative distribution function of mean net infiltration averaged over the full domain for the glacial-transition climate results. This figure also includes the cumulative distribution function of net infiltration for the present-day and monsoon climates (for

comparison). For the glacial-transition climate, the mean of the spatial net infiltration calculated for 40 realizations ranges from 6.6 to 64.7 mm/yr, with a median of 28.5 mm/yr.

Summary of Weighted Water Fluxes and Effect of Initial Conditions—A calculation of the weighted amount of water that is accounted for by each of the water balance components was performed over the infiltration modeling domain for each climate. The mean and standard deviation of each of these weighted mean water fluxes are listed in Tables 2.3.1-17 through 2.3.1-19 (SNL 2008a, Section 6.5.7.4, Tables 6.5.7.4-1 to 6.5.7.4-3) for each of the present-day and two future climate states, respectively. These climate means are expressed as both mm/yr and as a percentage of the mean annual precipitation. Net infiltration accounts for 8.0%, 8.7%, and 10.4% of precipitation for the present-day, monsoon, and glacial-transition climates, respectively. Evapotranspiration accounts for 87.7%, 84.9%, and 86.2% of precipitation for the present-day, monsoon, and glacial-transition climates, respectively. Runoff accounts for 2.1%, 5.4%, and 0.4% of precipitation for the present-day, monsoon, and glacial-transition climates, respectively. The remaining water balance amounts are attributed to change in storage and sublimation (Tables 2.3.1-17, 2.3.1-18, and 2.3.1-19) (SNL 2008a, Section 6.5.7.4).

Results from an alternative set of simulations using wetter initial water content conditions (IC 1 simulations) were conducted to test the effect of different water content conditions on infiltration, and are presented in Tables 2.3.1-17 through 2.3.1-19. This test is important because MASSIF resets initial water content conditions on October 1 for every simulated year. These IC 1 simulations are identical to the base case simulations, except that they were started with a higher soil moisture content initial condition. It is noted that the primary difference between the base case simulations and the alternative IC 1 simulations is that the IC 1 simulations end up with a mean change in storage which is negative and a slightly higher net infiltration than the base case runs. This negative change in storage indicates that, on average, the IC 1 runs are ending the year with lower soil moisture contents than were applied as initial conditions. The comparison between the base case model results and the IC model results indicate that the effects of initial water content conditions on net infiltration uncertainty is minor (SNL 2008a, Section 6.5.7.4).

Factors Influencing Temporal Variability of Net Infiltration—Net infiltration results were averaged over space and time for the purposes of comparing results within and between climates. Net infiltration is an episodic process. It tends to only occur during days with high precipitation, and may continue for an additional day or two. The results of these calculations shed light on the temporal nature of net infiltration at Yucca Mountain. In the analyses, long-term mean net infiltration was calculated as the weighted mean net infiltration for ten representative precipitation years, each with its associated probability of occurrence. In general, low probability years experience higher net infiltration but contribute only a small percentage to the long term mean. Since the sum of the probabilities of occurrence equals one, and the years were selected from a set of 1,000, it was possible to estimate a "recurrence interval" for each of the representative years based on its probability. It was also possible to calculate the percent contribution to the long-term mean net infiltration of each representative year. It was found that, as years with larger recurrence intervals were included, a greater percentage of the long-term mean could be estimated. The results suggest that about 80% of the long-term mean for present-day climate conditions is due to years with a recurrence interval of 10 years and less. The implication of these results is that net infiltration estimates based on relatively short historical weather records may tend to underestimate long-term net infiltration; however, not by more than 20% (SNL 2008a,

Section 6.5.7.5). Tables 2.3.1-10 through 2.3.1-12 show the exceedance probability, the mean annual net infiltration, the recurrence interval, and the fraction of contribution to long-term mean net infiltration for each of the 10 representative years for each of the three climates, respectively.

The recurrence interval with the largest contribution to long-term mean annual net infiltration is 3.57 years for all three climates. The next largest contribution to long-term mean annual net infiltration is 10 years for the present-day and monsoon climates, and 2.17 years for the glacial-transition climate. Tables 2.3.1-10 through 2.3.1-12 also show that the contribution to mean annual net infiltration from extreme recurrence intervals is often less than the contribution from the shortest recurrence interval. For example, during the glacial-transition climate, the shortest recurrence interval of one year produces a larger contribution to mean annual net infiltration than the 33 year, 100 year, 333 year, and 1,000 year recurrence intervals.

The mean net infiltration for each representative year is not always higher for years with greater annual precipitation, as factors other than total annual precipitation influence the magnitude of net infiltration. For example, annual precipitation may be very high because of an especially high amount of precipitation occurring on a single day. In such a case, runoff would tend to be higher and net infiltration lower than if several days during the year experienced large amounts of precipitation, but the annual total was less (SNL 2008a, Section 6.5.7.5). This is the case for the present-day and monsoon climates shown in Tables 2.3.1-10 and 2.3.1-11, respectively, in which net infiltration is highest for the year with a recurrence interval of 333 years. For the monsoon climate (Table 2.3.1-11), net infiltration calculated for the 1,000 year recurrence interval is less than the net infiltration calculated for the 33 year recurrence interval as a result of intense rainfall and subsequent high runoff.

Factors Influencing Spatial Variability of Net Infiltration—The local spatial variability in net infiltration is controlled by (1) spatial variations in the amount of precipitation; (2) spatial heterogeneity in soil, bedrock, and vegetation properties; and (3) lateral water distribution via runoff processes. In the MASSIF model, precipitation is represented as a stochastic process and is varied spatially only as a function of elevation via a lapse rate. The characterization of spatial heterogeneities of soil and bedrock properties is accomplished by dividing the model domain into distinct soil groups, soil depth classes, and bedrock type regions inside which the given properties are assumed to be homogeneous (SNL 2008a, Section 6.5.7.6). The result of this approach is that the MASSIF model likely underestimates the actual spatial variability in net infiltration while characterizing regional infiltration patterns (SNL 2008a, Section 6.5.7.6). This approach of lumping properties into groups makes comparison between model predictions for a given grid cell and field data (i.e., borehole data) challenging at best (SNL 2008a, Section 6.5.7.6).

One significant conclusion of the MASSIF results is the fact that most of the modeled net infiltration occurs in the regions with shallow soils rather than in the stream channels (SNL 2008a, Section 6.5.7.8). It is notable that, during the 1997 expert elicitation panel on unsaturated zone flow model issues (CRWMS M&O 1997b, Section 3.4.1), several experts suggested that the upper reaches of washes having shallow alluvium perhaps should be considered to be the locations of higher infiltration than the ridge-tops. This suggestion, with the results of the model validation activities using streamflow data (Section 2.3.1.3.4.1) and borehole data from Pagany Wash (Section 2.3.1.3.4.2.1), led to an alternative model study using variations of soil saturated hydraulic conductivities (SNL 2008a, Section 7.1.3.2[a]).

While calculating runoff at monitored streamflow gauge sites (SNL 2008a, Section 7.1.3.2[a]), a variation scenario was simulated for the Pagany Wash watershed in which the soil conductivity of the dominant soil type representing stream channels (soil type 3) was increased by an order of magnitude while the conductivity of the other soil types was decreased by a constant factor. This scenario was investigated as a result of model comparison to borehole UZ#4 (SNL 2008a, Section 7.2.1.1.2[a]). In order to explore the implications of the Pagany Wash study on the larger modeled domain, the four representative realizations (10th, 30th, 50th, and 90th) from the present-day climate simulations were run using an alternate soil conductivity assignment, as defined by the Pagany Wash variation scenario. Specifically, the four realizations were run with the following modifications: (1) the conductivity of soil types 3 and 4 were set to 7×10^{-6} m/s; (2) the rock conductivities were set uniformly to 10^{-3} m/s; and (3) the conductivity of the soil types other than 3 and 4 were reduced by a factor of 0.44. Soil types 3 and 4 were selected because, in general, these soil types are associated with the main stream channels. The choice of the specific soil conductivities is based on Pagany Wash simulations and data from a single high precipitation year, and this choice is probably not representative of the rest of the domain. Nevertheless, these results illustrate aspects of model sensitivity that are not explored in the sensitivity studies that look at spatial averages of net infiltration.

To quantitatively summarize these comparisons, two tables are presented. Table 2.3.1-20 compares mean net infiltration over two domains (net infiltration model domain, the unsaturated zone model domain, and a repository footprint) for each realization. In addition, the runoff fraction is compared and the total weighted precipitation for each realization is listed. The tabulated results suggest that mean net infiltration over these regions, and the total runoff leaving the domain, are not significantly altered by this variation in soil conductivity. In addition, it is significant that the relatively unfractured nonwelded Paintbrush nonwelded hydrogeologic unit (PTn) is expected to dampen and homogenize downward-moving transient pulses arising from episodic surface infiltration events (SNL 2007, Section 6.1.2).

Table 2.3.1-21 compares the percent of the total net infiltration that occurs in each soil group. It is here that a significant difference can be seen from the original base-case results. In the base-case realizations, between 76% and 97% of the total net infiltration occurred in areas covered with soil types 5, 7, or 9. In the alternate soil conductivity (Variation) runs, this percentage range fell to 34% to 70%. The fraction of the total net infiltration in soil types 3 and 4 increased from a range of 0.2% to 11% to a range of 20% to 55%. The results of the alternative model study suggest that the predicted mean net infiltration over relatively large areas (e.g., unsaturated zone model domain and repository footprint) is fairly stable. It is the spatial distribution of net infiltration that is especially sensitive to the spatial distribution of soil properties. This alternative model study provides greater confidence in the spatial averaged net infiltration values produced by the infiltration model (SNL 2008a, Section 7.1.3.2[a]).

2.3.1.3.3.2   Consideration of Uncertainty in the Infiltration Model

The specific purpose of the infiltration model is to provide a spatial representation, including epistemic and aleatory uncertainty, of the predicted mean annual net infiltration at the Yucca Mountain site during each climate. For each climate, the model produces maps of average annual infiltration as a function of location, with no time dependence. These output maps cover the variability and range of uncertainty in average annual net infiltration over the modeling domain. The

uncertainty in net infiltration calculated by MASSIF is a combination of uncertainties associated with individual parameters and modeling assumptions.

Infiltration predictions are limited by the uncertainty in future weather patterns. Although a substantial body of literature supports the use of stochastic precipitation models, there are no records to support extrapolation of historical weather records from the last few decades to 1,000 years. Each available and relatively complete precipitation record, whether from the Yucca Mountain site, from a nearby weather station, or from a site representative of a future climate, covers no more than about 60 years. The methods used to represent future climate conditions for this model are described in Section 2.3.1.3.2.1.1. Precipitation inputs are selected from 1,000 year stochastic simulations, assuring that the full range of annual precipitation uncertainty is considered, including years with heavy precipitation (SNL 2008a, Section 1.1[a]).

Infiltration predictions are also limited by uncertainties in soil, bedrock, and vegetation properties that encompass the 125 km^2 infiltration modeling domain. These uncertainties arise primarily from several sources including: (1) the use of pedotransfer functions to estimate soil hydrologic properties; (2) the calculation of bedrock saturated hydraulic conductivity; and (3) the uncertainty in soil depth for the shallow depth class (SNL 2008a, Section 6.5.2[a]).

Infiltration predictions are also limited by model uncertainties. Sources of model uncertainty in this study include (1) the accuracy of the coupled NDVI/FAO-56 approach for estimating evapotranspiration at the site; (2) the accuracy of the layered field capacity approach for representing subsurface water flow; (3) the accuracy of the assumption that evapotranspiration from bedrock is negligible; and (4) the accuracy of the distributed runoff model used to represent surface water flow. Model uncertainty items (1) and (3) are believed to cause a bias towards over-predicting net infiltration, while items (2) and (4) are not believed to cause a bias in predicting net infiltration. The results of model validation activities suggest that model uncertainty may be of a comparable magnitude to parameter uncertainty. Given the complexity of modeling net infiltration over such a large and heterogeneous domain, such uncertainty is not unexpected (SNL 2008a, Section 6.6.3[a]).

The approach used to capture the parameter uncertainty was to perform an initial parameter uncertainty screening in order to eliminate parameters that do not have a large contribution to uncertainty in net infiltration. Sensitive parameters were then included in the Latin Hypercube sampling of two replicates of 20 samples (40 realizations per climate) for use in calculating the net infiltration maps. For each realization, a separate weather input file was generated, which used the sampled values of these parameters, representing epistemic uncertainty. In addition, each of these weather file realizations used a different set of random numbers, which resulted in differing patterns of precipitation and reflected aleatory uncertainty (SNL 2008a, Sections 6.6.3[a] and 6.7). Finally, in an effort to confirm that the parameter screening process and criteria did not inadvertently exclude a parameter that significantly influenced mean net infiltration, an extended parameter sensitivity study was performed (SNL 2008a, Section 7.1.4).

2.3.1.3.3.2.1   Infiltration Uncertainty Analysis Methodology

The first step in the uncertainty analysis was the elimination of parameters that did not have a large contribution to uncertainty in net infiltration. This step considered two properties associated with

each parameter, its relative uncertainty and its influence on the average net infiltration (SNL 2008a, Appendix I, Section I1).

In several places, the MASSIF model uses a formula that is an approximation for a function or relationship, such as air temperature change with elevation. The formulas used to approximate these types of functions (i.e., linear versus exponential) have inherent uncertainties. In this analysis, uncertainties in formulas of these approximations are considered to be small compared to uncertainties in other parameters. Therefore, the parameter uncertainty analysis does not vary any coefficients of function approximations.

2.3.1.3.3.2.2   Uncertainty in Infiltration Data and Parameters and Sensitivity of the Model Output to These Data and Parameters

The parameters that influenced net infiltration were screened for inclusion in the uncertainty analysis (SNL 2008a, Appendix I, Sections I1.2, I1.3, I1.4, and I1.5). Screening was based on both the relative uncertainty of a parameter, and its influence on the average net infiltration. Parameters were screened into the uncertainty analysis if their relative standard deviation was above 15% or if they were representative of a material property that covered more than 15% of the unsaturated zone domain. This 15% threshold for parameter inclusion in the uncertainty analysis was validated during the extended sensitivity analysis (SNL 2008a, Section 7.1.4). Parameter uncertainty was propagated to net infiltration by way of a Monte Carlo analysis using Latin Hypercube sampling (SNL 2008a, Sections 6.5.5 and 6.5.6). The infiltration range of net infiltration was demonstrated to reasonably bound the estimates of net infiltration in a manner to preclude under-representation of the risk estimate (SNL 2008a, Section 8.3[a]).

Parameters were separated into two categories: those which were climate-independent, and those which varied (either in the nominal value or in the uncertainty range) by climate. Of the over 90 climate-independent parameters, 8 met the requirement for inclusion in the detailed uncertainty analysis (SNL 2008a, Appendix I):

- Soil characteristics, including the soil depth of the shallowest soil class (class 4), saturated hydraulic conductivities, K_{sat_rock}, of the most common bedrock units (units 405 and 406), and the soil water holding capacity, θ_{HC}, for the most common grouped soil unit (soil group 5/7/9)

- Evapotranspiration parameters, including the readily evaporable water (REW) and the evaporation layer depth (Z_e)

- Vegetation parameters, including the minimum crop coefficient for dry soil with no crop cover (K_{cmin}) and the slope of the relationship between the corrected normalized difference vegetation index and the basal crop coefficient (CK_{cb2}).

Approximately 30 other climate dependent parameters were screened for each climate state. For the present-day climate, four additional parameters were screened into the uncertainty analysis (SNL 2008a, Appendix I). These included two plant parameters (the mean plant height and the maximum effective rooting depth), and one of the annual average precipitation weather parameters, a_m. Another weather parameter, a_λ, was not varied independently, but rather was correlated with a_m. It

was included in the uncertainty analysis so that its value would remain consistent with the value of a_m. Therefore, a total of 11 parameters were screened into the uncertainty analysis for the present-day climate. These 11 parameters, ranges, and distribution types are shown in Table 2.3.1-22.

A total of 19 parameters were screened into the uncertainty analysis for the monsoon climate (SNL 2008a, Appendix I). These included two plant parameters (the mean plant height and the maximum effective rooting depth), the slope of precipitation duration versus amount of precipitation, and eight weather parameters. Four of the weather parameters (annual average precipitation values a_{00} and a_m, amplitude b_{m1}, and temperature parameter γwet_{max}) were varied independently. The remaining four weather parameters (a remaining average annual precipitation parameter, a_λ and the three remaining amplitude parameters, $b_{\lambda,1}$, $b_{00,1}$, $b_{10,1}$) were not varied independently, but rather were correlated with a_m and b_{m1}. These 19 parameters, ranges, and distribution types are shown in Table 2.3.1-23.

A total of 17 parameters were screened into the uncertainty analysis for the glacial-transition climate (SNL 2008a, Appendix I). Eight of these were the climate-independent parameters. The climate dependent parameters varied included two plant parameters (the mean plant height and the maximum effective rooting depth), both parameters of the precipitation duration model (only one was varied independently), and five weather parameters. Three of the weather parameters were varied independently (two of the annual precipitation parameters, a_{00} and a_m, and one of the phase parameters, $\theta_{\lambda,1}$). The other two weather parameters were the annual precipitation parameter a and a phase parameter $\theta_{m,1}$. These 17 parameters, ranges, and distribution types are shown in Table 2.3.1-24.

The uncertainty analyses were conducted to determine the influence of various parameters over their expected ranges, which include uncertainty. These analyses were developed in *Simulation of Net Infiltration for Present-Day and Potential Future Climates* (SNL 2008a, Section 6.7). The results of these analyses were the generation of 40 maps of net infiltration for each of the present day and two future climate states considered for the next 10,000 years. For a given climate, each of these 40 maps provided an equally probable outcome of net infiltration over the modeling domain. The range of net infiltration values within the set of 40 maps provided a reasonable estimate of the uncertainty in magnitude of net infiltration. This uncertainty was estimated using the structured Monte Carlo technique of Latin Hypercube sampling (SNL 2008a, Sections 6.5.5 and 6.5.6). This method propagates uncertainty in a collection of input parameters to uncertainty in model outputs (net infiltration).

For all climates, the sensitivity analyses show that there are two general features that control the uncertainty in the average annual net infiltration over the modeling domain. These features are the mean annual precipitation and the soil depth assigned to soil depth class 4. These two features explain about 70% of the variance in simulated infiltration when both epistemic and aleatory uncertainty is included. Mean annual precipitation is not sampled directly but is the result of a stochastic simulation of representative precipitation years that relies on a set of sampled stochastic parameters, which is different for each climate (SNL 2008a, Section 6.7.2).

The sensitivity of the uncertain parameter varied in the uncertainty analyses showed that soil depth in soil depth class 4 (shallow soils) and water holding capacity of soil group 5/7/9 (the most common

soil group) were the most important physical parameters in the MASSIF model. Future precipitation patterns was another significant source of uncertainty. It was determined that, while further data are not needed to develop sufficiently accurate estimates of infiltration for the purposes of the TSPA, such data would serve to reduce the uncertainty in predicted infiltration ranges (SNL 2008a, Section 8.3[a]).

An extended sensitivity study was conducted using 42 uncertain parameters. A list of these parameters, ranges, and distribution types is shown in Table 2.3.1-25. A total of 200 realizations were run for the Drill Hole Wash watershed, which covers most of the repository footprint, using a single present-day weather input file. The results of the extended parameter sensitivity study confirm that the initial parameter screening criteria used for the uncertainty analysis are valid. Approximately 80% of the variance in mean net infiltration in the set of 200 realizations can be accounted for by the uncertainty in the same two input parameters that describe most of the variability in the uncertainty analysis results (soil depth of soil depth class 4 and Holding Capacity of Soil Group 5/7/9). The other parameters explain less than 3% of each variance, and are therefore not considered to be as important for estimating mean net infiltration. It is worth noting that several of these other parameters were not screened into the initial uncertainty analysis; however, none of these other parameters account for more than 3% of the variance in net infiltration (SNL 2008a, Section 7.1.4).

2.3.1.3.4 Confidence Building and Abstraction of the Infiltration Model
[NUREG-1804, Section 2.2.1.3.5.3: AC 1(2), (3), AC 4(1), AC 5]

Confidence in the infiltration model was established by performing a number of confidence building activities during model development and performing post model development validation activities. Confidence building during model development included discussions of documented decisions and activities that were implemented during the model development process to verify that a reasonable, credible, and technical approach using scientific and engineering principles was taken. These activities also demonstrate that MASSIF can be applied to other sites to accurately predict water balance parameters such as evapotranspiration. Post-model validation activities included comparing the infiltration model and results to alternative modeling approaches and to other estimates of infiltration at Yucca Mountain, elsewhere in Nevada, and the desert southwest. The model development activities and post-development validation activities established the scientific bases for the infiltration model. Based on these confidence building activities, the infiltration model is considered to be sufficiently accurate, to the level of confidence required by the model's relative importance to performance assessment, and adequate for its intended purpose.

2.3.1.3.4.1 Confidence Building During Model Development

Confidence building for each of the primary components in the infiltration model (SNL 2008a, Section 7.1, Figure 7.1-1) was completed during model development. The following sections describe the validation activities performed to validate each of the primary components within the "control volume" of a grid cell in the infiltration model (Figure 2.3.1-39).

Precipitation (SNL 2008a, Section 7.1.1)—Several analyses were completed to build confidence in the stochastic precipitation model, including review of truncating the Fourier series to a single harmonic and comparison of generated mean annual precipitation ranges for the various climates

to measured data. The stochastic model used a truncated Fourier series (one-harmonic) to generate precipitation data. Data from this model were compared to a model using a two-harmonic truncated Fourier series (SNL 2008a, Section 7.1.1.1[a]). Adding another term to the Fourier series will always give a better fit, as this additional term accounts for the residual between the Fourier series and the actual data. For half of the selected sites, precipitation records show a two-seasons variation over the year (on average), and a one-harmonic truncated Fourier series fits the data well. The second harmonic correction provides significant improvement when the selected site presents distinct four-season variations or a strong gradient of differences for a period. However, for these cases it is not clear if the one harmonic fit will result in an underestimation or an overestimation of infiltration because the average annual precipitation is preserved, and only the monthly distribution is affected. The two-harmonic truncated Fourier series model required eight additional parameters. For simplicity, it was decided to limit the representation of daily precipitation over the year with a 2nd order Fourier series (the average and one harmonic). The estimate reasonably represents the variation of daily precipitation over the year. The cost of adding a second harmonic was deemed to be too high in complexity compared to the gain in accuracy, and thus was not used for this analysis.

An estimate of distribution of mean annual precipitation after aggregation of Fourier series parameters was also completed (SNL 2008a, Section 7.1.1.2). Annual precipitation at Yucca Mountain for future climates is an uncertain quantity. In order to represent the possible future precipitation at the site, several representative sites were selected for each climate. Each site had a different average annual precipitation record, representing the uncertainty. In order to capture this uncertainty, each site was first represented using 12 parameters. The variation of each parameter was studied in order to determine whether this variation was significant (and should be taken into account) or not. Significant parameters were associated with a distribution and were sampled from this distribution using Latin Hypercube sampling.

Two independent samples containing 20 replicates were created and used to estimate average annual precipitation. In order to verify that the distribution of average annual precipitation defined with the representative sites was captured correctly, they were compared with the distribution of average annual precipitation derived from these sites' records. Comparisons of actual and modeled precipitation distributions are illustrated using box-plots (Figures 2.3.1-40 through 2.3.1-42). A box-plot is comprised of a box where the top and bottom of the box represent the 75th and 25th percentile of the distribution, respectively. The dashed and solid lines within the box represent the mean and median values of the distribution, respectively. The top and bottom ends of the lines connecting the box (whiskers) represent the 90th and 10th percentile of the distribution, respectively. And the points above and below the whiskers represent the extreme observations within the distribution (SNL 2008a, Section 7.1.1.2).

The analysis found that after normalizing (for elevation) the precipitation from the 10 present-day Yucca Mountain meteorologic stations, the simulated and measured data were very closely matched (Figure 2.3.1-40). The last three boxes in Figure 2.3.1-40 are similar enough to have good confidence that annual precipitation is correctly represented for the present-day climate. Mean, median, as well as 10th, and 90th percentile values are almost identical for all three boxes (SNL 2008a, Section 7.1.1.3). Comparison of the predicted versus measured data for the monsoon climate state was reasonable, with about 75% of the measured data being within the range defined by the lower and upper bound of the monsoon climate representation (SNL 2008a, Section 7.1.1.4).

The monsoon climate data includes the ten present-day climate sites as lower bounds, and two sites (Hobbs, New Mexico, and Nogales, Arizona) as upper bounds for annual precipitation representation. The two upper-bound sites are considered to be representative of the weather at the top of Yucca Mountain and therefore, do not need to be adjusted for elevation. Even though their average annual precipitation is similar, the two upper-bound monsoon analogue sites have different behavior over the year. Hobbs features a longer but less intense monsoonal period, while Nogales presents a shorter (2 months) but more intense monsoonal period. The Hobbs and Nogales sites may underestimate annual precipitation for a monsoon climate identical to that of Owens Lake (used as reference) (BSC 2004a), so it was decided to consider the combination of parameters from Hobbs and Nogales giving the highest annual precipitation (a longer and more intense monsoonal period). This combination of parameters results in average annual precipitation that is generally between the upper and lower bound analogue site precipitation. However, this combination of parameters also results in some average annual precipitation amounts that are higher than either of the two upper-bound sites (Figure 2.3.1-41) (SNL 2008a, Section 7.1.1.4).

The glacial transition climate data includes only two sites for lower-bound and three sites for upper-bound precipitation representations (Figure 2.3.1-42). Both sites are considered to be representative of future weather at the top of Yucca Mountain, and therefore do not need to be adjusted for elevation. Distributions of mean annual precipitation based on the estimation of parameter uncertainty, cover most of the range defined by the five bounding sites. The average value for both replicates is almost identical, and is close to the mid-point value of the average of the two low-bound sites annual precipitation and the three upper-bound sites annual precipitation (Figure 2.3.1-42). Therefore, this model provides a reasonable representation of uncertainty in annual precipitation for the glacial transition climate (SNL 2008a, Section 7.1.1.5).

Evapotranspiration and Storage (SNL 2008a, Section 7.1.2)—The ability of the MASSIF model to simulate daily actual evapotranspiration and changes in daily soil water storage was evaluated by comparing MASSIF output to long-term observation data collected at lysimeter facilities at the Nevada Test Site (Desotell et al. 2006) and at the Reynolds Creek Experimental Watershed (Marks 2001). These lysimeter sites provide detailed water balance data that are especially valuable for evaluating model performance. The first lysimeter site is located near the Area 5 Radioactive Waste Management Site within the Nevada Test Site, and represents an analogue to the present-day climate conditions at the Yucca Mountain. The second site is located within the Reynolds Creek Experimental Watershed in southwestern Idaho, and represents a potential analogue to the future glacial-transition climate at Yucca Mountain. The climate at the Reynolds Creek Experimental Watershed is actually wetter and cooler than at Spokane, which is an analogue site for the upper limit of the glacial-transition conditions. Reynolds Creek Experimental Watershed was selected for this comparison because it represents significantly different conditions in terms of climate, soils, and vegetation from those at Yucca Mountain. In both cases two modeling approaches were used. First, MASSIF was used to simulate the mass of water in each lysimeter as a function of time. Second, a Richards equation–based model (HYDRUS-1D) was also applied to the same lysimeter data to provide a comparison to the MASSIF formulation.

The ability of MASSIF to simulate these data records provides additional model validation to establish confidence that the MASSIF mathematical model and its underlying conceptual model adequately represent with sufficient accuracy the phenomenon and processes in question.

Validation includes corroboration of model results with data acquired from two analogue sites, and corroboration of model results with other model results obtained from the implementation of mathematical models using the HYDRUS 1D code. A comparison of MASSIF and HYDRUS-1D simulations and lysimeter storage data from the NTS and Idaho lysimeters is shown in Figures 2.3.1-43 and 2.3.1-44, respectively. These comparisons indicate that MASSIF simulations compare well to both the soil physics based model HYDRUS-1D simulations, and to these lysimeter data sets (SNL 2008a, Section 7.1.2, Appendix J).

The simulations of the lysimeter data from Area 5 on the Nevada Test Site are summarized as follows:

- The simplified water balance approach incorporated in MASSIF allows for adequate simulation of water storage and evapotranspiration in both bare soil and vegetated Nevada Test Site lysimeters.

- The evapotranspiration parameters such as K_{cb}, K_{c_min}, and f_c estimated for the bare soil and vegetated lysimeters using MASSIF are in good agreement with the experimental data obtained for the plant association similar to the one present at the lysimeter site.

- The MASSIF results are comparable to the results obtained with physics-based models such as UNSAT–H (Desotell et al. 2006).

- MASSIF's ability to reproduce the lysimeter water storage over 10 years (bare soil) and 9 years (vegetated) confirms that the most important processes are represented correctly.

- The same tendencies in the differences between the observed and calculated storages were obtained with MASSIF. These tendencies are consistent with the ones described in the other studies related to the Nevada Test Site lysimeters (e.g., Desotell et al. 2006). These differences may indicate evaporation at depth in the lysimeters that is a phenomenon of the lysimeter but not of the natural conditions (SNL 2008a, Section 7.1.2.1[a]).

Lysimeter simulations at the Reynolds Creek Experimental Watershed are summarized as follows:

- The MASSIF water balance approach was capable of reproducing the changes in storage over the seven years of observations at the Reynolds Creek Experimental Watershed lysimeter site. This site is considerably different from the Nevada Test Site. The climate is wetter and cooler, with 21% of precipitation being snow, and the soils are finer with the smaller permeability and significantly higher field capacity and wilting point. The vegetation cover is twice as dense, and the plants species are different.

- The soil properties, evapotranspiration parameters, and infiltration estimated using MASSIF for the Reynolds Creek Experimental Watershed lysimeter fall within the site specific ranges obtained from the literature.

- The MASSIF and HYDRUS 1D results are fairly consistent. The same tendencies in differences between the observed and calculated storages were obtained with MASSIF and HYDRUS 1D.

- The infiltration predicted by MASSIF is in good agreement with the infiltration predicted by HYDRUS 1D.

- The MASSIF ability to adequately model Reynolds Creek Experimental Watershed lysimeter site confirms that the physical processes incorporated in MASSIF are applicable to a wide range of condition. Both present-day and future climates can be thus accurately represented (SNL 2008a, Section 7.1.2.2[a]).

Run-on/Runoff (SNL 2008a, Section 7.1.3)—The hydrologic processes of run-on and runoff are validated in the MASSIF model by comparison of measured streamflow data with MASSIF predictions of runoff (streamflow) at the discharge cells at the base of streamflow watersheds. Streamflow watersheds are sub-watersheds located within the primary 11 watersheds that encompass the Yucca Mountain infiltration model domain. A streamflow watershed is defined by the location of its streamflow gauge. That is, a streamflow watershed includes all the upstream cells that can contribute runoff that eventually flows through a given streamflow gauge. Streamflow and runoff are terms that are often used interchangeably. However, for this discussion, streamflow refers to the total amount of runoff within a streamflow watershed, while runoff can refer to total streamflow, or just the amount of runoff from one cell to another. Additional confidence building during model development is provided in this section by comparing streamflow data from the rare occasions during which streamflow has been recorded within the Yucca Mountain model domain, with MASSIF predictions of streamflow for those same streamflow events.

There are six streamflow gauges located within the Yucca Mountain infiltration model domain used in this analysis. These six gauges are part of the U.S. Geological Survey streamflow monitoring network (SNL 2008a, Section 7.1.3, Table 7.1.3-1). The Yucca Mountain infiltration model domain encompasses two Pagany Wash gauges, one Drill Hole Wash gauge, one Wren Wash gauge, and two Split Wash gauges. Figure 2.3.1-45 provides a map view of locations of watersheds and various field data, including streamflow gauges.

MASSIF calculations were performed for each of the watersheds for which runoff data was collected. Qualified runoff data exist for all of the streamflow gauges for water year 1995, and for some of the streamflow gauges for water years 1994 and 1998. All of the calculations were started at the beginning of water year 1994, and carried through to either water year 1995 or 1998, depending upon the existence of 1998 data for the particular watershed.

With the exception of soil saturated conductivity, all of the input values were nominal values, which are reported in *Simulation of Net Infiltration for Present-Day and Potential Future Climates* (SNL 2008a, Appendix I). Soil conductivities were varied by a single multiplicative factor between 0.1 and 1.2 in increments of 0.1. Hence, the first run multiplied all of the soil conductivities by 0.1; the next run multiplied all soil conductivities by 0.2, and so on. Weather data for the simulations were taken from qualified records for Yucca Mountain sites 1, 2, 3, and 6. Separate calculations were performed for each of the weather sets, and the results from the four calculations were compared.

While cumulative annual runoff is important, examination of the daily occurrence and the amount of runoff is also important. Comparisons were made to the runoff data using daily precipitation data from the four nearby Yucca Mountain rainfall measurement locations (Site 1, Site 2, Site 3, and Site 6). In general, MASSIF correctly predicted the timing and magnitude of runoff using the nominal parameter set with variations in the soil conductivity. Typically, the soil conductivities are reduced by multipliers of 0.3 to 0.7, which is within the range between the maximum and minimum soil conductivities for a given soil type from the Hanford soils data set (BSC 2006a, Table 6-7). Alternatively, the conductivity reduction could be explained by soil structure, which can dominate water sorption in soils. A comparison of measured versus modeled runoff is shown in Figure 2.3.1-46 for Upper Split Wash for a portion of water year 1995. In this figure, the high and low predicted runoff values correspond to soil conductivity multipliers of 0.2 and 0.4, respectively, for Sites 1 and 2. The high and low predicted values correspond to soil conductivity multipliers of 0.4 and 0.6, respectively, for Sites 3 and 6. Additional detail is provided in *Simulation of Net Infiltration for Present-Day and Potential Future Climates* (SNL 2008a, Section 7.1.3).

MASSIF was used to predict infiltration at a particular grid cell concurrent with measured data (the UZ#4 borehole (LeCain et al. 2002) near the mouth of Lower Pagany Wash). To match the measured infiltration, the soil saturated conductivity had to be increased by an order of magnitude, and the rock conductivity was increased so that it had no influence on the infiltration (Section 2.3.1.3.4.2.1). Hofmann et al. (2000) measured the saturated hydraulic conductivity of the soil at two Yucca Mountain locations. These locations included a measurement in Pagany Wash (near borehole UE-25 UZN #14) and a measurement on a stable terrace adjacent to Fortymile Wash (at borehole UE-25 UZN #85). They found that the saturated hydraulic conductivities were significantly higher than the nominal soil conductivity used in MASSIF, and that the value in Pagany Wash was an order of magnitude higher than the value on the stable terrace.

To test if this perturbation was consistent with the Pagany Wash streamflow gauge data, a variation scenario of the Pagany Wash calculations was performed by setting the soil and rock conductivities to those which matched the UZ#4 borehole data. The balance of the soil conductivities were varied, as before, using a soil saturated conductivity factor. The rest of the input parameters were set to their nominal values as in the base case scenario described above. Both sets of soil saturated conductivities were consistent with the measured runoff data for Pagany Wash (SNL 2008a, Section 7.1.3).

Despite the good agreement between the observed and predicted runoff in both of these scenarios, there was a pronounced difference in the spatial distribution of net infiltration for each of these scenarios—even though the mean value of net infiltration was nearly identical between scenarios. The main difference between the scenarios was the location of the net infiltration. In the base case scenario, net infiltration occurred primarily outside the central stream channel area and was highest in the higher portions of the watershed. In fact, there is little to no net infiltration in the upper reach of the channel, and only a minor amount of infiltration in the lower reach. In the variation scenario, the net infiltration in the upper part of the basin was slightly reduced while the infiltration in the lower reach of the channel increased greatly (SNL 2008a, Section 7.1.3.1).

This comparison between the base case and variation simulations of Pagany Wash illustrates an important point about the inherent uncertainty in the spatial distribution of net infiltration. Uniform effective soil conductivity values were not screened into the uncertainty analysis because the

parameter uncertainty was either low or the fraction of the unsaturated zone model domain that was covered by a given soil type was below the 15% criterion (SNL 2008a, Section 7.1.3). Soil conductivity was included in an extended parameter sensitivity study (SNL 2008a, Section 7.1.4). In order to account for the need to adjust soil conductivity to match observed runoff data as described in this section, the uncertainty distributions for soil conductivity were expanded. However, results of the expanded sensitivity study indicate that MASSIF results are not particularly sensitive to soil conductivity. This comparison suggests that there may be considerably more uncertainty as to where net infiltration is occurring than is represented by the 40 realizations used to characterize infiltration uncertainty (SNL 2008a, Section 7.1.3.1). However, it is important to note that the relatively unfractured nonwelded Paintbrush nonwelded hydrogeologic unit (PTn) is expected to dampen and homogenize downward-moving transient pulses arising from episodic surface infiltration events (SNL 2007, Section 6.1.2).

2.3.1.3.4.2   Post-Model Development Validation

The post-development validation methods used to validate the infiltration model include (1) corroboration of model results with data (e.g., field data, analogue studies) not previously used to develop or calibrate the model; and (2) corroboration of model results with other alternative mathematical model results.

2.3.1.3.4.2.1   Corroboration of Model Results with Data

Comparison of Model Predictions with Pagany Wash Infiltration Data from 1998 (SNL 2008a, Section 7.2.1.1—MASSIF was used to simulate infiltration at a monitor cell that contains the location of borehole UE-25 UZ #4 (also referred to as UZ #4). This is an instrumented borehole in Pagany Wash. The winter of 1997–1998 was an El Niño winter and therefore was considerably wetter than average winters. The total precipitation recorded at Site 3 for water year 1998 was 402.6 mm. In the spring of 1998, 183.4 mm of precipitation was recorded during 14 out of 23 days between February 2 and 24, and approximately 35,000 m^3 of runoff was recorded at the lower Pagany Wash streamflow gauge during this 23 day period in February 1998. LeCain et al. (2002) describe infiltration data collected at this borehole during the spring of 1998. Borehole UZ #4 is located in the alluvial deposits of Pagany Wash; a stream-carved, dry channel. This borehole was instrumented with temperature, pressure, and water potential sensors in July 1995, in order to gain insight into infiltration through the alluvial deposits of the usually dry stream channels (LeCain et al. 2002).

LeCain et al. (2002) describe two methods for estimating infiltration in Pagany Wash based on data collected at UZ #4. The first is an analytical method in which the infiltration flux is calculated from soil saturated conductivity, porosity, and velocity of a wetting front observed to pass from a depth of 3.0 m to 6.1 m. The second method uses a computer program to estimate infiltration flux given temperature data measured in UZ #4. The first method produced a percolation flux of 1.13 m, while the second method produced a percolation flux of 1 to 2 m.

First, MASSIF was used with nominal input values to simulate infiltration at the monitor cell containing borehole UZ#4. Infiltration for water year 1998 at UZ #4 was calculated to be 11.8 mm using precipitation data from the Site 6 station, and 28.3 mm using precipitation data from the Site 3 station. Second, soil and rock hydraulic conductivities (K_{sat}) for the grid cell containing borehole

UZ #4 were adjusted to test the sensitivity of infiltration to K_{sat}, and to demonstrate that modeled infiltration can match the measured infiltration reported by LeCain et al. (2002) with adjustments to K_{sat} values. Soil K_{sat} was increased by about one order of magnitude to a value of 7×10^{-6} m/s, and rock K_{sat} was increased to a value of 10^{-3} m/s so that it would not be a limiting factor on infiltration. The analytical method used by LeCain et al. (2002) to calculate infiltration flux from 3.0 to 6.1 m does not include rock hydraulic conductivity, so rock hydraulic conductivity should not be a limiting factor for a comparison with MASSIF. MASSIF calculated a total net infiltration for water year 1998 at the grid cell containing UZ #4 of 414 mm and 375 mm for Site 3 and Site 6 stations, respectively. When soil K_{sat} values were increased to 1×10^{-5} m/s, infiltration increased to 597 mm and 548 mm, for Site 3 and Site 6, respectively.

In the analytical method described by LeCain et al. (2002), if the value of soil porosity is changed from 0.31 to 0.157 m^3/m^3, which is the porosity assigned to the soil type in this grid cell, then the percolation flux would change from 1,130 mm to 573 mm. This is very close to the net infiltration flux calculated by MASSIF when soil and rock K_{sat} values are adjusted.

This comparison of percolation flux between MASSIF and an analytical method reported in (LeCain et al. 2002) shows that MASSIF calculated approximately the same amount of infiltration at UZ #4, if soil K_{sat} for that grid cell is increased by ~1.5 orders of magnitude, and if rock hydraulic conductivity for that grid cell is increased so that it is not a limiting factor. Although this increase in soil K_{sat} is outside of the standard error range in soil K_{sat} for soil type 3 (K_{sat} range = 9.5×10^{-7} to 6.2×10^{-7} m/s) (BSC 2006a, Table 6-7), it is within the range of maximum and minimum values (1.7×10^{-7} to 1.7×10^{-5} m/s), and this adjusted soil K_{sat} may be more appropriate for the soil near the grid cell containing UZ #4 on Yucca Mountain. In addition, these K_{sat} adjustments are consistent with the discussion on factors influencing spatial variability near the end of Section 2.3.1.3.3.1.2. The soil K_{sat} values reported in BSC (2006a) have transparency and traceability to Yucca Mountain textural data using pedotransfer functions, so they are appropriate and defensible for large-scale assessments of infiltration at Yucca Mountain. However, they are likely to be inaccurate for comparison to borehole-scale infiltration estimates, as shown in this validation calculation.

Hofmann et al. (2000) report measurements of soil saturated hydraulic conductivity at two locations at Yucca Mountain. These locations included a measurement in Pagany Wash, near borehole UE-25 UZN #14, and a measurement on a stable terrace adjacent to Fortymile Wash at borehole UE-25 UZN #85, both using a prototype-automated-infiltrometer. They measured a saturated hydraulic conductivity of 17.79 cm/hr (4.94×10^{-5} m/s) for the location in Pagany Wash and 1.78 cm/hr (4.94×10^{-6} m/s) for the terrace location (Hofmann et al., 2000, Table 4). The measurement in Pagany Wash corroborates the adjustments to soil conductivity that are required to match infiltration inferred at UZ #4 (SNL 2008a, Section 7.2.1.1.2[a]).

Discussion of Neutron Logging Data—Neutron logging data can be used in some cases for infiltration model validation and/or corroboration by comparing model-calculated volumetric water contents and/or infiltration fluxes to those obtained from neutron logging data. Available site neutron logging data are not adequate for validation or corroboration of MASSIF. The following discussion describes the dataset and provides limited comparisons between measured and modeled infiltration.

Neutron logging data were collected from mid-1989 through September 1995 at 99 boreholes; 95 of the 99 boreholes are located within the current infiltration model domain. All 95 boreholes are located within four watersheds; one borehole is located within Yucca Wash while the remaining 94 boreholes are located within Drill Hole Wash, Dune Wash, or Solitario Canyon 1 watersheds. The borehole depths range from 4.6 to 77.8 m (Flint and Flint 1995).

An uncertainty analysis of this dataset concluded that water content values from the neutron logging are accurate to approximately ±6% absolute water content within a 95% confidence interval (BSC 2006d, Section 5.3.2). Given a typical water content value of 20%, this uncertainty translates to a 30% relative error in the measured value. However, the precision of the measurement is higher (less than 2% relative difference), which suggests that estimates of changes in water content are more certain. This increased certainty is limited by the fact that precision errors associated with each log are additive when considering changes in water content over time.

This dataset was deemed to be of limited use for validation (or calibration) of MASSIF for several reasons. First, errors associated with water content derived from these measurements make direct comparison with simulated water contents problematic, especially since conditions at each borehole (such as soil depth and properties) are likely to differ from the average values assigned to the soil depth class and soil group assigned to the cell. Second, the field capacity modeling approach is a "lumped" approach, and is therefore not intended to be used to match moisture profiles with depth in the soil. Third, flux estimates using the change in water content over an interval require an estimate of the root-zone depth, which is likely to vary for each location. Despite these limitations, fluxes were estimated assuming a constant root-zone depth and compared with net infiltration calculated over the same time interval (see below). The following comparisons between measured and modeled infiltration provides justification for its exclusion from model validation.

Neutron logging measures the number of reflected (thermalized) neutrons at depth intervals in a region surrounding a borehole. The count of neutrons is also affected by the integrated properties of the material (density, mineral composition, etc.), and in relatively homogeneous materials has successfully been used to estimate water content. Several researchers have estimated net infiltration fluxes from neutron logging data collected at time intervals during which water content profiles were changing (e.g., Looney and Falta 2000, pp. 457 to 474; McElroy 1993, p. 13). However, many assumptions are required in order to estimate net infiltration flux from these measurements. Net infiltration flux can be estimated from the change in water content, with time, multiplied by a given depth interval, and then summing these changes, for depths below the root zone (Looney and Falta 2000, pp. 457 to 474; McElroy 1993, p. 13). Net infiltration flux can also be calculated as the change in integrated water content below the root zone, between two time periods. This method was implemented using MASSIF for the time period spanning the greatest increase in borehole water content between about January 1 and mid-March 1995. The root zone was assumed to be 1.6 m below the ground surface for soil depths of 1.6 m or greater, and the root zone was set equivalent to soil depth for soil depths less than 1.6 m.

The use of these methods for calculating flux within fractured rock from water content data has not been widely used, and limitations in the approach, as well as limitations within the dataset, should be acknowledged. For example, this approach assumes 1-D piston flow with no lateral flow at the soil–bedrock interface. The MASSIF model assumes that lateral flow is insignificant for estimating a water balance for a 30×30 m grid cell. However, this assumption may not be appropriate for

measurements occurring on the scale of a borehole, since the active fracture spacing in the bedrock is likely to be greater than the region measured by the neutron probe. In addition, single calibrations, independent of media, were developed for each neutron probe (BSC 2006d, Section 5.3.4), and were applied to all the neutron measurements made in various media (e.g., soil, weathered tuff near the soil-bedrock interface, or intact tuff). Since calibrations provide the means of interpreting water contents, the consequence of using a single calibration for different media is that there may be systematic errors in water contents for media not used in the calibration. In addition, as a result of the drilling methods, preferential pathways for water flow along the annulus space between the borehole casing and the geologic media may have been inadvertently created, and formerly solid rock may have been extensively fractured. Such fracturing would lead to erroneously high infiltration calculations using the neutron logging data.

Despite the limitations of the dataset and the assumptions inherent in calculating net infiltration from changes in water content, this 6-year dataset represents the only Yucca Mountain site-specific dataset that measured wetting front movement, depths of net infiltration—and indirectly—net infiltration flux, over a large area of the infiltration model area and over a period with wet years and dry years. Therefore, it is worthwhile to compare MASSIF predictions of net infiltration at the grid cells containing the neutron logging boreholes, with the net infiltration calculated from neutron logging data. Figure 2.3.1-47 (SNL 2008a, Section 7.2.1.1, Figure 7.2.1.1-2[a]) shows such a comparison for a period of net infiltration spanning the wet winter of 1995, using three precipitation stations with MASSIF. As the figure shows, the comparison is not good. Even the averaged net infiltration for all boreholes was not good (71 mm for MASSIF using Site 6 precipitation versus 200 mm from neutron logging data). This figure is included to demonstrate that the neutron logging data is not reliable for calculating net infiltration flux due to the preferential pathways through bedrock induced during drilling. This conclusion is supported by the lack of any corroborating data to support the high net infiltration fluxes at the neutron logging boreholes. In fact, all other types of data and analyses used to quantify net infiltration at Yucca Mountain are generally lower than the mean net infiltration calculated using MASSIF for present-day climate, and the MASSIF results are a factor of 3 lower than flux calculated from neutron logging data (for the time period discussed above) (SNL 2008a, Section 7.2.1.1.3[a]).

2.3.1.3.4.2.2   Comparison of Model Results with Other Models and Data from Comparable Environments

MASSIF results for present-day, monsoon, and glacial-transition climate states were compared to net infiltration and/or recharge estimates from other models and data from comparable environments (SNL 2008a, Section 7.2.1.2[a]). For these comparisons, net infiltration and recharge are assumed to be equivalent. These environments include other locations in Nevada, other locations in the southwestern United States, and other locations in the western United States. Estimates from locations in the southwestern U.S. are approximately analogous to the predicted recharge expected for the monsoon climate, based on the selection of analogue climate sites (BSC 2004a, Table 6-1). Estimates from locations in the western states are approximately analogous to the predicted recharge expected for the glacial-transition climate, based on the selection of analogue climate sites (BSC 2004a, Table 6-1). Recharge and net infiltration estimates for the Hanford site were also reviewed, although this site is quite dry and more analogous to Yucca Mountain under the present-day climate than the glacial-transition climate.

Comparison to Other Models—MASSIF results for present-day, monsoon, and glacial-transition climate states were compared to several published models of net infiltration and/or recharge versus precipitation, and are shown in Figure 2.3.1-48 (SNL 2008a, Section 7.2.1.2[a], Figure 7.2.1.2-1[a]). The publication dates of these models span nearly 60 years. Figure 2.3.1-48 demonstrates the similarity of these models, despite the advances made in hydrologic sciences over this time. The step function of the Maxey-Eakin model (Maxey and Eakin 1950, p. 40) is shown primarily for its historical significance as a well-recognized recharge model. Two modified Maxey-Eakin models (Nichols 2000, page C35; DOE 1997, Table 7-6), and a Maxey-Eakin model fit developed by Wilson and Guan (2004, Equation 12) are also shown in this figure. Figure 2.3.1-48 also shows MASSIF results compared to a model developed by Maurer and Berger (1997, Equation 9) for west-central Nevada. The Maurer and Berger model predicts water yield based on precipitation in which water yield is defined as subsurface flow plus surface runoff, so it is not directly comparable to other models, but it is included for comparison purposes nonetheless. Figure 2.3.1-48 also shows MASSIF results compared to a recent model developed by Faybishenko (2007, Equation 16) for Yucca Mountain using analogue meteorological data, and a fit to a dataset referred to as Davisson and Rose (Faybishenko 2007, Figure 10). MASSIF results for three climate states are above the general trend of most of these models at precipitation values less than 300 mm/yr, and approximately along the general trend of these models at precipitation values above 300 mm/yr.

A recent report by the Center for Nuclear Waste Regulatory Analyses staff describes models that were developed and used to calculate the areal average net infiltration, temporally averaged over the next one million years (Stothoff and Walter 2007). They also used these models to calculate areal average net infiltration, temporally averaged to represent the present-day climate. The areal averages are calculated for a 13 km² footprint box that overlaps the 5.7 km² repository footprint. Therefore, comparisons of the Center's net infiltration results are not exactly comparable with net infiltration for the repository footprint calculated using MASSIF due to the differences in footprint areas. Stothoff and Walter (2007) describe the Orbital-Cycle Climate for Yucca Mountain and Infiltration Tabulator for Yucca Mountain models used for their calculations of net infiltration. The Center's net infiltration results are shown in Figure 2.3.1-49 for present-day and million-year average net infiltration over the footprint box. Net infiltration results calculated using MASSIF are also shown in this figure. Figure 2.3.1-49 shows that MASSIF results for present-day are slightly higher than those calculated by Stothoff and Walter (2007), a result that is consistent with the comparison to other models shown in Figure 2.3.1-48. Figure 2.3.1-49 also shows MASSIF results for monsoon and glacial-transition climates which are lower than the million-year range reported by Stothoff and Walter (2007). As shown in Figure 2.3.1-49, the recent results reported by Stothoff and Walter (2007) corroborate and bound the range of net infiltration results calculated using MASSIF.

Infiltration Estimates for Other Locations in Nevada—The Nevada Division of Water Resources, Department of Conservation and Natural Resources, and the U.S. Geological Survey have divided Nevada into 14 Hydrographic Regions or basins, which are used to compile information on water resources. These regions are further subdivided into 232 Hydrographic Areas (256 Hydrographic Areas and Sub-areas, combined) for more detailed study. A variety of technical publications have reported recharge estimates for Nevada Hydrographic Areas. Noteworthy examples include two series of publications by the Nevada Department of Conservation and Natural Resources: (1) the Groundwater Resources Reconnaissance Series; and (2) the Water-Resources Bulletins. In many cases, multiple recharge estimates using different

methods, inputs and assumptions are available for the same area/sub-area (SNL 2008a, Section 7.2.1.2.1[a]).

Figure 2.3.1-50 (SNL 2008a, Section 7.2.1.2[a], Figure 7.2.1.2-2[a]) summarizes the basin-scale, net infiltration (or net recharge) predictions, and plots these data with the MASSIF net infiltration results for three climate states. The Maxey-Eakin (1950) model (represented as a stepped line on the figure) is also shown for reference. Note that the Maxey-Eakin model line does not match the individual basin-scale Maxey-Eakin model net infiltration estimates, which are shown as dark blue symbols on the figure. This is because each of these precipitation and recharge estimates is an area-weighted mean value derived from subareas of the basin in which precipitation is estimated locally. For each of these subareas an associated recharge amount is determined using the percent recharge values from Maxey-Eakin (1950, p. 40). Thus, the total precipitation and total recharge values are area-weighted mean values and vary depending on the precipitation patterns across the basin, which largely depend on the basin's topographic character. There is fairly good agreement among the methods for relatively low precipitation, but estimates tend to diverge as precipitation increases. The hydrographic areas closest to Yucca Mountain fall at the low end of the recharge scale (less than 10 mm/yr), and correspond well with the MASSIF net infiltration predictions for the present-day climate at Yucca Mountain. The MASSIF net infiltration predictions for the monsoon and glacial-transition climates are generally within the range for the wetter Nevada basins (SNL 2008a, Section 7.2.1.2.1[a]).

Infiltration Estimates for Other Locations in the Southwestern United States—Net infiltration data from the southwestern United States, including West Texas, New Mexico, and Arizona, are useful in assessing the model predictions for the monsoon climate. This region includes Hobbs, New Mexico, and Nogales, Arizona (sites identified as average upper bound monsoon climate analogues in *Future Climate Analysis* (BSC 2004a, Table 6-1). Estimates for groundwater recharge in various locations in West Texas, New Mexico, and Arizona, and net recharge estimates for other locations in the southwestern United States (SNL 2008a, Section 7.2.1.2.2), which illustrate that net recharge rates for the Southwestern United States, as a fraction of precipitation, remain consistent with Yucca Mountain and are typically between less than 1% and 10%. These data are compared with Yucca Mountain net infiltration rate predictions in Figure 2.3.1-51 (SNL 2008a, Section 7.2.1.2.2, Figure 7.2.1.2-3). A range of net recharge rates for a site in northeastern Arizona, calculated using ^{14}C radiocarbon age dating combined with numerical modeling is also shown in the figure even though this area is not a climate analogue for Yucca Mountain under future climate states (Zhu 2000).

Infiltration Estimates for Other Locations in the Western United States—Several sites on the Columbia Plateau in Eastern Washington (Spokane, Rosalia, and St. John) have been identified as average upper bound glacial-transition climate analogues. Data from the Columbia Plateau in Washington State are therefore useful because they provide inferences into potential precipitation and net recharge at Yucca Mountain during wetter climates. The Columbia Plateau's position in the rain shadow of the Cascade Mountains is also analogous to the Great Basin's position behind the Sierra Nevada Mountains.

Model-derived estimates of average groundwater recharge to the Columbia Plateau regional aquifer system have been reported by Bauer and Vaccaro (1990). The deep-percolation model for estimating recharge used precipitation, temperature, streamflow, soils, land-use, and altitude data to

calculate transpiration, soil evaporation, snow accumulation, snowmelt, sublimation, and evaporation of intercepted moisture. Estimated annual average precipitation, and recharge rates for the various zones included in the Columbia Plateau study, are summarized in *Simulation of Net Infiltration for Present-Day and Potential Future Climates* (SNL 2008a, Section 7.2.1.2.3[a]). The average annual precipitation for individual modeling zones ranges from approximately 168 mm/yr to 956 mm/yr. Most precipitation values are clustered near the postulated range for the glacial-transition lower bound mean annual precipitation (198 to 220 mm/yr). For these precipitation values, the recharge efficiency varies from about 0.1% to approximately 16%. The precipitation estimates that are within the upper half (0.51 to 0.98 probability) of the 40 realizations exhibit a recharge efficiency varying from approximately 9% to 46%. The Bauer and Vaccaro (1990) estimates are compared with predicted Yucca Mountain net infiltration rates in Figure 2.3.1-52. The Maxey-Eakin model is also shown in Figure 2.3.1-52 for reference.

Net Recharge and Net Infiltration Estimates for the Hanford Site—Fayer and Walters (1995) reported estimated net recharge rates at the Hanford site in eastern Washington. They mapped soil type and vegetation/land use categories to measured or estimated recharge rates from a variety of sources. Estimation methods included lysimeter studies, chloride mass balance calculations, ^{36}Cl studies, and computer modeling. The long-term average recharge rates varied from 2.6 mm/yr for several soil and vegetation combinations to 25.4 mm/yr for cheatgrass. The 30 year average annual precipitation value of 159 mm/yr for 1951-1980 is from Fayer and Walters (1995, Figure A.3). Maher et al. (2003) reported vadose zone infiltration rates of 4 to 10 mm/yr at the Hanford site. Their estimate was based on strontium isotope ratios measured in pore water, acid extracts, and sediments of a 70 m thick vadose zone core.

Although average annual precipitation at the Hanford site is closer to the Yucca Mountain present-day climate than the glacial-transition climate, the range in recharge rates from Fayer and Walters (1995, Table 4.1), and the range in infiltration rates from Maher et al. (2003), are shown plotted in Figure 2.3.1-52 (SNL 2008a, Section 7.2.1.2[a], Figure 7.2.1.2-4[a]) because the Hanford site is located in eastern Washington, like the analogue sites of Spokane, Rosalia, and St. John, Washington, which were selected to represent the upper glacial-transition climate.

2.3.1.3.4.2.3   Corroboration of MASSIF Model Results with Other Alternative Mathematical Model Results

As discussed previously, there are no site-specific measurements of net infiltration that can be used for model validation. An alternative model approach was used as part of the post-development validation for the MASSIF model. The approach consists of corroborating model results with other model results obtained from the implementation of mathematical models. The alternative model considered is a one-dimensional unsaturated flow model based on the Richards equation. The computer code HYDRUS 1D (Simunek et al. 2005) was used to perform the simulations. The summary of this validation study is provided below. The details concerning modeling setup and supporting calculations are in *Simulation of Net Infiltration for Present-Day and Potential Future Climates* (SNL 2008a, Appendix K).

Four model scenarios were implemented with both MASSIF and HYDRUS 1D in this validation analysis (Figure 2.3.1-53 (SNL 2008a, Section 7.2.2[a], Figure 7.2.2-1[a])). The four model scenarios represent one-dimensional homogeneous soil columns that are identical except for the

depth of soil and roots in each column. Model 1 had a depth of soil and roots of 50 cm. This depth increased by 50 cm in each subsequent model. The plant rooting depth was assumed to be equal to the soil depth. The simulations were performed for one water year (365 days).

It was anticipated that significant net infiltration would be generated in the case of model 1 (thin soils) and negligible or zero net infiltration would be generated in the case of the model 4 (thick soils). This is consistent with the Yucca Mountain site conceptual model, according to which most infiltration occurs in the places where soils are thin or absent (bedrock outcrops). The validation can be considered successful if the cumulative net infiltration estimates obtained with MASSIF and HYDRUS 1D are similar.

A typical comparison between the water storage and cumulative net infiltration calculated by MASSIF and HYDRUS 1D for the models is presented in Figure 2.3.1-54 (SNL 2008a, Section 7.2.2[a], Figure 7.2.2-3a[a]). A typical comparison between the annual values of the water balance components is presented in Figure 2.3.1-55 (SNL 2008a, Section 7.2.2[a], Figure 7.2.2-4a[a]). The summary of these results is in Table 2.3.1-26 (SNL 2008a, Section 7.2.2[a], Table 7.2.2-1[a]).

Comparison of the two data sets resulted in the following conclusions:

- The simplified water balance approach used in MASSIF produces annual net infiltration estimates that are very close to the estimates obtained with a physics based model, such as HYDRUS 1D.

- MASSIF is capable of reproducing the same timing of the net infiltration events as HYDRUS 1D. This means that the important physical processes resulting in net infiltration are adequately represented in MASSIF.

- The other water balance components, such as annual actual evapotranspiration and annual runoff, are in good agreement with the HYDRUS 1D estimates as well.

- The mean root squared difference between the daily storage value calculated by MASSIF and HYDRUS 1D was in the range from 9 to 33 mm, which corresponds to 2% to 7% of the annual precipitation.

2.3.1.3.4.3   Model Abstraction

The results of the climate and infiltration analyses described in Section 2.3.1 are transferred to downstream models by providing (1) the range of timing of climate change from present-day to monsoon, and from monsoon to glacial-transition climates; and (2) a set of four maps for each of the present-day, monsoon, and glacial-transition climates, showing areally distributed infiltration, and the prior weightings of those four maps.

The results from both the future climate analysis and the infiltration model are abstracted directly or indirectly into the site-scale unsaturated zone flow model, which, in turn, inputs three-dimensional unsaturated zone flow fields directly to the TSPA. For the infiltration model, characteristics of precipitation and air temperature for the lower-bound and upper-bound monsoon

and glacial-transition climate scenarios were determined by the climate analysis (BSC 2004a) and represented by present-day analogue meteorological sites. Precipitation and temperature records from the analogue sites were used directly to develop the daily climate input for the infiltration model. For each future climate state (monsoon and glacial-transition), at least two analogue sites were identified to represent the upper-bound and lower-bound scenarios, and multiple simulations were averaged (weighted on the basis of the occurrence of mean annual precipitation) for all model grid cells to obtain a single net infiltration estimate for each scenario (SNL 2008a, Sections 6.5.7[a], 6.5.1.4, and 6.5.1.5).

The climate analysis (BSC 2004a) also provides the range of timing of climate change over the next 10,000 years. The next 600 years are forecast to continue with present-day climate conditions. For the subsequent 1,400 years, a warmer and much wetter monsoon climate is forecast, which has approximately 60% greater average annual precipitation (Tables 2.3.1-2 and 2.3.1-3). The remainder of the 10,000 year period is forecast to experience a glacial transition climate that is wetter and cooler than the present-day and monsoon climates. Average precipitation during this glacial-transition climate state is slightly higher than during the monsoon climate (Section 2.3.1.2.3).

A set of four net infiltration maps for each of the present-day, monsoon, and glacial-transition climates (a total of 12 maps), showing areally distributed infiltration, and representing the 10th, 30th, 50th, and 90th percentile of infiltration, were developed. The prior weightings of these four maps are uniform, such that the weights are 0.2, 0.2, 0.3, and 0.3 for the 10th, 30th, 50th, and 90th percentile infiltration maps, respectively. The prior weightings for the four maps representing the present-day climate were adjusted for analysis of deep percolation in the unsaturated zone using calibration and validation datasets that were applied to present-day and future climates, as described in Section 2.3.2. This adjusted weighting scheme was used by the TSPA.

For the site-scale unsaturated zone flow model, 12 mapped distributions of net infiltration rates from the infiltration model (using the new weightings) were input as infiltration boundary conditions. Using these boundary conditions, the site-scale unsaturated zone flow model generated 12 base-case, three-dimensional flow fields, representing the range of estimated net infiltration for the present-day, monsoon, and glacial-transition climates. These flow fields, along with four others representing the post-10,000-year period, were used as primary input to the TSPA. The NRC has proposed revisions to 10 CFR Part 63 that specify how post 10,000-year percolation is to be modeled. This is presented in Section 2.3.2. Given this proposed regulation, there is no need to evaluate the post 10,000-year climate or net infiltration.

2.3.1.4   Conclusions

The climate analysis and infiltration model described in this section include features and processes that contribute to the capability of the Upper Natural Barrier, as described in Section 2.1.2.1. Some features and processes make significant contributions to the overall capability of the Upper Natural Barrier. Features that are important include the following:

- **Surface Runoff and Evapotranspiration**—Surface water runoff can remove significant amounts of water from the water balance. The quantification of evapotranspiration accounts for the spatial distribution of plants and the annual cycle of water use by plants.

- **Rock Properties of Host Rock and Other Units**—Rock properties of surficial bedrock, including bulk permeability, which affect the rate of water movement below the soil–bedrock contact.

- **Topography and Morphology**—Surficial topography, which affects the amount of runoff of precipitation events, with steeper slopes having more runoff and less infiltration than more gentle slopes.

- **Fractures**—Open fractures in the bedrock will tend to increase the bedrock effective hydraulic conductivity and result in an increased rate of net infiltration into the subsurface. However, a lower effective conductivity of the bedrock will tend to increase water storage in the surficial soil and increase the effectiveness of runoff and evapotranspiration, thereby reducing the rate of net infiltration into the subsurface.

Processes that make important contributions include the following:

- **Climate Change**—Future climate change, which affects the amount and timing of precipitation.

- **Climate Modification Increases Recharge**—Future climate changes affect the amount and timing of precipitation, as well as temperature, humidity, and vegetation, all of which affect evapotranspiration and net infiltration.

- **Precipitation**—The temporal and spatial distribution of precipitation, which affects the amount of water potentially available to run off, evaporate, transpire, or infiltrate.

- **Infiltration and Recharge**—These processes are the net result of all processes related to net infiltration and the availability of water for percolation through the unsaturated zone.

- **Fracture Flow in the Unsaturated Zone**—Fracture flow in the bedrock beneath the surficial soil affects the rate of water movement below the soil–bedrock contact, especially in areas of thin soils. The rate of water flow in fractures at the soil–bedrock interface is influenced by fracture properties such as fracture frequency and permeability.

Uncertainties Associated with Climate and Infiltration Features and Processes that Contribute to Performance of the Upper Natural Barrier—Uncertainty in forecasting future climate states for the next 10,000 years is related to both interpretation of paleoclimate data and selection of analogue meteorological sites to represent future climate conditions. There is also uncertainty in the selection of average sediment accumulation rates, which are used to project the duration of present-day and monsoon climate states.

There are significant uncertainties in boundary conditions related to precipitation estimates using synthetic datasets. There are additional uncertainties in geospatial properties, including soil depth, soil and bedrock hydraulic properties, and vegetation properties (including rooting depths).

Uncertainties related to the extent of data describing site-specific conditions at Yucca Mountain are captured by the range of variation and resulting uncertainty in infiltration estimates. The calculation

of 40 infiltration estimates via the Latin Hypercube sampling for each of the three climate states explicitly incorporates these uncertainties. The net infiltration averages of the 40 infiltration maps for each of the present-day, monsoon, and glacial-transition climates are generally considered to be conservative estimates of net infiltration for these three climates, based on the factors listed above, and based on the comparisons of MASSIF results to other published models shown in Figure 2.3.1-48.

Despite uncertainties in the climate and infiltration analyses, the abstractions of the range in timing of climate change, and the four average annual net infiltration maps representing the 10th, 30th, 50th, and 90th percentile maps for each climate, with associated prior weightings, are sufficient for the TSPA. This is because the range of timing of climate change is small compared to the total length of the glacial-transition period, and the post-10,000-year period, and because the prior weights of the infiltration maps are adjusted as described in Section 2.3.2.4.1.2.4.5. In addition, uncertainties in the spatial distribution of net infiltration are not considered to be significant given the damping and homogenizing of downward-moving transient pulses by the Paintbrush nonwelded hydrogeologic (PTn) unit.

Key Conservatisms in Models Used to Assess Barrier Capability—Several conservative assumptions may influence the capability of the uppermost component of the Upper Natural Barrier. The consequence of these assumptions is a model that generally predicts greater net infiltration into the unsaturated zone at Yucca Mountain than is indicated by other large-scale net infiltration models. For example, most of the comparable net infiltration (or recharge) models generally predict less infiltration than MASSIF (Section 2.3.1.3.4.2.2).

Because of conservatism in the treatment of parameter uncertainties and simplifying assumptions made in modeling infiltration processes, MASSIF model results are expected to predict greater net infiltration when compared to the other large-scale net infiltration models discussed in Section 2.3.1.3.4.2.2. Key aspects of MASSIF that likely contribute to the conservative assessment of net infiltration are: (1) soil depth of the shallow depth class; (2) soil water holding capacity; (3) bedrock K_{sat}; and (4) the lack of a mechanism to remove water from bedrock (i.e., via plant roots). Soil depth of the shallow soil depth class is the most sensitive parameter in the net infiltration model, and the range of uniform upscaled values of 0.1 to 0.5 m is conservative (Section 2.3.1.3.2.1.3). Soil water holding capacity inputs are generally lower than field data, which adds to model conservatism (Section 2.3.1.3.2.1.3). Bedrock K_{sat} inputs are considered to be higher than actual values based on comparison with data from Alcove 1 which adds to model conservatism (Section 2.3.1.3.2.1.4). The lack of a mechanism to remove water from bedrock is also a conservative feature of the net infiltration model. With respect to the tendency to underestimate the spatial variability of net infiltration, uncertainty in soil K_{sat} is likely to be the most significant uncertainty, but this uncertainty has little effect on the spatial average of net infiltration (SNL 2008a, Section 7.1.3.1).

Summary of Consistency Between TSPA Model Abstractions and Process Models—The TSPA model directly incorporates the results of the net infiltration model through the use of 12 flow fields representing the spatially distributed range of net infiltration fluxes at the top of the unsaturated zone for each of the three pre-10,000-year future climates states (present-day, monsoon, and glacial-transition) (Section 2.3.2). Other models that support the TSPA (Figure 2.3.1-2) are consistent with the net infiltration model in several important ways. For

example, the effects of future climate changes are propagated consistently through the unsaturated flow model, multiscale thermal-hydrologic model and unsaturated zone transport abstraction models.

Summary of Key Outputs Parameters Provided to the TSPA—Outputs from the climate analysis are the timing, duration, and characteristics of the three climate states expected to affect Yucca Mountain for the next 10,000 years. The infiltration model provides the spatially varying net infiltration maps for each of the three climate states: present-day, monsoon, and glacial-transition. Uncertainty in infiltration is incorporated through development of 40 infiltration maps for each of the three climate states resulting in the selection of the 10th, 30th, 50th, and 90th percentile infiltration maps that serve as the upper boundary condition for the site-scale unsaturated zone flow model, that is described in Section 2.3.2.4.1.2.4.5. The prior weights for these maps are 20%, 20%, 30%, and 30%, respectively. The flow fields generated by the site-scale unsaturated zone flow model are implemented sequentially in the TSPA over the three modeled periods: present-day conditions for the first 600 years; 1,400 subsequent years of a monsoon climate; and a glacial-transition climate for the remainder of the 10,000 years. For the post-10,000 year period, the NRC has specified a constant percolation flux distribution. Section 2.4.1 describes the implementation and integration of these outputs into the TSPA, and Figure 2.3.1-2 portrays the information transfer within the TSPA.

Duration of climate states are also provided to the three-dimensional and one-dimensional saturated zone flow and transport models described in Section 2.3.9. In addition, the infiltration model provides the net infiltration flux as part of the basis for scaling groundwater flux for the future climate states in the saturated zone transport submodel used in the TSPA (Section 2.4.2.3.2.1.10).

2.3.1.5   General References

Allen, R.G. 1997. "Self-Calibrating Method for Estimating Solar Radiation from Air Temperature." *Journal of Hydrologic Engineering, 2* (2), 56–67. New York, New York: American Society of Civil Engineers. TIC: 258131.

Allen, R.G.; Pereira, L.S.; Raes, D.; and Smith, M. 1998. *Crop Evapotranspiration, Guidelines for Computing Crop Water Requirements*. FAO Irrigation and Drainage Paper 56. Rome, Italy: Food and Agriculture Organization of the United Nations. TIC: 245062.

Allen, R.G.; Pereira, L.S.; Smith, M.; Raes, D.; and Wright, J.L. 2005. "FAO-56 Dual Crop Coefficient Method for Estimating Evaporation from Soil and Application Extensions." *Journal of Irrigation and Drainage Engineering, 131* (1), 2–13. Reston, Virginia: American Society of Civil Engineers. TIC: 257869.

Allen, R.G.; Walter, I.A.; Elliott, R.L.; Howell, T.; Itenfisu, D.; and Jensen, M. 2005. *The ASCE Standardized Reference Evapotranspiration Equation*. Reston, Virginia: American Society of Civil Engineers. TIC: 257138.

Altman, W.D.; Donnelly, J.P.; and Kennedy, J.E. 1988. *Qualification of Existing Data for High-Level Nuclear Waste Repositories: Generic Technical Position*. NUREG-1298. Washington, D.C.: U.S. Nuclear Regulatory Commission. TIC: 200652.

Bauer, H.H. and Vaccaro, J.J. 1990. *Estimates of Ground-Water Recharge to the Columbia Plateau Regional Aquifer System, Washington, Oregon, and Idaho, for Predevelopment and Current Land-Use Conditions*. Water-Resources Investigations Report 88-4108. Denver, Colorado: U.S. Geological Survey. ACC: MOL.20061115.0001.

Bausch, W.C. and Neale, C.M.U. 1987. "Crop Coefficients Derived from Reflected Canopy Radiation: A Concept." *Transactions of the ASAE, 30* (3), 703–709. St. Joseph, Michigan: American Society of Agricultural Engineers. TIC: 258520.

Bischoff, J.L.; Stafford, T.W., Jr.; and Rubin, M. 1997. "A Time-Depth Scale for Owens Lake Sediments of Core OL-92: Radiocarbon Dates and Constant Mass-Accumulation Rate." Chapter 8 of *An 800,000-Year Paleoclimatic Record from Core OL-92, Owens Lake, Southeast California*. Smith, G.I. and Bischoff, J.L., eds. Special Paper 317. Boulder, Colorado: Geological Society of America. TIC: 236857.

BSC (Bechtel SAIC Company) 2004a. *Future Climate Analysis*. ANL-NBS-GS-000008 REV 01. Las Vegas, Nevada: Bechtel SAIC Company. ACC: DOC.20040908.0005.

BSC 2004b. *Yucca Mountain Site Description*. TDR-CRW-GS-000001 REV 02 ICN 01. Two volumes. Las Vegas, Nevada: Bechtel SAIC Company. ACC: DOC.20040504.0008.

BSC 2004c. *Geologic Framework Model (GFM2000)*. MDL-NBS-GS-000002 REV 02. Las Vegas, Nevada: Bechtel SAIC Company. ACC: DOC.20040827.0008.

BSC 2006a. *Data Analysis for Infiltration Modeling: Development of Soil Units and Associated Hydraulic Parameter Values*. ANL-NBS-HS-000055 REV 00. Las Vegas, Nevada: Bechtel SAIC Company. ACC: DOC.20060912.0006.

BSC 2006b. *Data Analysis for Infiltration Modeling: Bedrock Saturated Hydraulic Conductivity Calculation*. ANL-NBS-HS-000054 REV 00. Las Vegas, Nevada: Bechtel SAIC Company. ACC: DOC.20060710.0001.

BSC 2006c. *Data Analysis for Infiltration Modeling: Technical Evaluation of Previous Soil Depth Estimation Methods and Development of Alternate Parameter Values*. ANL-NBS-HS-000077 REV 01. Las Vegas, Nevada: Bechtel SAIC Company. ACC: DOC.20060918.0009.

BSC 2006d. *Technical Evaluation and Review of Results, Technical Procedures, and Methods Related to the Collection of Moisture Monitoring Data Using Neutron Probes in Shallow Boreholes*. TDR-NBS-HS-000019 REV 00. Las Vegas, Nevada: Bechtel SAIC Company. ACC: DOC.20060425.0005.

CRWMS M&O (Civilian Radioactive Waste Management System Management & Operating Contractor) 1996. *The Vegetation of Yucca Mountain: Description and Ecology*. B00000000-01717-5705-00030 REV 00. Las Vegas, Nevada: CRWMS M&O. ACC: MOL.19970116.0055.

CRWMS M&O 1997a. *Engineering Design Climatology and Regional Meteorological Conditions Report.* B00000000-01717-5707-00066 REV 00. Las Vegas, Nevada: CRWMS M&O. ACC: MOL.19980304.0028.

CRWMS M&O 1997b. *Unsaturated Zone Flow Model Expert Elicitation Project.* Las Vegas, Nevada: CRWMS M&O. ACC: MOL.19971009.0582.

Day, W.C.; Potter, C.J.; Sweetkind, D.S.; Dickerson, R.P.; and San Juan, C.A. 1998. *Bedrock Geologic Map of the Central Block Area, Yucca Mountain, Nye County, Nevada.* Miscellaneous Investigations Series Map I-2601. Washington, D.C.: U.S. Geological Survey. ACC: MOL.19980611.0339.

DOE (U.S. Department of Energy) 1997. *Regional Groundwater Flow and Tritium Transport Modeling and Risk Assessment of the Underground Test Area, Nevada Test Site, Nevada.* DOE/NV-477. Las Vegas, Nevada: U.S. Department of Energy. ACC: MOL.20010731.0303.

DOE 2001. *Nevada Test Site 2000 Waste Management Monitoring Report Area 3 and Area 5 Radioactive Waste Management Sites.* DOE/NV/11718-582. Las Vegas, Nevada: U.S. Department of Energy, National Nuclear Security Administration, Nevada Operations Office. ACC: MOL.20040820.0136.

Desotell, L.T.; Hudson, D.B.; Yucel, V.; and Carilli, J.T. 2006. *Use of Long-Term Lysimeter Data in Support of Shallow Land Waste Disposal Cover Design.* DOE/NV11718--1148. Las Vegas, Nevada: U.S. Department of Energy, Nevada Site Office. ACC: MOL.20060413.0159.

Droogers, P. and Allen, R.G. 2002. "Estimating Reference Evapotranspiration Under Inaccurate Data Conditions." *Irrigation and Drainage Systems, 16*, 33–45. Dordrecht, The Netherlands: Kluwer Academic Publishers. TIC: 258242.

Duchemin, B.; Hadria, R.; Erraki, S.; Boulet, G.; Maisongrande, P.; Chehbouni, A.; Escadafal, R.; Ezzahar, J.; Hoedjes, J.C.B.; Kharrou, M.H.; Khabba, S.; Mougenot, B.; Olioso, A.; Rodriguez, J.-C.; and Simonneaux, V. 2006. "Monitoring Wheat Phenology and Irrigation in Central Morocco: On the Use of Relationships Between Evapotranspiration, Crops Coefficients, Leaf Area Index and Remotely-Sensed Vegetation Indices." *Agricultural Water Management, 79*, 1–27. New York, New York: Elsevier. TIC: 258870.

Faybishenko, B. 2007. "Climatic Forecasting of Net Infiltration at Yucca Mountain Using Analogue Meterorological Data." *Vadose Zone Journal, 6*, 77–92. Madison, Wisconsin: Soil Science Society of America. TIC: 259076.

Fayer, M.J. and Walters, T.B. 1995. *Estimated Recharge Rates at the Hanford Site.* PNL-10285. Richland, Washington: Pacific Northwest Laboratory. ACC: MOL.20061026.0075.

Fedors, R. 2007. "Soil Depths Measured at Yucca Mountain During Site Visits in 1998." Letter from R. Fedors to J. Guttmann, January 9, 2007. ACC: LLR.20070815.0081.

Flint, L.E. and Flint, A.L. 1995. *Shallow Infiltration Processes at Yucca Mountain, Nevada—Neutron Logging Data 1984-93*. Water-Resources Investigations Report 95-4035. Denver, Colorado: U.S. Geological Survey. ACC: MOL.19960924.0577.

Forester, R.M. 1983. "Relationship of Two Lacustrine Ostracode Species to Solute Composition and Salinity: Implications for Paleohydrochemistry." *Geology, 11* (8), 435–438. Boulder, Colorado: Geological Society of America. TIC: 222805.

Forester, R.M. 1985. "Limnocythere bradburyi N. SP.: A Modern Ostracode from Central Mexico and a Possible Quaternary Paleoclimatic Indicator." *Journal of Paleontology, 59* (1), 8–20. Tulsa, Oklahoma: Society of Economic Paleontologists and Mineralogists. TIC: 225826.

Forester, R.M.; Bradbury, J.P.; Carter, C.; Elvidge-Tuma, A.B.; Hemphill, M.L.; Lundstrom, S.C.; Mahan, S.A.; Marshall, B.D.; Neymark, L.A.; Paces, J.B.; Sharpe, S.E.; Whelan, J.F.; and Wigand, P.E. 1999. *The Climatic and Hydrologic History of Southern Nevada During the Late Quaternary.* Open-File Report 98-635. Denver, Colorado: U.S. Geological Survey. TIC: 245717.

Hansen, E.M.; Schwarz, F.K.; and Riedel, J.T. 1977. *Probable Maximum Precipitation Estimates, Colorado River and Great Basin Drainages.* Hydrometeorological Report No. 49. Silver Spring, Maryland: U.S. Department of Commerce, National Oceanic and Atmospheric Administration. TIC: 220224.

Hofmann, L.L.; Guertal, W.R.; and Flint, A.L. 2000. *Development and Testing of Techniques to Obtain Infiltration Data for Unconsolidated Surficial Materials, Yucca Mountain Area, Nye County, Nevada.* Open-File Report 95-154. Denver, Colorado: U.S. Geological Survey. TIC: 249343.

Hood, E.; Williams, M.; and Cline, D. 1999. "Sublimation from a Seasonal Snowpack at a Continental, Mid-Latitude Alpine Site." *Hydrological Processes, 13*, 1781–1797. New York, New York: John Wiley & Sons. TIC: 258621.

Irmak, S.; Howell, T.A.; Allen, R.G.; Payero, J.O.; and Martin, D.L. 2005. "Standardized ASCE Penman-Monteith: Impact of Sum-of-Hourly vs. 24-Hour Timestep Computations at Reference Weather Station Sites." *Transactions of the ASAE, 48* (3) 1063–1077. St. Joseph, Michigan: American Society of Agricultural Engineers. TIC: 258278.

Jensen, M.E.; Burman, R.D.; and Allen, R.G., eds. 1990. *Evapotranspiration and Irrigation Water Requirements*. ASCE Manuals and Reports on Engineering Practice No. 70. New York, New York: American Society of Civil Engineers. TIC: 246697.

Landwehr, J.M.; Coplen, T.B.; Ludwig, K.R.; Winograd, I.J.; and Riggs, A.C. 1997. *Data for Devils Hole Core DH-11*. Open-File Report 97-792. Reston, Virginia: U.S. Geological Survey. TIC: 245712.

LeCain, G.D.; Lu, N.; and Kurzmack, M. 2002. *Use of Temperature, Pressure, and Water Potential Data to Estimate Infiltration and Monitor Percolation in Pagany Wash Associated with the Winter*

of 1997–98 El Niño Precipitation, Yucca Mountain, Nevada. Water Resources Investigations Report 02-4035. Denver, Colorado: U.S. Geological Survey. TIC: 252641.

Litwin, R.J., Smoot, J.P., Durika, N.J., and Smith, G.I., 1999. "Calibrating Late Quaternary Terrestrial Climate Signals: Radiometrically Dated Pollen Evidence from the Southern Sierra Nevada, USA." *Quaternary Science Reviews*, *18*, 1151–1171. New York, New York: Pergamon Press. TIC: 245700.

Looney, B.B. and Falta, R.W., eds. 2000. *Vadose Zone, Science and Technology Solutions*. Two volumes. Columbia, Ohio: Battelle Press. TIC: 249256.

Ludwig, K.R.; Simmons, K.R.; Szabo, B.J.; Winograd, I.J.; Landwehr, J.M.; Riggs, A.C.; and Hoffman, R.J. 1992. "Mass-Spectrometric ^{230}Th–^{234}U–^{238}U Dating of the Devils Hole Calcite Vein." *Science*, *258*, 284–287. Washington, D.C.: American Association for the Advancement of Science. TIC: 237796.

Maher, K.; DePaolo, D.J.; Conrad, M.E.; and Serne, R.J. 2003. "Vadose Zone Infiltration Rate at Hanford, Washington, Inferred from Sr Isotope Measurements." *Water Resources Research, 39* (8), SBH 3-1–SBH 3-14. Washington, D.C.: American Geophysical Union. TIC: 259095.

Maidment, D.R., ed. 1993. *Handbook of Hydrology.* New York, New York: McGraw-Hill. TIC: 236568.

Marks, D. 2001. "Introduction to Special Section: Reynolds Creek Experimental Watershed." *Water Resources Research, 37* (11) 2817. Washington, D.C.: American Geophysical Union. ACC: MOL.20060712.0232.

Maurer, D.K. and Berger, D.L. 1997. *Subsurface Flow and Water Yield from Watersheds Tributary to Eagle Valley Hydrographic Area, West-Central Nevada*. Water-Resources Investigations Report 97-4191. Carson City, Nevada: U.S. Geological Survey. ACC: MOL.20060808.0017.

Maxey, G.B. and Eakin, T.E. 1950. *Ground Water in White River Valley, White Pine, Nye, and Lincoln Counties, Nevada.* Water Resources Bulletin No. 8. Carson City, Nevada: State of Nevada, Office of the State Engineer. TIC: 216819.

McElroy, D.L. 1993. *Soil Moisture Monitoring Results at the Radioactive Waste Management Complex of the Idaho National Engineering Laboratory, FY-1993*. EGG-WM-11066. Idaho Falls, Idaho: EG&G Idaho, Idaho National Engineering Laboratory. ACC: MOL.20061016.0249.

Nichols, W.D. 2000. *Regional Ground-Water Evapotranspiration and Ground-Water Budgets, Great Basin, Nevada*. U.S. Geological Survey Professional Paper 1628. Reston, Virginia: U.S. Geological Survey. ACC: LLR.20070213.0076.

Nobel, P.S. 1983. "Plants and Fluxes." *Biophysical Plant Physiology and Ecology.* Pages 461–523. New York, New York: W.H. Freeman and Company. TIC: 252952.

Reheis, M. 1999. "Highest Pluvial-Lake Shorelines and Pleistocene Climate of the Western Great Basin." *Quaternary Research*, *52* (2), 196–205. New York, New York: Academic Press. TIC: 245885.

Rodríguez, E.; Morris, C.S.; Belz, J.E.; Chapin, E.C.; Martin, J.M.; Daffer, W.; and Hensley, S. 2005. *An Assessment of the SRTM Topographic Products*. D-31639. Pasadena, California: Jet Propulsion Laboratory. ACC: MOL.20061011.0062.

Rousseau, J.P.; Kwicklis, E.M.; and Gillies, D.C., eds. 1999. *Hydrogeology of the Unsaturated Zone, North Ramp Area of the Exploratory Studies Facility, Yucca Mountain, Nevada.* Water-Resources Investigations Report 98-4050. Denver, Colorado: U.S. Geological Survey. ACC: MOL.19990419.0335.

SN0701T0502206.037. Massif Calculation of Net Infiltration at Yucca Mountain, Rev 1. Submittal date: 12/10/2007.

SNL (Sandia National Laboratories) 2006. *Data Analysis for Infiltration Modeling: Extracted Weather Station Data Used to Represent Present-Day and Potential Future Climate Conditions in the Vicinity of Yucca Mountain*. ANL-MGR-MD-000015 REV 00. Las Vegas, Nevada: Sandia National Laboratories. ACC: DOC.20070109.0002.

SNL 2007. *UZ Flow Models and Submodels*. MDL-NBS-HS-000006 REV 03 ADD 01. Las Vegas, Nevada: Sandia National Laboratories. ACC: DOC.20080108.0003; DOC.20080114.0001.

SNL 2008a. *Simulation of Net Infiltration for Present-Day and Potential Future Climates*. MDL-NBS-HS-000023 REV 01 ADD 01. Las Vegas, Nevada: Sandia National Laboratories. ACC: DOC.20080201.0002.

SNL 2008b. *Total System Performance Assessment Model /Analysis for the License Application.* MDL-WIS-PA-000005 REV 00 ADD 01. Las Vegas, Nevada: Sandia National Laboratories. ACC: DOC.20080312.0001.

SNL 2008c. *Particle Tracking Model and Abstraction of Transport Processes*. MDL-NBS-HS-000020 REV 02 ADD 02. Las Vegas, Nevada: Sandia National Laboratories. ACC: DOC.20080129.0008.

Scott, R.B. and Bonk, J. 1984. *Preliminary Geologic Map of Yucca Mountain, Nye County, Nevada, with Geologic Sections*. Open-File Report 84-494. Denver, Colorado: U.S. Geological Survey. ACC: HQS.19880517.1443.

Sharpe, S. 2003. *Future Climate Analysis—10,000 Years to 1,000,000 Years After Present.* MOD-01-001 REV 01. Reno, Nevada: Desert Research Institute. ACC: MOL.20030407.0055.

Shevenell, L. 1996. *Statewide Potential Evapotranspiration Maps for Nevada.* Report 48. Reno, Nevada: Nevada Bureau of Mines and Geology. ACC: MOL.20040820.0138.

Šimůnek, J.; van Genuchten, M.Th.; and Šejna, M. 2005. *The HYDRUS-1D Software Package for Simulating the One-Dimensional Movement of Water, Heat, and Multiple Solutes in Variably-Saturated Media*. Version 3.0. Riverside, California: University of California, Department of Environmental Sciences. ACC: MOL.20060828.0051.

Slate, J.L.; Berry, M.E.; Rowley, P.D.; Fridrich, C.J.; Morgan, K.S.; Workman, J.B.; Young, O.D.; Dixon, G.L.; Williams, V.S.; McKee, E.H.; Ponce, D.A.; Hildenbrand, T.G.; Swadley, W C; Lundstrom, S.C.; Ekren, E.B.; Warren, R.G.; Cole, J.C.; Fleck, R.J.; Lanphere, M.A.; Sawyer, D.A.; Minor, S.A.; Grunwald, D.J.; Laczniak, R.J.; Menges, C.M.; Yount, J.C.; Jayko, A.S.; Mankinen, E.A.; Davidson, J.G.; Morin, R.L.; and Blakely, R.J. 2000. *Digital Geologic Map of the Nevada Test Site and Vicinity, Nye, Lincoln and Clark Counties, Nevada, and Inyo County, California, Revision 4; Digital Aeromagnetic Map of the Nevada Test Site and Vicinity, Nye, Lincoln, and Clark Counties, Nevada, and Inyo County, California; and Digital Isostatic Gravity Map of the Nevada Test Site and Vicinity, Nye, Lincoln, and Clark Counties, Nevada, and Inyo County, California*. Open-File Report 99-554-A, -B, and -C. Denver, Colorado: U.S. Geological Survey. TIC: 248049; 251985; 251981.

Smith, A.J. and Forester, R.M. 1994. "Estimating Past Precipitation and Temperature from Fossil Ostracodes." *High Level Radioactive Waste Management, Proceedings of the Fifth Annual International Conference, Las Vegas, Nevada, May 22–26, 1994*, *4*, 2545–2552. La Grange Park, Illinois: American Nuclear Society. TIC: 210984.

Smith, G.I. and Bischoff, J.L., eds. 1993. *Core OL-92 from Owens Lake, Southeast California. Open-File Report 93-683.* Denver, Colorado: U.S. Geological Survey. TIC: 253391.

Stothoff, S. and Walter, G. 2007. *Long-Term-Average Infiltration at Yucca Mountain, Nevada: Million-Year Estimates*. CNWRA 2007-003. San Antonio, Texas: Center for Nuclear Waste Regulatory Analyses. ACC: LLR.20071108.0001.

Wilson, J.L. and Guan, H. 2004. "Mountain-Block Hydrology and Mountain-Front Recharge." In *Groundwater Recharge in a Desert Environment: The Southwestern United States*, Hogan, J.F.; Phillips, F.M.; and Scanlon, B.R., eds, *Water Science and Application 9*. Pages 113–137. Washington, D.C.: American Geophysical Union. TIC: 256760.

Winograd, I.J.; Coplen, T.B.; Landwehr, J.M.; Riggs, A.C.; Ludwig, K.R.; Szabo, B.J.; Kolesar, P.T.; and Revesz, K.M. 1992. "Continuous 500,000-Year Climate Record from Vein Calcite in Devils Hole, Nevada." *Science, 258,* 255–260. Washington, D.C.: American Association for the Advancement of Science. TIC: 237563.

Winograd, I.J.; Landwehr, J.M.; Ludwig, K.R.; Coplen, T.B.; and Riggs, A.C. 1997. "Duration and Structure of the Past Four Interglaciations." *Quaternary Research, 48,* 141–154. New York, New York: Academic Press. TIC: 236777.

Winograd, I.J.; Landwehr, J.M.; Coplen, T.B.; Sharp, W.D.; Riggs, A.C.; Ludwig, K.R.; and Kolesar, P.T. 2006. "Devils Hole, Nevada, δ^{18}O Record Extended to the Mid-Holocene." *Quaternary Research*, 66 202–212. New York, New York: Elsevier. TIC: 259665.

Zhu, C. 2000. "Estimate of Recharge from Radiocarbon Dating of Groundwater and Numerical Flow and Transport Modeling." *Water Resources Research, 36* (9), 2607–2620. Washington, D.C.: American Geophysical Union. TIC: 252313.

INTENTIONALLY LEFT BLANK

Table 2.3.1-1. Features, Events, and Processes Addressed in Climate and Infiltration

FEP Number and FEP Name	FEP Description	Summary of Technical Basis and Approach for FEP Inclusion
1.2.02.01.0A Fractures	Groundwater flow in the Yucca Mountain region and transport of any released radionuclides may take place along fractures. The rate of flow and the extent of transport in fractures are influenced by characteristics such as orientation, aperture, asperity, fracture length, connectivity, and the nature of any linings or infills.	The effects of fractures are also included in the treatment of bulk bedrock permeability used in the infiltration uncertainty for TSPA (BSC 2006b; SNL 2008a). Infiltration uncertainty is represented through 40 discrete infiltration maps of which four (10th, 30th, 50th, and 90th percentile) are selected to be sampled in TSPA according to weighting factors determined in the unsaturated zone flow analysis. (SNL 2007, Section 6.8.5). Fractures are included in the infiltration uncertainty analysis by incorporation of the fracture parameters for bedrock permeability distributions that are sampled as part of the assessment of infiltration uncertainty. The uncertainties for these parameters are described in *Simulation of Net Infiltration for Present-Day and Potential Future Climates* (SNL 2008a, Section 6.6) and in Section 2.3.1.3.3.2. These uncertainties are propagated through the net infiltration model and so are implicitly included in the output (weighting factors) passed to TSPA.
1.3.01.00.0A Climate change	Climate change may affect the long-term performance of the repository. This includes the effects of long-term change in global climate (e.g., glacial–interglacial cycles) and shorter-term change in regional and local climate. Climate is typically characterized by temporal variations in precipitation and temperature.	Global climate change is addressed in TSPA using a climate analysis based on the record of climate changes in the past, which is used to forecast the expected changes in climate for the future. The climate analysis is incorporated into TSPA through unsaturated zone flow fields which are calculated using different surface-water infiltration maps as a result of different climates (SNL 2007, Section 6.8.5) which correspond to three distinct future climate states: present-day, monsoon, and glacial-transition (Section 2.3.1.2.3.1.1). For the post-10,000 year period, a percolation flux is specified as 13 to 64 mm/yr in accordance with proposed 10 CFR 63.342(c)(2). Future climate conditions are addressed in the net infiltration model (SNL 2008a, Sections 6.5.1.4 and 6.5.1.5) through the selection of analogues at other locations with present-day climates representative of the range of future climate conditions at Yucca Mountain (BSC 2004a, Section 6.6). The meteorological data from these analogues are then used for modeling infiltration under future climate conditions at Yucca Mountain. A description of the modeling methods used for infiltration and of how infiltration is affected by climate is given in *Simulation of Net Infiltration for Modern and Potential Future Climates* (SNL 2008a, Section 6.3) and Section 2.3.1.3.3.1.2. The results of the net infiltration model are then used for computing unsaturated zone flow throughout the unsaturated zone flow model domain, which includes the repository waste emplacement zone. The site-scale unsaturated zone flow model uses the infiltration results as upper-boundary conditions for site-scale unsaturated zone flow calculations. (SNL 2007, Section 6.8.5). The unsaturated zone flow fields are used directly in TSPA.

Table 2.3.1-1. Features, Events, and Processes Addressed in Climate and Infiltration (Continued)

FEP Number and FEP Name	FEP Description	Summary of Technical Basis and Approach for FEP Inclusion
1.4.01.01.0A Climate modification increases recharge	Climate modification causes an increase in recharge in the Yucca Mountain region. Increased recharge might lead to increased flux through the repository, perched water, or water table rise.	The effects of climate changes on unsaturated zone flux through the repository are incorporated through the explicit simulations of unsaturated zone weighted flow fields corresponding to the 10th, 30th, 50th, and 90th percentile infiltrations of three distinct climates: present-day, monsoon, and glacial-transition (Section 2.3.1.3.3.1.2). The initial value of the relative weights for these four cases are 0.2, 0.2, 0.3, and 0.3, for the 10th, 30th, 50th, and 90th percentile maps, respectively. The values of these weights are adjusted as part of the unsaturated zone model calibration activities based on thermal and chloride data at depth, and described in Section 2.3.2.
2.2.03.02.0A Rock properties of host rock and other units	Physical properties such as porosity and permeability of the relevant rock units, soils, and alluvium are necessary for the performance assessment. Possible heterogeneities in these properties should be considered. Questions concerning events and processes that may cause these physical properties to change over time are considered in other FEPs.	Rock properties are defined for each of the stratigraphic units (layers) classified in the geological framework model, which is further developed into a model grid for the site-scale unsaturated zone flow model. Heterogeneity is modeled in terms of the sequence of hydrogeologic units and discrete faults. Therefore, rock properties are implicitly embedded in the TSPA through the output flow fields, with site-scale layering and faults explicitly taken into account. At the drift scale, the effects of rock heterogeneity on seepage are explicitly modeled through the use of geostatistical data constrained by field measurements of permeability and by seepage tests (Section 2.3.3). The effects of rock properties are also included in the treatment of infiltration uncertainty for TSPA (SNL 2008a). Infiltration uncertainty is represented through 40 discrete infiltration maps of which 4 are selected to be sampled in TSPA according to weighting factors developed in the unsaturated zone flow model. Rock properties are included through the fracture parameters of bedrock permeability. The uncertainties for these parameters are described in *Simulation of Net Infiltration for Present-Day and Future Climates* (SNL 2008a, Section 6.6). The uncertainties are propagated through the net infiltration model and so are implicitly included in the output (weighting factors) passed to TSPA. Heterogeneities in these properties are included in the input used in the analysis reported in *Simulation of Net Infiltration for Present-Day and Potential Future Climates* (SNL 2008a, Section 6.5.7[a]) and in Section 2.3.1.3.2.
2.2.07.08.0A Fracture flow in the UZ	Fractures or other analogous channels may act as conduits for fluids to move into the subsurface to interact with the repository and as conduits for fluids to leave the vicinity of the repository and be conducted to the saturated zone. Water may flow through only a portion of the fracture network, including flow through a restricted portion of a given fracture plane.	The hydrologic characteristics of the surficial soils above the repository are significant in affecting the amount of net infiltration following a precipitation event. Fracture flow in the bedrock beneath the surficial soils affects the rate of water movement below the soil and bedrock contact, especially in areas of thin soils. Fractures are included in the infiltration uncertainty analysis by incorporation of the fracture parameters for bedrock permeability distributions that are sampled as part of the assessment of infiltration uncertainty. The uncertainties for these parameters are described in *Simulation of Net Infiltration for Present-Day and Potential Future Climates* (SNL 2008a, Section 6.6) and in Section 2.3.1.3.3.2. These uncertainties are propagated through the net infiltration model and so are implicitly included in the output (weighting factors) passed to TSPA.

Table 2.3.1-1. Features, Events, and Processes Addressed in Climate and Infiltration (Continued)

FEP Number and FEP Name	FEP Description	Summary of Technical Basis and Approach for FEP Inclusion
2.3.01.00.0A Topography and morphology	This FEP is related to the topography and surface morphology of the disposal region. Topographical features include outcrops and hills, water-filled depressions, wetlands, recharge areas, and discharge areas. Topography, precipitation, and surficial permeability distribution in the system will determine the flow boundary conditions (i.e., location and amount of recharge and discharge in the system).	Topographical features, precipitation, and surficial permeability distribution are incorporated into the infiltration model (SNL 2008a). Topographical features are captured in the net infiltration model using digital elevation data. The impacts of topography and morphology on preferential flow and percolation in the unsaturated zone are incorporated into the TSPA through the unsaturated zone weighted flow fields that use the net infiltration model results (with initial weights) as upper boundary conditions (Section 2.3.1.1). The effects of rock properties are also included in the treatment of infiltration uncertainty. Infiltration uncertainty is represented through 40 discrete infiltration maps of which 4 are sampled in TSPA according to weighting factors determined in the unsaturated zone flow analysis. Precipitation and the surficial permeability distributions are captured in the uncertainty analysis via a Monte Carlo method. The uncertainty in surficial permeability and precipitation is captured in the four infiltration maps selected as boundary conditions of the unsaturated zone flow model for each climate state.
2.3.11.01.0A Precipitation	Precipitation is an important control on the amount of infiltration, flow in the unsaturated zone, seepage into the repository, and groundwater recharge. It transports solutes with it as it flows downward through the subsurface or escapes as runoff. Precipitation influences agricultural practices of the receptor. The amount of precipitation depends on climate.	Precipitation affects the net infiltration. These effects are captured in the net infiltration map outputs used as a boundary condition for the site-scale unsaturated zone flow models. Flow fields developed for use in TSPA using the site-scale unsaturated zone flow model include the effects of precipitation and changes of precipitation under future climate conditions and associated uncertainty. The effects of precipitation are also included in the treatment of infiltration uncertainty. Infiltration uncertainty is represented through 40 discrete infiltration maps of which 4 (at the 10th, 30th, 50th, and 90th percentiles) are sampled in TSPA according to weighting factors determined by the unsaturated zone flow analysis. Precipitation is incorporated in the infiltration uncertainty analysis through the Monte Carlo sampling.

Table 2.3.1-1. Features, Events, and Processes Addressed in Climate and Infiltration (Continued)

FEP Number and FEP Name	FEP Description	Summary of Technical Basis and Approach for FEP Inclusion
2.3.11.02.0A Surface runoff and evapotranspiration	Surface water runoff and evapotranspiration are components in the water balance, together with precipitation, infiltration, and change in soil water storage. Surface runoff produces erosion, and can feed washes, arroyos, and impoundments, where flooding may lead to increased recharge. Evapotranspiration removes water from soil and rock by evaporation and transpiration via plant root water uptake.	Surface runoff and evapotranspiration affect net infiltration. These effects are captured in the net infiltration map outputs used as boundary conditions for the site-scale unsaturated zone flow model. Flow fields developed for use in TSPA using the site-scale unsaturated zone flow model include the effects of precipitation and changes in precipitation under future climate conditions and associated uncertainty. The effects of surface runoff and evapotranspiration are incorporated in the infiltration model as part of the daily water balance. It is incorporated implicitly by inclusion of uncertainty as a component of the water balance at each grid cell in the net infiltration model and is indirectly included in the calculation of the weighting factors, which are passed to TSPA by the unsaturated zone flow analysis.
2.3.11.03.0A Infiltration and recharge	Infiltration into the subsurface provides a boundary condition for groundwater flow in the unsaturated zone. The amount and location of the infiltration influences the amount of seepage entering the drifts; and the amount and location of recharge influences the height of the water table, the hydraulic gradient, and therefore specific discharge. Different sources of infiltration could change the composition of groundwater passing through the repository. Mixing of these waters with other groundwaters could result in mineral precipitation, dissolution, and altered chemical gradients in the subsurface.	The hydrologic effects of infiltration and recharge are included in the infiltration model (see FEP 1.3.01.00.0A). The infiltration model includes the effects of seasonal and climate variations, climate change, soil and bedrock hydraulic and storage parameters, surface water runoff, and site topology (e.g., hillslopes and washes). The time dependence of infiltration results is linked to the timing of climate change (FEP 1.3.01.00.0A). This is incorporated into the TSPA through the unsaturated zone flow fields that use the net infiltration model results as upper boundary conditions. Infiltration uncertainty is documented in *Simulation of Net Infiltration of Present-Day and Future Climates* (SNL 2008a, Section 6.6). TSPA includes three distinct climate regimes: present-day, monsoon, and glacial-transition. Each climate regime was characterized using 40 infiltration rate maps, of which 4 are selected (10th, 30th, 50th, and 90th percentiles) to represent the range of outcomes. The initial value of the relative weights of the 40 maps per climate are equivalent such that each map has an equal probability of occurrence. The initial value of the relative weights for the four selected maps are 0.2, 0.2, 0.3, and 0.3 for the 10th, 30th, 50th, and 90th percentile realizations, respectively. The values of these weights are adjusted as part of the unsaturated zone model calibration activities described in Section 2.3.2.

Table 2.3.1-2.   Statistics and Selected Percentiles for Present-Day Average Net Infiltration [mm/yr] Results

Present Day Climate	Domain	R1 (mm/yr)	R2 (mm/yr)	R1 and R2 (mm/yr)	Precipitation (mm/yr)
Minimum [mm/yr]	Infiltration Modeling Domain (125 km^2)	2.0	3.1	2.0	133.6
	UZ Modeling Domain (39.8 km^2)	1.4	2.1	1.4	—
	Repository footprint (5.7 km^2)	1.5	1.9	1.5	—
10th Percentile	Infiltration Modeling Domain (125 km^2)	—	3.9	—	144.1
30th Percentile	Infiltration Modeling Domain (125 km^2)	—	7.3	—	160.6
Mean [mm/yr]	Infiltration Modeling Domain (125 km^2)	13.4	15.2	14.3	173.6
	UZ Modeling Domain (39.8 km^2)	14.0	15.7	14.9	—
	Repository footprint (5.7 km^2)	16.7	18.6	17.6	—
Median [mm/yr]	Infiltration Modeling Domain (125 km^2)	11.4	13.7	12.9	176.3
	UZ Modeling Domain (39.8 km^2)	12.0	12.7	12.3	—
	Repository footprint (5.7 km^2)	14.9	14.0	14.5	—
50th Percentile	Infiltration Modeling Domain (125 km^2)	—	13.0	—	189.3
90th Percentile	Infiltration Modeling Domain (125 km^2)	—	26.7	—	212.7
Maximum [mm/yr]	Infiltration Modeling Domain (125 km^2)	28.8	35.4	35.4	222.0
	UZ Modeling Domain (39.8 km^2)	32.2	40.3	40.3	—
	Repository footprint (5.7 km^2)	38.6	48.2	48.2	—
Standard Deviation [mm/yr]	Infiltration Modeling Domain (125 km^2)	8.3	9.5	8.8	25.4
	UZ Modeling Domain (39.8 km^2)	9.5	11.2	10.3	—
	Repository footprint (5.7 km^2)	11.5	13.6	12.5	—

NOTE: The Repository footprint refers to a 2002 version of the footprint rather than the 2007 footprint. The difference between these footprints is small, and the difference in average annual net infiltration between these footprints is insignificant.
R1 = Replicate #1; R2 = Replicate #2; UZ = unsaturated zone.

Source: SNL 2008a, Section 6.5.7.1[a], Combined Tables 6.5.7.1-1[a], 6.5.7.1-2[a], and 6.5.7.1-3[a]).

Table 2.3.1-3. Statistics and Selected Percentiles for Monsoon Average Net Infiltration [mm/yr] Results

Monsoon Climate	Domain	R1 (mm/yr)	R2 (mm/yr)	R1 and R2 (mm/yr)	Precipitation (mm/yr)
Minimum [mm/yr]	Infiltration Modeling Domain (125 km^2)	3.0	2.4	2.4	132.1
	UZ Modeling Domain (39.8 km^2)	1.9	1.2	1.2	—
	Repository footprint (5.7 km^2)	2.0	1.2	1.2	—
10th Percentile	Infiltration Modeling Domain (125 km^2)	6.3	—	—	206.5
30th Percentile	Infiltration Modeling Domain (125 km^2)	—	14.4	—	150.7
Mean [mm/yr]	Infiltration Modeling Domain (125 km^2)	23.5	27.6	25.5	275.2
	UZ Modeling Domain (39.8 km^2)	25.4	29.8	27.6	—
	Repository footprint (5.7 km^2)	30.5	35.3	32.9	—
Median [mm/yr]	Infiltration Modeling Domain (125 km^2)	23.3	20.4	22.8	274.8
	UZ Modeling Domain (39.8 km^2)	24.7	22.4	23.8	—
	Repository footprint (5.7 km^2)	29.3	27.1	28.4	—
50th Percentile	Infiltration Modeling Domain (125 km^2)	22.9	—	—	240.8
90th Percentile	Infiltration Modeling Domain (125 km^2)	52.6	—	—	310.2
Maximum [mm/yr]	Infiltration Modeling Domain (125 km^2)	52.6	83.4	83.4	484.7
	UZ Modeling Domain (39.8 km^2)	61.3	85.4	85.4	—
	Repository footprint (5.7 km^2)	74.5	95.3	95.3	—
Standard Deviation [mm/yr]	Infiltration Modeling Domain (125 km^2)	14.9	21.1	18.2	78.0
	UZ Modeling Domain (39.8 km^2)	17.1	22.8	20.0	—
	Repository footprint (5.7 km^2)	20.4	26.2	23.3	—

NOTE: The Repository footprint refers to a 2002 version of the footprint rather than the 2007 footprint. The difference between these footprints is small, and the difference in average annual net infiltration between these footprints is insignificant.
R1 = Replicate #1; R2 = Replicate #2; UZ = unsaturated zone.

Source: SNL 2008a, Section 6.5.7.2[a], Combined Tables 6.5.7.2-1[a], 6.5.7.2-2[a], and 6.5.7.2-3[a]).

Table 2.3.1-4.　Statistics and Selected Percentiles for Glacial-Transition Average Net Infiltration [mm/yr] Results

Glacial-Transition Climate	Domain	R1 (mm/yr)	R2 (mm/yr)	R1 and R2 (mm/yr)	Precipitation (mm/yr)
Minimum [mm/yr]	Infiltration Modeling Domain (125 km^2)	6.6	13.2	6.6	169.8
	UZ Modeling Domain (39.8 km^2)	4.2	8.0	4.2	—
	Repository footprint (5.7 km^2)	4.0	8.5	4.0	—
10th Percentile	Infiltration Modeling Domain (125 km^2)	—	13.2	—	271.7
30th Percentile	Infiltration Modeling Domain (125 km^2)	—	22.8	—	264.8
Mean [mm/yr]	Infiltration Modeling Domain (125 km^2)	30.8	29.2	30.0	283.4
	UZ Modeling Domain (39.8 km^2)	29.7	27.8	28.8	—
	Repository footprint (5.7 km^2)	39.9	37.5	38.7	—
Median [mm/yr]	Infiltration Modeling Domain (125 km^2)	28.5	28.1	28.5	291.5
	UZ Modeling Domain (39.8 km^2)	28.0	25.4	27.5	—
	Repository footprint (5.7 km^2)	38.6	35.9	38.6	—
50th Percentile	Infiltration Modeling Domain (125 km^2)	28.6	—	—	223.1
90th Percentile	Infiltration Modeling Domain (125 km^2)	—	47.0	—	286.6
Maximum [mm/yr]	Infiltration Modeling Domain (125 km^2)	64.7	56.2	64.7	379.3
	UZ Modeling Domain (39.8 km^2)	70.9	61.0	70.9	—
	Repository footprint (5.7 km^2)	97.3	81.7	97.3	—
Standard Deviation [mm/yr]	Infiltration Modeling Domain (125 km^2)	14.3	12.1	13.1	50.6
	UZ Modeling Domain (39.8 km^2)	16.5	14.2	15.2	—
	Repository footprint (5.7 km^2)	23.3	19.5	21.2	—

NOTE:　The Repository footprint refers to a 2002 version of the footprint rather than the 2007 footprint. The difference between these footprints is small, and the difference in average annual net infiltration between these footprints is insignificant.
　　　　R1 = Replicate #1; R2 = Replicate #2; UZ = unsaturated zone.

Source:　SNL 2008a, Section 6.5.7.3[a], Combined Tables 6.5.7.3-1[a], 6.5.7.3-2[a], and 6.5.7.3-3[a]).

Table 2.3.1-5. Data Sets Used in the Climate Analysis

Source	Duration of Data Available (years)	Duration of Data Used in Climate Analysis (years)	Purpose
Radiometric dating and δ^{18}O data from a calcite core at Devils Hole, Nevada[a]	507,900	425,000[b]	Establish cyclical nature of past climate and estimate timing of interglacial and glacial periods (Sections 2.3.1.2.1.2.2 and 2.3.1.2.2.1.1)
Earth-orbital parameters	10,000,000	800,000[c]	Establish 400,000-year repeating orbital cycle and timing of interglacial and glacial periods (Section 2.3.1.2.1.2.3)
Fish fossil abundance from Owens Lake, California[d]	800,000	Not directly used	Establish sequence of past climates and timing of full glacial periods (Sections 2.3.1.2.1.2.4 and 2.3.1.2.2.1.2)
Diatom data from Owens Lake, California[e]	500,000	400,000[f]	Establish sequence of past climates (Sections 2.3.1.2.1.2.4 and 2.3.1.2.2.1.2) Forecast exact timing of future climates (Sections 2.3.1.2.2.1.2 and 2.3.1.2.3.1)
Ostracode data from Owens Lake, California[g]	400,000	400,000[h]	Establish sequence of past climates (Sections 2.3.1.2.1.2.4 and 2.3.1.2.2.1.2) Forecast exact timing of future climates (Sections 2.3.1.2.2.1.2 and 2.3.1.2.3.1

Source: [a]Landwehr et al. 1997.
[b]BSC 2004a, Section 6.3, Figure 6-3.
[c]BSC 2004a, Section 6.4.
[d]Smith and Bischoff 1997, p. 121-125.
[e]Forester et al. 1999.
[f]BSC 2004a, Section 6.5.
[g]Forester et al. 1999.
[h]BSC 2004a, Section 6.5 and Figure 6-12.

Table 2.3.1-6.   Comparison of Meteorological Characteristics of Yucca Mountain and Climate Analogue Sites

Climate Regime	Location	Mean Annual Precipitation (mm)	Average Minimum and Maximum Temperature[a] (°C)
Present-Day	Site 1	183.3	10.7, 22.7
	Site 2	191.3	11.9, 20.4
	Site 3	207.8	11.4, 21.3
	Site 6	212.9	9.0, 21.2
	Site 9	110.2	10.8, 25.4
	40 MN[b]	209.0	Not provided
	Area 12 (MEDA 12)[b]	313.0	4.8, 15.2
	Cane Spring[b]	197.8	Not provided
	Amargosa Farms[b]	106.0	9.3, 27.6
	4JA (MEDA 26)[b]	145.0	10.5, 24.6
Monsoon Upper Bound	Nogales, Arizona	420.9	5.5, 26.1
	Hobbs, New Mexico	404.8	8.7, 24.7
Glacial-Transition Lower Bound	Delta, Utah	207.2	1.1, 18.8
	Beowawe, Nevada	241.1	-0.3, 17.9
Glacial-Transition Upper Bound	Rosalia, Washington	455.1	2.3, 14.5
	Spokane, Washington	419.4	2.9, 14.1
	St. John, Washington	430.5	2.3, 16.1

NOTE: [a]The average minimum and maximum temperatures represent averages across the period of record as noted in SNL 2006,Tables 7.1-2 and 7.1-3.
[b]For stations 40MN, Area12, Cane Spring, and 4JA, no temperature data was recorded. For two locations, Area12 and 4JA, a nearby NOAA station, designated as MEDA stations were used to obtain representative temperature records.

Source: SNL 2006,Tables 7.1-1, 7.1-2 and 7.1-3.

Table 2.3.1-7.   Nominal Values and Uncertainties for Parameters of the Weather Input File for the Present-Day Climate

Parameter Symbol	Nominal Value	Uncertainty Range	Uncertainty Distribution	Standard Error
a_{00}	0.934	0.924 to 0.944	uniform	0.006
$b_{00,1}$	0.027	0.027 ± 0.003	normal	0.003
$\theta_{00,1}$	−1.31 radians	-1.31 ± 0.09 radians	normal	0.09 radians
a_{10}	0.58	0.50 to 0.65	uniform	0.04
$b_{10,1}$	0.06	0.03 to 0.10	uniform	0.02
$\theta_{10,1}$	−1.5 radians	-1.5 ± 0.4 radians	normal	0.4 radians
a_{λ}	5.2 mm	4.0 to 6.5 mm	uniform	0.7
$b_{\lambda,1}$	0.7 mm	0.7 ± 0.2 mm	normal	0.2 mm
$\theta_{\lambda,1}$	+2.5 radians	$+2.5 \pm 0.7$ radians	normal	0.7 radians
a_m	0.78 mm	0.50 to 1.07 ln mm	uniform	0.16 ln mm
$b_{m,1}$	0.15 mm	0.15 ± 0.04 ln mm	normal	0.04 ln mm
$\theta_{m,1}$	+2.4 radians	$+2.4 \pm 0.4$ radians	normal	0.4 radians
αwet_{min}	9.1°C	8.6°C to 9.6°C	uniform	0.3°C
βwet_{min}	122 days	121 to 124 days	uniform	1 day
γwet_{min}	6.6°C	5.0°C to 8.1°C	uniform	0.9°C
αdry_{min}	9.7°C	9.4°C to 10.0°C	uniform	0.2°C
βdry_{min}	115 days	114 to 116 days	uniform	1 day
γdry_{min}	9.4C	6.9°C to 11.8°C	uniform	1.4°C
αwet_{max}	12.1°C	11.8°C to 12.4°C	uniform	0.2°C
βwet_{max}	117 days	116 to 118 days	uniform	1 day
γwet_{max}	14.8°C	13.9°C to 15.8°C	uniform	0.6°C
αdry_{max}	12.2°C	11.9°C to 12.4°C	uniform	0.1°C
βdry_{max}	110 days	109 to 110 days	uniform	0.3 days
γdry_{max}	20.0°C	19.2°C to 20.7°C	uniform	0.4°C
$u_2(1)$	2.36 m/s	2.36 ± 0.03 m/s	normal	0.03 m/s
$u_2(2)$	2.67 m/s	2.67 ± 0.04 m/s	normal	0.04 m/s
$u_2(3)$	2.84 m/s	2.84 ± 0.03 m/s	normal	0.03 m/s
$u_2(4)$	3.22 m/s	3.22 ± 0.04 m/s	normal	0.04 m/s

Table 2.3.1-7.   Nominal Values and Uncertainties for Parameters of the Weather Input File for the Present-Day Climate (Continued)

Parameter Symbol	Nominal Value	Uncertainty Range	Uncertainty Distribution	Standard Error
$u_2(5)$	2.97 m/s	2.97 ± 0.03 m/s	normal	0.03 m/s
$u_2(6)$	2.90 m/s	2.90 ± 0.02 m/s	normal	0.02 m/s
$u_2(7)$	2.75 m/s	2.75 ± 0.02 m/s	normal	0.02 m/s
$u_2(8)$	2.71 m/s	2.71 ± 0.02 m/s	normal	0.02 m/s
$u_2(9)$	2.64 m/s	2.64 ± 0.02 m/s	normal	0.02 m/s
$u_2(10)$	2.61 m/s	2.61 ± 0.03 m/s	normal	0.03 m/s
$u_2(11)$	2.47 m/s	2.47 ± 0.03 m/s	normal	0.03 m/s
$u_2(12)$	2.48 m/s	2.48 ± 0.03 m/s	normal	0.03 m/s

Source: SNL 2008a, Table F-22.

Table 2.3.1-8.   Nominal Values and Uncertainties for Parameters of the Weather Input File for the Monsoon Climate

Parameter Symbol	Nominal Value	Uncertainty Range	Uncertainty Distribution	Standard Error
a_{00}	0.920	0.896 to 0.944	uniform	0.014
$b_{00,1}$	0.02	−0.03 to +0.07	uniform	0.03
$\theta_{00,1}$	+2.00 radians	+1.74 to +2.25 radians	uniform	0.15 radians
a_{10}	0.58	0.50 to 0.67	uniform	0.05
$b_{10,1}$	−0.02	−0.13 to +0.10	uniform	0.07
$\theta_{10,1}$	+1.8 radians	+1.4 to +2.3 radians	uniform	0.3 radians
a_{λ}	6.5 mm	4.0 to 9.0 mm	uniform	1.4 mm
$b_{\lambda,1}$	1.6 mm	−1.3 to 4.5 mm	uniform	1.7 mm
$\theta_{\lambda,1}$	−1.6 radians	−2.0 to −1.1 radians	uniform	0.3
a_m	0.9 mm	0.5 to 1.3 ln mm	uniform	0.2 ln mm
$b_{m,1}$	0.1 mm	−0.3 to 0.5 ln mm	uniform	0.2 ln mm
$\theta_{m,1}$	−1.48 radians	−1.78 to −1.17 radians	uniform	0.18 radians
αwet_{min}	9.4°C	8.2°C to 10.5°C	uniform	0.7°C
βwet_{min}	122 days	119 to 124 days	uniform	1 day
γwet_{min}	7.4°C	5.0°C to 9.7°C	uniform	1.4°C
αdry_{min}	10.2°C	9.4°C to 11.0°C	uniform	0.5°C
βdry_{min}	117 days	114 to 120 days	uniform	2 days
γdry_{min}	8°C	5°C to 12°C	uniform	2°C
αwet_{max}	11.4°C	10.5°C to 12.4°C	uniform	0.5°C
βwet_{max}	115 days	112 to 118 days	uniform	2 days
γwet_{max}	18°C	14°C to 22°C	uniform	2°C
αdry_{max}	10.4	8.4°C to 12.4°C	uniform	1.2°C
βdry_{max}	113 days	109 to 117 days	uniform	2 days
γdry_{max}	23°C	19°C to 27°C	uniform	2°C
$u_2(1)$	2.36 m/s	2.36 ± 0.03 m/s	normal	0.03 m/s
$u_2(2)$	2.67 m/s	2.67 ± 0.04 m/s	normal	0.04 m/s
$u_2(3)$	2.84 m/s	2.84 ± 0.03 m/s	normal	0.03 m/s
$u_2(4)$	3.22 m/s	3.22 ± 0.04 m/s	normal	0.04 m/s

Table 2.3.1-8. Nominal Values and Uncertainties for Parameters of the Weather Input File for the Monsoon Climate (Continued)

Parameter Symbol	Nominal Value	Uncertainty Range	Uncertainty Distribution	Standard Error
$u_2(5)$	2.97 m/s	2.97 ± 0.03 m/s	normal	0.03 m/s
$u_2(6)$	2.90 m/s	2.90 ± 0.02 m/s	normal	0.02 m/s
$u_2(7)$	2.75 m/s	2.75 ± 0.02 m/s	normal	0.02 m/s
$u_2(8)$	2.71 m/s	2.71 ± 0.02 m/s	normal	0.02 m/s
$u_2(9)$	2.64 m/s	2.64 ± 0.02 m/s	normal	0.02 m/s
$u_2(10)$	2.61 m/s	2.61 ± 0.03 m/s	normal	0.03 m/s
$u_2(11)$	2.47 m/s	2.47 ± 0.03 m/s	normal	0.03 m/s
$u_2(12)$	2.48 m/s	2.48 ± 0.03 m/s	normal	0.03 m/s

Source: SNL 2008a, Table F-23.

Table 2.3.1-9.   Nominal Values and Uncertainties for Parameters of the Weather Input File for the Glacial Transition Climate

Parameter Symbol	Nominal Value	Uncertainty Range	Uncertainty Distribution	Standard Error
a_{00}	0.84	0.78 to 0.89	uniform	0.03
$b_{00,1}$	0.066	0.028 to 0.104	uniform	0.02
$\theta_{00,1}$	−1.12 radians	−1.12 ± 0.010 radians	normal	0.010 radians
a_{10}	0.54	0.47 to 0.62	uniform	0.04
$b_{10,1}$	0.07	0.02 to 0.11	uniform	0.03
$\theta_{10,1}$	−0.93 radians	−0.93 ± 0.84 radians	normal	0.84 radians
a_{λ}	3.8 mm	3.1 to 4.5 mm	uniform	0.4 mm
$b_{\lambda,1}$	0.6 mm	0.1 to 1.0 mm	uniform	0.3 mm
$\theta_{\lambda,1}$	—	−π to π radians	uniform	—
a_m	0.70 mm	0.48 to 0.92 ln mm	uniform	0.13 ln mm
$b_{m,1}$	0.12 mm	0.08 to 0.16 ln mm	uniform	0.02 ln mm
$\theta_{m,1}$	—	−π to π radians	uniform	—
αwet_{min}	8.4°C	6.3°C to 10.4°C	uniform	1.2°C
βwet_{min}	DOY 116	DOY 114 to 118	uniform	1 day
γwet_{min}	2.6°C	1.2°C to 3.9°C	uniform	0.8°C
αdry_{min}	9.6°C	7.5°C to 11.6°C	uniform	1.2°C
βdry_{min}	DOY 111	DOY 106 to 116	uniform	3 days
γdry_{min}	0.9°C	0.8°C to 2.6°C	uniform	1.0°C
αwet_{max}	11.8°C	10.1°C to 13.4°C	uniform	1.0°C
βwet_{max}	DOY 113	DOY 111 to 115	uniform	1 day
γwet_{max}	13.8°C	11.7°C to 15.9°C	uniform	1.2°C
αdry_{max}	14.4°C	13.8°C to 15.0°C	uniform	0.3°C
βdry_{max}	DOY 114	DOY 112 to 117	uniform	1 day
γdry_{max}	17.1°C	14.6°C to 19.6°C	uniform	1.4°C
$u_2(1)$	2.36 m/s	2.36 ± 0.03 m/s	normal	0.03 m/s
$u_2(2)$	2.67 m/s	2.67 ± 0.04 m/s	normal	0.04 m/s
$u_2(3)$	2.84 m/s	2.84 ± 0.03 m/s	normal	0.03 m/s
$u_2(4)$	3.22 m/s	3.22 ± 0.04 m/s	normal	0.04 m/s

Table 2.3.1-9.   Nominal Values and Uncertainties for Parameters of the Weather Input File for the Glacial Transition Climate (Continued)

Parameter Symbol	Nominal Value	Uncertainty Range	Uncertainty Distribution	Standard Error
$u_2(5)$	2.97 m/s	2.97 ± 0.03 m/s	normal	0.03 m/s
$u_2(6)$	2.90 m/s	2.90 ± 0.02 m/s	normal	0.02 m/s
$u_2(7)$	2.75 m/s	2.75 ± 0.02 m/s	normal	0.02 m/s
$u_2(8)$	2.71 m/s	2.71 ± 0.02 m/s	normal	0.02 m/s
$u_2(9)$	2.64 m/s	2.64 ± 0.02 m/s	normal	0.02 m/s
$u_2(10)$	2.61 m/s	2.61 ± 0.03 m/s	normal	0.03 m/s
$u_2(11)$	2.47 m/s	2.47 ± 0.03 m/s	normal	0.03 m/s
$u_2(12)$	2.48 m/s	2.48 ± 0.03 m/s	normal	0.03 m/s

Source: SNL 2008a, Table F-24.

Table 2.3.1-10. Comparison of the 10 Representative Years Used to Model Net Infiltration for the Present-Day Climate

Representative Year	Probability that Precipitation will be Exceeded (1-p)	Weights	Precipitation (mm/yr)	Mean Net Infiltration for Each Representative Year (mm/yr)	Recurrence Interval (yr)	Fraction of Contribution to Longterm Mean Infiltration
1	0.001	0.001	708	82.58	1,000.00	0.76
2	0.003	0.002	549	88.06	333.33	1.74
3	0.01	0.007	430	75.77	100.00	4.85
4	0.03	0.02	360	55.77	33.33	9.95
5	0.1	0.07	292	45.39	10.00	24.44
6	0.28	0.18	227	24.27	3.57	28.88
7	0.46	0.18	186	14.22	2.17	16.34
8	0.64	0.18	157	8.34	1.56	8.42
9	0.82	0.18	126	3.00	1.22	3.21
10	1	0.18	89	1.48	1.00	1.40

NOTE: Σ (weight * infiltration for a representative year) = mean net infiltration = 14.3 mm/yr.

Source: Columns 1, 2, 5, 6, 7: SNL 2008a, Table 6.5.7.5-1; weights (column 3): SNL 2008a, Section F4.1.2; precipitation (column 4): Output DTN: SN0701T0502206.037, average of 40 vectors in files: \Welcome to Massif\Massif\Present Day Uncertainty\Post Processing\Intermediate Output Files\PD_10yr_Yearly_PPT_R1.txt and PD_10yr_Yearly_PPT_R2.txt.

Table 2.3.1-11. Comparison of the 10 Representative Years Used to Model Net Infiltration for the Monsoon Climate

Representative Year	Probability that Precipitation will be Exceeded (1-p)	Weights	Precipitation (mm/yr)	Mean Net Infiltration for Each Representative Year (mm/yr)	Recurrence Interval (yr)	Fraction of Contribution to Longterm Mean Infiltration
1	0.001	0.001	1026	67.79	1,000.00	0.33
2	0.003	0.002	901	84.04	333.33	0.96
3	0.01	0.007	704	84.99	100.00	3.03
4	0.03	0.02	590	74.47	33.33	7.45
5	0.1	0.07	452	65.71	10.00	21.22
6	0.28	0.18	360	45.73	3.57	31.84
7	0.46	0.18	291	24.98	2.17	16.76
8	0.64	0.18	247	17.45	1.56	9.51
9	0.82	0.18	201	10.29	1.22	6.06
10	1	0.18	146	5.05	1.00	2.84

NOTE: Σ (weight * infiltration for a representative year) = mean net infiltration = 25.5 mm/yr.

Source: Columns 1, 2, 5, 6, 7: SNL 2008a, Table 6.5.7.5-2; weights (column 3): SNL 2008a, Section F4.1.2; precipitation (column 4): Output DTN: SN0701T0502206.037, average of 40 vectors in files: \Welcome to Massif\Massif\Monsoon Uncertainty\Post Processing\Intermediate Output Files\ MO_10yr_Yearly_PPT_R1.txt and MO_10yr_Yearly_PPT_R2.txt.

Table 2.3.1-12. Comparison of the 10 Representative Years Used to Model Net Infiltration for the Glacial Transition Climate

Representative Year	Probability that Precipitation will be Exceeded (1-p)	Weights	Precipitation (mm/yr)	Mean Net Infiltration for Each Representative Year (mm/yr)	Recurrence Interval (yr)	Fraction of Contribution to Longterm Mean Infiltration
1	0.001	0.001	567	96.45	1,000.00	0.37
2	0.003	0.002	514	64.04	333.33	0.69
3	0.01	0.007	473	78.96	100.00	2.07
4	0.03	0.02	432	64.75	33.33	4.76
5	0.1	0.07	384	53.44	10.00	12.56
6	0.28	0.18	337	40.90	3.57	24.85
7	0.46	0.18	301	32.01	2.17	19.38
8	0.64	0.18	273	27.07	1.56	15.45
9	0.82	0.18	245	20.50	1.22	11.75
10	1	0.18	194	13.33	1.00	8.13

NOTE: $\sum$ (weight * infiltration for a representative year) = mean net infiltration = 30.0 mm/yr.

Source: Columns 1, 2, 5, 6, 7: SNL 2008a, Table 6.5.7.5-3; weights (column 3): SNL 2008a, Section F4.1.2; precipitation (column 4): Output DTN: SN0701T0502206.037, average of 40 vectors in files: \Welcome to Massif\Massif\Glacial Uncertainty\Post Processing\Intermediate Output Files\ GT_10yr_Yearly_PPT_R1.txt and GT_10yr_Yearly_PPT_R2.txt.

Table 2.3.1-13. Nominal Values and Standard Error for K_{sat}, θ_s, and θ_{WP}

Saturated Hydraulic Conductivity (K_{sat_soil})				
Soil Group	Mean Ln (K_{sat_soil}), (cm/sec)	Standard Error (Ln)	Nominal Value (cm/s)[a]	Nominal Value (m/s)
1	−9.436	0.196	7.98×10^{-5}	7.98×10^{-7}
2/6	−9.105	0.175	1.11×10^{-4}	1.11×10^{-6}
3/4	−9.571	0.137	6.97×10^{-5}	6.97×10^{-7}
5/7/9	−9.593	0.079	6.82×10^{-5}	6.82×10^{-7}
Saturated Water Content (θ_s)				
Soil Group	Mean θ_s (m³/m³)	Standard Error (m³/m³)	Nominal Value (m³/m³)[b]	
1	0.23	1.31×10^{-2}	0.23	
2/6	0.21	1.18×10^{-2}	0.21	
3/4	0.16	6.69×10^{-3}	0.16	
5/7/9	0.23	7.61×10^{-3}	0.23	
Permanent Wilting Point (θ_{WP})				
Soil Group	Mean θ_{WP} (m³/m³)	Standard Error (m³/m³)	Nominal Value (m³/m³)[b]	
1	0.040	0.003	0.040	
2/6	0.037	0.003	0.037	
3/4	0.024	0.001	0.024	
5/7/9	0.039	0.002	0.039	

NOTE: [a]Nominal values of saturated hydraulic conductivity are equal to $\exp(\ln(K_{sat\_soil}))$ for each soil group.
[b]Nominal values of θ_s and θ_{WP} are equal to mean values of θ_s and θ_{WP} for each soil group.

Source: SNL 2008a, Section 6.5.2.3, Table 6.5.2.3-1.

Table 2.3.1-14. Nominal Values and Standard Error for θ_{FC}, and θ_{HC}

Soil Field Capacity (θ_{FC})					
Soil Group	Mean θ_{FC}[a] (−0.10 bar) (m³/m³)	Standard Error (m³/m³)	Mean θ_{FC}[b] (−0.33 bar) (m³/m³)	Standard Error (m³/m³)	Nominal Value (m³/m³)
1	0.183	0.012	0.125	0.011	0.155
2/6	0.177	0.012	0.123	0.010	0.151
3/4	0.123	0.006	0.075	0.004	0.100
5/7/9	0.208	0.007	0.134	0.005	0.172
Soil Water Holding Capacity (θ_{HC})					
Soil Group	Mean θ_{HC} (−0.10 bar θ_{FC}) (m³/m³)	Standard Error (m³/m³)	Mean θ_{HC} (−0.33 bar θ_{FC}) (m³/m³)	Standard Error (m³/m³)	Nominal Value (m³/m³)
1	0.143	0.010	0.085	0.009	0.115
2/6	0.140	0.010	0.086	0.008	0.114
3/4	0.098	0.005	0.051	0.003	0.076
5/7/9	0.169	0.005	0.095	0.004	0.133

NOTE: [a]Field capacity defined as moisture content at a pressure of −0.10 bar.
        [b]Field capacity defined as moisture content at a pressure of −0.33 bar.

Source: SNL 2008a, Section 6.5.2.3, Table 6.5.2.3-2.

Table 2.3.1-15. Bulk Bedrock Mean K_{sat} Values

Infiltration Hydrogeologic Unit		Mean (m/s)	Lithostratigraphic Name	Lithostratigraphic Unit Symbol
Number	Symbol			
401	hcr4	1.8×10^{-6}	Tiva Canyon Tuff—crystal-rich nonlithophysal zone, subvitrophyre transition subzone	Tpcrn4
402	hcr3	1.2×10^{-6}	Tiva Canyon Tuff—crystal-rich nonlithophysal zone, pumice-poor subzone	Tpcrn3
403	hcr2	1.8×10^{-6}	Tiva Canyon Tuff—crystal-rich nonlithophysal zone, mixed pumice subzone	Tpcrn2
404	hcr1	7.7×10^{-7}	Tiva Canyon Tuff—crystal-rich lithophysal zone	Tpcrl
405	hcul	1.1×10^{-6}	Tiva Canyon Tuff—crystal-poor upper lithophysal zone	Tpcpul
406	hcmn	1.3×10^{-6}	Tiva Canyon Tuff—crystal-poor middle nonlithophysal zone	Tpcpmn
407	hcll	1.1×10^{-6}	Tiva Canyon Tuff—crystal-poor lower lithophysal zone	Tpcpll
408	hcln	1.7×10^{-6}	Tiva Canyon Tuff—crystal-poor lower nonlithophysal zone	Tpcpln
409	hcv2	9.2×10^{-7}	Topopah Canyon Tuff—crystal-poor, vitric, moderately welded subzone	Tpcpv2
410	hcv1	2.7×10^{-6}	Tiva Canyon Tuff—crystal-poor, vitric, nonwelded subzone	Tpcpv1
411	hbt4	1.4×10^{-5}	Pre-Tiva Canyon bedded tuff	Tpbt4
412	hym	4.9×10^{-6}	Yucca Mountain Tuff (not divided, total formation)	Tpy
413	hbt3	3.9×10^{-6}	Pre-Yucca Mountain bedded tuff	Tpbt3
414	hpc	3.1×10^{-6}	Pah Canyon Tuff (not divided, total formation)	Tpp
415	hbt2	9.4×10^{-6}	Pre-Pah Canyon bedded tuff	Tpbt2
416	htrv3	1.7×10^{-5}	Topopah Spring Tuff—crystal-rich, vitric, nonwelded to moderately welded subzones	Tptrv3-2
417	htrv1	3.3×10^{-5}	Topopah Spring Tuff—crystal-rich, vitric, densely welded subzone	Tptrv1
418	htrn	1.5×10^{-6}	Topopah Spring Tuff—crystal-rich nonlithophysal, vapor-phase corroded subzone	Tptrn2

Table 2.3.1-15. Bulk Bedrock Mean K_{sat} Values (Continued)

Infiltration Hydrogeologic Unit		Mean (m/s)	Lithostratigraphic Name	Lithostratigraphic Unit Symbol
Number	Symbol			
419	htrl	1.2×10^{-6}	Topopah Spring Tuff—crystal-rich transition subzone	Tptrn1, Tptrl1
420	htul	9.0×10^{-7}	Topopah Spring Tuff—crystal-poor upper lithophysal zone	Tptpul
421	htmn	1.3×10^{-6}	Topopah Spring Tuff—crystal-poor middle nonlithophysal zone	Tptpmn
422	htll	1.2×10^{-6}	Topopah Spring Tuff—crystal-poor lower lithophysal zone	Tptll
423	htln	1.7×10^{-6}	Topopah Spring Tuff—crystal-poor lower nonlithophysal zone	Tptpln
424	htpv3	8.5×10^{-7}	Topopah Spring Tuff—crystal-poor, citric, densely welded subzone	Tptpv3
425	htv2v	8.0×10^{-6}	Topopah Spring Tuff—crystal-poor, vitric, moderately welded subzone	Tptpv2
426	htv2z	9.4×10^{-7}	Topopah Spring Tuff—crystal-poor, zeolitic, moderately welded subzone	Tptpv2
427	htv1v	1.0×10^{-5}	Topopah Spring Tuff—crystal-poor, vitric, nonwelded subzone	Tptpv1
428	htv1z	9.4×10^{-7}	Topopah Spring Tuff—crystal-poor, zeolitic, nonwelded subzone	Tptpv1
429	hacv	2.0×10^{-4}	Calico Hills Formation—pyroclastic rocks flow	Tac
430	hacz	9.4×10^{-7}	Calico Hills Formation—pyroclastic rocks flow	Tac
431	habtv	—	Pre-Calico Hills—bedded tuff	Tacbt
432	habtz	9.4×10^{-7}	Pre-Calico Hills—bedded tuff	Tacbt
433	hpuvv	—	Prow Pass Tuff—upper vitric	Tcpuv
434	hpuvz	9.4×10^{-6}	Prow Pass Tuff—upper vitric	Tcpuv
435	hpuc	1.5×10^{-6}	Prow Pass Tuff—upper crystallized	Tcpuc
436	hpmlc	1.2×10^{-6}	Prow Pass Tuff—moderately welded and crystallized	Tcpm
437	hpbvz	6.4×10^{-7}	Pre-Prow Pass—bedded tuff	Tcpbt
438	hbucm	2.1×10^{-6}	Bullfrog Tuff—welded and crystallized	Tcbuc, Tcbm, Tcblc

Source: SNL 2008a, Table 6.5.2.6-1; BSC 2006b, Table 6-3a.

Table 2.3.1-16. Best-Fit Parameter Values Describing the Relationship between NDVI' and K_{cb}

Parameter Description	Symbol	Nominal Value (mean)	Standard Deviation	Distribution	Climate
Slope between NDVI' and K_{cb}	C_{Kcb1}	9.7	2.1	normal	all
Intercept for linear regression between NDVI' and K_{cb}	C_{Kcb2}	−0.05	0.05	normal	all

Source: SNL 2008a, Table 6.5.3.7-4.

Table 2.3.1-17. Average and Standard Deviations of Weighted Mean Water Fluxes Fractions for the Present Day Climate Simulations (Fraction of Precipitation)

Present Day Climate	Mean (mm/yr)	SD (mm/yr)	Mean (% precip)	SD (% precip)	Mean IC1 (mm/yr)	SD IC1 (mm/yr)	Mean IC1 (% precip)	SD IC1 (% precip)
Precipitation	173.6	25.1	NA	NA	173.6	25.1	NA	NA
Infiltration	14.3	8.7	8.02%	4.50%	14.8	8.8	8.29%	4.50%
ET	151.6	20.1	87.68%	5.66%	158.9	20.5	92.02%	6.58%
Runoff	3.7	2.8	2.07%	1.56%	3.7	2.8	2.07%	1.56%
Sublimation	0.7	0.2	0.42%	0.11%	0.7	0.2	0.42%	0.11%
Storage	3.3	3.3	1.82%	1.77%	-4.6	3.9	-2.80%	2.42%
Snow	0.0	0.0	0.00%	0.00%	0.0	0.0	0.00%	0.00%

NOTE: IC1 indicates results from alternative simulation using wetter initial conditions than for base case simulations. NA = not applicable.

Source: SNL 2008a, Section 6.5.7.4, Table 6.5.7.4-1.

Table 2.3.1-18. Average and Standard Deviation of Weighted Mean Water Fractions Fluxes for the Monsoon Climate Simulations (Fraction of Precipitation)

Monsoon Climate	Mean (mm/yr)	SD (mm/yr)	Mean (% precip)	SD (% precip)	Mean IC1 (mm/yr)	SD IC1 (mm/yr)	Mean IC1 (% precip)	SD IC1 (% precip)
Precipitation	275.2	77.0	NA	NA	275.2	77.0	NA	NA
Infiltration	25.5	17.9	8.69%	4.75%	26.1	18.0	8.89%	4.73%
ET	230.4	57.8	84.88%	8.18%	238.3	58.1	88.01%	8.93%
Runoff	15.6	12.1	5.35%	3.63%	15.6	12.1	5.36%	3.63%
Sublimation	0.1	0.2	0.04%	0.07%	0.1	0.2	0.04%	0.07%
Storage	3.6	8.6	1.04%	2.92%	-4.9	9.4	-2.29%	3.56%
Snow	0.0	0.0	0.00%	0.00%	0.0	0.0	0.00%	0.00%

NOTE: IC1 indicates results from alternative simulation using wetter initial conditions than for base case simulations.
NA = not applicable.

Source: SNL 2008a, Section 6.5.7.4, Table 6.5.7.4-2.

Table 2.3.1-19. Average and Standard Deviation of Weighted Mean Water Fractions Fluxes for the Glacial-Transition Climate Simulations (Fraction of Precipitation)

Glacial-Transition Climate	Mean (mm/yr)	SD (mm/yr)	Mean (% precip)	SD (% precip)	Mean IC1 (mm/yr)	SD IC1 (mm/yr)	Mean IC1 (% precip)	SD IC1 (% precip)
Precipitation	283.4	50.0	NA	NA	283.4	50.0	NA	NA
Infiltration	30.0	12.9	10.38%	3.66%	30.5	12.9	10.57%	3.61%
ET	243.7	41.7	86.16%	3.90%	254.6	42.2	90.15%	4.46%
Runoff	1.1	1.2	0.39%	0.47%	1.1	1.2	0.39%	0.47%
Sublimation	3.6	0.8	1.27%	0.21%	3.6	0.8	1.27%	0.21%
Storage	5.1	3.9	1.79%	1.29%	-6.4	4.7	-2.38%	1.86%
Snow	0.0	0.0	0.00%	0.00%	0.0	0.0	0.00%	0.00%

NOTE: IC1 indicates results from alternative simulation using wetter initial conditions than for base case simulations.
NA = not applicable.

Source: SNL 2008a, Section 6.5.7.4, Table 6.5.7.4-3.

Table 2.3.1-20. Comparison of Mean Net Infiltration Results of the Soil Conductivity Variation Simulations with Results of the Uncertainty Analysis

Present-Day Climate				
Percentile	10th	30th	50th	90th
Replicate	R2	R2	R2	R2
Realization	10	2	8	14
Entire Domain Infiltration (mm/yr)	3.9	7.3	13.0	26.7
Entire Domain Variation Infiltration (mm/yr)	4.1	7.7	15.9	27.2
UZ Infiltration (mm/yr)	3.3	5.9	10.8	28.3
UZ Variation Infiltration (mm/yr)	3.5	5.9	13.4	27.3
Repository Infiltration (mm/yr)	3.9	6.5	10.9	34.4
Repository Variation Infiltration (mm/yr)	3.9	4.9	9.5	28.3
Runoff Fraction (%)	0.9	1.8	3.8	1.3
Runoff Fraction Variation (%)	0.8	1.6	3.2	1.1
Mean Annual Precipitation (mm/yr)	144.1	160.6	189.3	212.7

NOTE: The Repository footprint refers to a 2002 version of the footprint rather than the 2007 footprint. The difference between these footprints is small, and the difference in average annual net infiltration between these footprints is insignificant.
UZ = unsaturated zone.

Source: SNL 2008a, Section 7.1.3.2[a], Table 7.1.3.2-1[a].

Table 2.3.1-21. Comparison of Percent of the Total Net Infiltration Occurring in Each Soil Group Between the Soil Conductivity Variation Simulations and the Results of the Uncertainty Analysis

Present-Day Climate	Percent of Net Infiltration [%]			
Percentile	10th	30th	50th	90th
Replicate	R2	R2	R2	R2
Realization	10	2	8	14
Soil Group 1 (%)	0.2	0.7	3.5	0.0
Soil Group 1 Variation (%)	0.0	0.1	0.6	0.0
Soil Groups 2/6 (%)	0.4	1.0	5.2	0.0
Soil Groups 2/6 Variation (%)	0.0	0.1	0.7	0.0
Soil Groups 3/4 (%)	1.4	2.3	10.6	0.2
Soil Groups 3/4 Variation (%)	19.7	35.4	55.1	24.9
Soil Groups 5/7/9 (%)	85.7	88.6	76.0	97.1
Soil Groups 5/7/9 Variation (%)	66.6	54.6	34.4	69.9
Soil Group 8 (%)	12.3	7.3	4.7	2.7
Soil Group 8 Variation (%)	13.7	9.8	9.2	5.2

Source: SNL 2008a, Section 7.1.3.2[a], Table 7.1.3.2-2[a].

Table 2.3.1-22. 11 Parameters Screened into the Uncertainty Analysis for the Present-Day Climate

Parameter Symbol	Parameter Name and Description	Uncertainty Range	Uncertainty Distribution
Parameters Varied Independently in Uncertainty Analysis for Present-Day Climate[a]			
a_m	Annual average of the natural logarithm of the amount of daily rainfall on days with precipitation (Section 6.5.1.2)	0.50 to 1.07 (ln mm)	uniform
h_{plant}	Plant height (Section 6.5.3.3)	0.2 m to 0.6 m	uniform
Z_r	Maximum rooting depth (Section 6.5.3.2)	0.6 m to 2.6 m	uniform
$depth_{soil}(4)$	Soil depth for soil depth class 4 (Section 6.5.2.4.1[a])	0.1 m to 0.5 m	uniform
$K_{sat\_rock}(405)$	Bulk saturated hydraulic conductivity of bedrock Infiltration Hydrogeologic Unit 405 (Section 6.5.2.6)	7.6×10^{-8} m/s to 4.8×10^{-6} m/s	loguniform
$K_{sat\_rock}(406)$	Bulk saturated hydraulic conductivity of bedrock Infiltration Hydrogeologic Unit 406 (Section 6.5.2.6)	2.1×10^{-8} m/s to 7.7×10^{-6} m/s	loguniform
$\theta_{HC}(5/7/9)$	Holding capacity of soil group 5/7/9 (Section 6.5.2.3)	0.09 to 0.17 (m^3/m^3)	uniform
REW	Readily evaporable water (Section 6.5.4.2)	2 to 10 mm	uniform
K_{c_min}	Minimum transpiration coefficient (K_c) (Section 6.5.4.2)	0.0 to 0.2 (unitless)	50% of values = 0.0, 50% of values vary linearly from 0.0 to 0.2 [pdf is $(0.2 - K_{cmin})/0.04$]
Z_e	Evaporation layer depth (Section 6.5.4.2)	0.1 to 0.2 m	uniform
C_{Kcb2}	Slope of the NDVI' – K_{cb} function (Section 6.5.3.7)	9.7 ± 2.1 (unitless)	normal
Parameters Correlated with Other Parameters That Varied Independently in Uncertainty Analysis for Present-Day Climate[b]			
a_λ	Annual average of the mean amount of daily rainfall on days with precipitation (Section 6.5.1.2)	4.0 to 6.5 mm	uniform

NOTE:　[a]See Table I-2.
　　　　　[b]See Table I-3.
　　　　　All Section numbers refer to Sections in SNL 2008a.

Source:　SNL 2008a, Appendix I, Tables I-2 and I-3.

Table 2.3.1-23. 19 Parameters Screened into the Uncertainty Analysis for the Monsoon Climate

Parameter Symbol	Parameter Name and Description	Uncertainty Range	Uncertainty Distribution
Parameters Varied Independently in Uncertainty Analysis for Monsoon Climate[a]			
a_{00}	Annual average of the probability of no precipitation given that the previous day was dry (Section 6.5.1.2)	0.896 to 0.944 (unitless)	uniform
a_m	Annual average of the natural logarithm of the amount of daily rainfall on days with precipitation (Section 6.5.1.2)	0.5 to 1.3 (ln mm)	uniform
$b_{m,1}$	Amplitude of the annual variation in the median amount of daily rainfall on days with precipitation (Section 6.5.1.2)	−0.3 to +0.5 mm	uniform
γwet_{max}	Annual average maximum daily temperature on days with precipitation (Section 6.5.1.2)	14 C to 22 C	uniform
h_{plant}	Plant height (Section 6.5.3.3)	0.2 m to 0.6 m	uniform
Z_r	Maximum rooting depth (Section 6.5.3.2)	0.6 m to 2.6 m	uniform
Rate of duration increase with precipitation	Slope of the relationship between duration of daily precipitation and amount of daily rainfall (Section 6.5.1.7[a])	0.14 hr/mm to 0.43 hr/mm	uniform
$depth_{soil}(4)$	Soil depth for soil depth class 4 (Section 6.5.2.4.1[a])	0.1 m to 0.5 m	uniform
$K_{sat\_rock}(405)$	Bulk saturated hydraulic conductivity of bedrock Infiltration Hydrogeologic Unit 405 (Section 6.5.2.6)	7.6×10^8 m/s to 4.8×10^6 m/s	loguniform
$K_{sat\_rock}(406)$	Bulk saturated hydraulic conductivity of bedrock Infiltration Hydrogeologic Unit 406 (Section 6.5.2.6)	2.1×10^8 m/s to 7.7×10^6 m/s	loguniform
$\theta_{HC}(5/7/9)$	Holding capacity of soil group 5/7/9 (Section 6.5.2.3)	0.09 to 0.17 (m^3/m^3)	uniform
REW	Readily evaporable water (Section 6.5.4.2)	2 to 10 mm	uniform
K_{c_min}	Minimum transpiration coefficient (K_c) (Section 6.5.4.2)	0.0 to 0.2 (unitless)	50% of values = 0.0, 50% of values vary linearly from 0.0 to 0.2 [pdf is $(0.2K_{cmin})/0.04$]
Z_e	Evaporation layer depth (Section 6.5.4.2)	0.1 to 0.2 m	uniform

Table 2.3.1-23. 19 Parameters Screened into the Uncertainty Analysis for the Monsoon Climate (Continued)

Parameter Symbol	Parameter Name and Description	Uncertainty Range	Uncertainty Distribution
C_{Kcb2}	Slope of the NDVI'—K_{cb} function (Section 6.5.3.7)	9.7 ± 2.1 (unitless)	normal
Parameters Correlated with Other Parameters that Varied Independently in Uncertainty Analysis for Monsoon Climate[b]			
a_λ	Annual average of the mean amount of daily rainfall on days with precipitation (Section 6.5.1.2)	4.0 mm to 9.0 mm	uniform
$b_{00,1}$	Amplitude of the annual variation in the probability of no precipitation given that the previous day was dry (Section 6.5.1.2)	-0.03 to $+0.07$ (unitless)	uniform
$b_{10,1}$	Amplitude of the annual variation in the probability of no precipitation given that precipitation occurred during the previous day (Section 6.5.1.2)	-0.13 to $+0.10$ (unitless)	uniform
$b_{\lambda,1}$	Amplitude of the annual variation in the mean amount of daily rainfall on days with precipitation (Section 6.5.1.2)	-1.3 mm to $+4.5$ mm	uniform

NOTE: [a]See Table I-5.
[b]See Table I-6.
All Section numbers refer to Sections in SNL 2008a.

Source: SNL 2008a, Appendix I, Tables I-5 and I-6.

Table 2.3.1-24. 17 Parameters Screened into the Uncertainty Analysis for the Glacial-Transition Climate

Parameter Symbol	Parameter Name and Description	Uncertainty Range	Uncertainty Distribution
Parameters Varied Independently in Uncertainty Analysis for Glacial Transition Climate[a]			
a_{00}	Annual average of the probability of no precipitation given that the previous day was dry (Section 6.5.1.2)	0.78 to 0.89 (unitless)	uniform
a_m	Annual average of the natural logarithm of the amount of daily rainfall on days with precipitation (Section 6.5.1.2)	0.48 to 0.92 (ln mm)	uniform
$\theta_{\lambda,1}$	Phase of the annual variation of mean daily rainfall on days with precipitation (θ_λ in Section 6.5.1.2)	$-\pi$ radians to $+\pi$ radians	uniform
Rate of duration increase with precipitation	Slope of the relationship between duration of daily precipitation and amount of daily rainfall (Section 6.5.1.7[a])	0.32 to 0.71 hr/mm	uniform
h_{plant}	Plant height (Section 6.5.3.3)	0.6 to 1.8 m	uniform
Z_r	Maximum rooting depth (Section 6.5.3.2)	1.0 to 4.0 m	uniform
$depth_{soil}(4)$	Soil depth for soil depth class 4 (Section 6.5.2.4.1[a])	0.1 to 0.5 m	uniform
$K_{sat\_rock}(405)$	Saturated hydraulic conductivity of bedrock Infiltration Hydrogeologic Unit 405 (Section 6.5.2.6)	7.6×10^{-8} m/s to 4.8×10^{-6} m/s	loguniform
$K_{sat\_rock}(406)$	Saturated hydraulic conductivity of bedrock Infiltration Hydrogeologic Unit 406 (Section 6.5.2.6)	2.1×10^{-8} m/s to 7.7×10^{-6} m/s	loguniform
$\theta_{HC}(5/7/9)$	Holding capacity of soil group 5/7/9 (Section 6.5.2.3)	0.09 to 0.17 (m^3/m^3)	uniform
REW	Readily evaporable water (Section 6.5.4.2)	2 to 10 mm	uniform
K_{c_min}	Minimum transpiration coefficient (K_c) (Section 6.5.4.2)	0.0 to 0.2 (unitless)	50% of values = 0.0, 50% of values vary linearly from 0.0 to 0.2 [pdf is $(0.2-K_{cmin})/0.04$]
Z_e	Evaporation layer depth (Section 6.5.4.2)	0.1 to 0.2 m	uniform
C_{Kcb2}	Slope of the NDVI'—K_{cb} function (Section 6.5.3.7)	9.7 ± 2.1 (unitless)	normal

Table 2.3.1-24. 17 Parameters Screened into the Uncertainty Analysis for the Glacial-Transition
              Climate (Continued)

Parameter Symbol	Parameter Name and Description	Uncertainty Range	Uncertainty Distribution
Parameters Correlated with Other Parameters That Varied Independently in Uncertainty Analysis for Glacial Transition Climate[b]			
a_λ	Constant term in Fourier series for $\lambda(d)$	3.1 to 4.5 mm	uniform
$\Theta_{m,1}$	Phase of first-order term in Fourier series for $m(d)$	$-\pi$ radians to $+\pi$ radians	uniform
Intercept−1	Minimum precipitation duration	0.70 to 1.22 hr	uniform

NOTE: [a]See Table I-8.
        [b]See Table I-9.
        All section numbers refer to sections in *Simulation of Net Infiltration for Present-Day and Potential Future Climates* (SNL 2008a).

Source: SNL 2008a, Appendix I, Tables I-8 and I-9.

Table 2.3.1-25. Parameter List for Extended Sensitivity Analysis Using One Watershed

	LHS Name	Symbol or Description	Distribution	P1	P2	Units
1	lnRks_401	$K_{sat\_rock}(401)$	Loguniform	−15.38	−11.94	m/s
2	lnRks_402	$K_{sat\_rock}(402)$	Loguniform	−17.26	−11.97	m/s
3	lnRks_403	$K_{sat\_rock}(403)$	Loguniform	−15.42	−11.94	m/s
4	lnRks_404	$K_{sat\_rock}(404)$	Loguniform	−17.64	−12.4	m/s
5	lnRks_405	$K_{sat\_rock}(405)$	Loguniform	−16.39	−12.25	m/s
6	lnRks_406	$K_{sat\_rock}(406)$	Loguniform	−17.68	−11.77	m/s
7	lnRks_407	$K_{sat\_rock}(407)$	Loguniform	−17.78	−12.01	m/s
8	lnRks_408	$K_{sat\_rock}(408)$	Loguniform	−17.09	−11.55	m/s
9	lnRks_412	$K_{sat\_rock}(412)$	Loguniform	−12.59	−11.88	m/s
10	lnRks_414	$K_{sat\_rock}(414)$	Loguniform	−13.55	−12.02	m/s
11	lnRks_418	$K_{sat\_rock}(418)$	Loguniform	−16.92	−11.75	m/s
12	SDepth2	$depth_{soil}(2)$	Normal	10.9	22	m
13	SDepth3	$depth_{soil}(3)$	Uniform	2.1	3.2	m
14	SDepth4	$depth_{soil}(4)$	Uniform	0.1	0.5	m
15	Kc_min	K_{c_min}	Cumulative	—	—	none
16	Hc_579	$\Theta_s(5/7/9)$	Uniform	9.00×10^{-2}	0.17	none
17	Hc_26	$\Theta_s(2/6)$	Uniform	8.00×10^{-2}	0.15	none
18	Hc_34	$\Theta_s(3/4)$	Uniform	5.00×10^{-2}	0.1	none
19	lnKs_579	$K_{sat\_soil}(5/7/9)$	Lognormal	−10.34	−8.85	cm/s
20	lnKs_26	$K_{sat\_soil}(2/6)$	Lognormal	−10.15	−8.06	cm/s
21	lnKs_34	$K_{sat\_soil}(3/4)$	Lognormal	−10.49	−8.65	cm/s
22	SWC_579	$\Theta_s(5/7/9)$	Normal	0.21	0.25	none
23	SWC_26	$\Theta_s(2/6)$	Normal	0.17	0.25	none
24	SWC_34	$\Theta_s(3/5)$	Normal	0.14	0.18	none
25	p	p	Uniform	0.5	0.8	none
26	Z_r	Z_r	Uniform	0.6	2.6	m
27	h_plant	h_{plant}	Uniform	0.2	0.6	m
28	K0wint	$K_{o\ winter}$	Uniform	0	10	°C
29	K0rest	$K_{o\ rest}$	Uniform	0	10	°C

Table 2.3.1-25. Parameter List for Extended Sensitivity Analysis Using One Watershed (Continued)

	LHS Name	Symbol or Description	Distribution	P1	P2	Units
30	Sublim	$C_{sublime}$	Uniform	0	0.2	none
31	MAXPREC	Maximum daily precipitation	Uniform	496	983	mm
32	PREC_LR	$C_{Precipcor}$	Normal	4.1	8.5	%/100m
33	Smelt	$C_{snowmelt}$	Uniform	1	3	none
34	TEMP_LR	LR	Uniform	6.50×10^{-3}	1.00×10^{-2}	°C/m
35	FDOY_DP	starting DOY for winter dew point	Uniform	274	335	none
36	LDOY_DP	ending DOY for winter dew point	Uniform	90	151	none
37	SLPRD	slope	Normal	0.23	0.53	—
38	COEFHAR	K_{Rs}	Uniform	0.15	0.22	°C$^{-0.5}$
39	Z_e	Z_e	Uniform	0.1	0.2	m
40	REW	REW	Uniform	2	10	mm
41	C_Kcb2	C_{Kcb2}	Normal	3.2	16.2	none
42	albedo	α_T	Uniform	0.15	0.9	none

NOTE: P1 and P2 represent minimum and maximum values for uniform distributions and 0.1% and 99.9% values for normal distributions. Values are natural log transformed for loguniform and lognormal distributions.

Source: SNL 2008a, Section 7.1.4, Table 7.1.4-1.

Table 2.3.1-26. Summary of the Water Balance Results

Model	Code	Annual Water Balance Constituents				Mean Root Squared Error	
		Infiltration	Actual ET	Runoff	Change in Storage	mm	% Precipitation
		mm	mm	mm	mm		
Model 1	MASSIF	120.4	326.7	0.70	25.3	8.9	1.9
	HYDRUS-1D	120.5	336.8	2.5	9.6		
Model 2	MASSIF	63.9	377.8	0.70	30.8	17.1	3.6
	HYDRUS-1D	49.3	390.6	2.5	24.5		
Model 3	MASSIF	13.5	427.1	0.70	31.9	26.1	5.5
	HYDRUS-1D	0	425.1	3.7	39		
Model 4	MASSIF	0	437.5	0.70	35.0	33.4	7.1
	HYDRUS-1D	0	404.9	0.45	53.5		

Source: SNL 2008a, Section 7.2.2[a], Table 7.2.2-1[a].
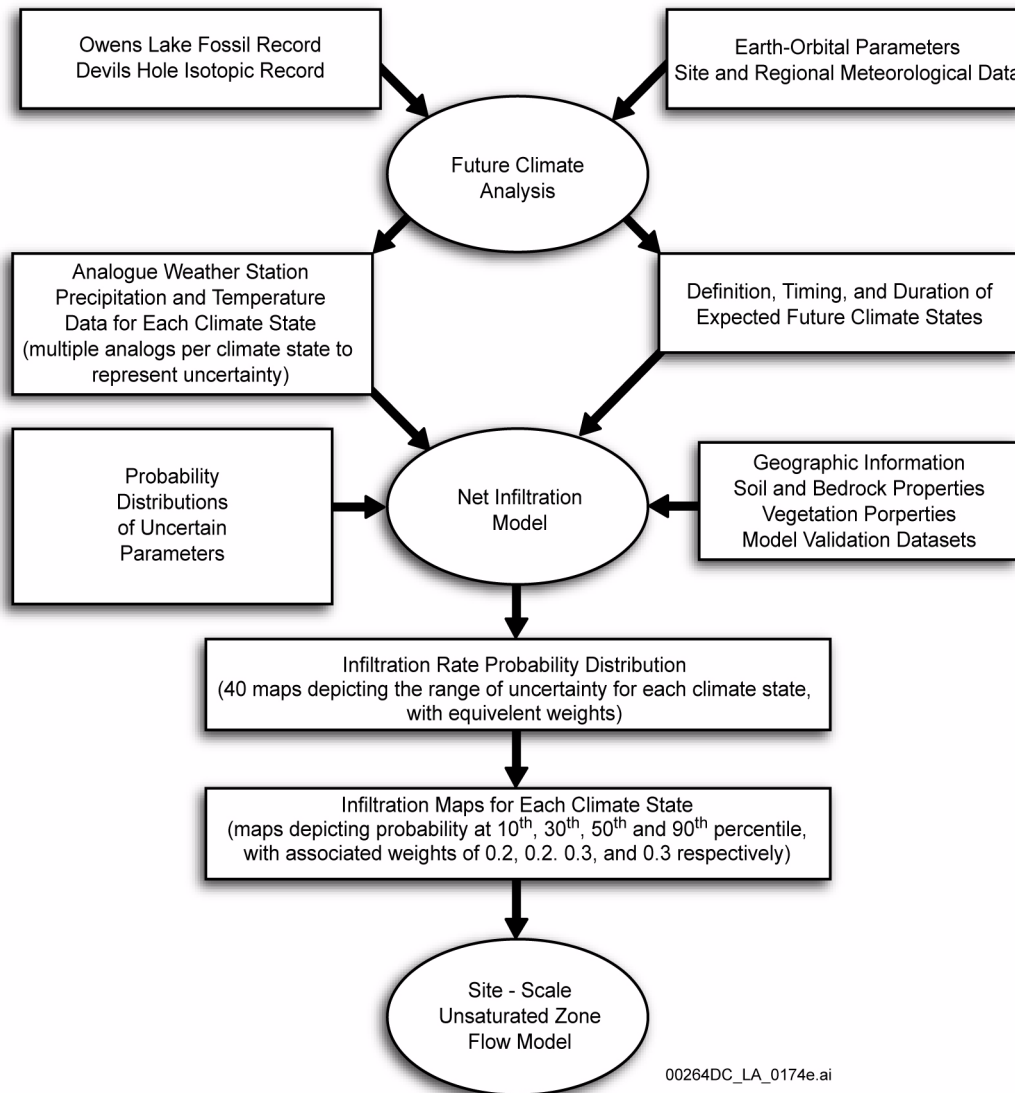
Figure 2.3.1-1. Climate Analysis and Infiltration Model Linkages

NOTE: Data and results are represented by rectangles; analyses and models are represented by ovals.
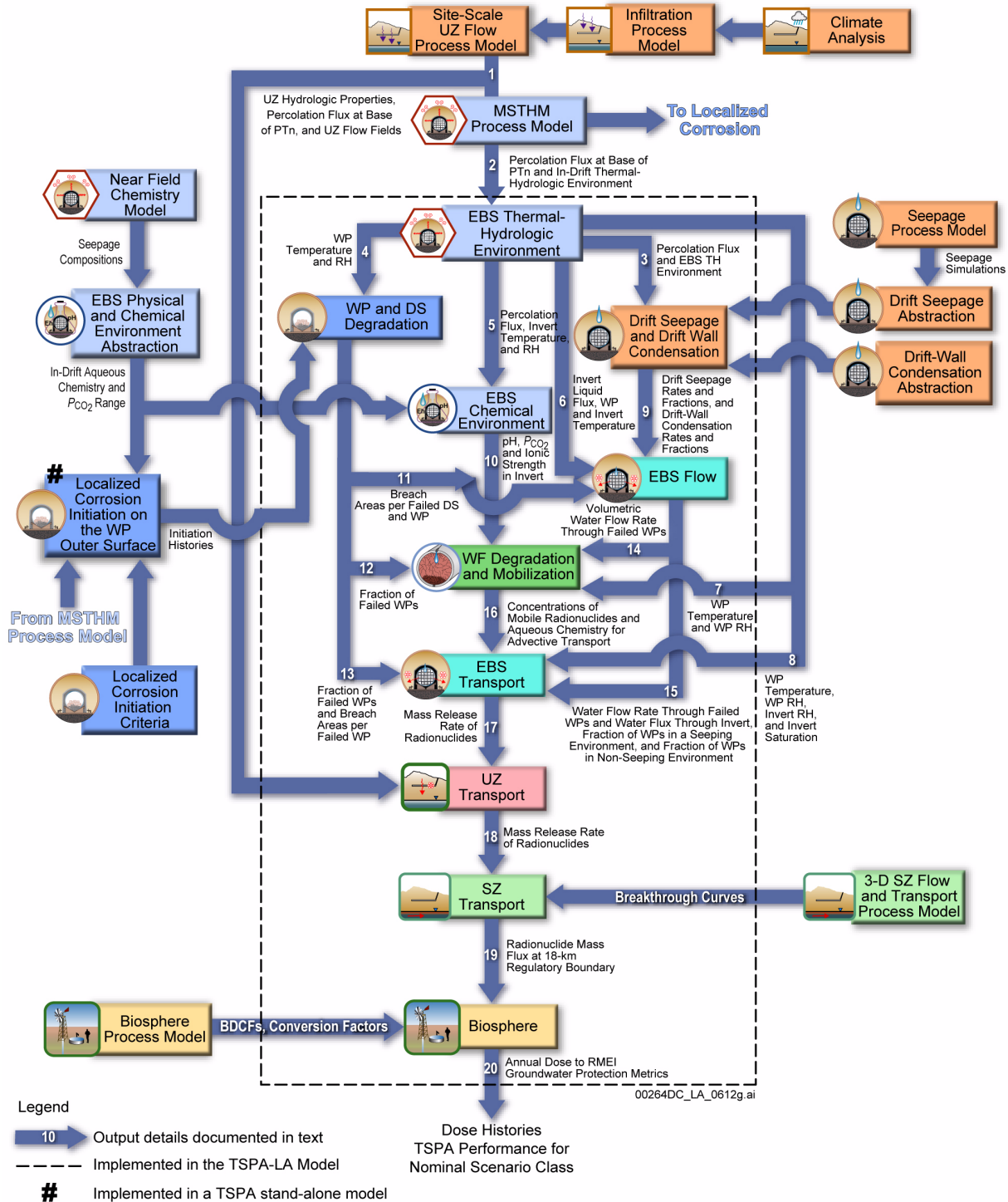
Figure 2.3.1-2.   Information Transfer among the Principal Model Components of the TSPA Nominal Scenario Class Model

NOTE: For details about outputs and information transfer shown on this figure, see Section 2.4.2.3.2.1. The infiltration process model shown in the figure is also called the net infiltration model.

DS = drip shield; EBS = Engineered Barrier System; LC = localized corrosion; PA = performance assessment; RH = relative humidity; SZ = saturated zone; TH = thermal-hydrologic; THC = thermal-hydrologic-chemical; UZ = unsaturated zone; WF = waste form; WP = waste package.
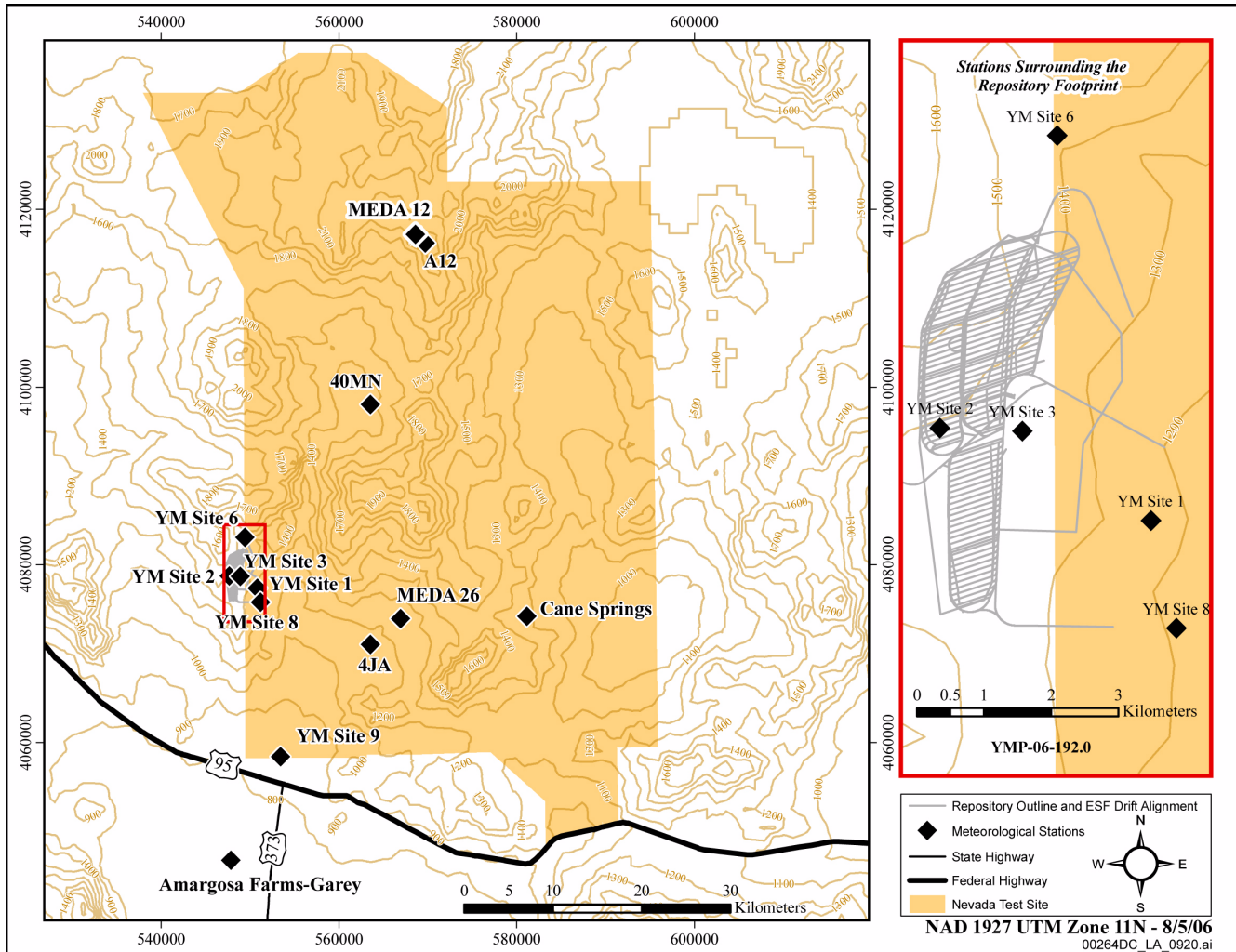
Figure 2.3.1-3. Meteorological Stations Locations Used to Represent Yucca Mountain Present-Day Climate Conditions

NOTE: Repository footprint and Nevada Test Site boundary are shown for illustration purposes only.

Source: SNL 2006, Figure 4.1-1.

Stations	UTM Zone	Northing (m)	Easting (m)	Elevation (m)
Beowawe, NV	11	4492427	545134	1433
Rosalia, WA	11	5230937	472242	731
St. John, WA	11	5214377	454454	593
Spokane, WA	11	5281077	452469	717
Delta, UT	12	4354776	362098	1409
Nogales, AZ	12	3468210	507923	1162
Hobbs, NM	13	3623072	674919	1116
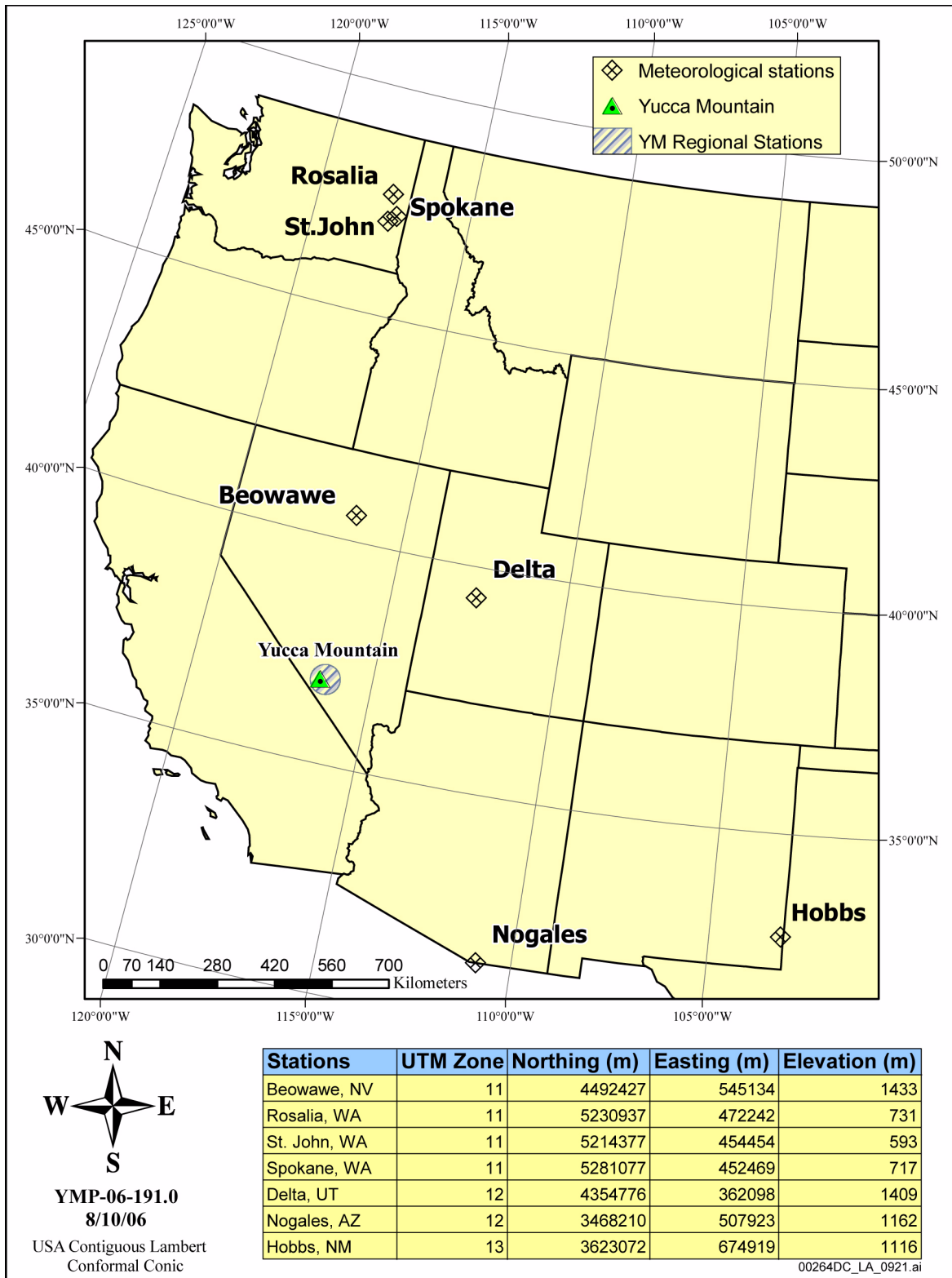
Figure 2.3.1-4.   Locations (as NAD 27 coordinates) of Meteorological Stations Used to Represent Future Climates at Yucca Mountain

Source: SNL 2006, Figure 4.1-2.
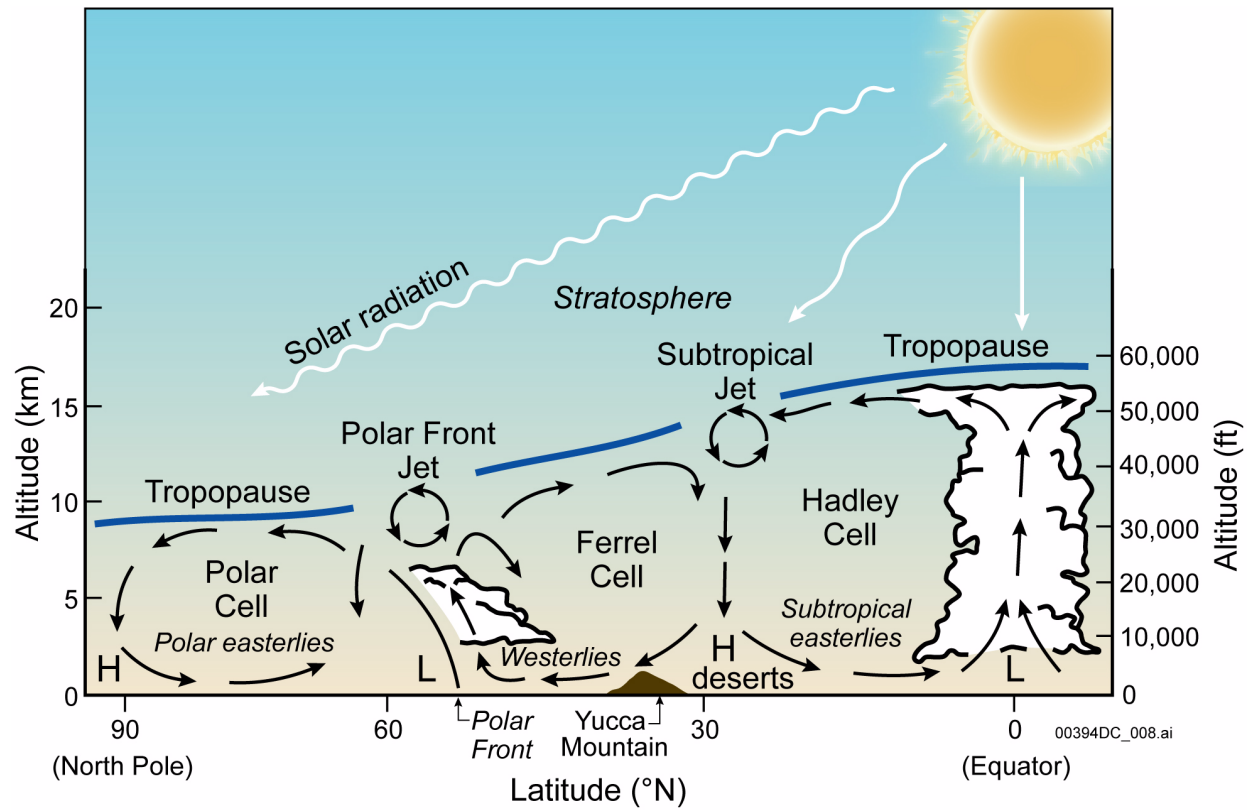
Figure 2.3.1-5. Generalized View of Atmosphere Circulation under Present-Day Climatic Conditions

NOTE: Time approximates autumnal equinox.
        H = high pressure dominates; L = low pressure dominates; arrows show dominant direction of air.

Source: BSC 2004a, Figure 6-2.
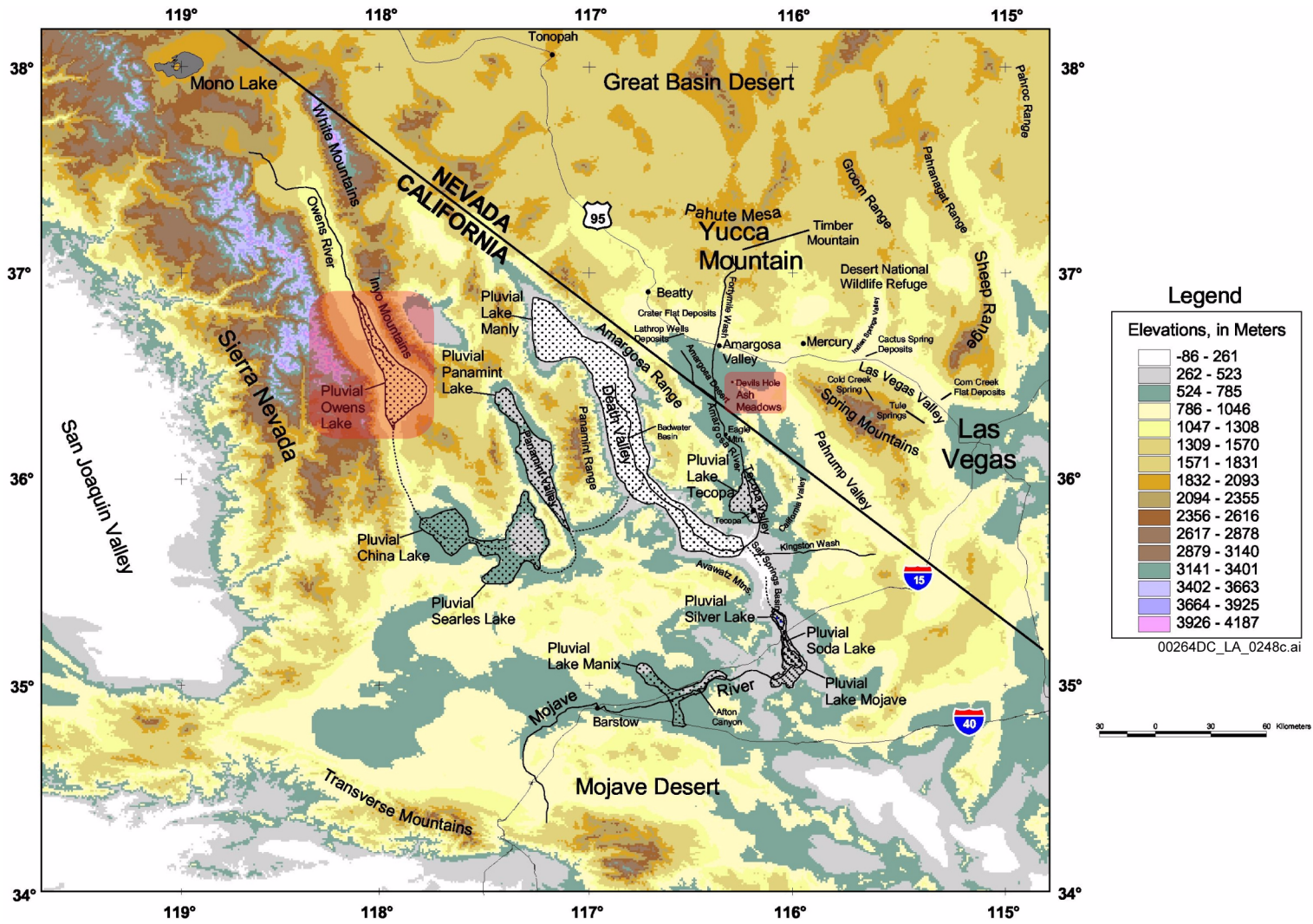
Figure 2.3.1-6. Localities Important to Past and Future Climate Estimates in the Yucca Mountain Area

Source: BSC 2004b, Figure 6-1.
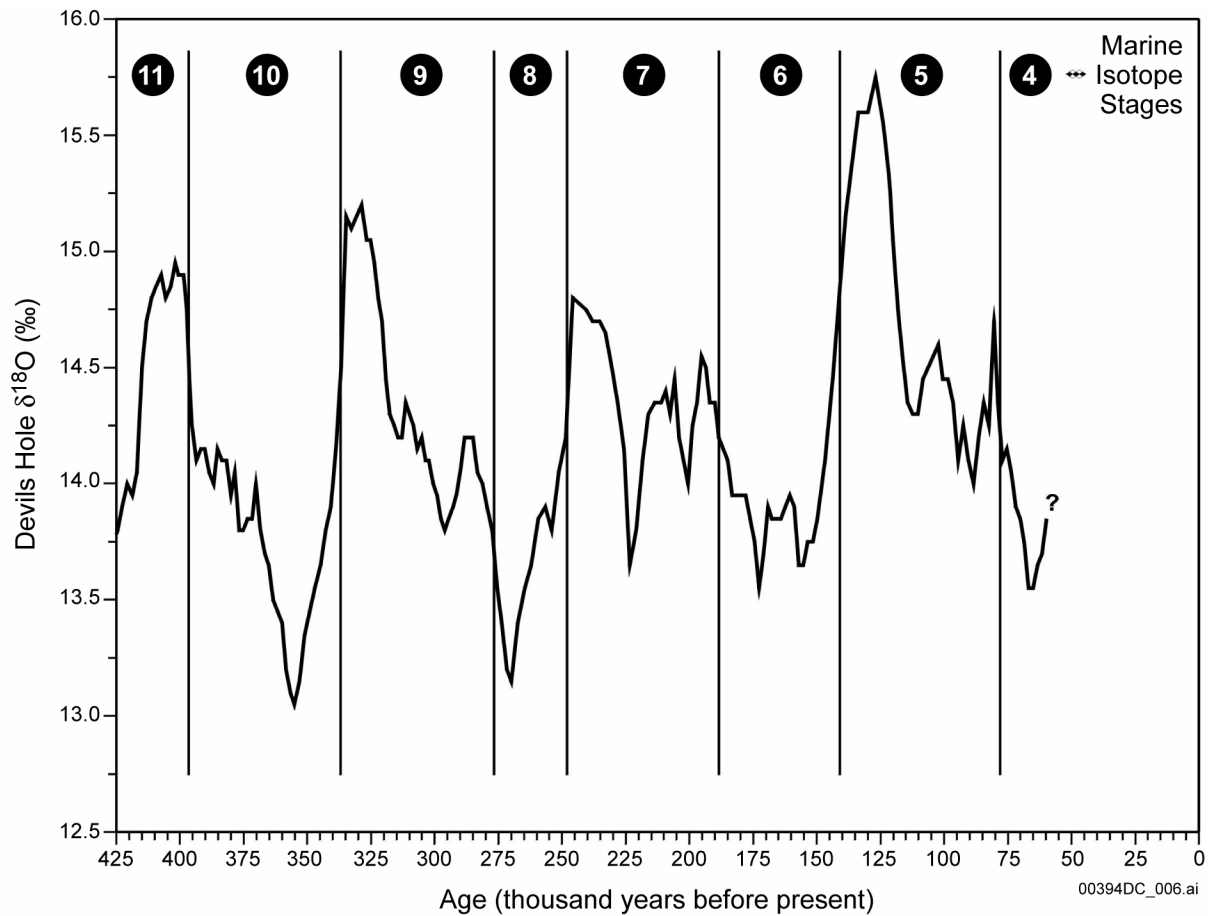
Figure 2.3.1-7.   Devils Hole Stable Isotope Record Showing the Timing and Cyclical Nature of Climate
                    Change

NOTE: High values represent warm climates, and low values represent cold climates. Stable isotope data are
        reported relative to Vienna Standard Mean Ocean Water. Odd-numbered marine isotope stages correspond to
        interglacial climates; even-numbered marine isotope stages correspond to glacial climates.

Source: BSC 2004a, Figure 6-3.
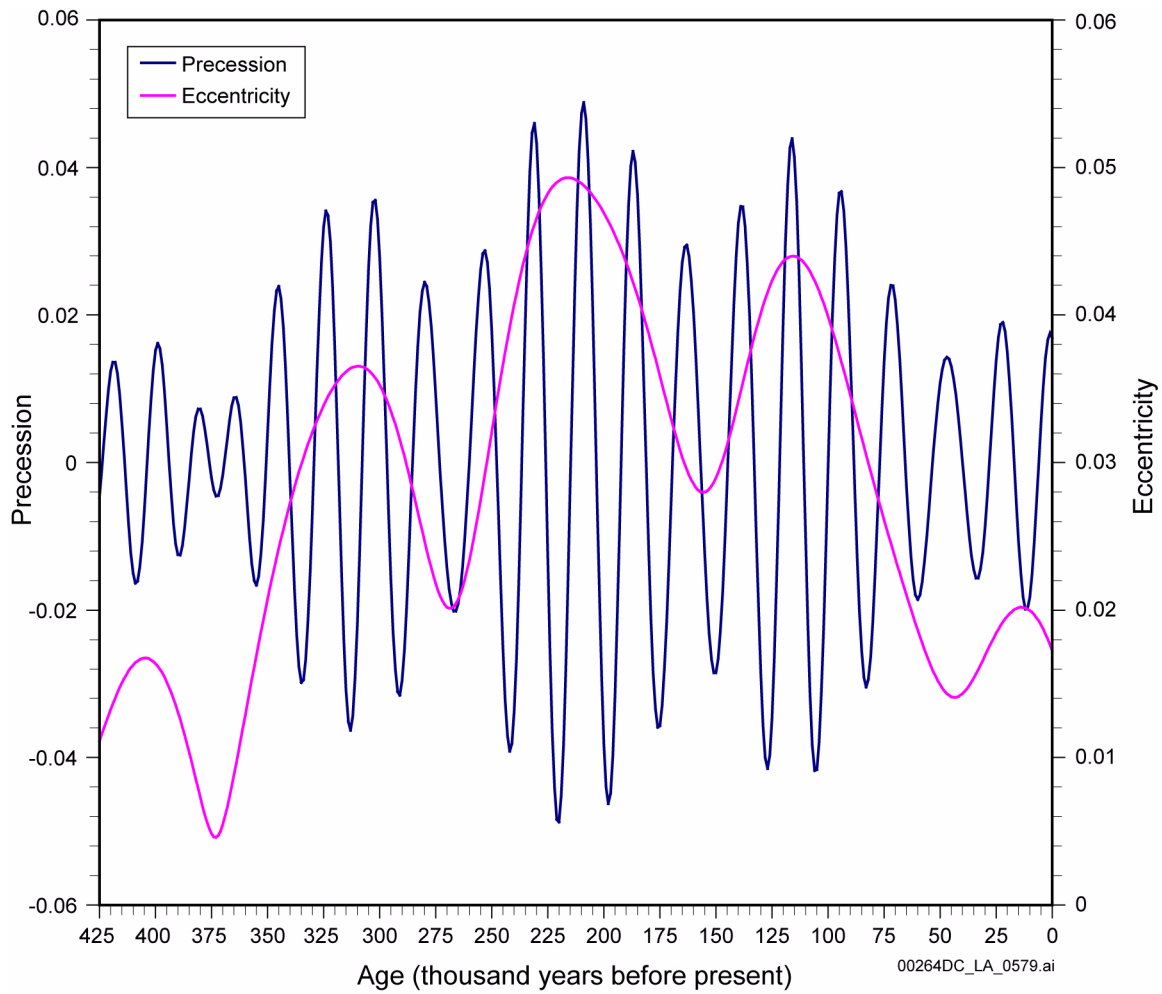
Figure 2.3.1-8. Relationship between Precession and Eccentricity for the Past 425,000 Years

NOTE: By convention, a maximal positive precession is a summer radiation maxima in the southern hemisphere; whereas, a minimal (most negative) value is a summer radiation maxima in the northern hemisphere.

Source: BSC 2004a, Figure 6-5.
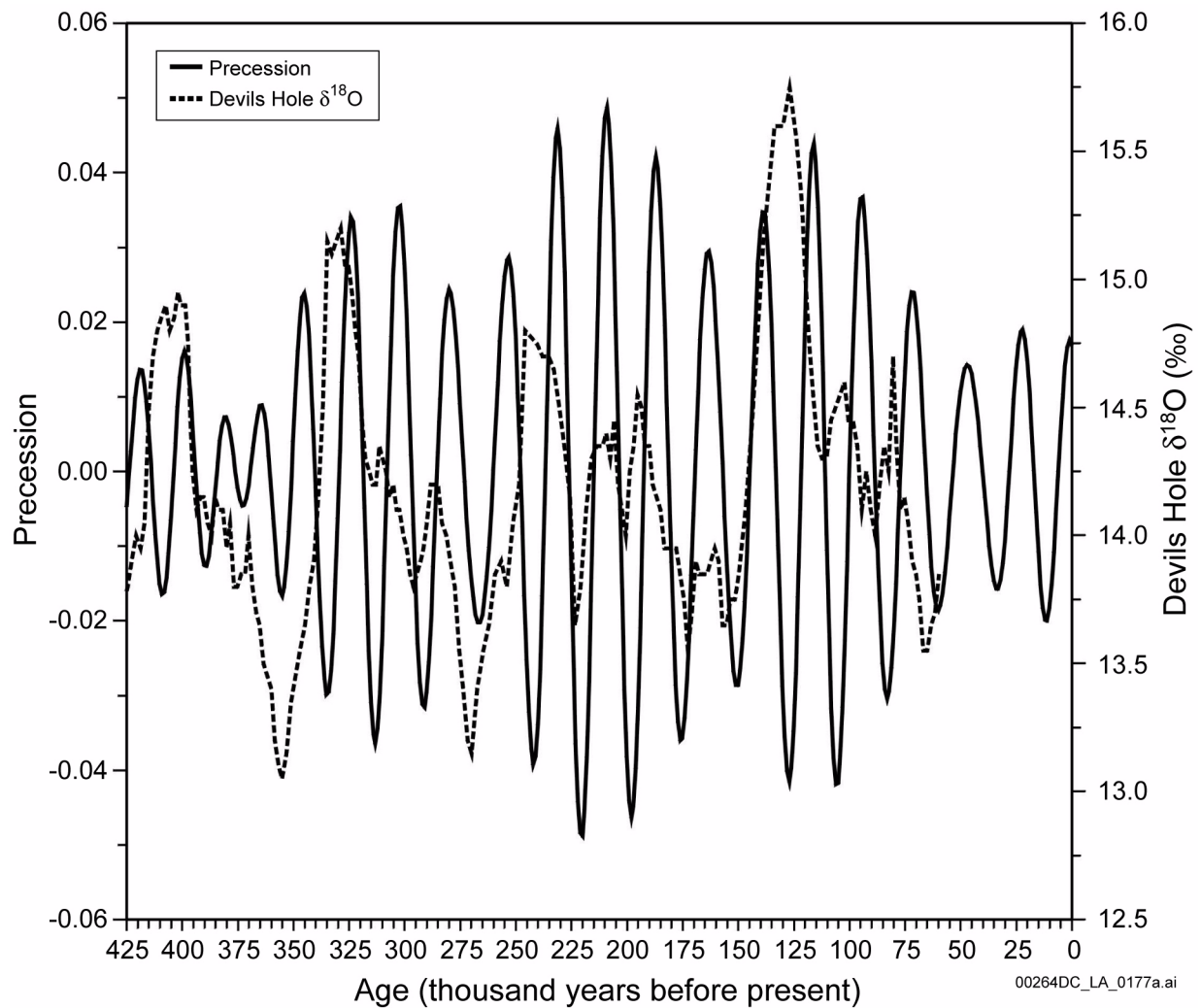
Figure 2.3.1-9.   Relationship of Precession to the Devils Hole Stable Isotope Climate Proxy Record during a Long Climate Cycle

NOTE: Stable isotope data are reported relative to Vienna Standard Mean Ocean Water. By convention, a maximal positive precession is a summer radiation maxima in the southern hemisphere; whereas, a minimal (most negative) value is a summer radiation maxima in the northern hemisphere.

Source: BSC 2004a, Figure 6-6.
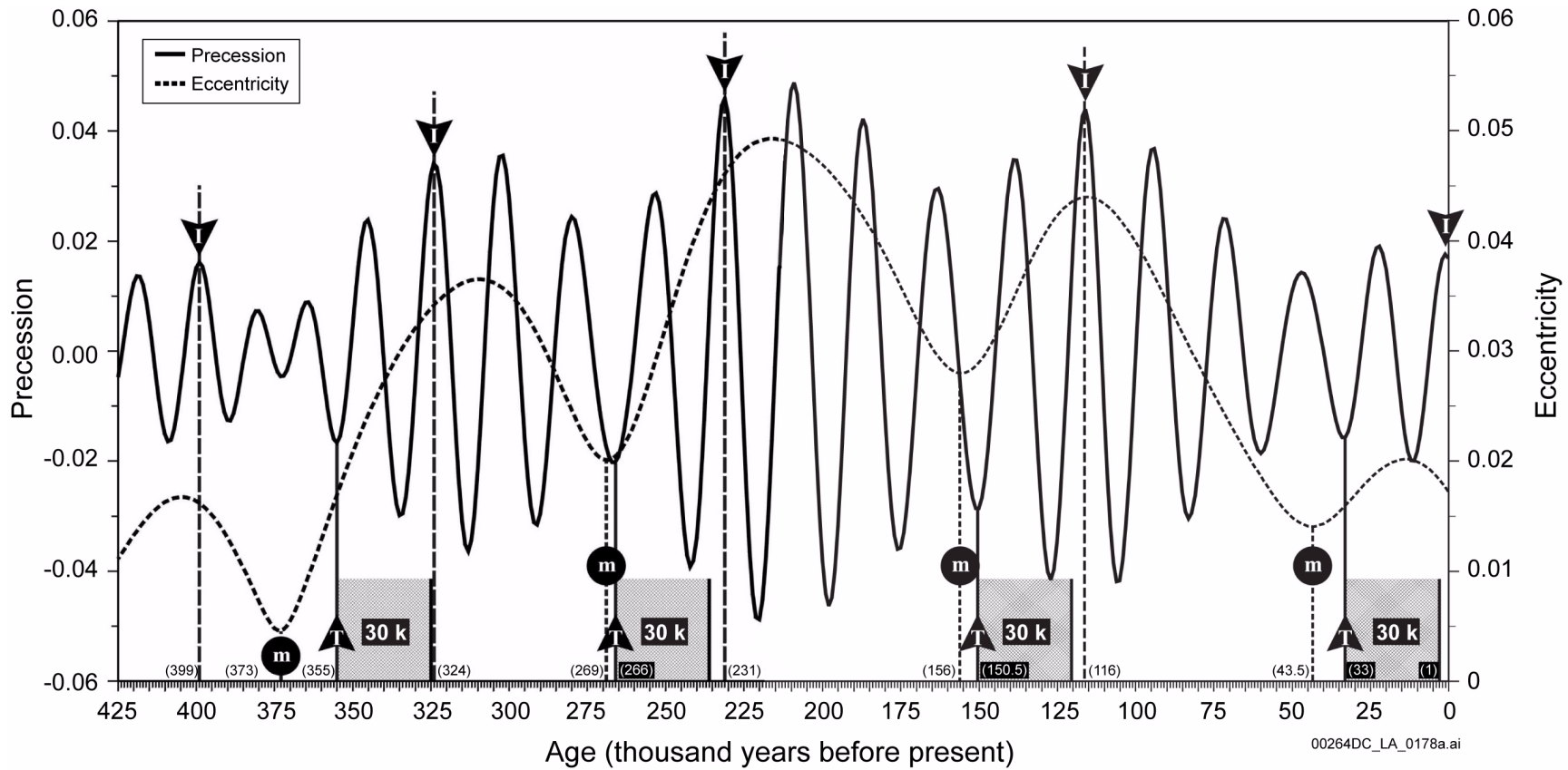
Figure 2.3.1-10.   Relationship between the Timing of Past Climate Change and Earth-Orbital Parameters during a Long Climate Cycle (continued in Figure 2.3.1-11)

NOTE: Ages for I and T are shown in parentheses at bottom of graph in thousands of years before present. By convention, a maximal positive precession is a summer radiation maxima in the southern hemisphere; whereas, a minimal (most negative) value is a summer radiation maxima in the northern hemisphere.
I = initiation of transition to glacial climate; m = minimum eccentricity value; T = initiation of transition to interglacial climate.

Source: BSC 2004a, Figures 6-7 and 6-8.
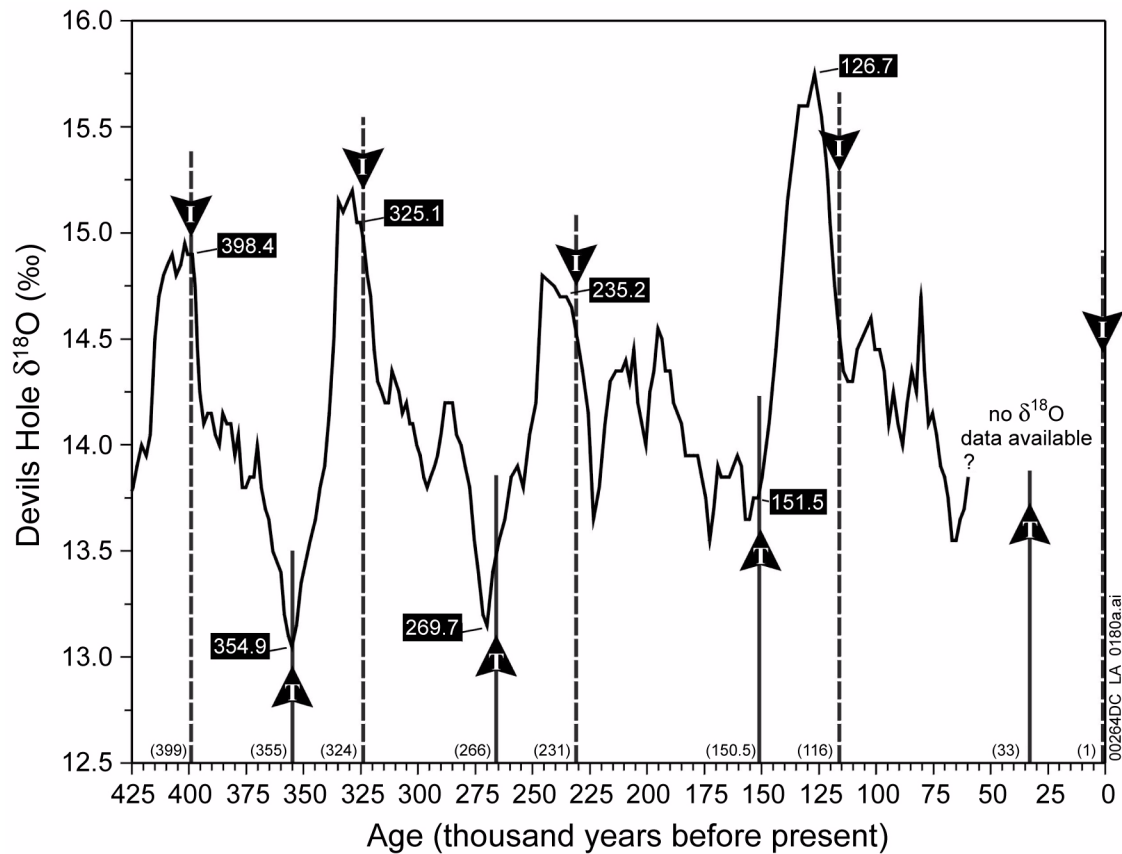
Figure 2.3.1-11.   Relation of Glacial–Interglacial Transitions Based on Orbital Parameters and the Timing of Climate Change Defined by the Devils Hole Climate Proxy Record

NOTE: Stable isotope data are reported relative to Vienna Standard Mean Ocean Water. Ages for I and T are shown in parentheses at bottom of graph in thousands of years before present. Ages for inflection points are shown in boxes.
I = initiation of transition to glacial climate; T = initiation of transition to interglacial climate.

Source: BSC 2004a, Figure 6-9.
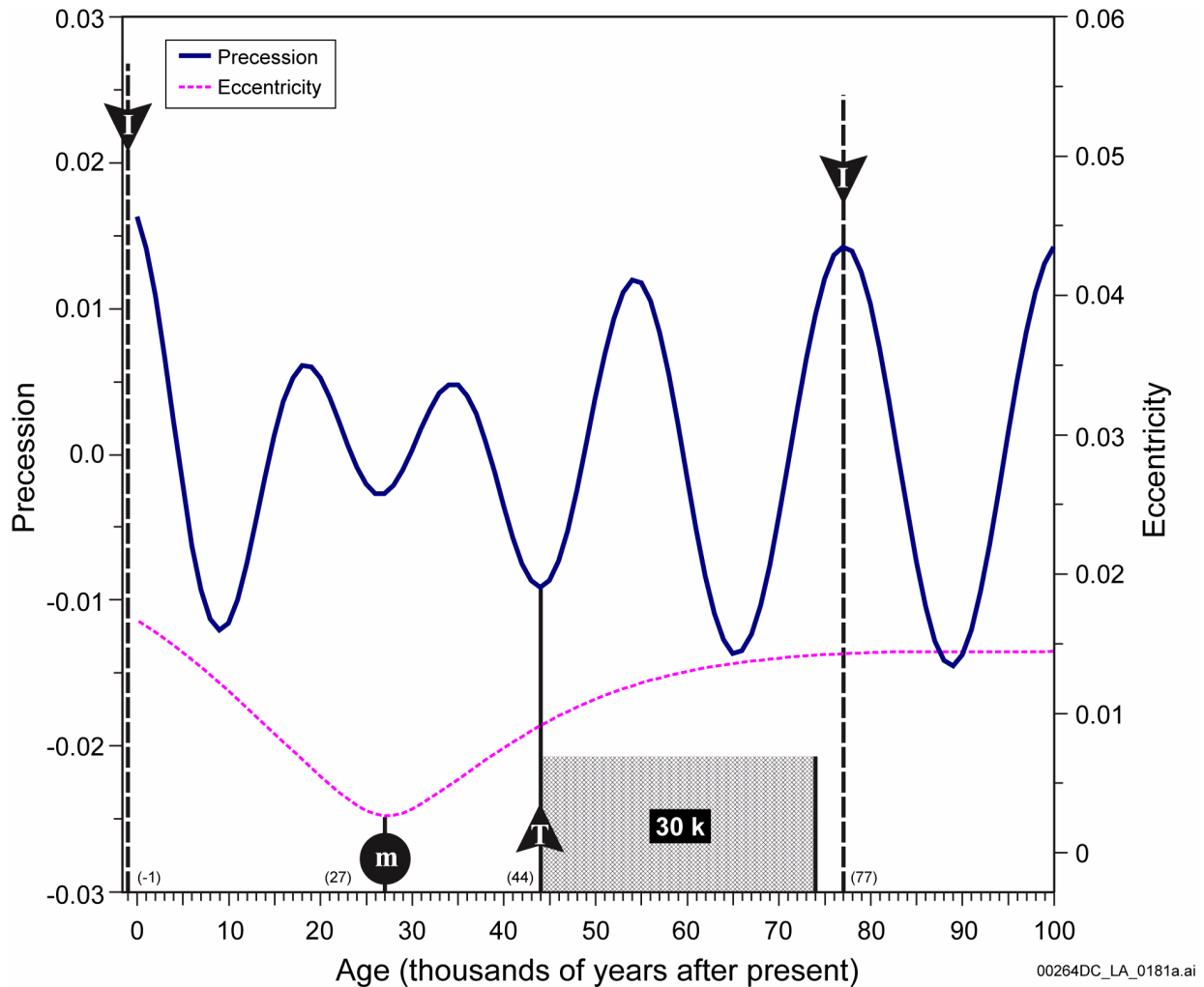
Figure 2.3.1-12. Forecast of Timing of Future Climate Change during the Next 100,000 Years

NOTE: Ages for I and T are shown in parentheses at bottom of graph in thousands of years after present. By
convention, a maximal positive precession is a summer radiation maxima in the southern hemisphere;
whereas, a minimal (most negative) value is a summer radiation maxima in the northern hemisphere.
I = initiation of transition to glacial climate; m = minimum eccentricity value; T = initiation of transition to
interglacial climate.

Source: BSC 2004a, Figure 6-10.
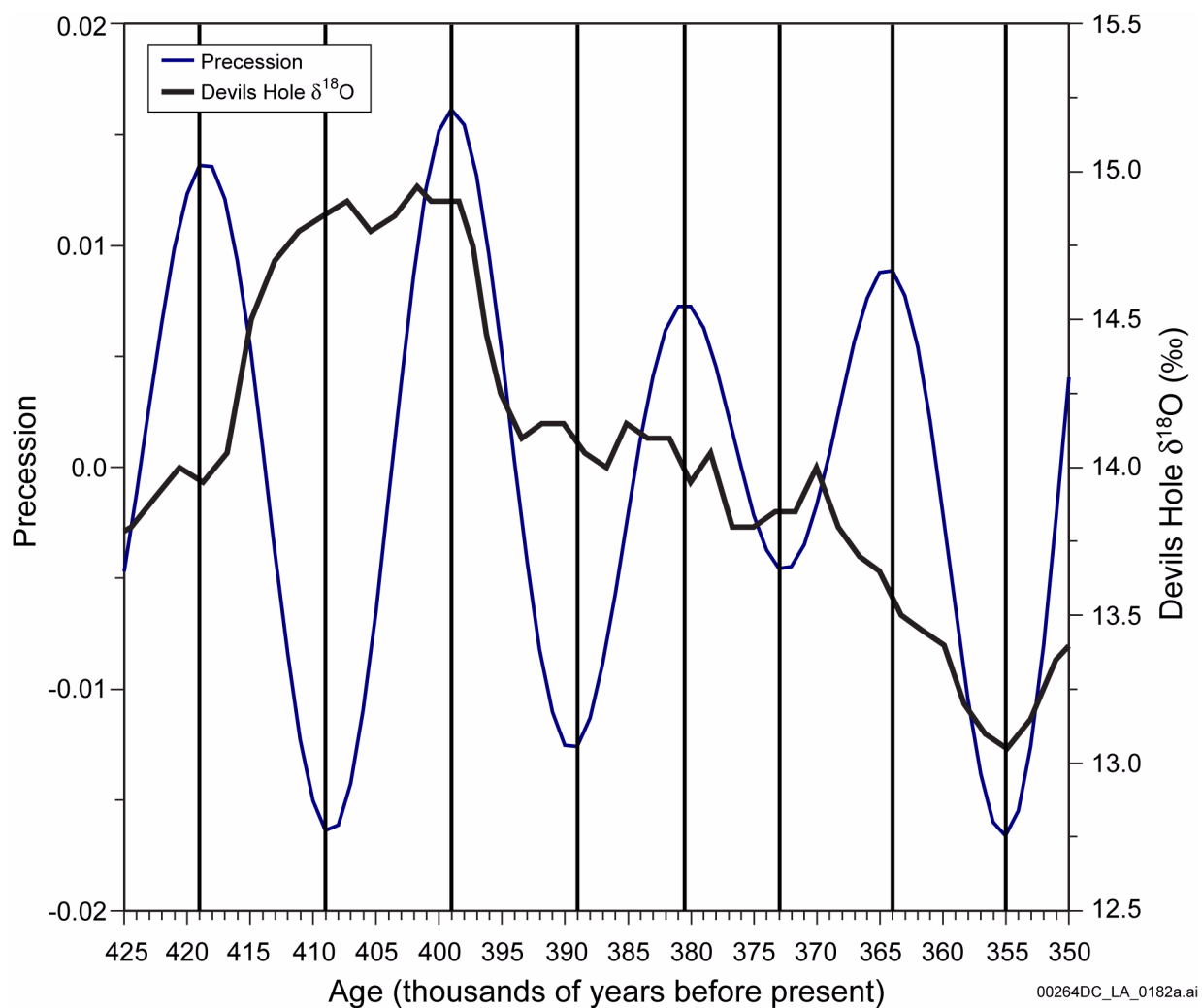
Figure 2.3.1-13.   Relation between Precession and the Timing of Climate Change in Part of the Devils Hole Record from 425,000 to 350,000 Years Ago

NOTE: Stable isotope data are reported relative to Vienna Standard Mean Ocean Water. By convention, a maximal positive precession is a summer radiation maxima in the southern hemisphere; whereas, a minimal (most negative) value is a summer radiation maxima in the northern hemisphere.

Source: BSC 2004a, Figure 6-11.
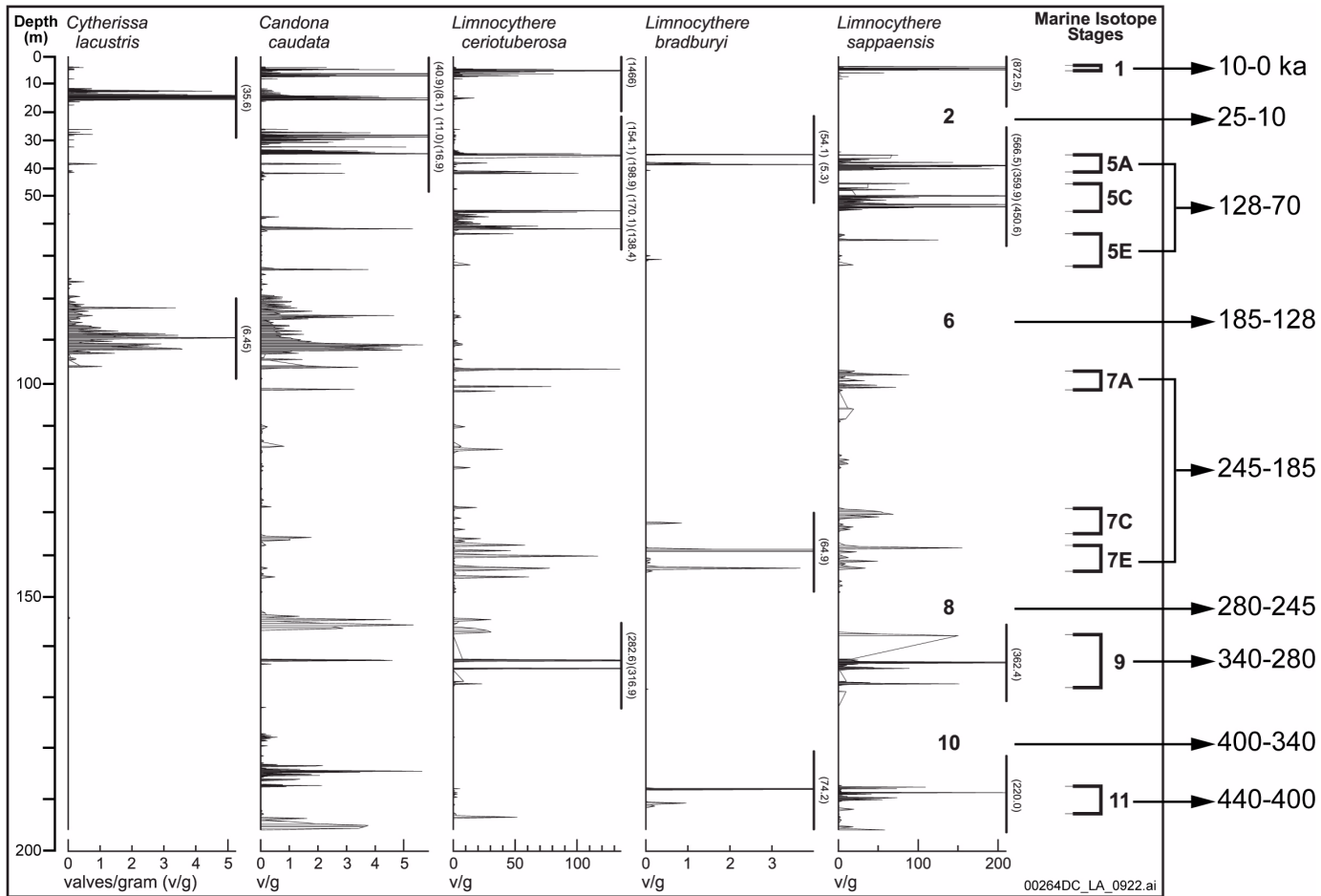
Figure 2.3.1-14. Owens Lake Ostracode Species Stratigraphic Distributions

NOTE: Interglacial marine isotope stages (odd numbers) shown in the right column, inferred glacial marine isotope stages (even numbers) shown under *L. sappaensis* column are from Forester et al. (1999, Figures 8 and 9, pp. 19 and 20), and Winograd, Landwehr et al. (1997). Bars centered on data spikes indicate data points beyond the scale of the graph, values to the right of bars are data values at spike apex.

Source: BSC 2004a, Figure 6-12.
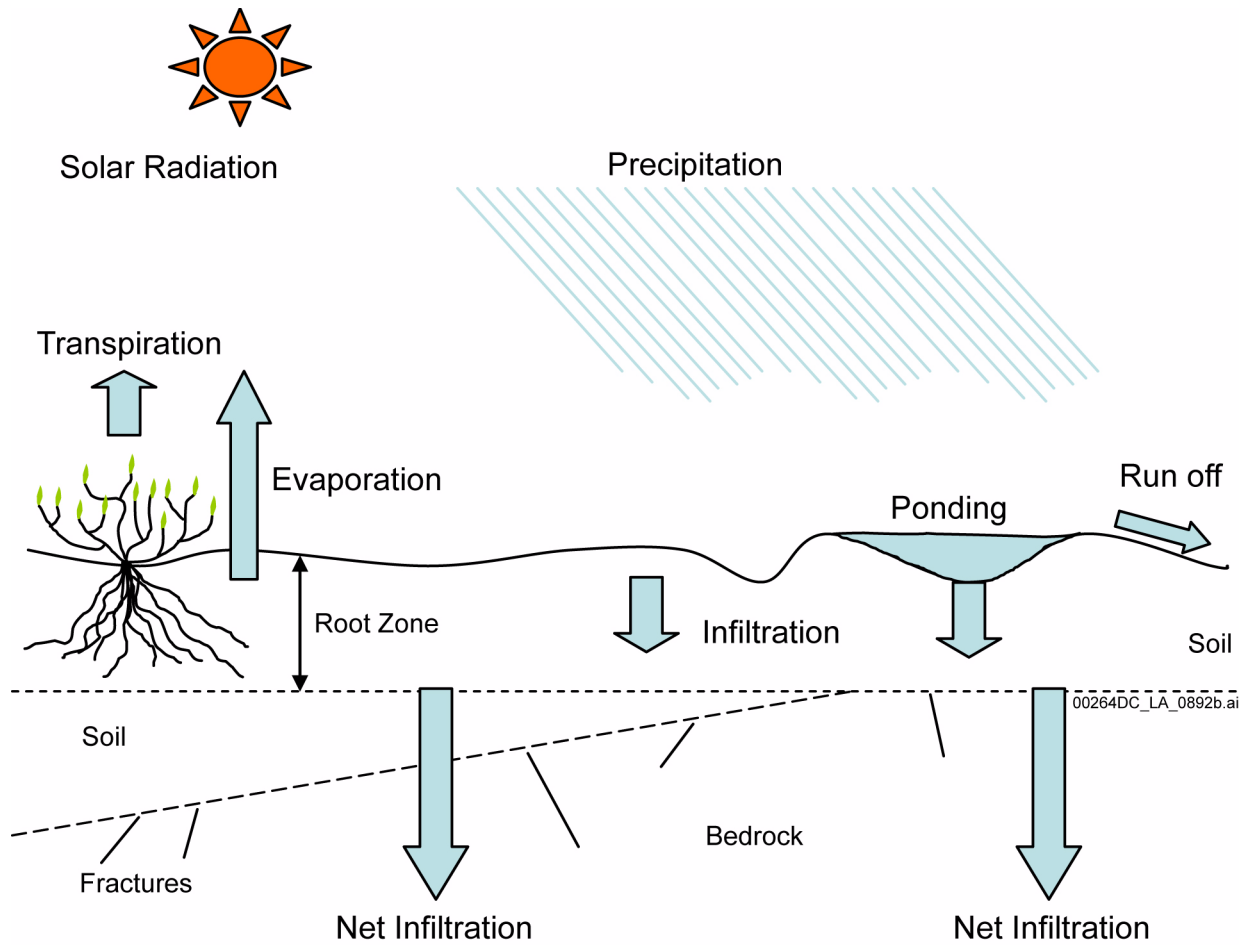
Figure 2.3.1-15. Processes Controlling Net Infiltration

NOTE: Figure not to scale.

Source: SNL 2008a, Section 6.2.1[a], Figure 6.2.1-1[a].
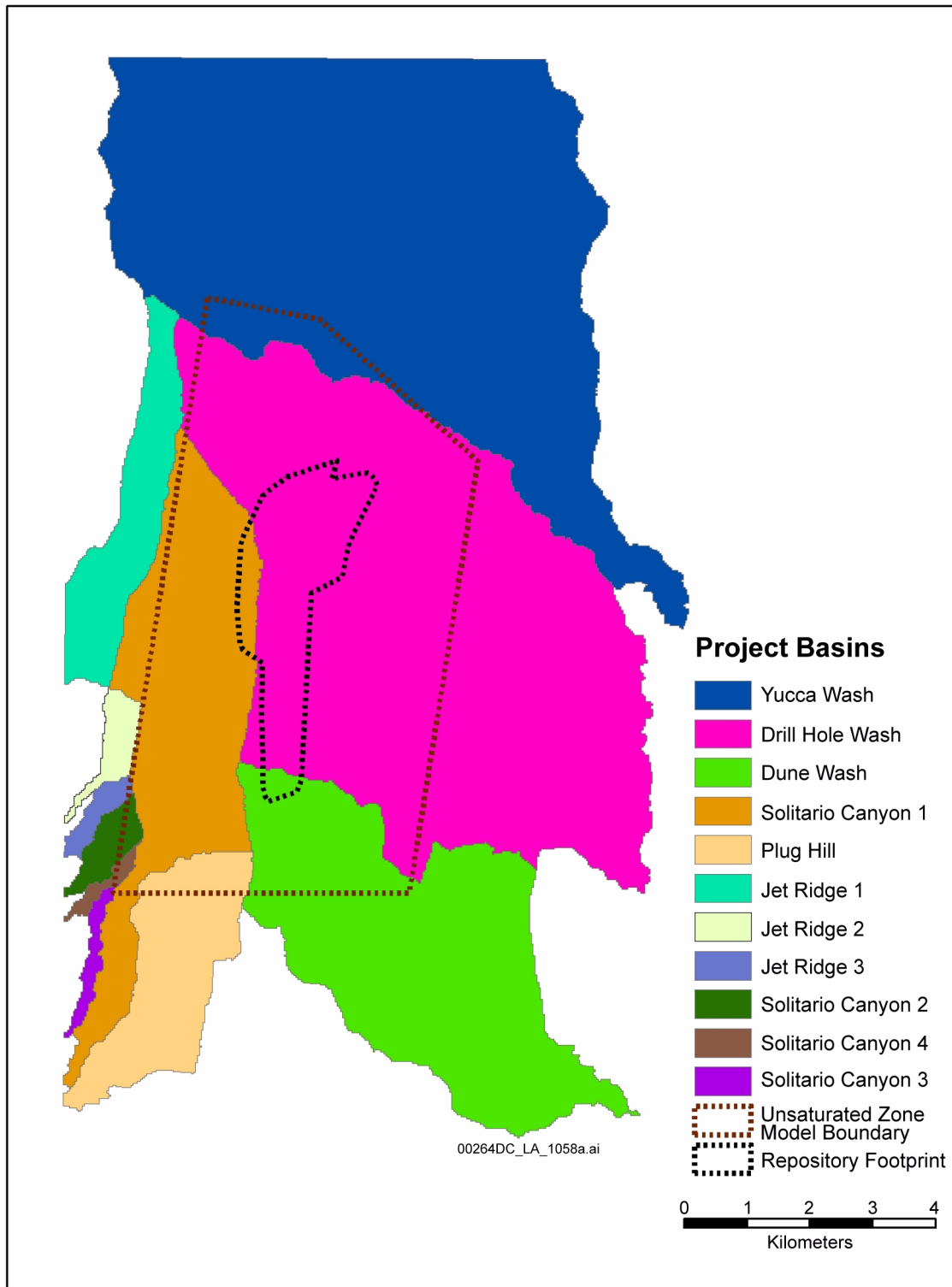
Figure 2.3.1-16. Yucca Mountain Watersheds

NOTE: Repository footprint is shown for illustration purposes only.

Source: SNL 2008a, Section 6.5.2.1[a], Figure 6.5.2.1-2[a].
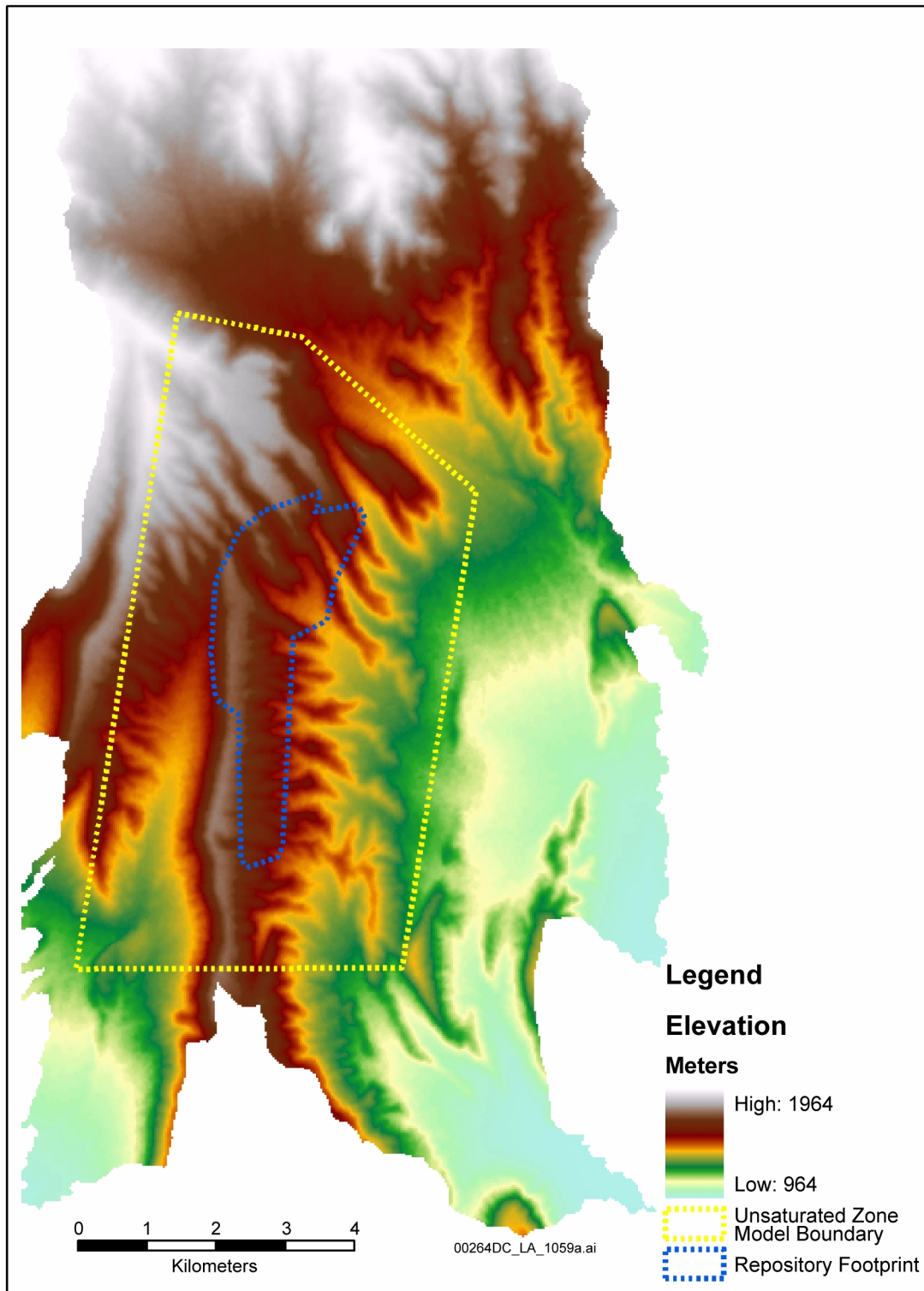
Figure 2.3.1-17. Elevation over the Model Area

NOTE: Repository footprint is shown for illustration purposes only.

Source: SNL 2008a, Section 6.5.2.1[a], Figure 6.5.2.1-3[a].
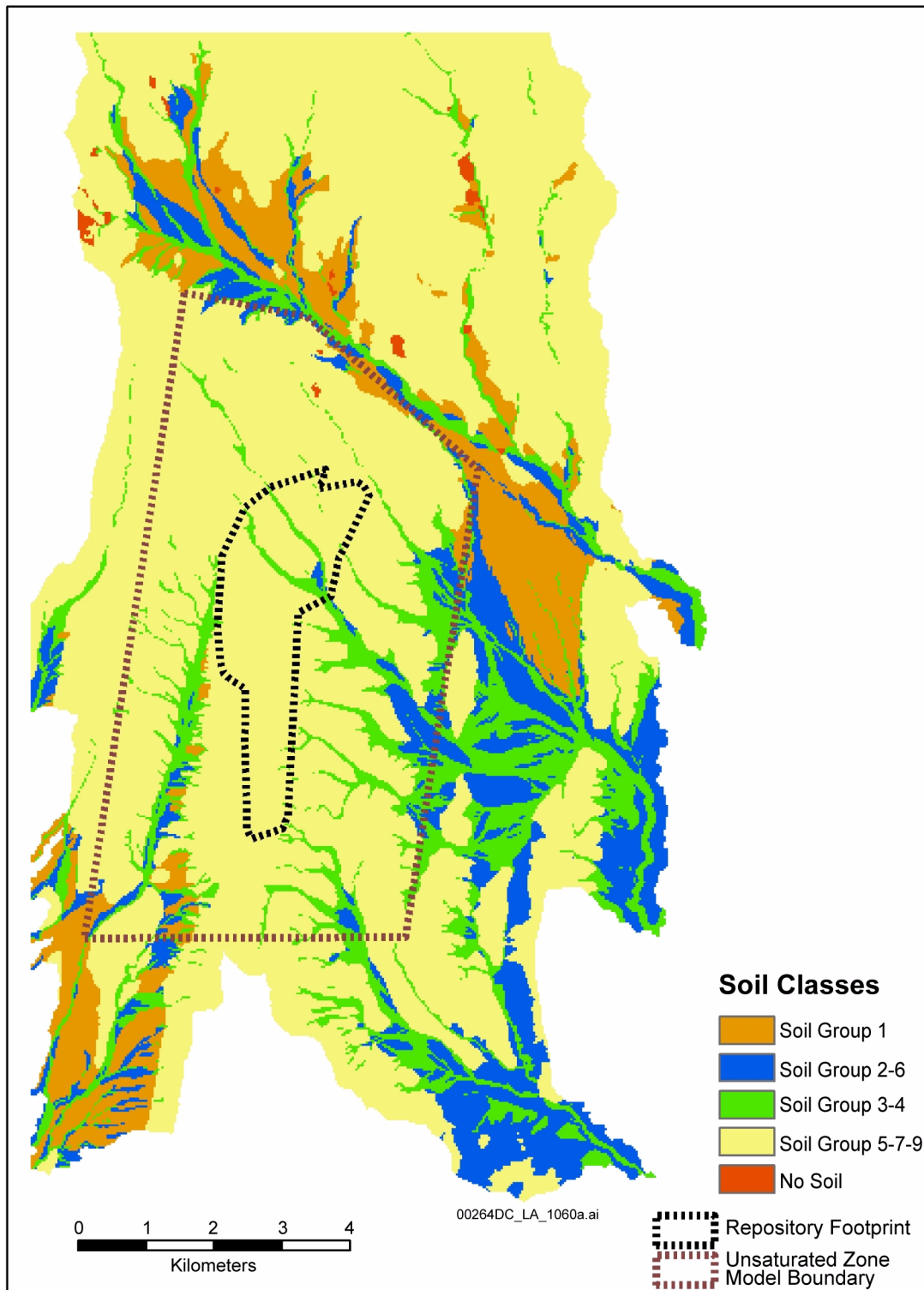
Figure 2.3.1-18. Map Showing Distribution of Alternative Soil Groupings over the Infiltration Domain

NOTE: Repository footprint is shown for illustration purposes only.

Source: SNL 2008a, Section 6.5.2.2[a], Figure 6.5.2.2-2[a].
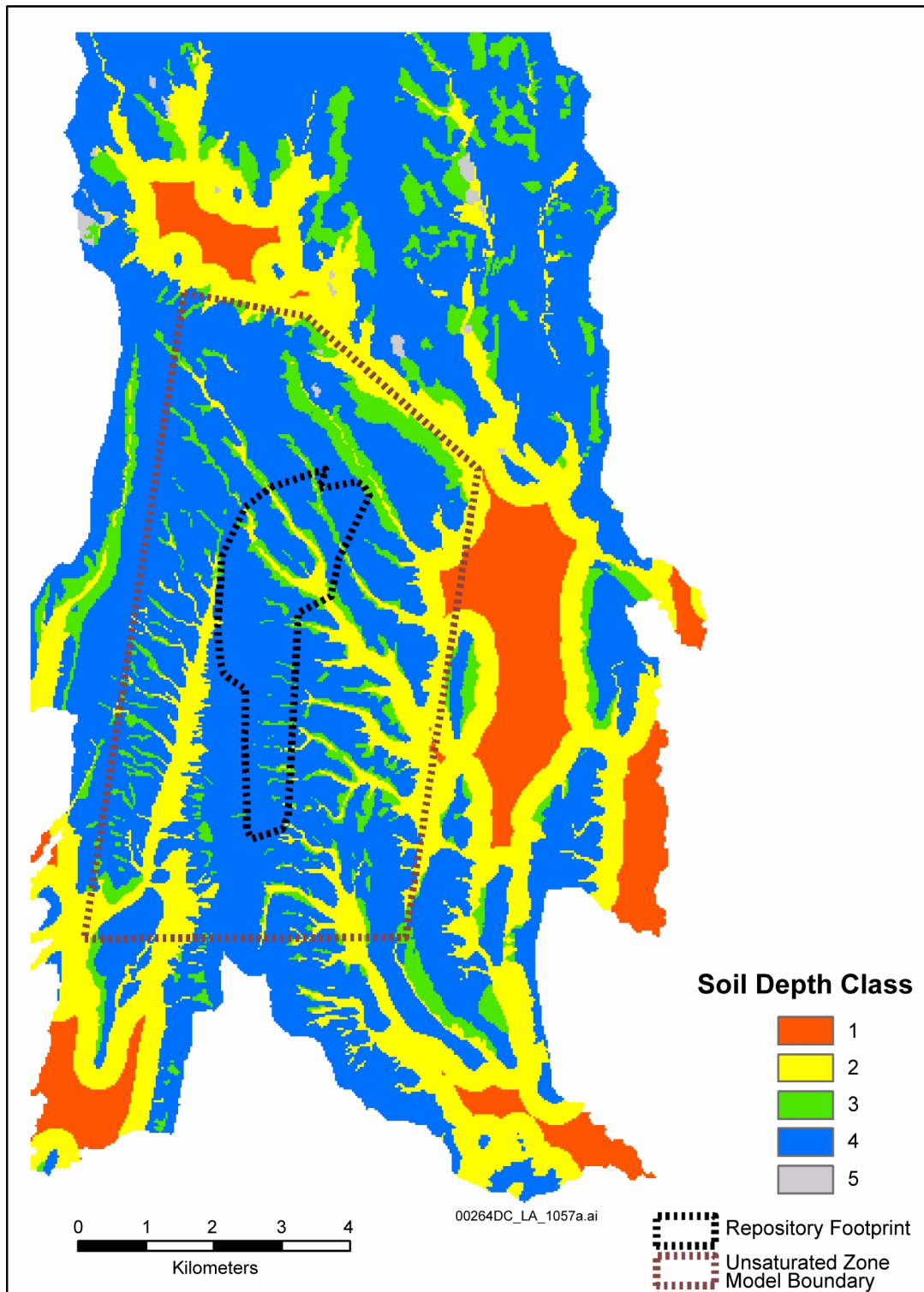
Figure 2.3.1-19. Map Showing Distribution of Soil Depth Classes over the Infiltration Domain

NOTE: Repository footprint is shown for illustration purposes only.

Source: SNL 2008a, Section 6.5.2.4[a], Figure 6.5.2.4-1[a].
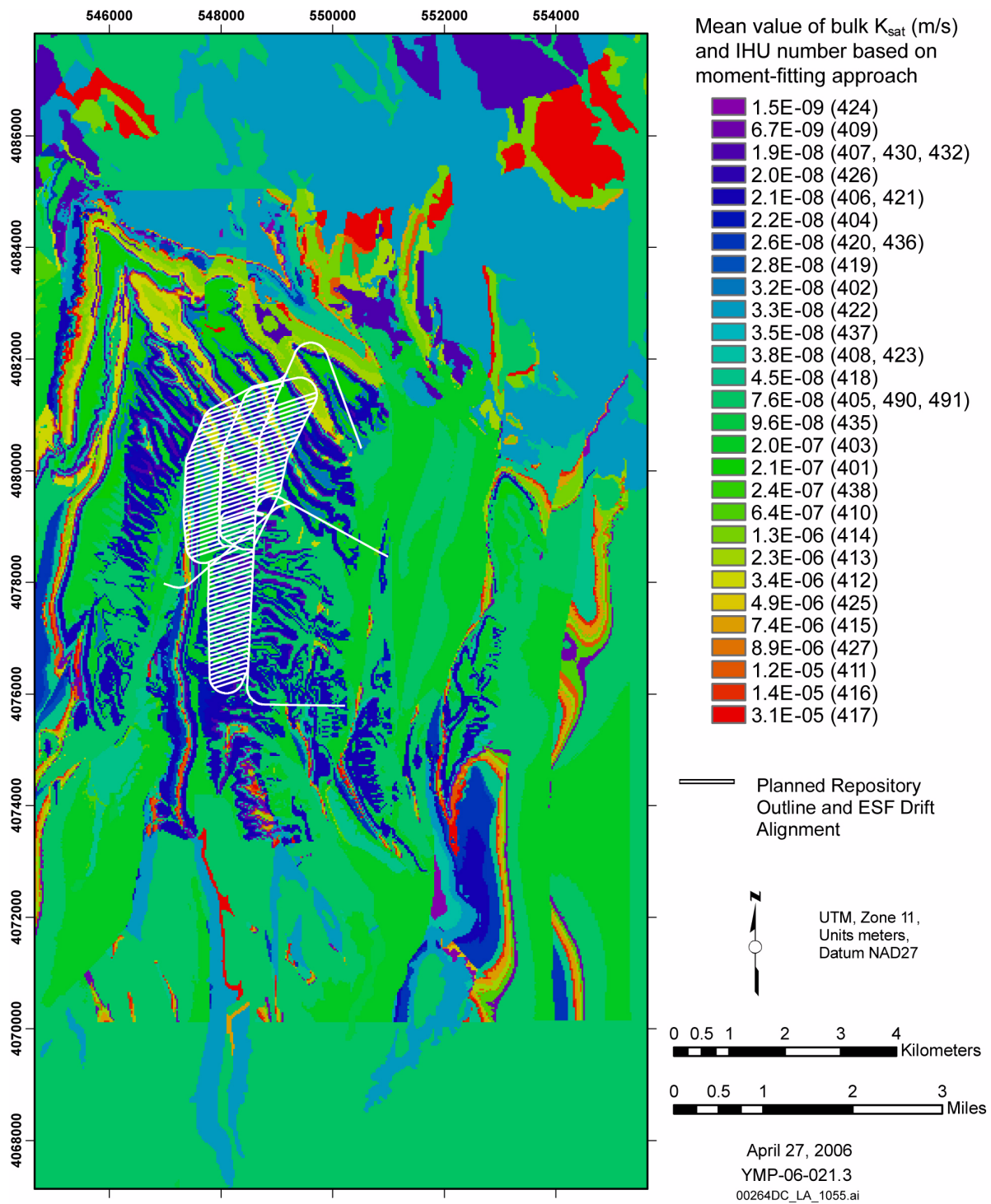
Figure 2.3.1-20.   Distribution of Saturated Hydraulic Conductivity over the Model Area Based on the Consideration of Filled Fractures

NOTE: Repository footprint is shown for illustration purposes only.
        IHU = Infiltration Hydrogeologic Unit

Source: SNL 2008a, Section 6.5.2.6, Figure 6.5.2.6-1.
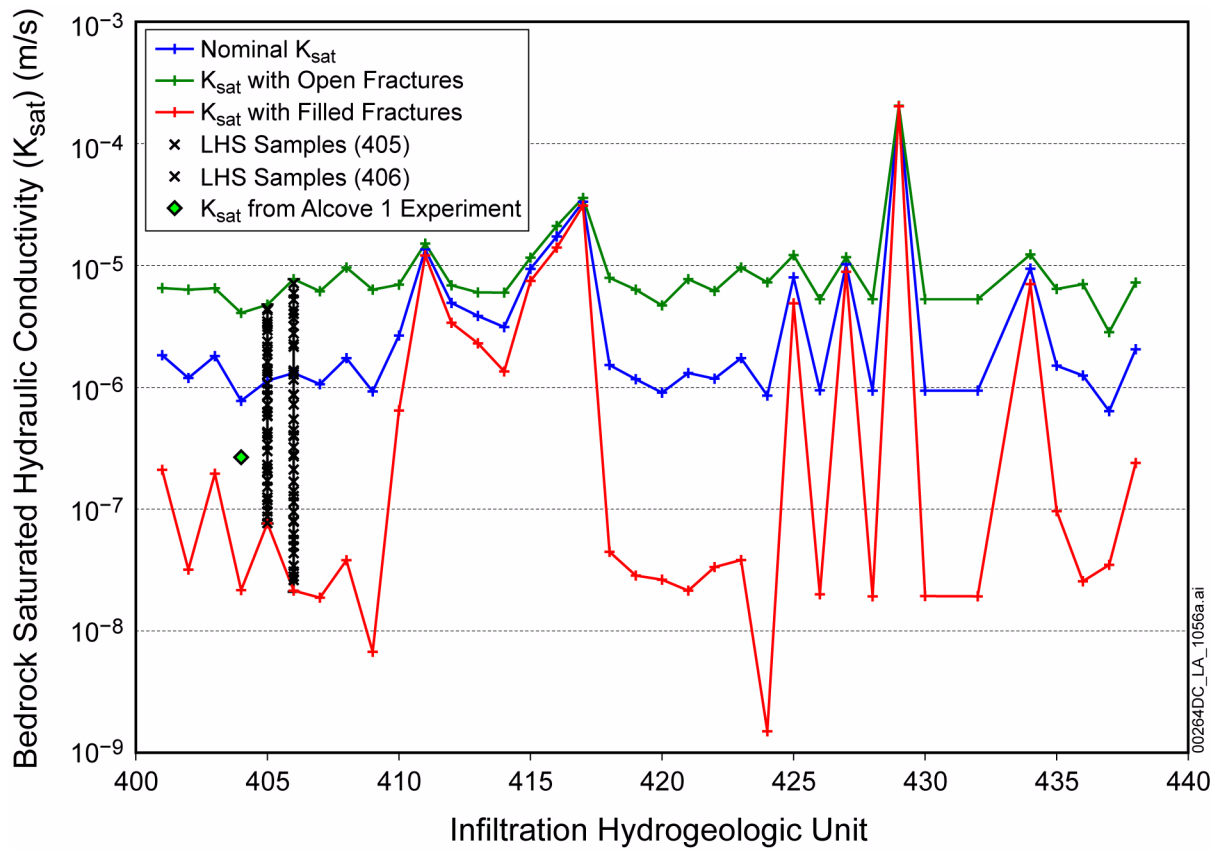
Figure 2.3.1-21.   Nominal, Lower Bound, and Upper Bound Values of Bulk Bedrock Saturated Hydraulic Conductivity, K_{sat}, with Comparison to the Alcove 1 Infiltration Test

NOTE: LHS = Latin Hypercube sampling.

Source: SNL 2008a, Section 6.5.2.6, Table 6.5.2.6-1. Alcove 1 K_{sat} from BSC 2006b, Section 6.4.5.3. Latin Hypercube sampling datapoints from MASSIF output DTN: SN0701T0502206.037 (\Welcome to Massif\Massif\Present Day Uncertainty\LHS_PD_R1.OUT and LHS_PD_R2.OUT).
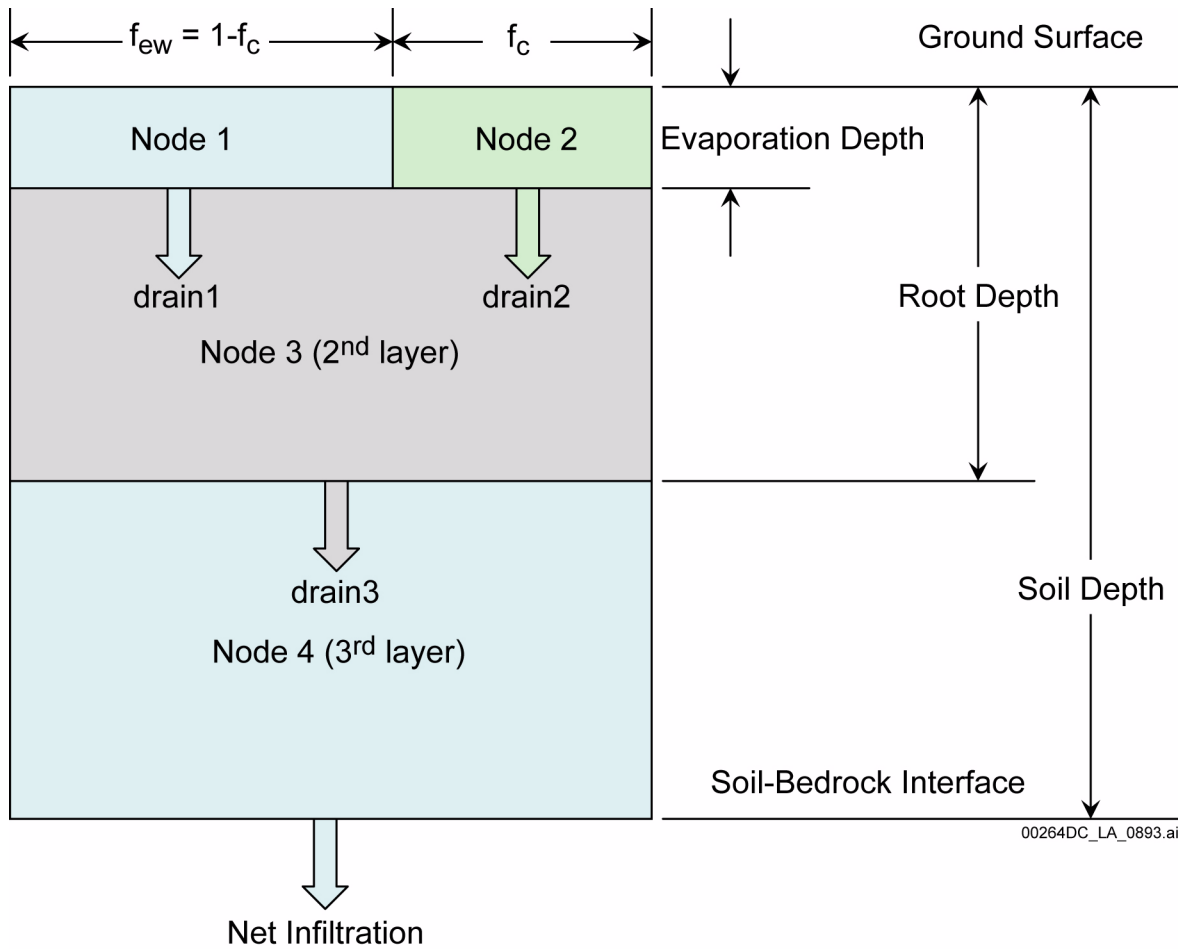
Figure 2.3.1-22. Schematic Showing the Vertical Soil Layers and Computational Nodes Present in a Single Model Cell

NOTE: f_c is the fraction of the surface covered by the vegetation canopy and f_{ew} is the fraction of the surface that is exposed and wetted.

Source: SNL 2008a, Section 6.4.2, Figure 6.4.2-1.
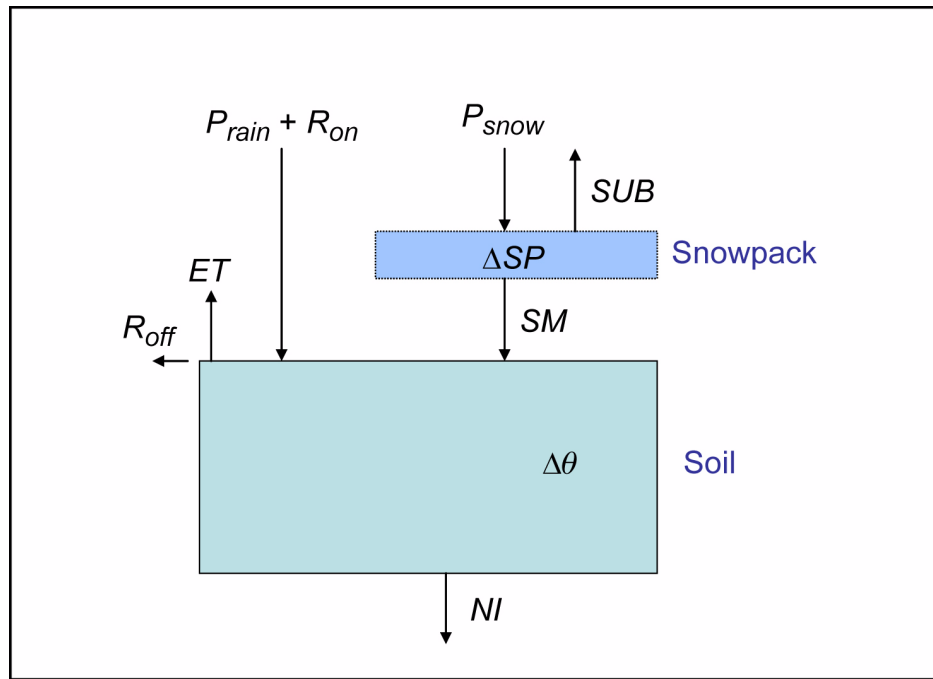
Figure 2.3.1-23. Schematic Showing the Water Reservoirs and Fluxes Included in the Water Balance
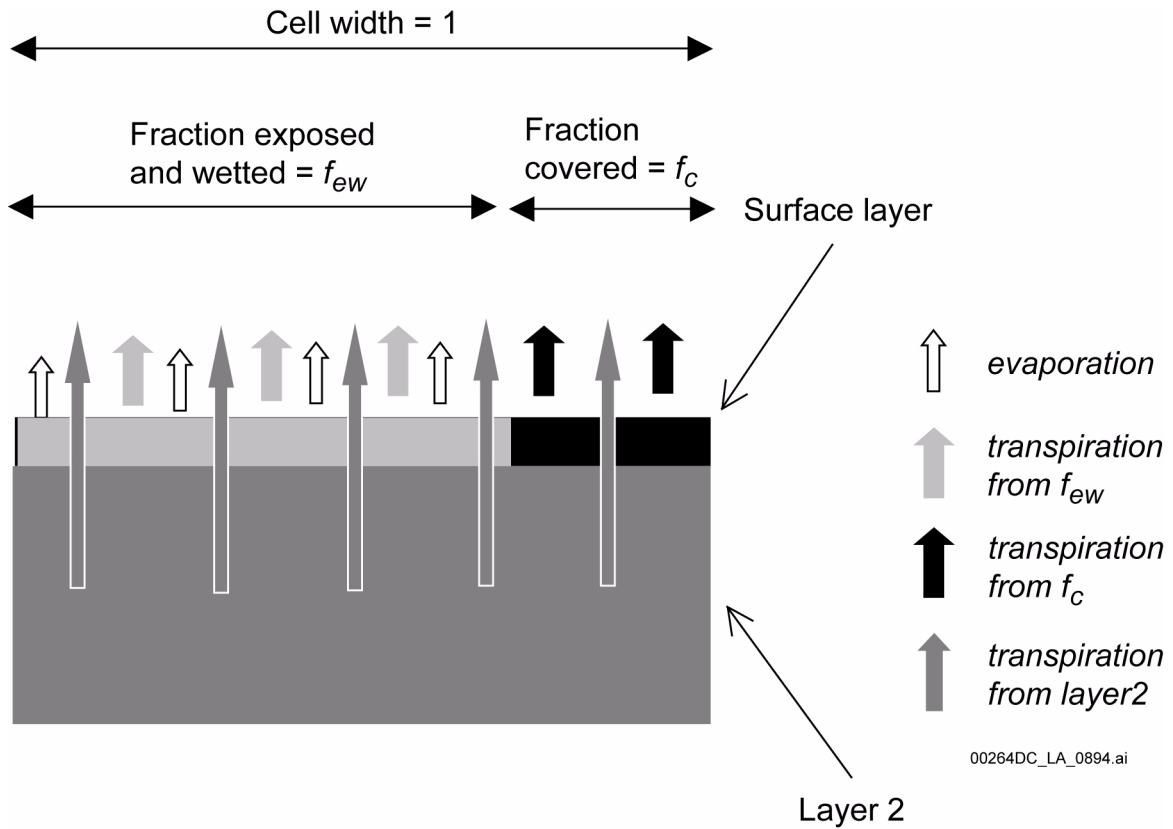
Source: SNL 2008a, Figure 6.4-1.

Figure 2.3.1-24. Evaporation and Transpiration from the f_{ew} and f_c Portions of the Root Zone

NOTE: Derived from conceptual model presented in Allen et al. 1998, pp. 135 to 158. A diffusive evaporation component is part of the transpiration from layer 2.
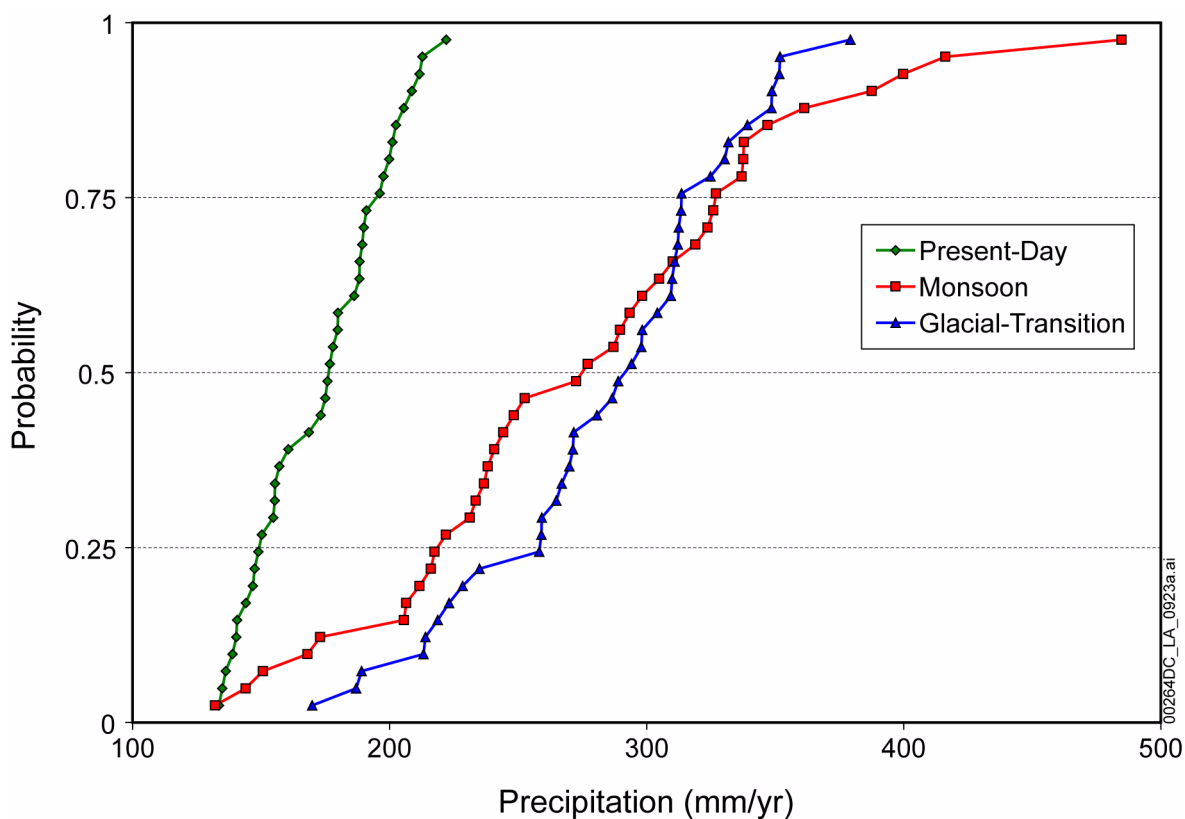
Source: SNL 2008a, Section 6.4.4, Figure 6.4.4-1.

Figure 2.3.1-25.   Cumulative Distribution Function of Precipitation for Present Day, Monsoon, and
Glacial-Transition Climates

NOTE: Figure is generated in Excel using precipitation data shown in SNL 2008a, Figures 6.5.7.1-1[a], 6.5.7.2-1[a],
and 6.5.7.3-1[a]. Data are ranked and plotted versus probability (rank/41). A total of 40 realizations (2 LHS
replicates) define the distribution.

Source: SNL 2008a, Sections 6.5.7.1[a], 6.5.7.2[a], and 6.5.7.3[a]; Figures 6.5.7.1-1[a], 6.5.7.2-1[a], and 6.5.7.3-1[a].
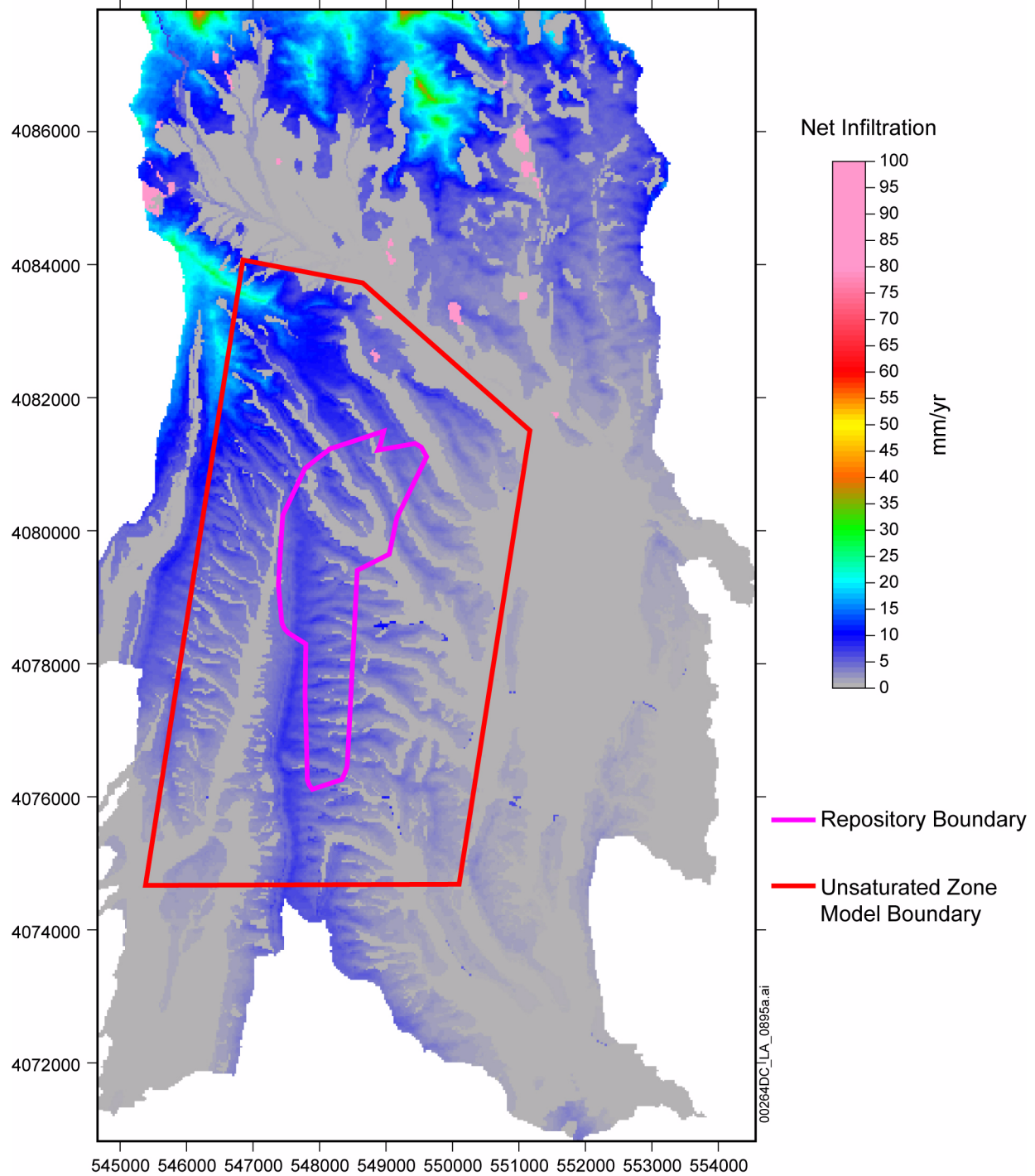
Figure 2.3.1-26. Present Day, 10th Percentile Net Infiltration Map (Replicate R2, Realization 10)

NOTE: Repository footprint is shown for illustration purposes only.
        UZ = unsaturated zone.

Source: SNL 2008a, Section 6.5.7.1[a], Figure 6.5.7.1-2[a].